Structural parameters and dynamics of lyotropic liquid crystalline phases in hydrated monolinolein

Tsing-Young Dora Tang

Department of Chemistry

Imperial College London

A thesis submitted for a degree of Doctor of Philosophy

20th July 2010

I declare that the work presented in this thesis is my own except where noted.

For Min Tang and Chin Lai

Abstract

To date, the stability of inverse bicontinuous cubic phases and the mechanism of lamellar to cubic transitions are poorly understood due to limited experimental resolution and reproducibility.

Systematic experimental data is imperative for reasonable testing and verification of established theoretical models in this area. This thesis focuses on two aspects of lyotropic phase behaviour; the equilibrium behaviour of lyotropic liquid crystalline phases and the transitions between the equilibrium states.

When monolinolein (ML) is mixed with water it forms a variety of inverse lyotropic phases, for example the lamellar, inverse bicontinuous phases (Q_{II}^{G} and Q_{II}^{D}) and the inverse hexagonal phase (H_{II}) which makes this lipid an ideal candidate for study of these phases. The monolinolein equilibrium phase behaviour has been characterised as a function of pressure, temperature and hydration using SAXS (small angle X-ray scattering) and the data used to verify the existence of the pivotal surface in the Q_{II}^{G} phase. Knowing the location of the pivotal surface allows one to calculate the total energy of these structures.

The second part of this thesis discusses the kinetics of the lamellar to Q_{II}^{G} transition in monolinolein under limited hydration conditions using the pressure jump time resolved X-ray diffraction technique. Lamellar to inverse bicontinuous cubic phase transitions are relevant to fundamental cellular processes such as membrane fusion and fission due to structural similarities of the mechanisms. The sequence of structural changes observed from kinetic experiments are discussed in relation to the Stalk Mechanism and the data analysed using a quantitative model.

Acknowledgments

My memory of the last few years has been sepearated into a series of events and milestones. The progression of these events would not have been possible without the people who have shared, guided and supported me over this journey and I would like to express my deepest gratitude to them.

Firstly, John Seddon and Richard Templer, who gave me the opportunity to work on a truly challenging and fascinating project. Under their supervision and with their wisdom, knowledge and support they have opened the doors of scientific research to me and have been truly inspirational. I would specifically like to thank Richard for his guidance and patience during the writing up period and John for always having an open door and for his time and patience during the proof-reading stage.

Professor Roland Winter; Christoph Jeworrek and Yong Zhai at the Univeristy of Dortmund for their invaluable help and use of the high pressure sample cell and densimeter.

To all past and present members of the membrane biophysics and liquid crystals group, it has been a real pleasure working with such a fun-loving, talented and sincere group of people.

Oscar Ces for his infectious enthusiasm for the subject and his friendship. Nick Brooks who has been so helpful and generous with his time, for his advice, assistance and support each day, specifically before, during and after the synchrotron trips and during the writing up stage. Adam Squires for helpful and enlightening discussions on cubic phases and their kinetics. Annela Seddon for her friendship and specific help proofreading aspects of this thesis. Gemma Shearman, Chandrasheckar Kulkarni who I have had the pleasure of working closely with on beamline alighnment and all things lyotropic and beamline alignment. Beatrice Gauthe whose assistence during synchrotron trips and on in house beamlines has been invaluable for the work undertaken. Thanks to team ESRFs, Nick Brooks, Oscar Ces, Beatrice Gauthe, Gemma Shearman, Josh Matthews, Suzie Squire, Claire Stanley, Natalia Goerhing, Duncan Casey and Arwen Tyler who have selflessly endured sleepless nights to acquire experimental data and have always make the whole experience more entertaining. Jess, Arwen, Claire and Nat for their friendship over the past few years and lively chats we have shared. To Rosa, Sowmya, Hanna, Chris, Steve, Charles, Charlotte, Sarra and Xav for making each day different.

Sabrina, Radha, Kenga, Rosi and Chung for being there during the dark times; Elton Jackson for his consistency and patience. Alan Tung for out of hours IT support. Andy McCafferty who has endured each day with me and helped me through the bad and good times.

Finally my family for their unconditional love and support; Joanne and Matthew for coming to my rescue on more than one occasion and providing me with somewhere to live; Eileen for her unwavering support and weekly food packages. My parents who believed that education gave options and choices for a better life and worked tirelessly and selflessly so that we could have that choice. None of this would have been possible without them.

Table of Contents

Abstract 3

Acknowledgments 4

Table of Contents 5

Chapter 1 : Introduction 10

1.1. Amphiphiles- definition, biological relevance 10

1.2 Theory of phase behaviour 12

1.2.1 Lipid aggregation ; Lateral stress profile 12

1.2.2 Lateral stress profile 14

1.2.3. Interfacial Curvature 16

1.3. Mesophases formed by monoacylglycerols. 17

1.3.1 The one dimensional lamellar phase 17

1.3.3 Inverse hexagonal phases 18

1.3.4 Inverse Bicontinuous Cubic Phases. 19

1.3.5. Fluid Isotropic 22

1.3.6. Relative curvature of the phases 22

1.4. Energetics and phase stability 24

1.4.1 Curvature elastic energy 24

1.4.2 Packing Frustration (g_{PF}) 26

1.4.3. Lyotropic phase behaviour 27

1.5 Measuring the curvature elastic energy from a surface: the neutral and pivotal surfaces 29

1.5.1 Finding the position of the pivotal surface-geometric models 30

1.5.2. The parallel interface model (PIM) 33

1.5.3. Constant mean curvature model (CMCM) 35

1.5.4 The pivotal surface and predicting lyotropic liquid crystalline phase behaviour. 37

1.6 Pressure and temperature: driving factors for phase transitions. 37

1.6.1 Why is so little known about the dynamics of phase transitions? 38

1.6.2 Lamellar to cubic transitions as models for membrane fusion 39

1.6.3 Stalk Model 40

1.6.3.1. The origins of the stalk. 40

1.6.3.2. The shape of the lipid stalk 41

1.6.3.3. From a stalk to a hemifusion diaphragm to a fusion pore 42

1.6.4. Cubic phases from fusion pores 43

1.6.4.1. Cubic to cubic phase transitions 44

1.7. Kinetics of lamellar to cubic phase transitions 45
1.7.1. Mechanisms 45
1.7.2 Cooperative unit 45
1.7.3 Quantifying lamellar to cubic phase transitions 46
1.8 Overview 51
Chapter 2 : Materials and Methods 53
2.1. Sample Preparation 53
2.1.1. Sample preparation for temperature dependent SAXS experiments 53
2.1.2. Sample preparation for pressure dependent SAXS experiments 54
2.2 Testing sample degradation using TLC 55
2.3 X-ray scattering 55
2.3.1 In house X-ray apparatus: Bede Microsource 56
2.3.2 Synchrotron experiments: ID02 59
2.3.2.1 High Pressure cell 60
2.4. Typical diffraction patterns for the lyotropic liquid crystalline phases 62
2.4.1 Lamellar phase 62
2.4.2 Inverse Hexagonal phase 63
2.4.3 Inverse bicontinuous cubics 65
2.5 Image analysis 67
2.5.1. Absolute Intensities 67
2.5.2 Obtaining lattice parameters from pixel position 69
2.5.3. Image visualisation: AXcess 71
2.6 Polarising Microscopy 73
2.7 High Pressure densimeter 74
2.7.1 Instrumentation calibration 75
2.7.2. Sample preparation for high pressure density measurements 76
2.7.3 Sample loading 76
Chapter 3 : Pressure and Temperature Phase behaviour of Monolinolein & Water 78
Abstract: 78
3.1. Introduction 79
3.2. Materials and methods: 80
3.2.1. Sample preparation 80
3.2.2. Methods: recalculation of water contents (pressure dependent studies) 83
3.2.3 Polarising microscopy:verification of phase boundaries at high temperatures 86
3.2.4 Methods: Obtaining rational equilibration times 88
3.2.4.1 Sample equilibration for temperature dependent experiments 89

3.2.4.2 Sample equilibration for pressure dependent experiments 90
3.2.5. Instrumentation 92
3.3 Results 92
3.3.1 Temperature-composition phase diagram 92
3.3.1.1. Comparisons to previous characterised Phase diagrams 98
3.3.1.2. Calculation of excess water points: 100
3.3.2 Pressure dependent phase behaviour in limited hydrated monolinolein 102
3.3.3 Equilibrium studies in the reverse direction: shift of pressure-temperature phase boundaries 105
3.4 Chapter Summary 106
Chapter 4 : Determination of the pivotal surface in the Q_{II}^{G} phase: comparison of the constant mean curvature model and the parallel interface model 108
Abstract: 108
4.1. Introduction: 109
4.2. Molecular volume of limited hydration monolinolein 109
4.2.1 Materials and Methods 110
4.2.2 Results 111
4.2.2.1. Molecular volumes at intermediate temperatures 113
4.2.2.2. Molecular volumes at intermediate pressures 114
4.2.2.3. Density at intermediate temperatures and pressure 115
4.2.3 Density measurement errors 116
4.2.4 Overview of density experiments 117
4.3. Obtaining A_n and V_n from model fitting 117
4.3.1. Method: fitting to geometric models 118
4.3.2 Results from Model fitting 121
4.3.2.1 Atmospheric pressure - function of temperature 121
4.3.2.2 Constant temperature and varying pressures 126
4.3.3. Discussion: The pivotal surface in fixed hydration Q_{II}^{G} phase: 136
4.3.3.1. Temperature effects on the location of the pivotal surface 136
4.3.3.2. Pressure effects on the location of the pivotal surface 138
4.3.3.2. Temperature effects on the cross-sectional area at the pivotal surface 139
4.3.3.3. Pressure effects on the cross-sectional area at the pivotal surface 140
4.3.4. Comparisons between the CMCM and PIM as descriptions for the pivotal surface geometry 141
4.3.4 .1. Atmospheric pressure, as a function of temperature 141
4.3.4.2. Constant temperature (30 ^{o}C) and as a function of pressure 143

4.3.5 Summary 145
4.4. Pressure and temperature effects on the lipid geometry and properties of the pivotal surface: overview 145
4.4.1 Effects of temperature and pressure on the lipid geometry: lipid length and headgroup area 146
4.4.2 Effects of temperature and pressure on the properties of the pivotal surface 148
4.5 Chapter summary 150
Chapter 5 : Structural transformations in lamellar to cubic phase transitions. 152
Abstract: 152
5.1.Introduction 153
5.2. Materials and Methods 154
5.3. Overview 158
5.3.1. Discussion: Structural behaviour of the intermediate and the Q_{II}^{G} phase 160
5.3.2. Structural behaviour of the Q_{II}^{G} phase 164
5.4. Chapter Summary 167
Chapter 6 : Kinetics of the lamellar to Q_{II}^{G} phase transition - model fitting to experimental data 168
Abstract: 168
6.1. Introduction 169
6.2. Materials and methods 173
6.2.1 Data analysis 176
6.2.2. Lamellar to Q_{II}^{G} phase transition - Avrami model 178
6.2.3 Exponential decay for lamellar phase decay: 184
6.2.4. Avrami fitting for the Q_{II}^{G} to lamellar phase transition: 186
6.3. Effect of Pressure Jump amplitude on the rate constant 188
6.3.1. Results: Summary of fitting parameters 189
6.3.2. Pressure jump amplitude effect on the rate constant 192
6.3.3 Ln k vs P_{amp} dependence: 22.1 wt% Water 192
6.3.4. Pressure dependence on the rate constant: 18 wt% water 197
6.3.4.1. Lamellar to Q_{II}^{G} transition at 18.1 ^{o}C 198
6.3.4.2 Q_{II}^{G} to lamellar transition at 11.8 ^{o}C 199
6.4. Physical meaning of dimensionality, *n* for nucleation growth mechanisms 200
6.5 Chapter Summary 203
Chapter 7 : Quantitative model for the kinetics of the lamellar to Q_{II}^{G} phase transition 204
Abstract: 204
7.1 Introduction 205
7.1.1 The model 206

7.2. Temperature correction for reverse transitions 208
7.3. Curvature of transition state ($H^{\#}$) 211
7.4. The cooperative unit 212
7.5 Activation energy 213
7.7. Volume of activation 215
7.7. Summary 217
Chapter 8 : Summary and further work 218
Bibliography 224
Appendix A 232
Appendix B 234
Appendix C 244
Appendix D 256

Chapter 1 : Introduction

1.1. Amphiphiles- definition, biological relevance

The word amphiphile originates from the Greek, where amphis means 'both' and philia means 'love' and describes the characteristics of a molecule containing both hydrophilic and hydrophobic components. One such molecule is a lipid, which has a hydrophobic hydrocarbon chain attached to a hydrophilic head group. Biology has exploited the amphiphilic characteristics of the lipid and utilised them as the main constituent of the cell membrane, where the lipids aggregate to form a fluid, permeable bilayer.

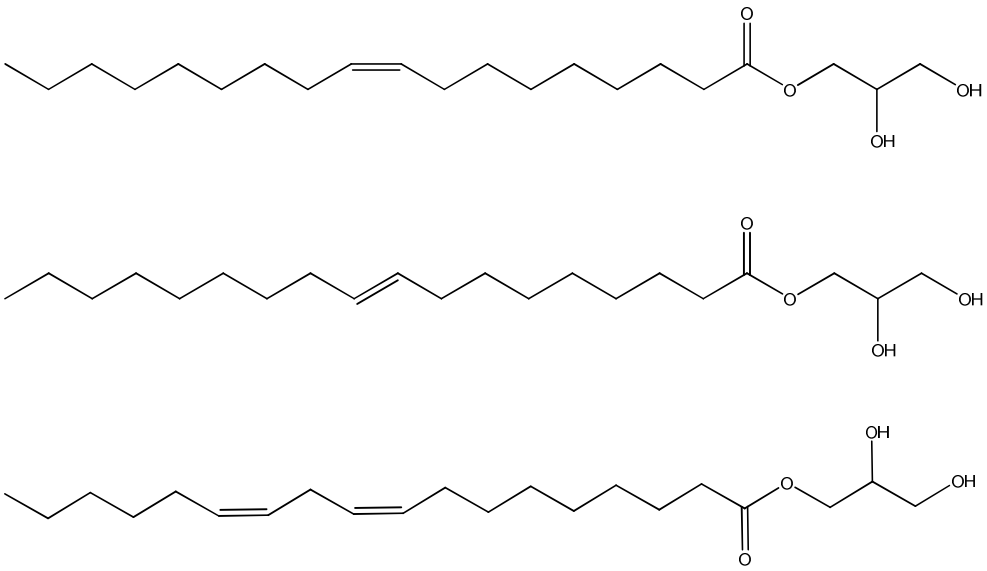


Figure 1.1 Molecular structures for monoacylglycerols: Monoolein (top) monoelaidin (middle) and monolinolein (bottom) whose structures differ from the saturation of the 18 carbon chain.

The variety of lipids found within the membrane allow the bilayers to adopt different curvatures which is believed to play an important role in membrane function and biophysicists have explored the role of curvature and lipid polymorphism in biological systems [1-5]. Microscopy data has shown that curved structures are present in biological structures [6-8], in cell membranes [4] and skeletons of sea-urchins [9] as well as in artificial systems such as lyotropic liquid crystals [10] and condensed inorganic mesoporous structures [11]. The observation of curved structures in different natural and synthesised examples highlights the importance of curvature on phase stability and function.

Within the cell there are hundreds of different types of lipid and it is believed that membrane curvature is induced by an asymmetry of lipids [12]. However under the correct conditions lipid bilayers consisting of one type of lipid are capable of forming a diverse variety of phases. In the monoacylglycerols it has been documented that they will form a variety of curved and non-curved structural phases when mixed with water [13-16].

The most well known example of a monoacylglycerol, is monoolein (MO) which has an 18 carbon chain, with a cis double bond on carbon 9, attached to a glycerol head group via an ester linkage. Different monoacylglycerols are defined by the length and degree of saturation of the hydrocarbon chain. For example monoelaidin (ME), has a trans double bond on carbon 9 of a 18 carbon acyl chain; in monolinolein (ML) there are two cis double bonds at carbon 9 and carbon 12 on a carbon 18 chain (Figure 1.1).

This thesis will focus on the phase behaviour of monoacylglycerols, specifically monolinolein. Monoolein with water is perhaps the most studied lipid system; consequently it has been the most widely used monoacylglycerol for technological processes [17-19]. The low cost and ready availability of the monoacylglycerols nominates these lipids as worthy candidates for materials in bio and nano technology [20, 21], however the lack of understanding with regards to their phase behaviour has thus far limited their exploitation. By continuing the work on the monoacylglycerols it will be possible to directly correlate differences in structure of the lipid to differences in mesoscopic behaviour, building a body of knowledge with the ultimate goal of fully predicting theoretical phase diagrams for any lipid system.

1.2 Theory of phase behaviour

1.2.1 Lipid aggregation ; Lateral stress profile

When lipid and water are mixed the head groups will favour complete submersion in water which is energetically unfavourable for the hydrophobic tails. The system will therefore arrange itself to minimise the hydrophobic interactions; this is commonly known as the hydrophobic effect [22, 23].

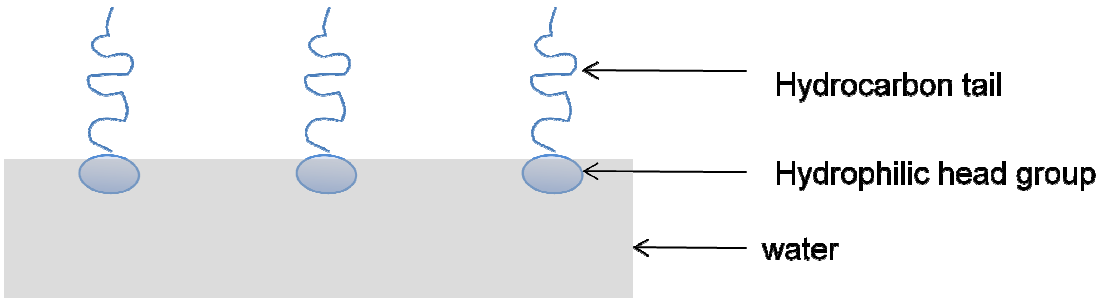


Figure 1.2 The hydrophobic effect will force the hydrocarbon chains away from water. At low lipid concentrations the head groups will be surrounded by water molecules and the hydrocarbon chains will project away from the water.

When the concentration of the amphiphiles is low (below the critical micelle concentration , CMC) the amphiphiles will arrange themselves along the water-air interface with head groups surrounded by water and the hydrocarbon chains exposed to the air. As the concentration of amphiphiles increases (above the CMC) the entropic cost of the molecules assembling is less than the energy of hydrating the hydrocarbon chains and it becomes energetically favourable for the lipids to form micelles. It is possible for the lipids to form two types of micelles, the first, known as Type I, describes curvature of the head groups toward the solvents, here the head groups will come together in the centre of the micelle and the hydrocarbons chains radiate outwards. The second is a Type II system where the head groups curve away from the solvent exposing the head

groups and the hydrocarbon chains meet in the centre of the micelle (Figure 1.3). Typically micelles will have monomer numbers between 30 and 200.

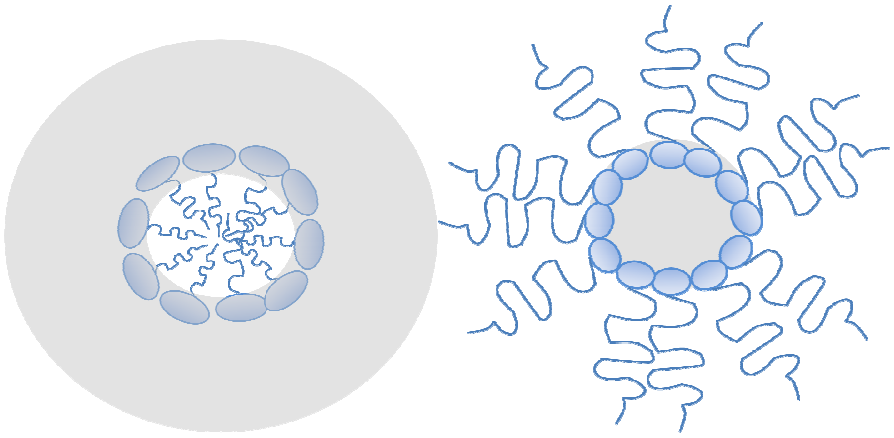


Figure 1.3 Depending on the structure of the lipid, micelles will either curve away from the water –Type I (left) or curve towards the water –Type II (right).

Curvature towards or away from the water will be dominated by the structure of the lipid. If the area at the head group is more than the area at the tail region Type 1 structures are favoured; if the head group area is greater than the area in the tail region Type II structures are favoured. Monoacylglycerols form Type II which are structurally biologically relevant.

An increase in micelle radius as concentration of lipids is increased becomes energetically unfavourable as voids form in the centre of the micelle. To accommodate for this, the micelle will change its shape, either by elongating or flattening to form cylinders or discs of lipid. When lipid concentration is increased further, the lipids become translationally ordered and form two coupled monolayers or a bilayer where the hydrocarbon chains have no contact with the aqueous solution and the hydrophilic head groups are exposed to the water (Figure 1.4).

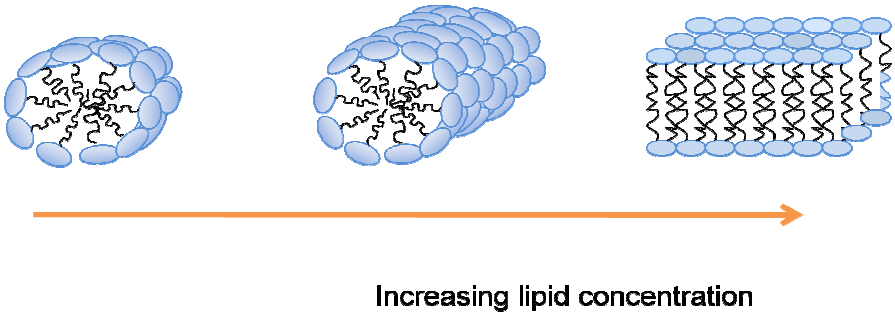


Figure 1.4 Increasing the lipid concentration will force the lipids to form different shaped aggregates, increasing lipid concentration from left to right sees a spherical micelle become cylindrical. When there is a high enough lipid concentration a lipid bilayer will form.

1.2.2 Lateral stress profile

When the lipid concentration is large enough to form bilayers, the molecules are close enough to laterally interact with one another and the lateral stress along the length of the lipid will vary.

Repulsions between the head groups will arise due to electrostatic, steric and hydration effects. The closer the head groups are, the greater the positive pressure (negative stress) in the bilayer as the repulsion effect increases. Interactions at the head group will be strongly dependent on the structure of the head group; if the head group has the ability to form H-bonds the head groups will be pulled together and the pressure will be negative (positive stress). At the interfacial region (where the polar region meets the apolar region) tension will arise as the lipids try to pack closely together to minimise the contact between the water and the hydrophobic tails leading to a large negative pressure in this region. In the tail region, collisions between the fluid chains leads to a positive pressure as the chains will try and repel one another (Figure 1.5).

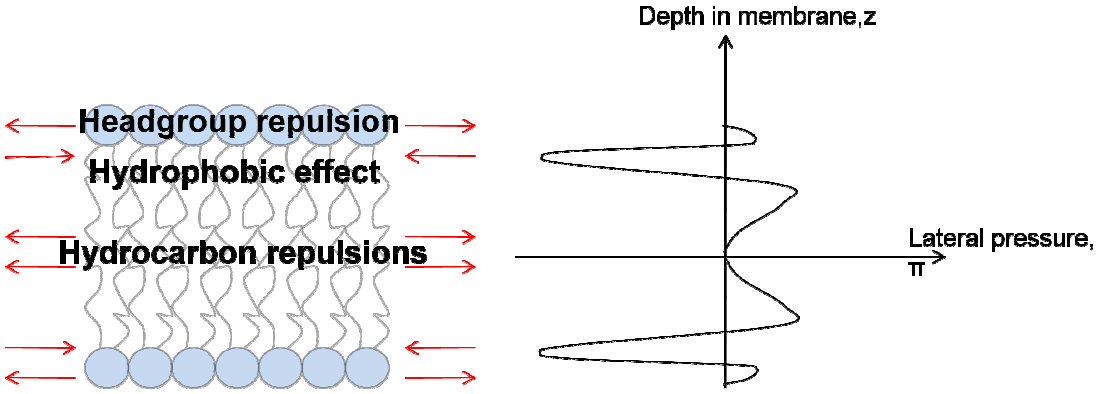


Figure 1.5 Due to the interactions between lipids in a bilayer, lateral stress will be experienced along the length of the lipid. The cartoon on the left demonstrates the pressures within the bilayer and the diagram on the right illustrates the lateral stress along the length of the lipid.

If the integral of the stress along the length lipid is not equal to zero, a bending moment or torque will be experienced in the monolayer. The torque tension is given by the first moment of the integral of the lateral stress (Equation 1.1).

$$\tau = \int -\pi\,(z)dz \neq 0 \qquad \text{Equation 1-1}$$

If the individual monolayers were to curve, voids would form between the bilayers creating a large energetic cost. To avoid this, the monolayers remain as flat bilayers but will have a desire to curve leading to *curvature frustration*. If the curvature frustration is large, the bilayer will change its topology to form a curved bilayer and a phase transition will take place. The spontaneous curvature is the curvature of a system when it is at its minimum energy and is proportional to the torque tension. In a Type II system the spontaneous curvature is negative.

1.2.3. Interfacial Curvature

Curvature, *C*, is defined mathematically as the reciprocal of the radius of curvature (Equation 1.2). The two principle curvatures, C_1 and C_2 are defined from a normal drawn from any point on a surface which are the maximum and minimum radii of curvature and are perpendicular to each other.

$$C = \frac{1}{R} \qquad \text{Equation 1-2}$$

The curvature of a surface can then be described through the mean *(H)* (Equation 1.3) and Gaussian Curvatures *(K)* (Equation 1.4). For a flat surface *H*=*K*=0 and for a cylindrical surface *K*=0 and *H* < 0. More complex structures can be described through the mean and Gaussian curvatures, for example for a saddle surface (Figure 1.6) *H*=0 and K< 0 where the principal curvatures are equal and opposite.

$$H = \frac{1}{2}(C_1 + C_2) \qquad \text{Equation 1-3}$$

$$K = C_1 . C_2 \qquad \text{Equation 1-4}$$

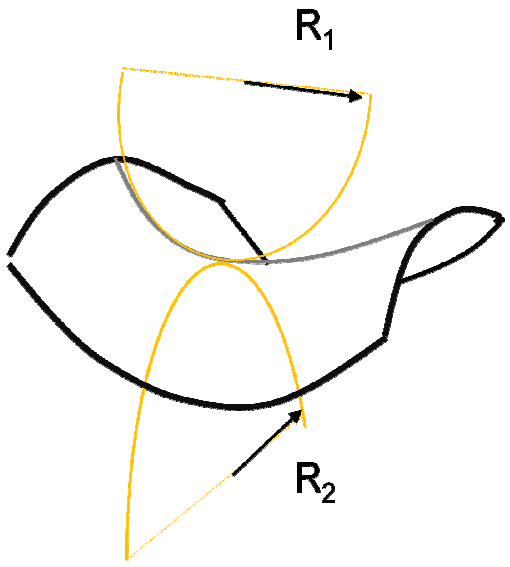


Figure 1.6 Schematic of a saddle surface with the principal curvatures shown and defined.

1.3. Mesophases formed by monoacylglycerols.

Monoacylglycerols form a variety of liquid crystalline phases with different curvatures and will be described in the following sections.

1.3.1 The one dimensional lamellar phase

The lamellar phase consists of stacks of bilayers separated by water channels, with the headgroups pointing towards the water and the tail regions away from the water (Figure 1.7). As the bilayer is flat, it can be seen that $H = 0$ and $K = 0$. There are a number of different lamellar structures whose structures differ through the mobility of the lipid. The two lamellar phases which will be discussed in this section are the lamellar gel phase and the fluid lamellar phase.

In the gel lamellar phase (L_β), the hydrocarbon chains are frozen in a straight and rigid conformation with a typical repeat spacing of 4.2Å. In this configuration there are small amounts of rotation about the molecular long axis and the head groups are disordered. In the fluid lamellar phase (L_α) the chains are fluid and have an increased number of trans-gauche rotamers in the hydrocarbon chain. The lipids are able to rotate freely in the molecular long axis and diffusion of the lipids occurs readily.

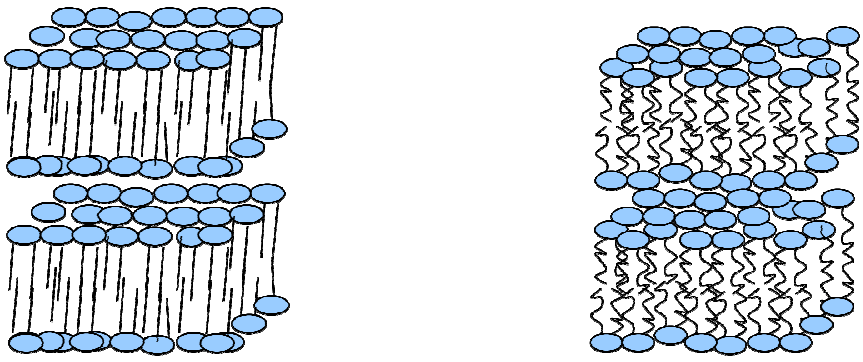


Figure 1.7 Cartoons of the lamellar gel phase (left) and fluid lamellar phase (right).

The lamellar phase has a repeating unit cell in one dimension consisting of a layer of water and one bilayer. The lattice parameter or d-spacing, a, can be defined by Equation 1.5.

$$a = d_L + d_w \qquad \text{Equation 1-5}$$

d_l is the bilayer thickness and d_w is the water layer thickness. The lipid volume fraction can be calculated from Equation 1.6.

$$\phi_L = \frac{d_L}{a} \qquad \text{Equation 1-6}$$

It is believed that in our model systems the lamellar phase will be in the form of multi lamellar vesicles (MLVs) [24].

1.3.3 Inverse hexagonal phases

The inverse hexagonal phase consists of cylinders of lipid, with the hydrocarbon chains radiating outwards which pack into a 2-dimensional hexagonal lattice where $H<0$ and $K=0$. Although the inverse hexagonal phase is not discussed in detail in this thesis it is observed in the phase diagrams of the monolinolein water system above 65^{o}C and above 28% wt water.

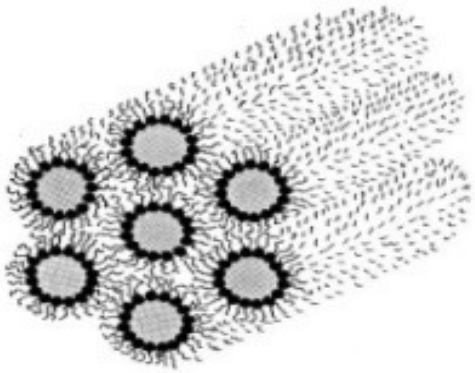
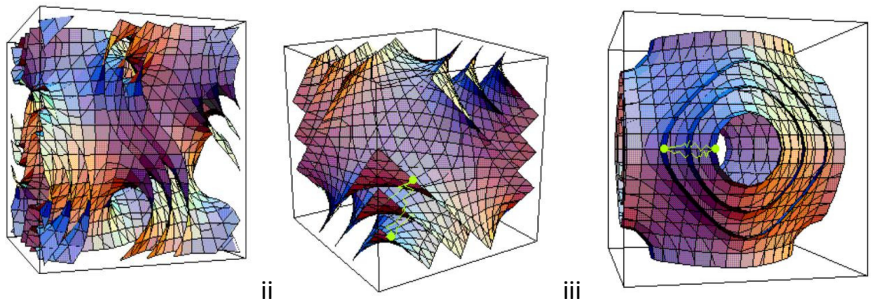


Figure 1.8 [25] Cartoon showing 2 dimensional hexagonal packing of cylinders of the H_{II} phase.

1.3.4 Inverse Bicontinuous Cubic Phases.

It has been widely recognised that bicontinuous structures are important in condensed atomic and molecular systems. The bicontinuous cubic phases are based on the Triply Periodic Minimal surfaces (TPMS), whose mean curvature is zero everywhere on its surface. There are a large number of mathematically found minimal surfaces, however this thesis is only concerned with the structures based on the D, G and P minimal surfaces [26, 27].

The lyotropic liquid crystalline phases consist of a single continuous bilayer whose midplane is draped over the minimal surface periodically dividing 3D space into two distinct water channels. The bicontinuous cubic phases form when $H=0$ and $K<0$ i.e. when $C_1<0$ and $C_2>0$ and the surface is a saddle surfaces.



i ii iii

Figure 1.9. [28] Unit cells Q_{II}^{G}, Q_{II}^{D} and Q_{II}^{P} phases (left to right) which are examples of inverse bicontinuous phases. Green lipids show the orientation of the bilayer.

The three cubic phases, relevant to this thesis are the Q_{II}^{G}, Q_{II}^{D} and Q_{II}^{P} phases; where G is the gyroid, D is the diamond and P is primitive and refers to the minimal surfaces on which these structures are based. The structures can be described through the genus, topology and dimensionless surface area, which enable us to characterise and differentiate between these structures.

The genus, g is a description of the number of 'handles' the structure contains, for example a gobstopper, with no handles will have a genus of 0; a ring donut contains 1 handle and has a genus of 1 and a pretzel, with 3 handles has a genus of 3. The 3 minimal surfaces, G, D and P all have a genus of 3 [26] which is the lowest topology encountered for a three-dimensional periodic network.

The Euler-Poincare characteristic χ describes the topology of a closed surface and originates from a description of polyhedra where

$$\chi \equiv V - E + F \qquad \text{Equation 1-7}$$

V is the number of vertices, *E* is the number of edges and *F* is the number of faces and can be related to the genus, *g*, by Equation 1.8.

$$\chi(g) = (2 - 2g)$$ Equation 1-8

For the minimal surfaces, G, D and P, $\chi = -4$.

The geometry (Gaussian curvature, *K*) can be related to the topology of the surface (χ) through the Gauss-Bonnet relation (Equation 1.9)

$$\int K\, dA = 2\pi\chi$$ Equation 1-9

A final description of the minimal surfaces is the dimensionless surface area σ_{TPMS} which is given by Equation 1.10.

$$\sigma_{TPMS} = \left(\frac{S_{TPMS}}{V_{TPMS}^{\frac{2}{3}}}\right)$$ Equation 1-10

where S_{TPMS} is the surface area of the minimal surface in a unit cell of volume V_{TPMS}. For the G, D and P minimal surfaces σ_{TPMS} are 2.42, 2.35 and 2.45 respectively.

Using these descriptions it is not apparent that the structures can be differentiated, however a distinction should be made between the unit cells of the minimal surfaces and the liquid crystalline phases, where the unit cells of the liquid crystalline phases do not correspond to the unit cells of the minimal surfaces. The former are more commonly described by their crystallographic space groups which describe the symmetry elements of the phase Ia3d (Q_{II}^{G}), Pn3m (Q_{II}^{D}) and Im3m (Q_{II}^{P}). The Q_{II}^{G} phase unit cell has twice the volume of the G minimal surface unit cell, the Q_{II}^{D} phase unit cell has half the volume of the D surface unit cell and the Q_{II}^{P} unit cell has the same volume as the unit cell of the P minimal surface unit cell. Consequently the geometric parameters *g*, χ and σ will differ and are summarised in Table 1.1. For the remainder of the thesis the phases will be referred

to using the liquid crystalline nomenclature i.e. Q_{II}^{G} for crystallographic space group Ia3d and minimal surface G.

Minimal surface	Space group	Phase	g	χ	σ
G	Ia3d	Q_{II}^{G}	5	-8	3.0915
D	Pn3m	Q_{II}^{D}	2	-2	1.9189
P	Im3m	Q_{II}^{P}	3	-4	2.3451

Table 1-1 Geometric parameters and nomenclature describing the inverse bicontinuous cubic phases.

1.3.5. Fluid Isotropic

The fluid isotropic L_2 phase has no long range order. The lipids form inverse micelles which are free flowing and isotropic throughout the sample and is typically seen at high temperatures when hydrocarbon chains are highly disordered.

1.3.6. Relative curvature of the phases

Figure 1.10 shows the relative mean curvature of the lyotropic liquid crystalline phases discussed in this thesis. The lamellar phase has zero curvature; the negative interfacial curvature increases from left to right where the curvature in the inverse bicontinuous cubic phases is less than the H_{II} phase but greater than in the lamellar phase. For the bicontinuous cubic phases the Q_{II}^{P} is the least compact with the largest water content and the Q_{II}^{G} phase, the most compact with the smallest water content. The fluid isotropic phase has the larger negative interfacial curvature compared to the H_{II} phase.

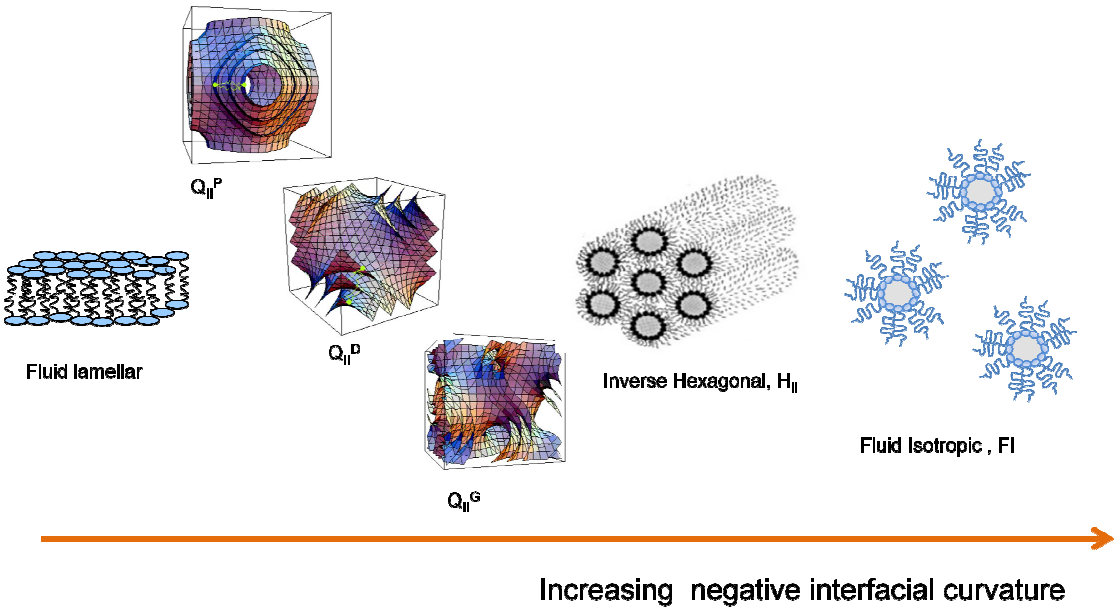


Figure 1.10 Schematic to show increasing negative mean curvature from left to right in phases observed in the monoacylglycerols. Where lamellar phase has the smallest curvature and the Fluid Isotropic phase the largest negative curvature in this series.

It is possible for Type II lipids to form more highly curved but structured phases than H_{II} and these are known as the inverse micellar phases. In these phases the lipids form micelles which pack either into a cubic array to form an Fd3M phase [29-32] or a 3D hexagonal array to form the $P6_3/mmc$ phase [33] .

1.4. Energetics and phase stability

The total free energy (G) of the observed structures can be considered in terms of three factors: the curvature elastic energy g_c; packing frustration, g_{PF}; and a third term, which accounts for other interactions such as hydration forces and electrostatic forces, g_{inter} (Equation 1.11).

$$G = g_c + g_{PF} + g_{inter} \qquad \text{Equation 1-11}$$

The final term is usually assumed to be zero when the inter bilayer spacing is greater than 5Å therefore only the curvature elastic energy and the packing frustration contribute to the free energy of the system.

1.4.1 Curvature elastic energy

The curvature elastic energy is defined as the energy cost associated with bending the membrane per unit area of bending and was first investigated by Helfrich in the 1970's [34]. In his analysis, he reduces the bilayer to an infinitely thin elastic sheet so it can be treated mathematically.

Changes to the curvature of the surface can be described in terms of the mean and Gaussian curvatures. The energy required to change the curvature of the membrane is dependent on the energy required to bend the surface and to change the Gaussian curvature and is described by Helfrich ansatz (Equation 1.12).

$$g_c = 2\kappa\,(H - H_0)^2 + \kappa_G K$$ Equation 1-12

κ is the bending modulus (units of J) and relates to the energy required to bend the surface, κ_G is the Gaussian Curvature modulus and is the energy required to change the Gaussian curvature (units of J). H_0 is the spontaneous mean curvature and describes the mean curvature when the system is at its lowest energy (m^{-1}). H is the mean curvature (nm^{-1}) and K is the Gaussian curvature (nm^{-2}). Collectively these parameters are known as the curvature elastic parameters.

It has been shown that the first moment of the lateral stress profile will give the bending moment of the bilayer (Equation 1.1). Further to this the curvature elastic parameters for a thin elastic sheet can be related to the lateral stress across a bilayer (Figure 1.5) [34, 35].

$$\kappa^b H_0 = -\frac{1}{2}\int_{-1}^{l} \pi\,(z)dz$$ Equation 1-13

$$\kappa^b = \frac{1}{2}\int_{-l}^{l} -\frac{\delta\pi(z)}{\delta H} z\,dz$$ Equation 1-14

$$\kappa_G^b = \int_{-l}^{l} -\pi(z)z^2 dz$$ Equation 1-15

Where -π (z) is the lateral stress at a distance z through the lipid film. κ^b is the bending modulus for the bilayer and κ_G^b is the Gaussian modulus for a bilayer.

The origin of the integration is taken at the bilayer midplane. For these integrals to be applicable in curved bilayers it is assumed that there is little or no stretching at the neutral surface, which will be discussed in more detail later sections.

1.4.2 Packing Frustration (g_{PF})

Packing frustration is best described through the example of the inverse hexagonal phase. In the hexagonal phase the membranes will curve to form long cylinders which pack together. As the cylinders pack together into a two dimensional hexagonal lattice, hydrophobic voids will form between the cylinders Figure 1.11. To fill the void, the system is forced to adopt a non-uniform interfacial curvature and the hydrocarbon chains will stretch or compress to fill the volume. This has a large energy cost (Figure 1.11).

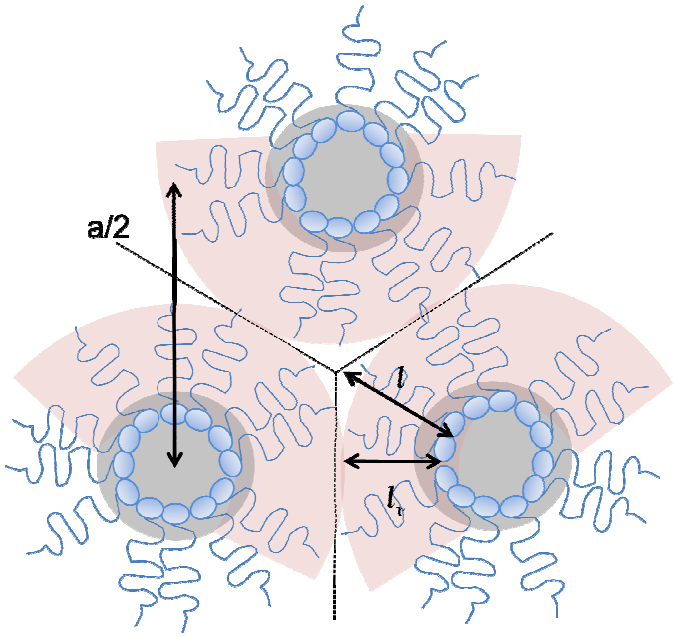


Figure 1.11 Cartoon to show the voids which arise from hexagonal packing which gives rise to packing frustration.

To calculate the packing frustration, the alkyl chain is assumed to act as a harmonic spring.

$$g_{PF} = \lambda\,(l^2 - l_r^2)a^2$$ Equation 1-16 [36]

where λ is the chain extension modulus, l, the monolayer width on the interface, l_r is the relaxed state of the hydrocarbon chain (l_r) and a is the lattice parameter.

Calculations of hexagonal packing have shown that empty voids account for approximately 9% of the hydrophobic interior and packing frustration for the H_{II} phase will be large. Generally, the inverse cubic phases will have a reduced packing frustration and the stability of cubic phases will be dependent on the contributions of the curvature elastic energy and the packing frustration.

1.4.3. Lyotropic phase behaviour

Little is understood about the relationship between the structure of the lipid and stability of the mesophase specifically in the inverse bicontinuous cubic phases. It is possible to determine the phase behaviour of lipid systems experimentally. One example is monoolein (Figure 1.12) whose phase behaviour was characterised by Briggs and Caffrey [37].

The lamellar phase is seen at low water contents and low temperatures, as water content is increased the curvature of the phase increases and inverse bicontinuous cubic phases form. At high water contents and high temperatures increased negative interfacial curvature is seen and the H_{II} phase forms.

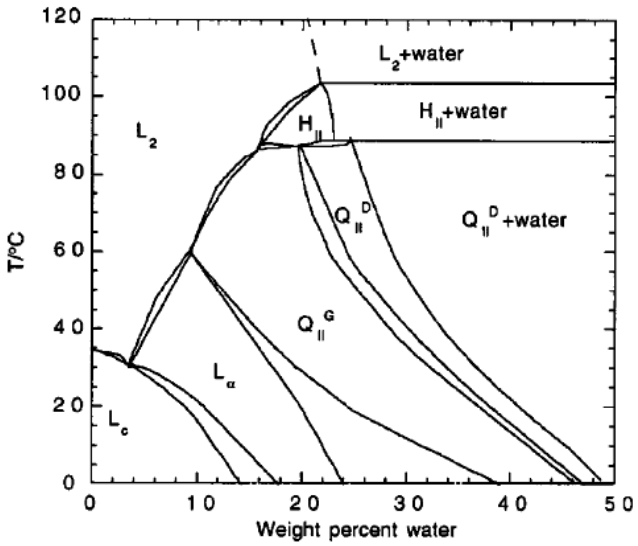
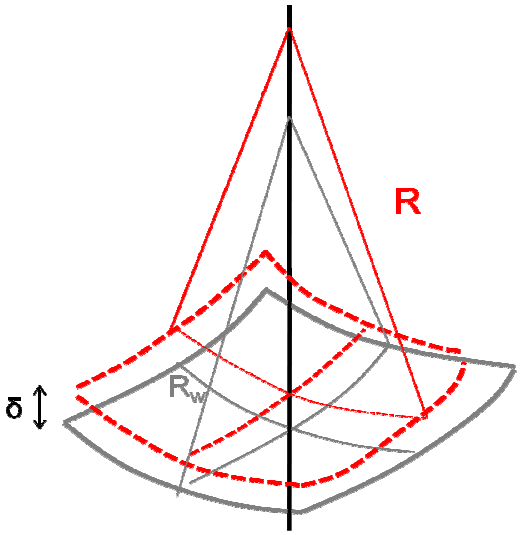


Figure 1.12 [37] Phase diagram for MO at varying water contents and temperature. L_2 is the fluid isotropic phase and L_c is the lamellar crystalline phase.

As lipid and water interactions are so complex it has been difficult to fully understand the factors which stabilise the Q_{II} phases and their existence and position in phase diagrams. Theoretical work in this area has postulated that the phase sequence from lamellar to Q_{II} phases is a result of competition between the hydrophobic effect and interactions between the lipid head group and entropy in the hydrocarbon chain. [38, 39]

1.5 Measuring the curvature elastic energy from a surface: the neutral and pivotal surfaces

The curvature of the monolayer will vary depending on the position in the bilayer from which it is defined (Figure 1.13). It is important to specify a surface within the bilayer where the curvature elastic energy can be measured from.



$$\frac{1}{R_w} < \frac{1}{R}$$

Figure 1.13 Cartoon to show the change in curvature depending on the position of measurement within the bilayer. Red dotted surface represents the bilayer midplane where the curvature will be greater than at the outer surface (grey surface).

One such surface is the neutral surface [40]-[41], defined mathematically, is the surface where the bending and stretching moments are decoupled. Another surface, where the curvature can be defined from, is the pivotal surface [42, 43]; at this surface the area will not change on monolayer bending and is defined experimentally. The pivotal surface will therefore be the subject of further discussion in this thesis.

The pivotal surface can be defined through three parameters, A_n, V_n and V which are the area at the pivotal surface, the distance between the pivotal surface and the minimal surface, and the molecular volume respectively and will be known as the pivotal surface parameters (Figure 1.14). In order to locate the pivotal surface, a relationship needs to be made between the lattice parameter, the local properties of the bilayer (molecular parameters of lipid) and the global properties of the mesophase (topology and geometry of the phase). These models will be discussed in more detail in the following sections.

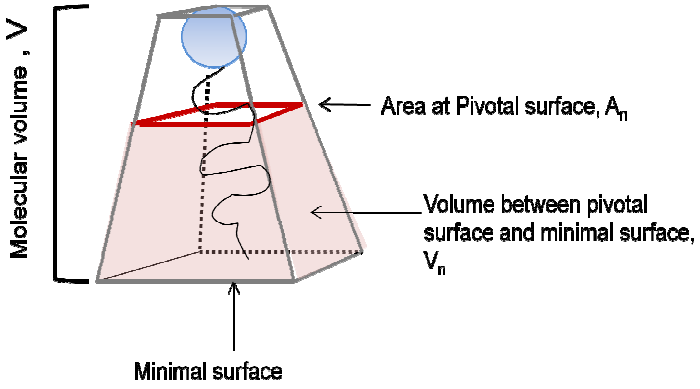


Figure 1.14 Cartoon to show the pivotal surface parameters V_n, A_n and V in a lipid.

1.5.1 Finding the position of the pivotal surface-geometric models

The presence of the pivotal surface has been observed in the inverse hexagonal phase [42] where its location was found based on the cylindrical geometry of the phase. Likewise, it is possible to locate the position of the pivotal surface in the inverse bicontinuous cubic phases using geometric models. To this end, two geometric models have been established, the constant mean curvature model and the parallel interface model [44]. In these models, the bilayer is forced to adopt particular geometries; the first, which is mathematically easier to model, describes a bilayer

configuration when the surface of the bilayer or pivotal surface is equidistant and normal to the bilayer midplane and is known as the parallel interface model (PIM). The second, the constant mean curvature model (CMCM), describes an interface where the bilayer and the pivotal surface are constrained to a constant curvature over the surface (Figure 1.15).

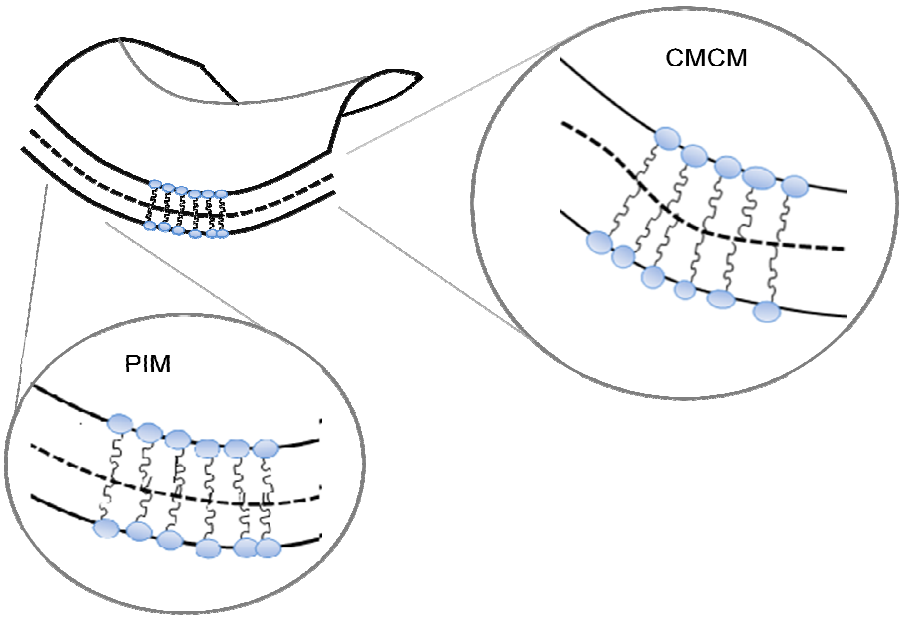


Figure 1.15 Cartoon to show the geometric differences in the parallel interface model (PIM) and the constant mean curvature model (CMCM). In PIM the bilayer is constrained equidistant and normal to the bilayer midplane and in the CMCM the bilayer is constrained to adopt a constant mean curvature interface.

It is likely that frustrations and energy costs will arise from these constraints. If the bilayer is constrained to a parallel interface, energy costs from curvature stress will dominate; if the bilayer is constrained to a constant curvature, the chain lengths of the hydrocarbon chains will vary across the monolayer and energetic costs from packing frustration will dominate. The existence of the pivotal surface has not been explicitly shown in the bicontinuous cubics and the location of the pivotal surface in bicontinuous cubics found using these models will be discussed in Chapter 4.

Theory has suggested that the PIM may be a good geometric and mathematical description for inverse bicontinuous cubic phases. The model predicts that the Q_{II}^{G}, Q_{II}^{D} and Q_{II}^{P} phases are related through the Bonnet transformation [45] where the Bonnet transformation provides a transition pathway for the triply periodic minimal surfaces. The Bonnet angle in the Weierstrass equations, (mathematical descriptions of the TPMS [46]) is changed to transform one minimal surface into another, and the minimal surfaces isometrically map onto one another. In this transformation the Gaussian Curvature, *K*, all angles, distances and areas on the surface are preserved. The experimental data have shown that the cubic phases coexist with the Bonnet ratio (where the lattice parameters of two cubic phases have a certain ratio of lattice parameters) [47-49]. However, whilst this model suggests that the three bicontinuous cubic phases are energetically degenerate, experimental evidence has consistently shown that the three cubic phases are stable as separate phases [50-52]. Therefore, the parallel interface model breaks down when the curvature is high and the lattice parameter is small. This can be rationalised by considering a patch that is parallel to the minimal surface with a measured chain variance. When the curvature increases in the system, the cross-sectional area of the patch will change and the variance in the hydrocarbon chain length increases. The frustration becomes so large that it becomes energetically unfavourable for the pivotal surface to remain parallel to the minimal surface [50] and it may prefer to adopt a different configuration such as a constant mean curvature interface.

Predictions made by the CMCM breaks the energetic degeneracy in the cubic phases [53] and predicts that the inverse bicontinuous phase will be seen, with increasing hydration, in the following sequence Q_{II}^{G}, Q_{II}^{D}, Q_{II}^{P}. This has been seen in the experimental systems of 2:1 LA/DLPC and monoelaidin with water [50, 51]. The fact that the cubic phases have not been seen simultaneously suggests that the bilayer and the pivotal surface will more likely lie at a constant mean curvature.

Most models developed to treat the pivotal surface problem in the Q_{II} phases have utilised the parallel interface model, however it is considered that the constant mean curvature model also plays a contributory role to the configuration of the bilayer and the pivotal surface and the bilayer sit somewhere between the two extremes.

A mathematical summary of the two models will be given in the following sections.

1.5.2. The parallel interface model (PIM)

The derivation of the parallel interface model was undertaken by applying the rules of differential geometry and will be briefly described here, full details can be found in [44].

The area of a patch *A(ξ)* on a parallel surface, ξ from the minimal surface is related to an original patch A(0) by :

$$A(\xi) = A(0)(1 + K\,\xi^2) \qquad \text{Equation 1-17}$$

where K is the Gaussian Curvature.

The volume occupied by the patch and its projection from the minimal surface is given by Equation 1.18.

$$v(\xi) = A(0)\xi\,(1 + \tfrac{1}{3}K\,\xi^2) \qquad \text{Equation 1-18}$$

The patch on the parallel surface *A(ξ)* can be translated to an area on the pivotal surface A_n, and $v(\xi)$ can be translated to V_n, the volume between the minimal surface, and the pivotal surface where ξ is the distance between the pivotal surface and the minimal surface.

In the parallel interface model the curvature is inhomogeneous over the surface and it is appropriate to define the Gaussian curvature, *K*, A_n and V_n as surface averages $<K>$, $<A_n>$, $<V_n>$ respectively.

Combining Equation 1.17 and Equation 1.18 gives

$$\frac{< A_n >}{< v_n >} = \frac{1}{\xi}\left(\frac{1 + < K > \xi^2}{1 + \frac{1}{3} < K > \xi^2}\right) \qquad \text{Equation 1-19}$$

<K> can be related to the geometry of the surface using the Gauss-Bonnet ratio (Equation 1.19).

$$< K >= \frac{2\pi\chi}{\sigma_0 a^2}$$

Equation 1-20

The variation of ξ with water volume fraction, ϕ_w, is determined from the following Equation 1.21 [54].

$$\frac{< v_n >}{< V >}(1-\phi_w) = \; 2\,\sigma_0\left(\frac{\xi}{a}\right) + \frac{4}{3}\,\pi\,\chi\left(\frac{\xi}{a}\right)^3$$

Equation 1-21

Combining Equations 1.19- 1.21 and solving gives a relationship between the lattice parameter (a), water volume fraction ($\emptyset_w$) of the phase and the pivotal surface parameters (A_n, V_n, V) (Equation 1.22).

$$a = \frac{V_n}{A_n \times (1-\phi_w)}\left(-2\sigma + \frac{2^{\frac{5}{3}}\sigma^2}{\left(4\sigma^3+9\pi\chi(1-\phi_w)^2\left(\frac{V_n}{V}\right)^2+3(1-\phi_w)\left(\frac{V_n}{V}\right)\sqrt{\pi\chi\left(8\sigma^3+9\pi\chi(1-\phi_w)^2\left(\frac{V_n}{V}\right)^2\right)}\right)^{\frac{1}{3}}} + \right.$$

$$\left. 2^{\frac{1}{3}}\left(4\sigma^3 + 9\pi\chi(1-\phi_w)^2\left(\frac{V_n}{V}\right)^2 + 3(1-\phi_w)\left(\frac{V_n}{V}\right)\sqrt{\pi\chi\left(8\sigma^3 + 9\pi\chi(1-\phi_w)^2\left(\frac{V_n}{V}\right)^2\right)}\right)^{\frac{1}{3}}\right)$$

Equation 1-22

ϕ_w is the water volume fraction and can be calculated from the water content (wt % water) from Equation 1.23.

$$\phi_w = \frac{C_w}{C_w + ((1 - C_w) * (\frac{\rho_w}{\rho_l})} \qquad \text{Equation 1-23 [54]}$$

Where C_w is the water content (wt% water); ρ_w is the density of water; ρ_l is the density of lipid.

From this derivation, the pivotal surface in an inverse bicontinuous cubic phase can be located by measuring the change in lattice parameter as function of the water volume fraction and fitting to Equation 1.22.

Estimates of the pivotal surface have been calculated for monoolein at 25°C using an earlier version of this model [55], the accuracy of the model was limited by the accuracy of the swelling data. Chapter 3 describes the acquisition of swelling data for monolinolein and water as a function of pressure and temperature where the lattice parameter, a, can be used to find the position of the pivotal surface.

1.5.3. Constant mean curvature model (CMCM)

The constant mean curvature model describes an interface where the bilayer and the pivotal surface are constrained to a constant curvature over the surface, the hydrocarbon chains are forced to stretch and compress to account for this and the variance in chain length requires energy. Like the pivotal surface model, relationships need to be made between the pivotal surface parameters and experimental data. Surface evolver [56], a programme which 'evolves' a surface to its minimum energy, was used to calculate the curvature, volumes and surface areas of the minimised constant mean curvature structures at varying water contents. The computed dimensionless surface area and curvature are obtained for surfaces with increasing water contents and the results are fit to a power series of ϕ_n ($\phi_n = \frac{v_n}{V}(1 - \phi_w)$), to obtain the relationship given in Equation 1.24 [36, 57].

$$S_n = a^2 \sum_{i=0} \sigma_i \phi_n^{2i}$$ Equation 1-24

Where S_n is the area of the pivotal surface; a is the lattice parameter and σ_i are σ_0 = 3.0915; σ_1 = -1.3317; σ_2 = -0.19974; σ_3 = -0.80113

The area of the pivotal surface of a monolayer in a unit cell is given by Equation 1.25.

$$S_n = \frac{A_n}{2} \frac{a^3(1-\phi_w)}{V}$$ Equation 1-25

Combining Equations 1.24 and Equation 1.25 the following relationship between the pivotal surface parameters (A_n, V_n, V), water volume fraction (φ_w) and lattice parameter is obtained.

$$a = 2 \sum_{i=0} \frac{\sigma_i [(\frac{v_n}{V})(1-\phi_w)]^{2i}}{(\frac{A_n}{V})(1-\phi_w)}$$ Equation 1-26

Using Equation 1.26, the properties of the constant mean curvature model can be obtained from experimental swelling data which has been undertaken for the monolinolein system and will be discussed in detail in chapter 4.

1.5.4 The pivotal surface and predicting lyotropic liquid crystalline phase behaviour.

The importance of the pivotal surface location has been discussed in Section 1.4.4., as a surface from which the free energy of the phase can be calculated from (Equation 1.11). An experimentally verified pivotal surface in the inverse bicontinuous cubic phases will make it possible to accurately calculate free energies for these structures. It is generally believed that compromises made between curvature elastic stress and packing frustration drive the stability of one phase over another; however, there is still some way to go before theoretical phase diagrams can be constructed for any lipid system. In addition, the dynamics of these phase transitions are poorly understood and work in this area is still in its infancy. The dynamics of phase transitions, specifically, the lamellar to Q_{II}^{G} transition, will be the focus of the latter part of this thesis.

1.6 Pressure and temperature: driving factors for phase transitions.

Changes to the structure of the lipid caused by a change in external parameters such as pressure or temperature will affect the distribution of lateral stress along its length leading to changes in curvature frustration within the bilayer. By increasing the temperature, the lateral stress in the chain region will increase as the number of repulsions between the hydrocarbon chains increases thus increasing the desire for curvature. When pressure is increased, the stress in the chains in the chain region reduces as the chains are physically compressed together.

Phase transitions can be induced by either a change in pressure or temperature, where change in an external parameter drives the system into a new configuration altering the preferred curvature and free energy of the system, consequently inducing a phase transition. There are several advantages of using pressure over temperature as the thermodynamic trigger.

1. Pressure propagates very quickly through the sample ensuring that any observations are due to the structural lipid rearrangements rather than the sample reacting to a thermodynamic change.

2. Pressure can be propagated effectively in both the forward and reverse directions.

3. The solvent properties in the system will not be significantly altered by changes in pressure.

1.6.1 Why is so little known about the dynamics of phase transitions?

The details of the mechanisms of a lamellar to cubic phase transition are still unclear despite the plethora of theoretical work that has been undertaken in this area [5, 58-66]. To begin to elucidate the mechanism of lamellar to cubic phase transitions and challenge the theoretical predictions, it is vital that there is a substantial body of experimental data.

In the past, the identification and use of a technique which was capable of detecting transitions on the millisecond scale was difficult. However, the advent of powerful synchrotron radiation sources such as the European Synchrotron Radiation facilities (ESRF) in Grenoble, Diamond Light Source (DLS) in Oxford and Soleil in Paris coupled to advances in camera technology have made X-ray diffraction an ideal tool for probing structural changes of lyotropic phase transitions [67] [68]. Further to this, lipid-water samples have been considered notoriously difficult to manipulate and make reproducible; these issues have been overcome [69] and it is now increasingly possible to acquire reliable time resolved data which means that there is a huge potential for advancement in this area.

1.6.2 Lamellar to cubic transitions as models for membrane fusion

In the cell, membrane fusion is a complex, but fundamental process where the cell membrane will change from a surface with zero curvature to negative curvature and then back to zero curvature again. It is generally considered that the membrane fusion process involves fusion proteins, enzymes and lipids where the fusion proteins and enzymes will promote fusion and the lipid matrix will undergo a structural rearrangement. SNARE (Soluble NSF (N-ethymaleimide Sensitive Fusion) Attachment Protein Receptors) proteins accelerate membrane fusion by bringing the two cells into close proximity to allow lipid rearrangement to occur; specific enzymes such as sphingomyelinase and phospholipase will promote fusion by catalysing the formation of lipids promoting negative mean curvature [70].

The lipid matrix plays an important role in membrane fusion by changing its structure and curvature. The ability for the cell membrane to change in this way is attributed to the self assembly properties of the lipids. It is often difficult to study the structural changes of the lipid matrix in cells due to the complexity of the cell membrane which consists of a variety of different classes of lipids, such as phospholipids, glycolipids and monoacylglycerols as well as various proteins. However, it is possible to undertake studies in model lipid systems to simulate changes in the lipid matrix and gain an understanding of mechanistic and kinetic processes that might occur during cell fusion. The structural changes that occur in the lamellar to cubic transition have been shown to share the same properties as those involved in membrane fusion [71] which means that lamellar to inverse cubic transitions are a good model system to investigate membrane fusion processes further.

Despite experimental difficulties, there has been a wealth of theoretical predictions for the mechanistic steps of membrane fusion and lamellar to cubic transitions [70-74]. The model which is considered most energetically feasible is the Stalk Mechanism which is discussed in the following sections.

1.6.3 Stalk Model

The notion of stalk theory arose in the 1980's when point defects were identified through freeze fracture electron microscopy between unilamellar vesicles [75]. The point defects were termed stalks and it was proposed that they were intermediates in membrane fusion. Through theoretical modelling of protein-free lipid systems a model for lamellar to cubic transitions has been postulated.

1.6.3.1. The origins of the stalk

As the bilayers come close together they will experience intermembrane forces, which arise from attractive Van der Waals forces, repulsive hydration forces and undulation forces. When the intermembrane forces are balanced the bilayers will typically be separated by 2 - 3 nm of water. When the intermembrane distance is small the hydration force are the most effective. For a point defect to occur these forces will need to be overcome and the bilayers are required to be close enough together for lipid rearrangement to occur. If the bilayer stacks are close together the thermal undulations will be sufficient enough for the outer membranes to interact and form protrusions Figure 1.16 [76]. The point like protrusions are precursors to stalks and are lower in energy and therefore do not affect the kinetic rate.

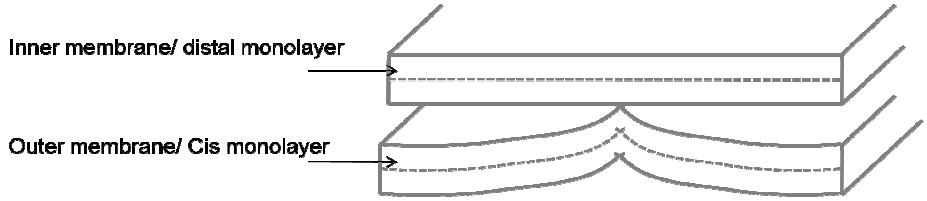


Figure 1.16 Cartoon to show a point defect where the outer membrane of one bilayer makes contact with the outer bilayer of the other bilayer.

In biological systems, the distances between cells are typically an order of magnitude larger than those seen in model systems, however the presence of SNARE proteins [77, 78] allows cell membranes to be brought close together for point protrusions to form.

1.6.3.2. The shape of the lipid stalk

Early predictions [79] of the shape of the stalk proposed that it was spherical (Figure 1.17 left), however the energy for a spherical stalk is too large due to the hydrophobic voids that would form (Figure 1.17). Further calculations of the stalk energy involved tilting the lipids which minimised the contact area filling the hydrophobic interstices effectively lowering the energy [62, 80]. It is believed that the stalk is the lowest energy contact between the two membranes.

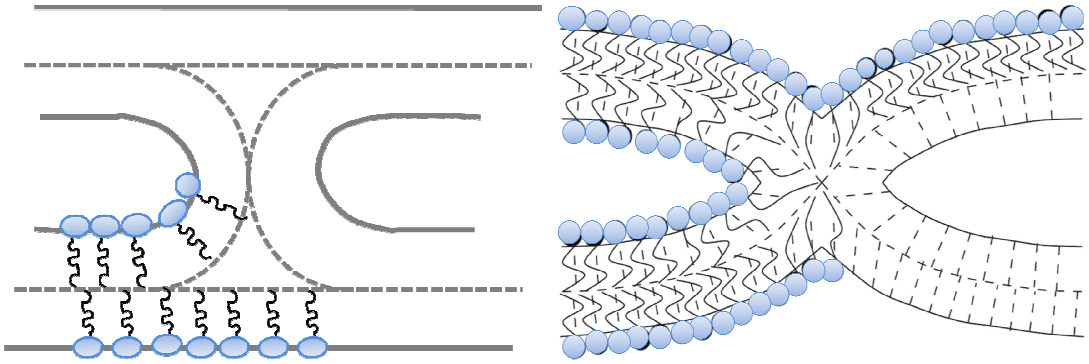


Figure 1.17 Cartoon showing the different structures hypothesised for the stalk. Left, spherical stalk with large hydrophobic voids has a very high energy. Right, stalk generated from tilting the lipids and minimising the contact area of lipids. This leads to a lower energy stalk than the spherical stalk.

The energy for a DOPC (1,2-dioleoyl-sn-glycero-3-phosphocholine) stalk of width 25nm was calculated to be 45 *kT* [81], for an equivalent stalk in DOPE (1,2-dioleoyl-sn-glycer0-3-phosphoethanolamine) the energy was calculated to be -30 *kT* [81]. The values suggest that spontaneous fusion occurs in DOPE which agrees with experimental results [82]. Further calculations undertaken on the DOPE-Me system by Siegel and Kozlov including a value for κ_G have predicted that stalk formation will occur at the same temperature as the appearance of inverted phases [83]. In addition a stalk intermediate has been identified in experimental systems [84, 85] which suggests that membrane fusion and lamellar to cubic phase transitions will progress via the stalk mechanism.

1.6.3.3. From a stalk to a hemifusion diaphragm to a fusion pore

Due to the orientation of the lipids, the stalk intermediate will experience tilt and bending deformations. Tension will arise and cause the stalk to expand forming a hemifusion diaphragm [82]. The diaphragm consists of a single bilayer composed of the inner leaflets of two bilayers (Figure 1.18 bottom). The newly merged membranes will have negative curvature and the presence of Type II lipids will favour the formation of a hemifusion diaphragm.

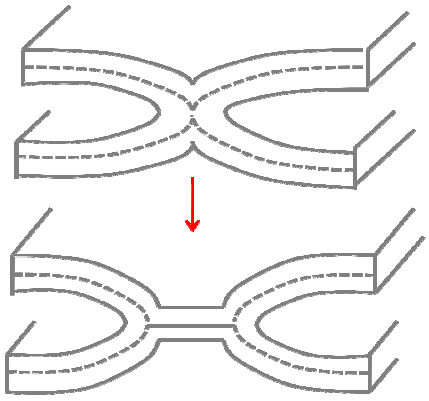


Figure 1.18 A stalk (top) will expand into a hemifusion diaphragm (bottom) due to the bending and tilting deformations experienced by the lipids which have formed the stalk.

The expansion of a stalk into a hemifusion diaphragm is driven by the decrease of the negative curvature energy of the outer monolayer; however, the hemifusion diaphragm is not energetically favoured as there is large curvature energy at the trans monolayer and perimeter of the intersection.

If the spontaneous curvature is sufficiently negative, a lateral tension will be generated close to the diaphragm rim (Figure 1.19 left); when the tension reaches a critical point it will be favourable for the bilayer to rupture and form a fusion pore or interlamellar attachment (ILA) (Figure 1.19 right). If the spontaneous curvature is not sufficiently negative an external driving force will be required to pull the hemifusion diaphragm apart, which is often provided by a protein. Once the fusion pore or interlamellar attachment has formed the content of the cell or water between the bilayers can move freely through the system.

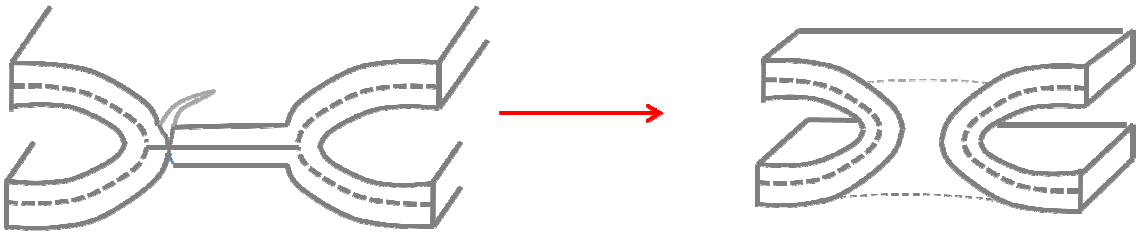


Figure 1.19 The hemifusion diaphragm will experience a large lateral tension at the rim as the lipids have a strong propensity for negative curvature. If the tension is large enough the diaphragm will rupture (left) and form fusion pore or interlamellar attachment (ILA) (right).

1.6.4. Cubic phases from fusion pores

Cubic phases form fusion pores or ILAs, however the mechanism by which this will occur is still unclear. It has been postulated by Siegel and Epand [86] that the fusion pores arrange into a square lattice which transforms into a Q_{II}^{P} phase. Conversion into the other cubic phases will occur after the initial formation of a Q_{II}^{P} phase. It is suggested that a square lattice of fusion pores will have a tendency to repel each other and it would be energetically more favourable for the fusion pores to

form a hexagonal array prior to Q_{II}^{D} formation. Indeed precursor Q_{II}^{D} and Q_{II}^{P} structures have been seen as intermediates in the lamellar to Q_{II}^{D} transition in excess water for monoelaidin system [69].

1.6.4.1. Cubic to cubic phase transitions

The Bonnet transformation provides a transition pathway for the triply periodic minimal surfaces and has been described previously. Whilst the Bonnet transformation is a good description of structure transformation in the minimal surfaces the mechanism of phase transformation is unlikely to go via this process as interconversion of the cubic phases via the Bonnet transformation would involve tearing and rearranging the surface which is physically unreasonable.

There have been two approaches to cubic to cubic transformations, the first describes mechanistic pathways via transformations of the underlying water channels [28, 87, 88] and occurs via pulling and stretching of the water channels. For example, the Q_{II}^{P} phase will transform into the Q_{II}^{D} phase when the 6-fold junction in the Q_{II}^{P} phase is pulled apart into two 4-way junctions of the Q_{II}^{D} phase, the surfaces will slowly rearrange due to changes in the underlying water channels. However, it has been found that intermediates involved in this transformation are high in energy and it is unlikely that cubic to cubic transformations progress via this mechanism.

The second approach involves rhombehedral and tetragonal distortions of the bilayer surface [89-92] as phase transformation takes place. The lipid-water interface is modelled to either the constant mean curvature model or the parallel interface model and distortions to the bilayer occurwhen the packing frustration and curvature stress are minimised. It is believed that cubic to cubic transitions are likely to go via this pathway as the energies of the intermediates are lower than those predicted via stretching of the water channels. However, there is currently no experimental evidence to support either of these transformations.

1.7. Kinetics of lamellar to cubic phase transitions

Development of a quantitative kinetic model for the lamellar to cubic phase transition has been hindered by experimental difficulties. These problems are being overcome and a quantitative model has recently been developed by Squires [93] for lyotropic liquid crystalline phase transitions.

1.7.1. Mechanisms

Phase transition mechanisms can be described through different kinetic processes: nucleation-growth, spinodal decomposition and Martensitic transformations. In this thesis, lyotropic phase transitions will be decribed through the nucleation-growth process. In the nucleation-growth mechanism, nucleation sites will form randomly and the sites will grow into domains of the new phase once an energetic barrier has been overcome. In this mechanism the new phase will grow at the expense of the old phase and the difference in the free energy between the new and old phases is the driving force for the transformation.

Part of the difficulty in quantifying lyotropic phase transitions is in identifying the kinetic mechanism the transition might follow. Chapters 5 and 6 of this thesis will discuss the mechanism most appropriate to describe the lamellar to Q_{II}^{G} transition in the monolinolein-water system.

1.7.2 Cooperative unit

The kinetics of phase transitions in lyotropic liquid crystals should be considered in terms of a transformation unit consisting of a number of lipids, rather than individual lipids. The definition and quantification of the number of lipids, N_{coop}, in a cooperative unit has been described by Schoppe [94].

Recently, Squires [93] has postulated another way in which N_{coop} can be obtained. This method involves the analysis of rates of the forward and reverse processes of the desired transformation pathway. This model will be discussed further in the subsequent sections.

1.7.3 Quantifying lamellar to cubic phase transitions

The basis of the Squires model can be described by the initial phase A and the final product phase B. For B to form, an energy barrier ($\Delta G^{\#}$) has to be overcome. The free energy of the initial and final energy will be dependent on the external parameters such as pressure or temperature. If pressure is the external trigger, increasing the size of the jump, forcing the system further and further into phase B will lower the energy of the transition state and the activation energy. Increasing the pressure change between the start and final materials causes the gap between the energy levels to decrease which lowers the energy of the transition state and increasing the rate of reaction.

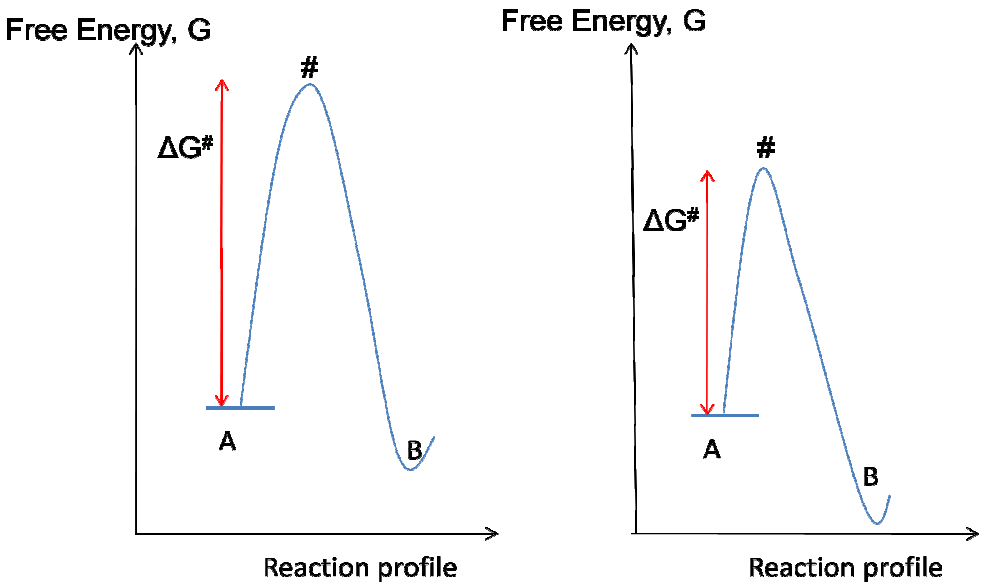


Figure 1.20 Schematics of reaction profile for a starting phase A and final product phase B with a transition state #. $\Delta G^{\#}$ is the activation energy required to reach the transition state from the starting phase. $\Delta G^{\#}$ can be reduced by jumping further into phase B either by pressure or temperature.

It is assumed in this model that the main driving force for the phase transition is a difference in curvature between the initial and final states, therefore changes in free energy (*G*) between the initial state A, final state B and the transition state (#) are solely attributed to changes in the curvature elastic energy and are given by equations 1.27 which was previously stated as equation 1.12.

$$g_c = 2\kappa\,(H - H_0)^2 + \kappa_G K \qquad \text{Equation 1-27}$$

κ is the bending modulus (units of k_BT) and relates to the energy required to bend the surface, κ_G is the Gaussian Curvature modulus and is the energy required to change the Gaussian curvature (units of k_BT). H_0 is the spontaneous mean curvature and describes the mean curvature when the system is at its lowest energy (m^{-1}). H is the mean curvature (nm^{-1}) and *K* is the Gaussian curvature (nm^{-2}).

The curvature elastic energy and therefore the free energy of the product (G^B) and the transition state ($G^{\#}$) are given by equation 1-28 and 1-29 respectively.

$$G^B = g_c^B = 2\kappa\,(H_B - H_0)^2 + \kappa_G K_B \qquad \text{Equation 1-28}$$

$$G^{\#} = g_c^{\#} = 2\kappa\,(H^{\#} - H_0)^2 + \kappa_G K^{\#} \qquad \text{Equation 1-29}$$

The molar free energy for a cooperative unit at the pivotal surface is given by Equation 1.30.

$$G = N_A N_{coop} A_n g_c \qquad \text{Equation 1-30}$$

Where N_a is Avogadro's number, N_{coop} is the number of lipid molecules in a cooperative unit, A_n is the area at the pivotal surface and g_c is the curvature elastic energy per unit area.

At the phase boundary, the $G^A = G^B$, and the difference between the activation energy and the initial and final states will be equal.

$$\Delta G^{\#\prime} = G^{\#\prime} - G^{A\prime} = G^{\#\prime} - G^{B\prime} \qquad \text{Equation 1-31}$$

Therefore for a transition from A to B, combining Equation 1.30 and Equation 1.31 gives Equation 1.32.

$$\Delta G^{\#}_{(p,T)} = \Delta G^{\#} + N_A N_{coop} A_n \left(\left(g^{\#}_{c\,(p,T)} - g_c^{\#\prime} \right) - \left(g_{A(p,T)} - g'_A \right) \right) \qquad \text{Equation 1-32}$$

where $\Delta G^{\#}_{(p,T)}$ is the activation energy at a given pressure and temperature.

Substituting Equations 1.28 and 1.29 into Equation 1.32 we obtain.

$$\Delta G^{\#}_{(p,T)} = \Delta G^{\#} - 4\kappa N_A N_{coop} A_n \left(\left(H_{0(p,T)} - H'_0 \right) (H^{\#} - H_A) \right) \qquad \text{Equation 1-33}$$

The activation energy can be related to the rate of the reaction by the Arrhenius equation

$$k_{AB} = F\, e^{\frac{\Delta G^{\#}_{(p,T)}}{RT}} \qquad \text{Equation 1-34}$$

Where *k* is the rate constant, *F* is the pre- exponential factor, *R* is the gas constant and *T* is the temperature.

Rearranging Equation 1.34 and substituting into Equation 1.33 gives

$$ln\, k_{AB} = ln\, F - \frac{\Delta G^{\#}_{(p,T)}}{RT} + \frac{4\kappa\, A_n}{RT}\, N_A N_{coop}(H^{\#} - H_A)\left(H_{0(p,T)} - H'_0\right) \quad \text{Equation 1-35}$$

and for the reverse direction

$$ln\, k_{AB} = ln\, F - \frac{\Delta G^{\#}_{(p,T)}}{RT} + \frac{4\kappa\, A_n}{RT}\, N_A N_{coop}(H^{\#} - H_B)\left(H_{0(p,T)} - H'_0\right) \quad \text{Equation 1-36}$$

In order to obtain quantitative descriptions of the transition state and the cooperative unit, relationships between experimental data need to be established.

From equations 1-35 and 1-36 plots of ln *k* as a function of H_0 will give straight lines with gradients

$$\frac{d}{dH_0} lnk_{AB} = \frac{4\kappa\, A_n}{RT}\, N_A N_{coop}(H^{\#} - H_A) \quad \text{Equation 1-37}$$

and

$$\frac{d}{dH_0} lnk_{BA} = \frac{4\kappa\, A_n}{RT}\, N_A N_{coop}(H^{\#} - H_B) \quad \text{Equation 1-38}$$

It is assumed that H_0 is linearly dependent on pressure which is a reasonable assumption as H_0 is linearly dependent on temperature [95].

$$C_p = \frac{dH_0}{dp} \quad \text{Equation 1-39}$$

And pressure dependence of ln *k* can be established.

$$\frac{d}{dp} lnk_{AB} = \frac{d}{dH_0} lnk_{AB} \frac{dH_0}{dp} = C_p \frac{d}{dH_0} lnk_{AB}$$ Equation 1-40

From equations 1-37, 1-38 and 1-40 a relationship between the ratio of the gradients of ln *k* plots as a function of pressure and the mean curvature of the transitions state, $H^{\#}$, can be made.

$$\frac{\frac{d}{dH_0} lnk_{AB}}{\frac{d}{dH_0} lnk_{BA}} = \frac{\frac{d}{dp} lnk_{AB}}{\frac{d}{dp} lnk_{BA}} = \frac{(H^{\#} - H_A)}{(H^{\#} - H_B)}$$ Equation 1-41

The mean curvature of the transition state can therefore be obtained from ln k vs Pressure plots for the forward and reverse phase transitions.

The number of lipids in a cooperative unit is obtained from the difference between dln *k*/d*P* in the forward and reverse directions.

$$\frac{d}{dp} lnK_{AB} - \frac{d}{dp} lnK_{BA} = C_p \frac{4\kappa A_n}{RT} N_A N_{coop} (H_B - H_A)$$ Equation 1-42

Where *Cp* is $\frac{dH_{0(p,T)}}{dp}$ and Equation 1.42 rearranges to

$$N_{coop} = \frac{\frac{d}{dp} lnK_{AB} - \frac{d}{dp} lnK_{BA}}{C_p \frac{4\kappa A_n}{RT} N_A (H_B - H_A)}$$ Equation 1-43

From the Squires model it would be possible to obtain quantitative descriptions of the transition state and the cooperative unit. However, the model only accounts for free energy contributions from the curvature elastic stress. In reality there will also be energy contributions from packing frustration of the hydrocarbon chains in the cubic phases. Analysis of experimental data for a Q_{II}^{G} to Q_{II}^{D} transition for monoolein at 30% wt water has been undertaken and it has been found that reasonable values have been obtained for the mean curvature and N_{coop}, where the cooperative unit has been calculated to consist of 4-10 unit cells. Chapter 7 will discuss the validity of the Squires model for describing lamellar to Q_{II}^{G} transitions.

1.8 Overview

Lyotropic liquid crystalline phases have been the topic of research for over 4 decades, however the energetics of the phases are still not entirely understood due to the complex interactions that arise when amphiphilic molecules are mixed with water. In particular, the inverse bicontinuous cubics based on the TPMS have been an intriguing problem for mathematicians, physicists and biophysicists. Understanding mesoscopic phase behaviour from molecular structure could have far reaching implications where amphiphiles can be exploited as advanced materials in nano and bio technologies.

In liquid crystals the energetic of phases can be calculated from the pivotal surface. However, the location of the pivotal surface in bicontinuous cubics has not been verified and is dependent on reliable experimental data. The first part of this thesis focuses on the phase behaviour of a model membrane system, monolinolein and water. The acquisition of equilibrium phase diagrams as a function of pressure and temperature (Chapter 3) serves two objectives:

1. In order to relate lipid structure to mesophase behaviour experimental phase diagrams need to be constructed. The construction of monolinolein phase diagrams adds to the body of research already undertaken in this area. [13-16, 96-99]
2. To obtain a substantial body of reliable lattice parameter data as a function of water content that can be used to confirm the existence of the pivotal surface in the inverse

bicontinuous cubic phases. In Chapter 4 the parallel interface model (PIM) and the constant mean curvature model (CMCM) will be used to calculate the position of the pivotal surface in a limited hydrated Q_{II}^{G} phase.

The second part of this thesis focuses on the dynamic behaviour of the lamellar to Q_{II}^{G} using the Pressure Jump time resolved X-ray diffraction technique. Understanding lamellar to cubic phase transitions could lead to a deeper understanding of the processes and energetics involved in fundamental cellular processes such as membrane fusion. This area of research is in its infancy as there has been limited reproducible experimental data available to establish a quantitative model of the lamellar to Q_{II}^{G} transition. However, experimental data from synchrotron radiation facilities will be used to discuss and present the following ideas:

- Q_{II}^{G} phase formation is limited by ILA formation whose rate of formation is affected by the external thermodynamic parameter. Once the Q_{II}^{G} phase has formed bilayer relaxation drives formation of the Q_{II}^{G} phase and its approach to equilibrium (Chapter 5)

- The growth and decay of phases involved in the lamellar to Q_{II}^{G} phase transition fit to nucleation–growth models such as the Avrami model (Chapter 6) which can be used to obtain rate constants of the transition.

- The Squires model can be successfully used to give a quantitative description of the lamellar to Q_{II}^{G} phase transition from analysis of rates obtained from fitting to experimental data from forward and reverse transitions. (Chapter 7)

The thesis will be concluded with a Summary and a brief Discussion of further work.

Chapter 2 : Materials and Methods

2.1. Sample Preparation

The requirement that samples should be homogeneous to produce reliable data has been discussed in detail in [100]. It has been found that different lipids may respond differently to sample homogenising techniques, for example Conn [100] states that ME (monoelaidin) and water require mechanical mixing to ensure sample homogeneity whereas MO (monoolein) and water will homogenise without mechanical mixing through successive freeze-thaw cycles. Chapter 3 discusses different techniques that have been undertaken to homogenise ML (monolinolein) -water samples. The most successful technique is outlined here.

Monolinolein was purchased from Larodan Fine Chemicals, Malmo, Sweden and used without further purification. Prior to use, the lipid was lyophilised for at least 24 hours in the dark to ensure complete removal of excess solvent.

2.1.1. Sample preparation for temperature dependent SAXS experiments

For in house, variable temperature experiments, lipid water mixtures were made directly in 1.5mm diameter special glass X-Ray capillaries (Gulmay Medical Ltd., Reading, UK). Lyophilized ML (typically 2 – 4 mg) was centrifuged to the bottom of the capillary and weighed. A known amount of HPLC-grade water (Sigma-Aldrich Co. UK) was then added to the capillary and centrifuged at 2400rpm for approximately 10 secs to ensure all of the water was at the bottom of the capillary and the sample was weighed to 6 decimal places. The water content (*wt%* water) of the sample was calculated using Equation 2.1.

$$C_w\,(\%\ wt\ water) = \frac{m_{H_2O}}{(m_{H_2O} + m_{lipid})}$$ Equation 2-1

The capillaries were flames sealed and further sealed with Silicon Sealant (Dow Corning Corp., USA) then left at room temperature in the dark for 5-6 hours to allow the silicon sealant to cure.

To homogenise the mixture, the samples were subjected to at least 30 freeze-thaw cycles across the chain melting transition, <0^{o}C. After every 5 freeze-thaw cycles, the sample was centrifuged at 2400rpm to ensure that all of the lipid mixture was at the bottom of the capillary. To test sample homogeneity, X-ray diffraction images were taken over the vertical length of the sample to ensure the lattice parameter was constant throughout the vertical scan. Once homogenised, the sample was stored at -20^{o}C until experiments were undertaken. The weight of the sealed capillary before and after each temperature scan experiment was noted to check for water loss from the capillary.

2.1.2. Sample preparation for pressure dependent SAXS experiments

For synchrotron based pressure dependent experiments, teflon spacers were used to contain the sample. These consist of a ring of teflon, with thicknesses of 1mm to 1.5mm with a central, 3 mm, diameter hole to contain the sample. Mylar windows are fixed to the teflon with double sided adhesive tape. These sample holders typically require larger quantities of sample (typically 50 mgs) compared to glass capillaries, although the diameter of the central hole can be reduced to reduce the required sample volume.

Specific water content samples of ML and water samples were prepared in a similar way to temperature dependent experiments: lipid and water were weighed into a glass vial which was then centrifuged. The sample vials were sealed with PTFE tape and parafilm to prevent water loss from the vial and subjected to over 50 freeze thaw cycles. More freeze thaw cycles were required for sample homogenisation compared to temperature dependent experiments due to the increased sample volume. Intermittently the samples were mechanically mixed and centrifuged

after every 15 cycles. The samples were stored at -20^{o}C and transferred to a teflon spacer immediately before the experiment.

2.2 Testing sample degradation using TLC

Monolinolein can degrade at the ester linkage which connects the acyl chain to the headgroup. Thin Layer Chromotography (TLC) was used to test for sample degradation and was carried out according to the standard procedure [101].

The solvent mixture consisted of 96:4 chloroform: acetone and the TLC plates were aluminium sheets with silica gel 60, F254 (Merck, Hertfordshire, UK). The sample was dissolved in the solvent mixture and spotted on the TLC plate 8mm from the base. The TLC plate was placed into a solvent bottle with a depth of 5mm solvent and the solvent was allowed to move up the front of the plate. Once the solvent had moved up 6/8 the length of the plate it was removed from the solvent bottle, allowed to dry and then sprayed with a mixture of sulphuric acid/nitric acid/water (4:3:3), left to dry and then heated.

When monolinolein has not degraded a charred smear appears at RF=0.29 which indicates unsaturated compounds, on degradation the monolinolein molecule will degrade into a glycerol head group, RF=0.93 and an acyl chain which appears as a smeared, charred line between 0<RF<0.29.

2.3 X-ray scattering

Lyotropic liquid crystals have long range order but individual molecules are not fixed onto their lattice points (short range disorder) with typical repeat unit cells ranging from 45 Å to 300 Å for structures studied in this thesis. They can be readily probed by X-rays which have a typical wavelength of 0.2 Å to 20 Å, typically X-rays with energies of 8 keV (1.54 Å) or 16.5 keV (0.7514 Å) are used for our experiments. When lipid-water samples are homogenised they will form evenly sized domains with different orientations which give rise to characteristic powder diffraction

patterns which differ according to the crystallographic space group and symmetry elements of the phase.

X-ray scattering is the main technique used in this thesis for the characterisation of lyotropic liquid crystalline phases. X-ray diffraction theory will not be discussed in detail here and the reader will be referred to the large array of published text books on the subject [102-104].

2.3.1 In house X-ray apparatus: Bede Microsource

Temperature dependent equilibrium studies were undertaken using the in house beamline, a Bede Microsource.

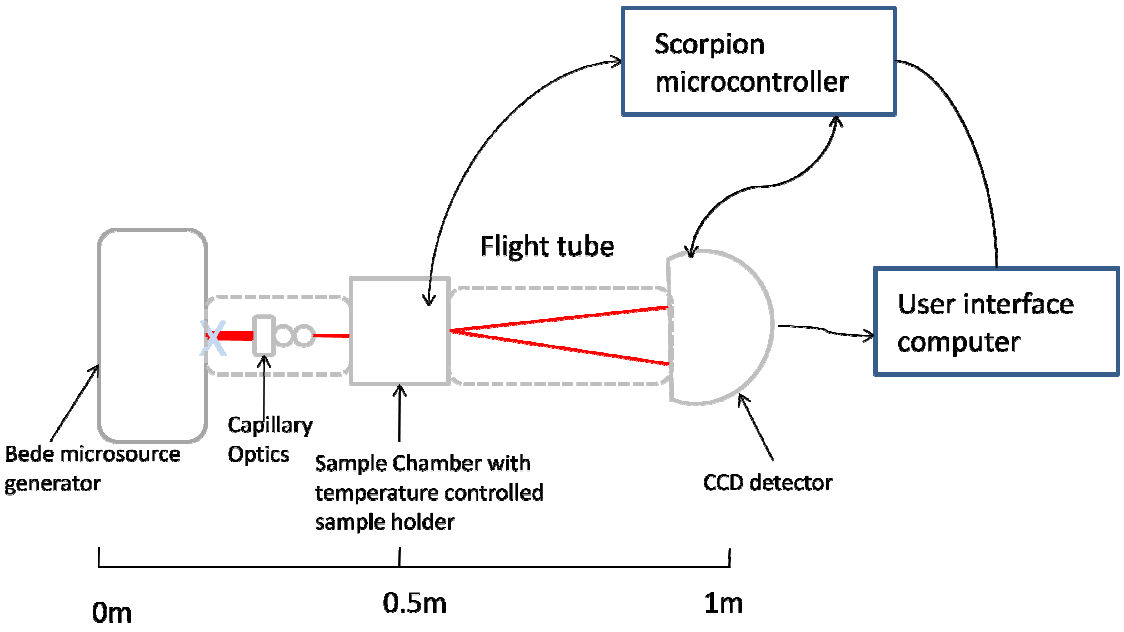


Figure 2.1 Schematic of Bede Microscource, an in house beamline designed and built by A. Heron and B Gauthe [105].

The Bede Microscource^{TM} (Bede, UK) has a copper anode and produces characteristic K_β (1.3922 Å) and K_α (1.542 Å) radiation. K_β radiation is removed by a Ni filter and the K_α radiation is focused onto the sample, within 1.5 mm glass capillaries, by monolithic polycapillary optics (X-ray Optical Systems, Inc., USA). The sample capillaries are held in a custom designed sample holder with Peltier driven temperature control (Melcor, USA). A Pt100 (TC limited, Uxbridge, UK) resistive thermosensor relays the temperature of the thermal jacket to a microcontroller which controls the temperature to ± 0.05 ^{o}C [105].

Diffraction images were acquired on a Gemstar intensified CCD detector (Photonic Science Ltd, Battle, UK) interfaced with a PC. The detector-PC interface used a digital LVDS (low voltage digital signal) Picasso PCI-LS frame grabber card (ARVOO imaging products, Netherlands).

In a CCD detector, the diffracted X-ray beams hit a phosphorous screen and are converted into visible light (Figure 2.2). These photons are amplified by an image intensifier and are then detected by CCD chip. The diffraction image is then relayed to a PC for processing (to correct for spatial distortion, dark current and other constant instrumental factors), storage and analysis. The CCD detector is connected to recirculating water to reduce background noise which can arise from heat generated at the CCD chip. The resolution of the diffraction images will be dependent on the detector pixel size and size of the X-ray beam.

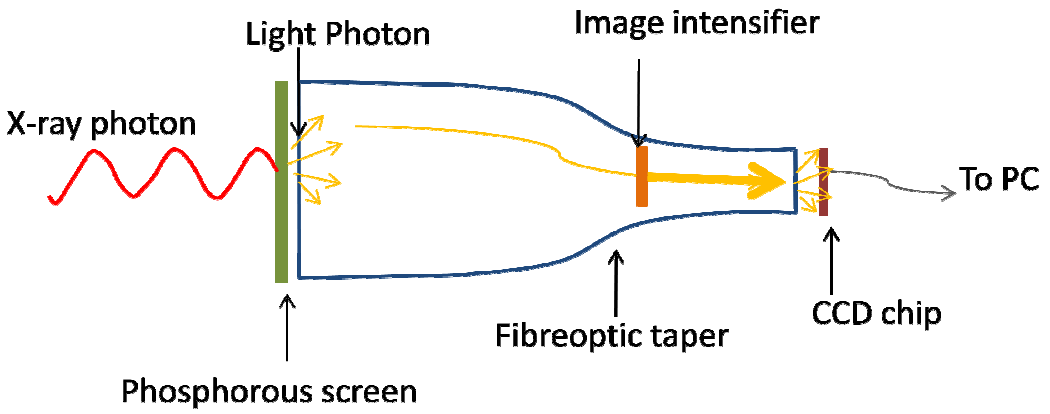


Figure 2.2 Schematic of a CCD detector where an X-ray photon will hit the phosphorous screen where it will be converted to visible light which goes down the fibre optic taper to an image intensifier where it is amplified. The intensifier emits brighter light which is detected by a CCD chip and relayed to a PC.

Automation of temperature control, waiting times and image acquisition was achieved using a Scorpion microprocessor which is interfaced to the computer and controlled through AXcess, written by A. Heron using the IDL language [106].

To prevent damage to the CCD detector, a lead beamstop is placed close to the detector to absorb the direct beam and enable the diffracted beam to be detected. The diffracted X-rays are less bright than the direct beam which would instantly oversaturate the detector. Long camera exposures are avoided; instead multiple images with short exposure time (typically 30 secs) are taken and summed.

For WAXS (wide angle X-ray scattering) experiments the detector was moved closer to the sample chamber and offset.

Using the Bede, it was possible to undertake temperature dependent SAXS (small angle x-ray scattering) and WAXS (wide angle X-ray scattering) experiments to map the ML phase diagram (see Chapter 3) however due to the length of exposure time required to obtain diffraction images, it is

not suitable for time-resolved studies. Time-resolved experiments were undertaken at ID02 beamline at the European Synchrotron Radiation Facility (ESRF), Grenoble.

2.3.2 Synchrotron experiments: ID02

Beamline ID02 at the European Synchrotron radiation Facility (ESRF) is a high brilliance, variable wavelength X-ray beam which has been used to probe out of equilibrium dynamics of soft matter such as lyotropic liquid crystals of Angstrom to micron length scales with a millisecond time resolution. A schematic of the beamline is shown in Figure 2.3

X-rays are produced by a triple undulator source which gives extremely high photon flux. The X-ray beam is monochromated by a liquid nitrogen cooled Si-111 monochromator and focused by a Rhodium-coated, double focusing toroidal mirror. The monochromator can select wavelengths between 0.155 nm and 0.073 nm.

For these experiments, a X-ray beam with λ = 0.07514 nm, dimensions of 200 µm x 400 µm and a maximum photon flux at the sample position of 4×10^{13} photons s^{-1} at 100 mA was used.

Diffraction images were recorded on a FreLon Kodak CCD detector which includes a FReLon (Fast-Readout, Low Noise) CCD with a maximum frame rate of 15 frames/sec. With this time resolution, it is possible to detect structural changes during lyotropic phase transitions.

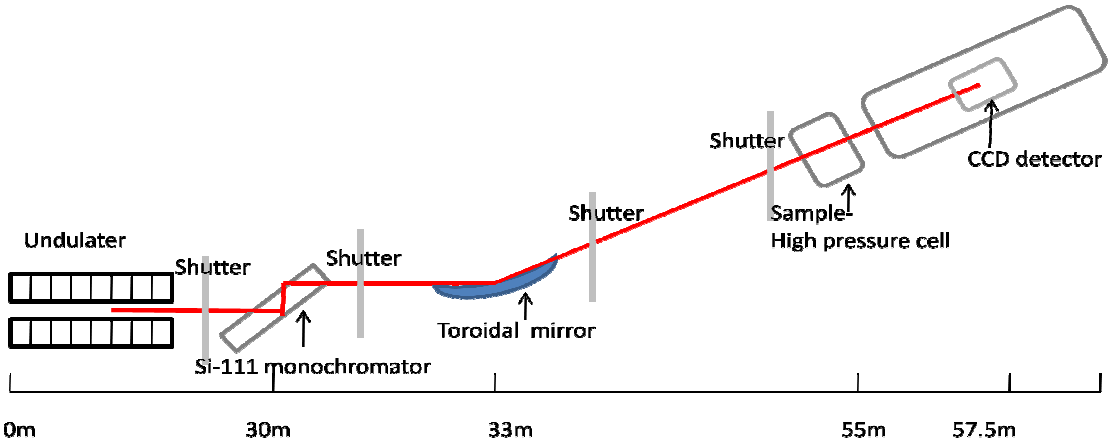


Figure 2.3 Schematic of the ID02 beamline (not to scale) at the ESRF, Grenoble, where the X-ray source is beyond the undulaters, which produce a high flux of X-rays. The X-rays are focused by a toroidal mirror onto the sample and the detector is placed beyond the sample to detect the diffraction pattern.

2.3.2.1 High Pressure cell

All experiments undertaken at ID02 beamline used a high pressure sample cell with diamond windows designed and built at the University of Dortmund [107]. The cell was designed specifically to facilitate time-resolved X-ray diffraction studies at synchrotron sources with a pressure jump time resolution of less than 7 ms. The pressurising medium is water and pressures of 1 bar to 4000 bar (accuracy ± 10 bar) can be achieved through a manual pumping system. The pressure of the system is measured through two calibrated strain gauge based full bridged pressure transducers (Sensotec Model UHP 721-03, Columbus OH). The cell (Figure 2.4) is constructed from a Ni-Cr-Co alloy, Nimonic 90 and its temperature is controlled via circulating water from an external water bath (accurate ± 0.2 ^{o}C). The cell temperature is measured using a thermocouple sensor embedded in the jacket of the cell. The sample is contained in a teflon spacer (described previously) and is surrounded by the pressuring medium; X-rays are allowed into and out of the cell through two flat diamond windows which are glued onto metal supports.

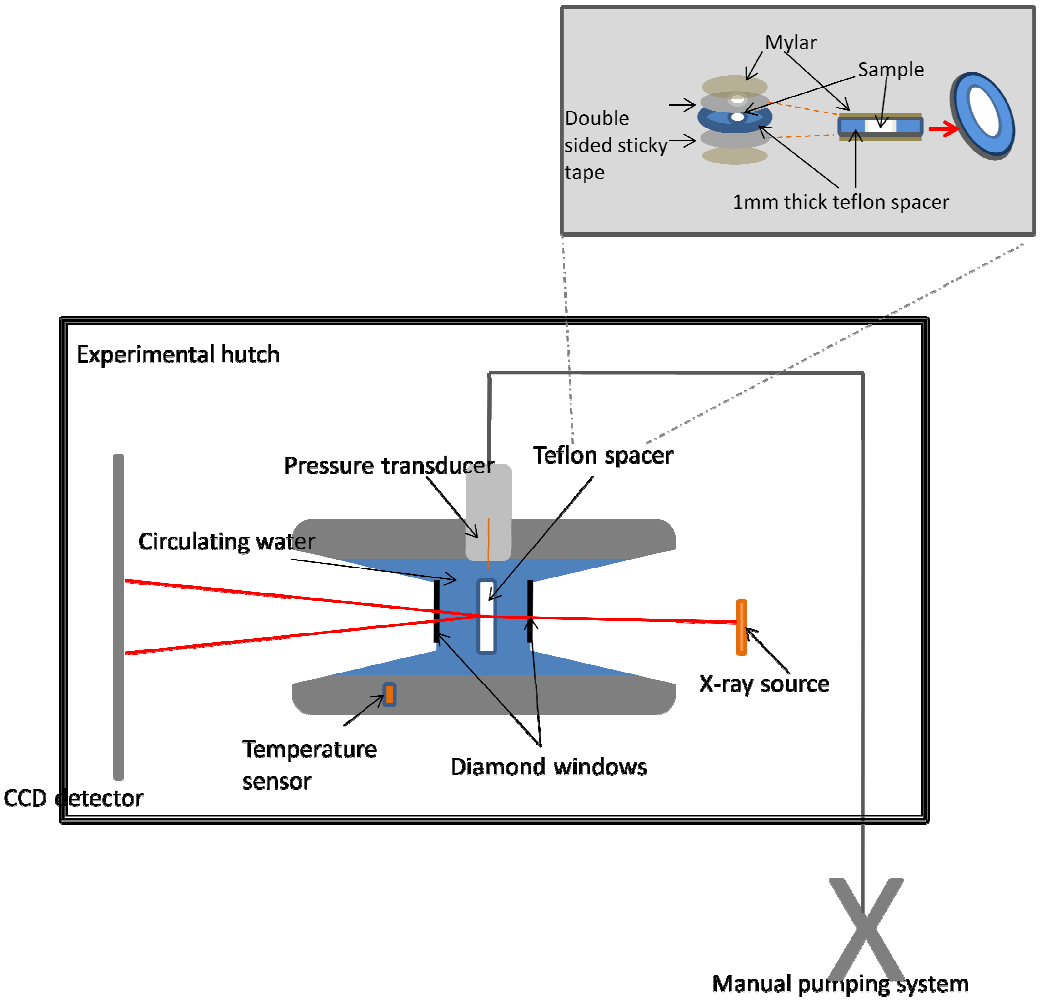


Figure 2.4 Cartoon of diamond pressure cell designed and built at the University of Dortmund. The X-rays penetrate a diamond window, then hit the sample. The resulting diffracted photons pass through the other diamond window and travel to the CCD detector. The sample held in a Teflon spacer is surrounded by the pressurising medium, water, and the pressure can be changed by an external pressurising pump. Pressure is measured by a pressure transducer and temperature is measured by a thermocouple.

2.4. Typical diffraction patterns for the lyotropic liquid crystalline phases

Examples of diffraction patterns are summarised in this section. Different phases have different symmetry elements which enable unambiguous identification of liquid crystalline phases provided that there are a sufficient number of visible reflections.

2.4.1 Lamellar phase

The lamellar phase, previously described in the Introduction, consists of a stack of bilayers interdispersed with layers of water with a repeat spacing of d where d is the bilayer repeat spacing (Figure 2.5).

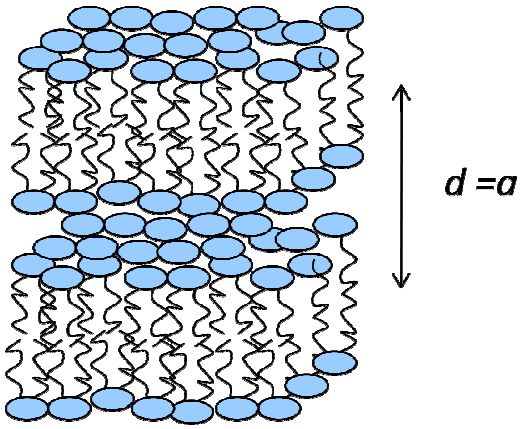


Figure 2.5 Cartoon showing the repeat spacing for the fluid lamellar phase.

The periodicity of the lamellar phase is one-dimensional therefore two of the Miller indices are always 0 and the reciprocal lattice is described by S_{001}. Diffraction from these planes gives rise to diffraction patterns with a series of concentric circles corresponding to hkl reflections: 001, 002, 003, 004 etc.

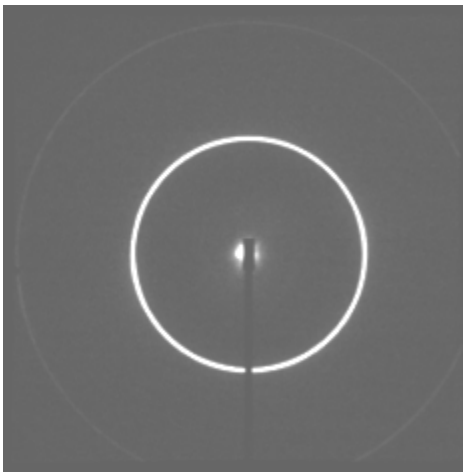


Figure 2.6 A typical diffraction pattern for the lamellar phase with a strong 001 reflection and a weak 002 reflection.

Different types of lamellar phases (for example gel and fluid) can be distinguished by differences in wide angle diffraction. Gel phases exhibit one or more sharp peaks at approximately 4.2 Å and the fluid lamellar phase shows a broad hump at 4.6 Å. These peaks correspond to ordering of the chains (gel-like or fluid-like).

2.4.2 Inverse Hexagonal phase

The inverse hexagonal phase is based on a 2-dimensional lattice, therefore the miller indices for one dimension, l, will be zero and the reciprocal lattice can be described by S_{hk}. The reciprocal spacings are related to the Miller indices by

$$S_{hk} = \frac{2(h^2 + k^2 + hk)^{\frac{1}{2}}}{\sqrt{3}\,a} \qquad \text{Equation 2-2}$$

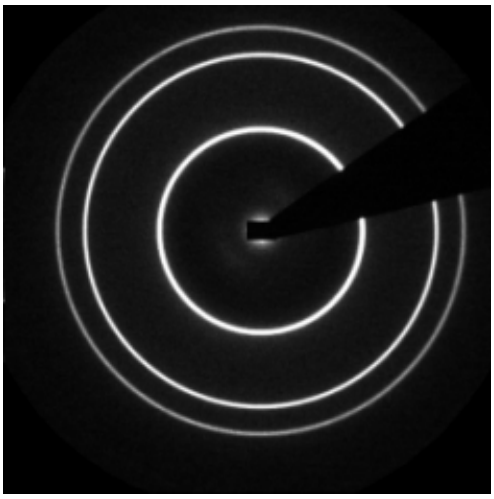


Figure 2.7 typical diffraction pattern for the inverse hexagonal phase with Bragg reflections with ratio √1: √3: √4.

The diffraction patterns appear in the ratio √1 (100); √3 (110); √4 (200); √7 (210); √9 (300); √12 (220) etc.

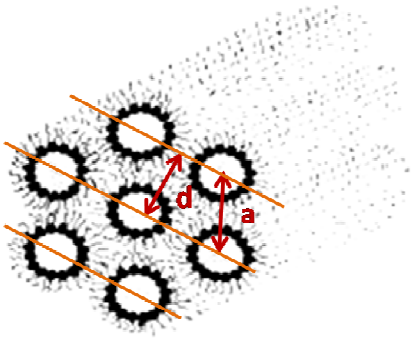


Figure 2.8 Schematic showing difference between lattice parameter, a, and the d-spacing, d, for the inverse hexagonal phase.

A distinction should be made between the lattice parameter, *a*, and the d-spacing, *d*, which is the distance between two parallel planes in a lattice (Figure 2.8), and the relationship between *a* and *d* is given by Equation 2.3.

$$a = \frac{2}{\sqrt{3}}\, d \qquad \text{Equation 2-3}$$

2.4.3 Inverse bicontinuous cubics

The inverse bicontinuous cubic phases have a 3-dimensional periodicity and the d-spacing, *d*, can be related to the reciprocal lattice spacings by Equation 2.4.

$$S_{hkl} = \frac{(h^2 + k^2 + l^2)^{\frac{1}{2}}}{a} \qquad \text{Equation 2-4}$$

Due to the symmetry selection rules for the crystallographic space groups Ia3d (Q_{II}^{G}), Pn3m (Q_{II}^{D}) and Im3m (Q_{II}^{P}), systematic absences will arise and some of the Bragg peaks are omitted, so characteristic diffraction patterns with peaks at specific ratios are seen. The ratios for each of the inverse bicontinuous cubic phases are shown inTable 2.1.

The lattice parameter of the unit cell for each inverse bicontinuous phase is given by $\frac{1}{S} \times (h^2 + k^2 + l^2)$.

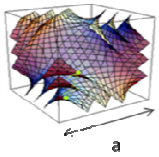
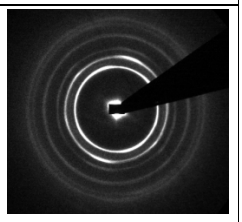
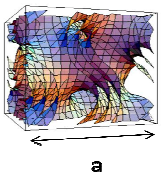
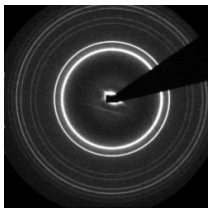
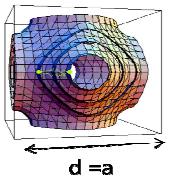
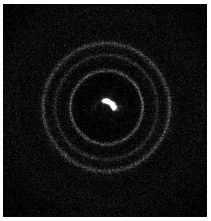
Phase/ (symmetry)	Ratio of peaks and corresponding miller indices [108]	Example diffraction patterns
Q_{II}^{D} (Pn3m) 	√2: (110) √3: (111) √4: (200) √6: (211) √8: (220) √9: (221) √10: (310)	
Q_{II}^{G} (Ia3d) 	√6: (211) √8: (220) √14: (321) √16: (400) √20: (420) √22: (332) √24: (422) √26 (431)	
Q_{II}^{P} (Im3m) 	√2: (110) √4: (200) √6: (211) √8: (220) √10: (310) √12: (222) √14: (321) √16 (400)	

Table 2-1. Characteristic peaks and diffraction patterns of bicontinuous cubic liquid crystalline phases in monolinolein and water.

2.5 Image analysis

Image analysis of diffraction patterns was undertaken using a programme written in LabVIEW by N. Brooks. It was possible to obtain absolute intensities and lattice parameters for each diffraction pattern using this programme.

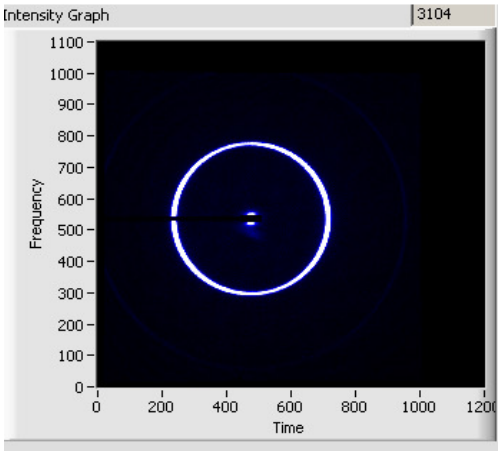
2.5.1. Absolute Intensities

To obtain absolute intensities, a number of corrections are applied to the X-ray diffraction. Some of these corrections are applied transparently by the beamline software before the diffraction image is saved.

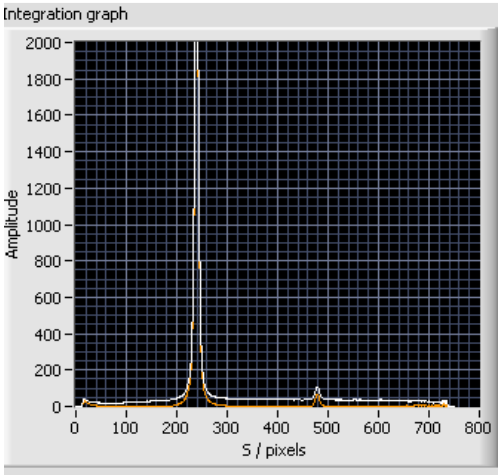
1. Subtraction of CCD dark image, which are images are taken without the beam with the same exposure time as the diffraction image and account for dark current in the detector.
2. Spatial distortion correction of the detector.
3. Flat field corrections where the image is normalised by a quantum efficiency matrix to account for slight variations in gain factor across the detector

After applying instrumental corrections, the diffraction image is saved and can be loaded into the LabVIEW programme (Figure 2.9 i) where image analysis can be undertaken. To convert the relative intensities into absolute intensities, background from parasitic scatter is removed and the intensity is divided by the sample thickness.

i)



ii)



iii)

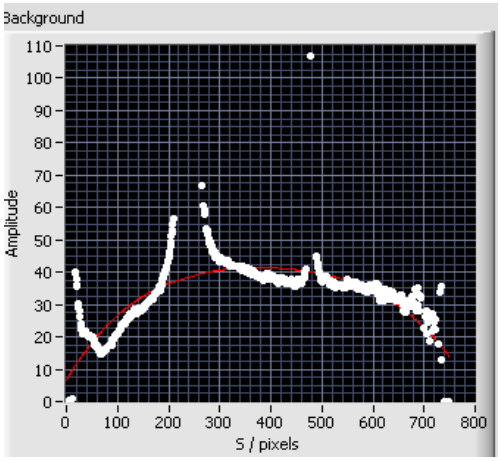


Figure 2.9 Examples of windows from the LabVIEW programme for image analysis i) diffraction images with dark image removal and spatial and flat field corrections. ii) radial integration of the diiffraction image (white) and with background removal (orange). iii) polynomial fit (red) to integration data with gradient threshold below 1 rad^2 m^{-1} pixel^{-1}.

Once the image has been loaded into the programme (Figure 2.9 i), a radial integration from the centre of the diffraction pattern is carried out to produce a one dimensional integration graph (Figure 2.9 ii). To obtain an approximate background, a 4th order polynomial is fitted (Figure 2.9 iii red line) only to the integration data which have an absolute derivative below a threshold gradient of 1 rad^2 m^{-1} pixel^{-1} (Figure 2.9 iii white); this aims to model the scattering which does not give rise to sharp diffraction peaks. This model background is then subtracted from the original integration graph (Figure 2.9 ii orange plot).

A plot of intensity against pixel position, P, is then output to Excel where the absolute intensities can be obtained by dividing by the measured sample thickness.

2.5.2 Obtaining lattice parameters from pixel position

The LabVIEW programme outputs the absolute intensity at pixel position, P. The pixel axis can be converted to a scattering vector by calibration with silver behenate (AgBe) which has a known repeat d-spacing of 58.38 Å. From the calibration the sample to detector distance can be calculated in terms of pixels and then converted to Å by following the subsequent steps:

1. Using Bragg's law (Equation 2.5) the scattering angle for AgBe can be calculated, as λ and d are known (0.7514 Å and 58.38 Å respectively).

$$\lambda = 2\, d\, sin\theta \qquad \text{Equation 2-5}$$

2. The first peak position for AgBe is found at 190 pixels. Using trigonometry (Figure 2.10) the sample to detector distance can be calculated in pixels (Equation 2.6).

$$tan\, 2\theta = \frac{190}{A} \qquad \text{Equation 2-6}$$

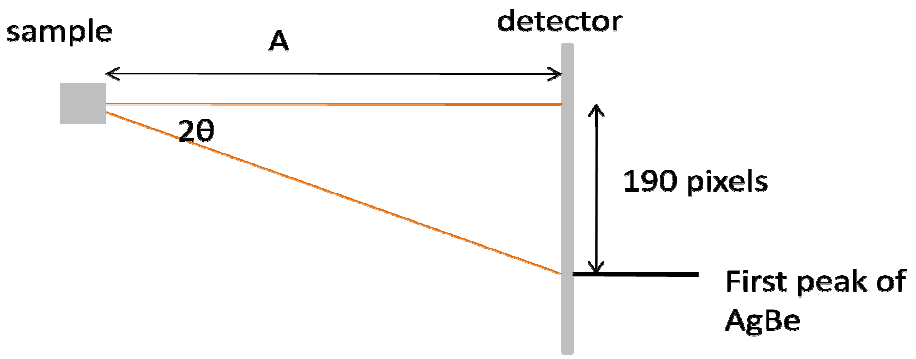


Figure 2.10 Schematic of sample to detector calibration for AgBe where the scattering angle $\boldsymbol{\theta}$ *is obtained from Bragg's law and the sample to detector distance in pixels is calculated from trigonometry.*

3. Having obtained the sample to detector position, *A*, it is now possible to calculate the scattering angle, θ', for any peak position, *P*.

$$\frac{\theta\prime}{360} = \frac{P}{2\pi A} \qquad \text{Equation 2-7}$$

4. The scattering angle θ' can now be put back into Bragg's Law (Equation 2.5) and the d-spacing calculated obtained

5. The d-spacing is then converted to lattice parameter; for the bicontinuous cubics the d-spacing is multiplied by the peak index.

2.5.3. Image visualisation: AXcess

Multiple images were visualised using the IDL-based AXcess software which was developed by Dr. A. Heron [109]. This programme has the added possibilities of image analysis, and camera and Scorpion control of the Bede beam line. The advantage of using AXcess for image visualisation is that large number of images can be plotted sequentially to form stack plots allowing large amounts of data to be compared simultaneously. This is especially useful for kinetic studies where there are often over 140 images for one pressure jump.

Like the LabVIEW programme, the sample to detector distance can be calibrated using AgBe with a known d-spacing of 58.38 Å. Radial integration of the diffraction images (Figure 2.11 i) produces 1-dimensional plots (Figure 2.11 ii) which can be stacked sequentially to form 'stack plots' (Figure 2.11 iii). Using AXcess, the graphics of stack plots can be changed (Figure 2.11 iii-iv) to facilitate effective visualisations of the data where comparisons and trends in phase transitions can be directly seen and compared.

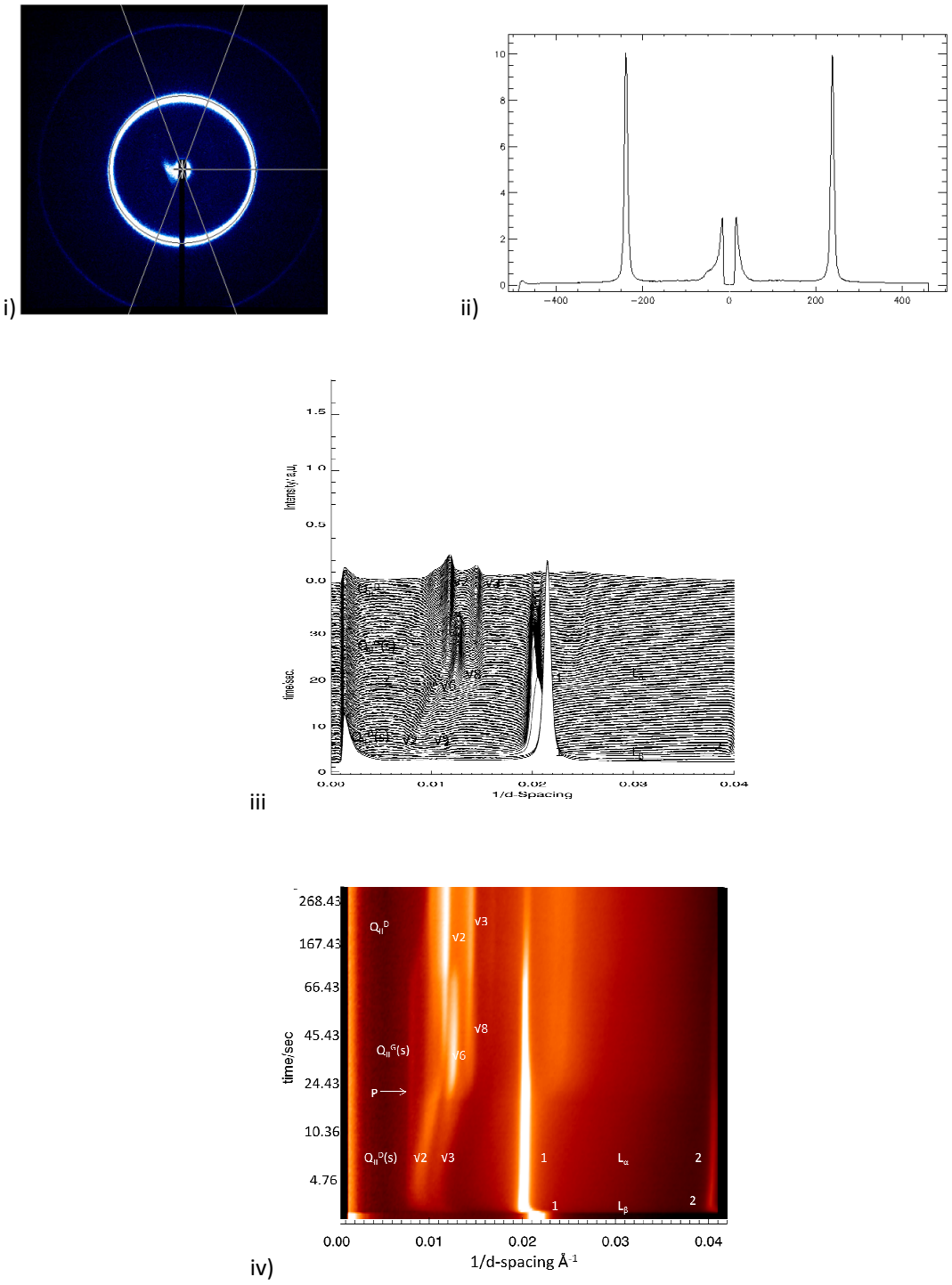


Figure 2.11 Examples of windows from the AXcess programme for image visualisation of large quantities of data. i) diffraction image with relevant corrections undertaken. ii) radial integration of the diffraction image to give a 1-dimensional integration graph. iii) accumulation of 1- d integration graphs sequentially stacked to form a wire stack plot iv) a shaded stack plot which shows a top down view of the pressure jump.

2.6 Polarising Microscopy

Polarising microscopy has been used for identifying liquid crystal phases. Some liquid crystalline phases are optically anisotropic which means that they can rotate the plane of polarised light and are said to be birefringent. Different liquid crystal phases tend to show characteristic birefringence patterns which allow them to be characterised using polarising microscopy.

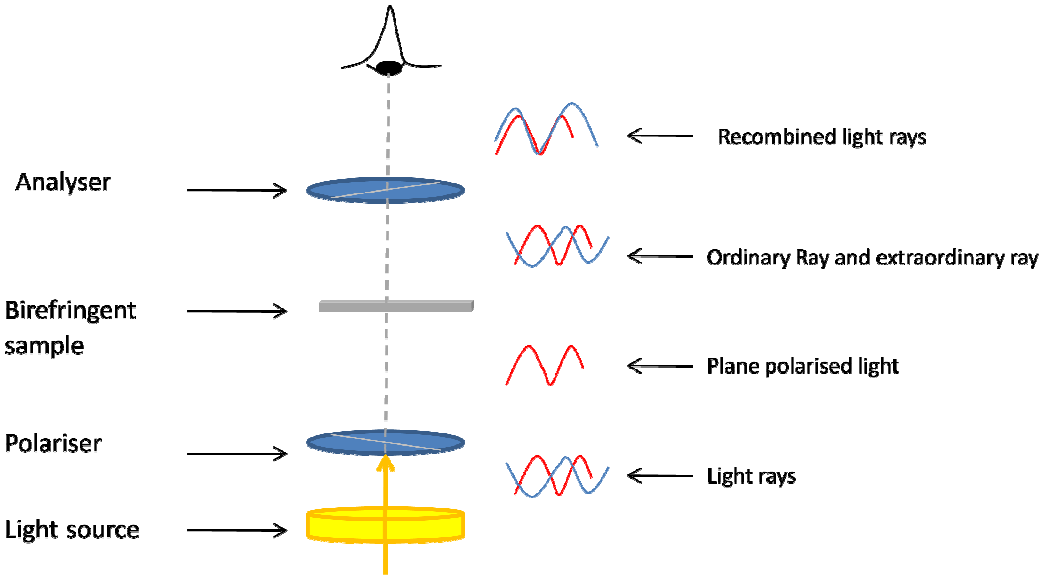


Figure 2.12 Schematic of polarising microscopy. Light passes through the polariser, is rotated, passed through a birefringent sample and then through an analyser to the eye.

A polarising microscope contains two polarising filters, a polariser and an analyser. The polariser is placed before the sample and is fixed, whilst the analyser is placed after the sample and can be rotated. When the polarisers and analysers are set at 90^{o} to each other no light will pass through the microscope to the eye. If a birefringent sample, such as a lamellar or hexagonal liquid crystal phase, is placed between the polarisers, the polarisation plane of the incident light is rotated and some light can pass through the analyser. For an optically isotropic sample, i.e. the inverse bicontinuous phases, the light will remain unchanged as it moves through the sample and none will be able to pass through the analyser.

The polarising microscope used during this work was a Nikon Eclipse E600, with a Nikon DXM1200F digital camera used to capture images. The camera was controlled on a PC using the NIKON ACT-1 (2.70) software and temperature could be controlled using a Linkam Analysa Dynamic temperature control stage with an accuracy of ± 0.1 ^{o}C.

2.7 High Pressure densimeter

Density measurements of lipids can be carried out by using an Anton Paar DMA 60/512P (Graz Austria) vibrating tube densimeter as a function of pressure and temperature. From the density measurements the specific volume and molecular volume can be calculated.

The apparatus consists of a steel u-tube with an internal volume of 2.5 ml whose temperature can be controlled to ± 0.1 ^{o}C by a recirculating water bath; the temperature is measured by a Pt100 sensor embedded in the U-tube. Insulation of the U-tube is provided by foam surrounding.

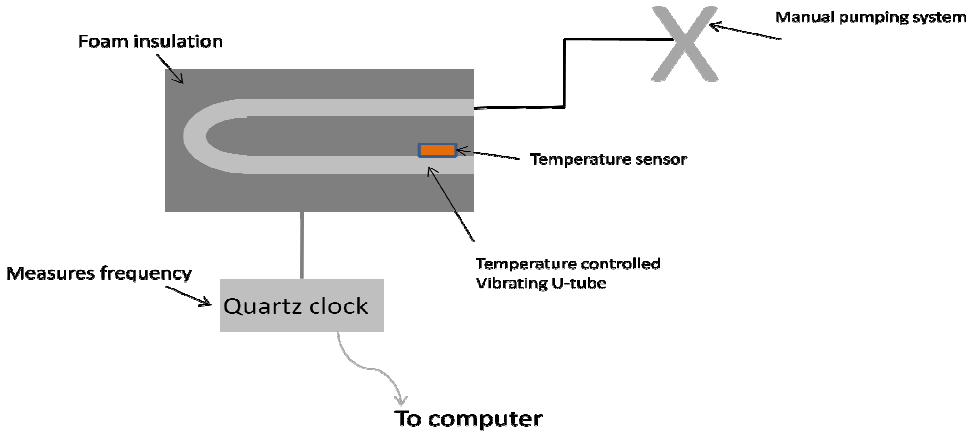


Figure 2.13 Schematic of the high pressure density meter with an oscillating U-tube surrounded by recirculating water and foam. The oscillations of the U-tube are measured using a quartz clock which is connected to a computer. Pressure is changed from a manual pumping system whose pressurising medium is distilled water.

The U-tube is electronically excited and the frequency of oscillation is measured by a quartz clock (Hewlett Packard 5318B).

$$f = \frac{1}{2\pi}\sqrt{\frac{C}{M}} \qquad \text{Equation 2-8}$$

where C is the elastic constant and M is the body of mass.

The frequency is affected by the sample contained within the U-tube, and from rearrangement of Equation 2.8 the density can be obtained:

$$f = \frac{1}{2\pi}\sqrt{\frac{C}{M_u + \rho V_u}} \qquad \text{Equation 2-9}$$

Where M_u is the mass of the tube and the V_u is the internal volume of the U-tube.

High pressure density measurements up to 700 bar were undertaken at 100 bar intervals by the use of an external manual pressurising pump (accurate to +/- 10 bar) which used distilled water as its pressurising medium. Measurements were taken from an average of 21 measurements whose oscillations were < 10^{-6} g/ml.

2.7.1 Instrumentation calibration

The densimeter was calibrated with water and benzene as these density values are well established. Milli-Q water was used for sample preparation of the lipid/water mixtures and was used for calibration to maintain consistency.

2.7.2. Sample preparation for high pressure density measurements

High pressure density measurements (see later section) required large quantities of sample (5 g) and to ensure sample homogeneity, the samples were prepared at the desired water content in smaller quantities (approximately 1 g). The mixtures were prepared in a similar way as the samples prepared for X-ray diffraction but were prepared in 5 ml plastic vials. Known amounts of lipid and water were weighed into the vial and all the contents were centrifuged to the bottom of the vial. The vial was sealed with PTFE-tape and parafilm and then centrifuged up and down over 15 times on a relatively low speed (80 rpm) to mechanically mix the lipid and water mixture. The mixture was then subjected to over 50 freeze thaw cycles with up and down centrifugation at low speed. The individual samples were then combined and centrifuged up and down at a medium speed (1600 rpm) 5 times and subjected to 10 freeze thaw cycles. The sample was stored under nitrogen and at -20 ^{o}C until the experiment.

2.7.3 Sample loading

For accurate density measurements it is important that the sample in the U-tube is free of air bubbles. In highly viscous samples such a limited hydrated monolinolein, this was extremely difficult to achieve. To load samples into the U-tube with minimal air bubbles, a filling device was designed and built at the University of Dortmund.

The device was made of hardened stainless steel (Figure 2.14). Sample is smeared onto the inner walls of the filling device, after which a teflon plug and an additional plug were placed on top of the sample to prevent pressuring medium (distilled water) from contaminating the lipid water mixture. The remaining space within the device was filled with milli Q water and the lid was placed onto the device and attached to an external pressuring pump. The other end has a small outlet which is connected to the vibrating U-tube of the densimeter. The sample is slowly loaded into the U-tube using the external pressuring system until the U-tube is filled. Teflon plugs are placed on either end of the U-tube to avoid contact between the pressurising medium (distilled water) and the sample.

Since during sample preparation and sample loading, water may have been lost or gained from the system, after the experiment the sample was retrieved and weighed into a sample tube. It was then lyophilised for 48 hours and re-weighed to determine the water content using Equation 2.1.

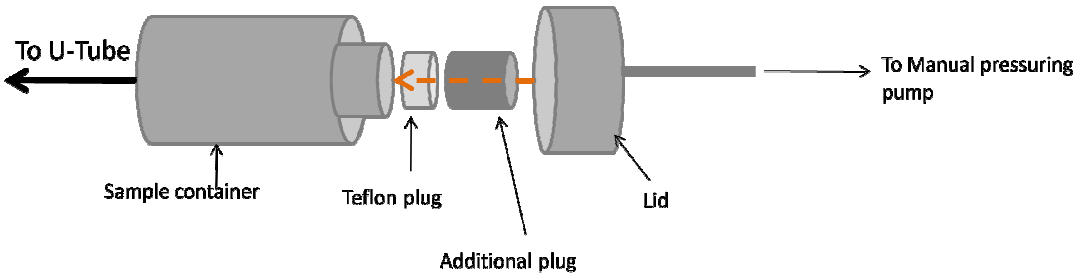


Figure 2.14 Schematic of filling device for high pressure density meter. The sample is loaded onto the walls of the sample container and a teflon plug and additional plug are pushed into the sample container. The remainder of the sample container is filled with distilled water and the lid screwed on and connected to a manual pumping system. The other end of the sample container is connected to the U-tube sample chamber.

Chapter 3 : Pressure and Temperature Phase behaviour of Monolinolein & Water

Abstract:

This chapter describes the phase behaviour of monolinolein (ML) and water as a function of temperature and pressure. The temperature composition phase diagram has been characterised at atmospheric pressure using SAXS, WAXS and polarising microscopy from 0 ^{o}C to 75 ^{o}C at 5 ^{o}C intervals with 10 min equilibration time. A region of the temperature-composition phase diagram (15 wt% water to 27 wt% water) was probed using pressure. Seven pressure-temperature phase diagrams are reported at ambient temperatures (10 ^{o}C to 40 ^{o}C) and from 1 bar to 3000 bar at 100 bar intervals, with 2 min equilibration time.

3.1. Introduction

It has been well documented that the hydrophobic effect plays an important role in the self assembly of amphiphilic molecules in water. The biological human cell membrane consists of more than 1000 types of lipid [110], within which are embedded a wide range of membrane proteins. All of these components play active and deliberate roles in the structure and function of the cell membrane, such as cell signalling, trafficking, and fusion and fission processes. To increase our understanding of these processes it is important to understand the role of lipid structure on the macroscopic properties of mesophases.

Contributions to the energetics of lyotropic liquid crystalline phases are believed to come from curvature elastic energy and packing frustration (Section 1.3.). An understanding of how curvature elastic parameters, defined by the Helfrich ansatz, are affected by pressure and temperature could be crucial for calculating energetics of particular mesophases under specific conditions. It is also possible to make deductions about phase stability from direct experimental studies of mesophase behaviour using a top down approach.

The phase behaviour of monolinolein has already been characterised, firstly in 1965 with the pioneering work by Lutton [96], and later by Caffrey [111] and De Campo [112]; the latter study was performed on a 93.8% pure sample. It has been documented that the purity of the lipid will affect the intrinsic phase behaviour of lipid and the location of the phase boundaries [113]. To fully understand stability of mesoscopic phases the samples should be as pure as possible and this has motivated the characterisation of 99% pure monolinolein (ML).

Temperature has been the most studied thermodynamic parameter and studies on a range of systems describe how temperature affects the bilayer through changes to the lipid. In Type II lipids increasing temperature will increase the energy in the lipid chain and increasing the propensity for curvature towards water. The shape of the lipid will become more cone-like and the bilayer will have a tendency to curve towards the water.

Hydrostatic pressure, has not been as extensively studied as temperature, due to the requirement of specialised equipment [107], but it has been shown to affect phase changes in lyotropic liquid crystals [114-117]. Affecting changes in pressure and temperature have qualitatively opposing effects where increasing the pressure will increase the propensity for a less curved mesophase.

However, previous studies have shown that pressure can be used to probe a different phase space to temperature [114]. For example, a system at high temperature and pressure may not be identical to its original system which is attributed to changes in bending rigidity. Probing a system using changes in pressure and temperature could lead to a deeper understanding of mesophase behaviour and unveil new possibilities for modelling of mesophase energetics.

There are a limited number of documented experiments that have involved high pressure equilibrium experiments. Most of the work in this area has been undertaken on excess water samples where the samples are easier to manipulate and make homogeneous compared to fixed hydration samples [14, 114, 115, 118, 119].

In the first part of the chapter I will discuss the techniques and methodologies that have been employed to ensure sample homogeneity for pressure and temperature dependent studies. The second part of the chapter will show the temperature-composition phase diagram for monolinolein and seven limited hydrated (15 wt% water and 28 wt% water) pressure temperature phase diagrams.

3.2. Materials and methods:

Monolinolein (99% pure) was purchased from Larodan (Malmo, Sweden) and used without further purification.

3.2.1. Sample preparation

Sample homogeneity is crucial for consistent and reliable results. Freeze-thawing the lipid-water mixture over the chain melting regime has been shown to be the most efficient way of creating a uniformly homogeneous sample with small domains [100]. However, different sample preparation techniques will affect the overall sample homogeneity and this section describes three different techniques employed for sample preparation. The success of the technique is affirmed by uniformly homogeneous samples detected using SAXS. Images were taken along the length of the

capillary at 0.5-1 mm increments and radial integration of the images were stacked to generate a stack plot of the length of the capillary. Relative d-spacings and phases are compared along the length of the capillary; in a homogenous sample the phase and d-spacing are consistent along its length. ML (Larodan fine chemicals, Malmo, Sweden) was made to 33 wt% water using HPLC grade water (Sigma Aldrich, UK) and measured at 25 ^{o}C where a Q_{II}^{D} phase is expected.

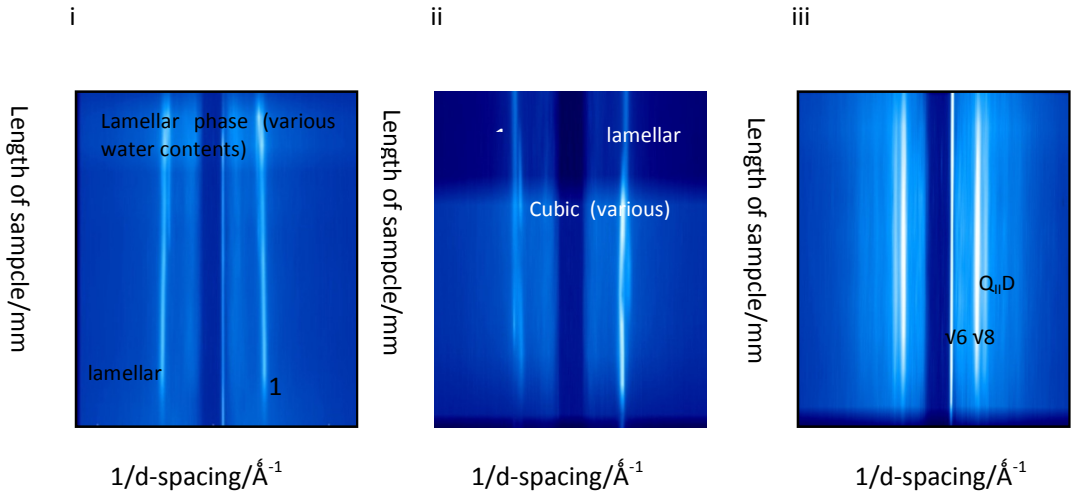


Figure 3.1 Stackplots of diffraction images taken over the length of the capillary after different sample preparations techniques for a 33 wt%. water sample at 25^{o}C 1) known amounts of lipid and water were placed into an Eppendorf tube, freeze-thawed over 20 times and a small amount transferred to a capillary. The capillary was heat sealed and further sealed with silicon sealent; 2) known amounts of lipid and water were placed into a glass vial and screwed onto an Alexei-fuge. Another glass vial was screwed onto the other end of the Alexei-fuge and the sample centrifuged backwards and forwards. After 20 forward and reverse centrifugations a small amount of sample was placed into a glass capillary, heat sealed and further sealed; 3) known amounts of lipid and water were placed directly into a capillary and centrifuged to the bottom. The capillary was heat-sealed and further sealed with silicon sealant and the lipid water mixture underwent over 20 freeze-thaw cycles.

1) Approximately 20 mg of sample were prepared in a glass vial. The sample was mechanically mixed with a microspatula then centrifuged to the bottom of the vial when 20 freeze thaw cycles were performed on the sample. Approximately 3 mg of sample was transferred to a thin walled 1.5 mm diameter special glass capillary (Capillary Tube supplies, Reading, UK)

and centrifuged to the bottom, the capillary was heat sealed and then further sealed with silicon sealant (Dow Corning Corp.) and stored at -20 ^{o}C until further use.

During mechanical mixing and sample transfer to the capillary, sample, water or both can be lost. In addition, over 5 min of centrifugation was required to force the sample to the bottom of the capillary. During this time it is likely that water is lost from the sample as heat is generated during centrifugation. The resulting stack plot (Figure 3.1 i) shows the lamellar phase over the length of the capillary indicating that water loss from the sample.

2) Approximately 20 mg of 33 wt% water sample was made in a glass vial. To homogenise the sample the mixture was centrifuged through an Alexei-fuge, a teflon tube with a small hole of diameter 2 mm bored through the centre. Glass vials are screwed into both ends of the Alexei-fuge centrifugation of the sample into a glass vial forces the lipid mixture through the hole and shear flow mechanically mixes the sample (Figure 3.2). Once the sample had been centrifuged up and down over 20 times, approximately 3 mg of sample was transferred into the 1.5 mm special glass capillary (Capillary Tube supplies, Reading, UK). The advantage of this technique over technique (1) is that water loss to the atmosphere is reduced. However, the high viscosity of the sample meant that the lipid mixture would stick to the inner walls of the Alexei-fuge leading to an inhomogeneous sample. The results show 2 or 3 different phases present along the length of the sample, Figure 3.1 ii.

3) Technique 3 proceeded via direct preparation of a 33 wt% water sample into the capillary (Capillary Tube supplies, Reading, UK). The capillary was flame sealed and then further sealed with silicon sealant. At least 30 freeze thaw samples were undertaken on the sample which was centrifuged after every 5 freeze-thaw cycles to ensure lipid and water was at the bottom of the capillary. The advantage of this technique is that once the lipid and water are inside the capillary there is minimal water or lipid loss from the capillary. The results show sample homogeneity throughout the length of the capillary where one phase with constant d-spacing is observed.

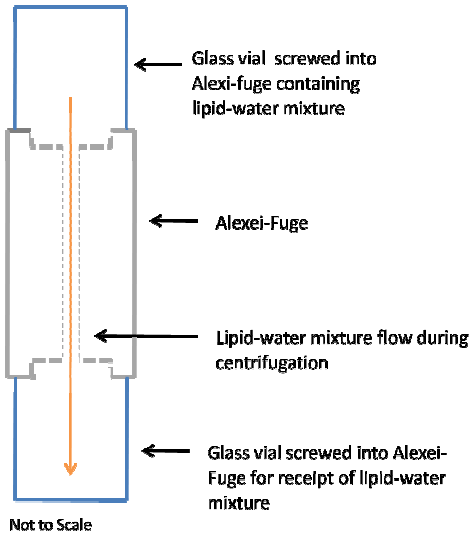


Figure 3.2 Schematic of a side view of the Alexei-fuge with a central bore of 2 mm diameter. Two glass vials are screwed into both ends of the Alexei-fuge, one containing the lipid and one empty. The whole thing is centrifuged and the lipid water mixture is forced through the central bore into the empty glass vial. The Alexei- fuge and glass vials are inverted and centrifuged over 20 times.

3.2.2. Methods: recalculation of water contents (pressure dependent studies)

Pressure dependent experiments required larger amounts of sample and approximately 50 mg of sample were made for each experiment. The principles of sample preparation remained the same where known amounts of water and sample were placed into a glass vial, mechanically mixed and freeze-thawed over 30 times and stored at -20 ^{o}C until further use.

The samples were placed into teflon based sample containers immediately before the experiment, *the sample having the consistency of hard butter*. These sample containers (teflon spacers) consist of a ring of teflon, with thicknesses of 1 mm to 1.5 mm and a 3 mm diameter hole in the centre to contain the sample. Mylar windows are fixed to the teflon with double sided adhesive tape.

As large amounts of sample were prepared and transferred into teflon spacers, errors in water hydration were likely to occur from water and lipid loss. To ensure correct water contents the

sample was recalculated from measured lattice parameters using the following relationships described in the introduction.

PIM:

$$a = \frac{V_n}{A_n \times (1-\phi_w)}\left(-2\sigma + \frac{2^{\frac{5}{3}}\sigma^2}{\left(4\sigma^3+9\pi\chi(1-\phi_w)^2\left(\frac{V_n}{V}\right)^2+3(1-\phi_w)\left(\frac{V_n}{V}\right)\sqrt{\pi\chi\left(8\sigma^3+9\pi\chi(1-\phi_w)^2\left(\frac{V_n}{V}\right)^2\right)}\right)^{\frac{1}{3}}} + 2^{\frac{1}{3}}\left(4\sigma^3+9\pi\chi(1-\phi_w)^2\left(\frac{V_n}{V}\right)^2+3(1-\phi_w)\left(\frac{V_n}{V}\right)\sqrt{\pi\chi\left(8\sigma^3+9\pi\chi(1-\phi_w)^2\left(\frac{V_n}{V}\right)^2\right)}\right)^{\frac{1}{3}}\right)$$

Equation 3-1

CMC

$$a = 2 * \sum_{i=0} \frac{\sigma_i[\left(\frac{V_n}{V}\right)(1-\phi_w)]^{2i}}{\left(\frac{An}{V}\right)(1-\phi_w)}$$

Equation 3-2

where a is the lattice parameter;

V_n is the volume between the minimal surface and the pivotal surface;

A_n is the area at the pivotal surface;

V is the molecular volume;

ϕ_w is the water volume fraction;

σ is the dimensionless surface area;

χ is the Euler characteristic;

σ_i is the calculated dimensionless surface area for constant mean curvature model.

To obtain the water content A_n, V_n and V (area the neutral surface, volume between the neutral surface and the minimal surface and the molecular volume respectively) were obtained from analysis of data at 1 bar and 30 ^{o}C (see Chapter 4).

A_n^{PIM}=37.13 ± 1.77 Å^2, V_n^{PIM} = 607.85± 41.66 Å^3

A_n^{CMCM}=37.48± 1.69 Å^2, V_n^{CMCM}= 592.3 ± 38.5 Å^3.

The recalculated water contents and the difference between the expected water content and the calculated water content are shown Table 3.1**.** The recalculated water content for each model is the same to 1 d.p. The difference between the expected water content and the calculated water content are attributed to experimental error during sample preparation and transfer. An increase in water content is attributed to lipid loss during mechanical mixing and sample transfer and a decrease in water content is attributed to water loss from the sample during freeze thaw cycling.

	PIM		**CMCM**	
expected water content/ wt%	calculated water content/ wt%	difference between expected and calculated / wt%	calculated water content/ wt%	difference between expected and calculated water content / wt%
23.0	22.21	-0.79	22.21	-0.79
19.0	17.13	-1.87	17.15	-1.85
20.7	15.72	-4.98	15.75	-4.95
26.1	26.91	0.82	26.91	0.82
28.0	25.39	-2.61	25.39	-2.61
31.0	24.81	-6.19	24.81	-6.18
23.0	20.89	-2.13	20.9	-2.12

Table 3-1 Summary of the expected water contents and the actual water contents, and the difference between the expected water content and the actual water content calculated from lattice parameter data using equations 3.1 and 3.2.

3.2.3 Polarising microscopy:verification of phase boundaries at high temperatures

At high temperatures, i.e. above 40 ^{o}C, it is difficult to assign diffraction patterns as the diffraction became 'spotty' with additional scattering at low scattering angle (high d-spacing) (Figure 3.3). Increased spottiness in a diffraction pattern is an indication of sample alignment where domains begin to orientate in the same direction [120, 121]. Radial integration of diffraction patterns show multiple peaks which are difficult to assign to a particular phase and have been ambiguously assigned to two coexisting phases, the Q_{II}^{G} and the Q_{II}^{D}. Sample alignment could arise as a consequence of a phase transition, however there has been no indication of sample alignment for cubic to cubic phase transitions in other monoacyglycerol systems [48] and it is unlikely that this is the cause of spottiness in the diffraction pattern. It is more likely that domain alignment arises from shear flow. At high temperatures water will begin to evaporate from the sample and 'drag' the lipid domains into an aligned orientation.

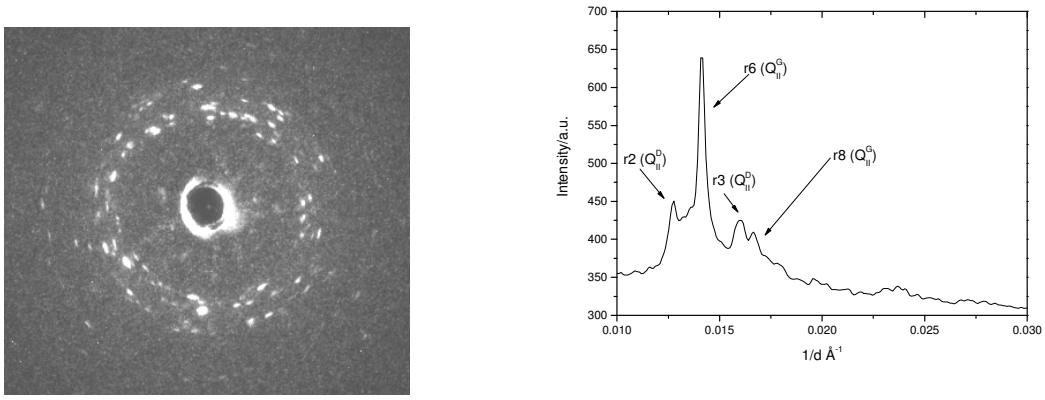


Figure 3.3 Example of a spotty diffraction image (left) and its 1d radial integration (right) for a 25 wt% water sample at 45^{o}C. Analysis of the 1d plot shows v6 and v8 reflections for Q_{II}^{G} phase and v2 and v3 reflections for Q_{II}^{D} phase. The diffraction image was taken on the Bede beamline.

If water is lost at higher temperature, phase boundaries will be shifted to lower hydration and lower temperatures. Polarising optical microscopy (Nikon E600Pol) was used to verify the

temperatures of phase transitions previously determined by SAXS. Images were taken using the Nikon full colour CCD camera (more details can be found in Chapter 2 Materials and Methods)

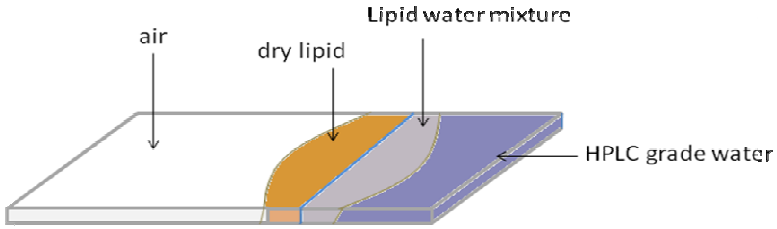


Figure 3.4 Cartoon of water penetration experiment of monolinolein and water in a flattened capillary. The dry lipid is placed into the flat capillary; water is added from one side to ensure a gradient of water through the lipid sample, with dry lipid on the left and increasing water hydration to the right until the lipid is in coexistence with excess water.

Optical polarising microscopy of lipid water mixtures was undertaken using the water penetration technique where dry lipid was placed into a flattened capillary (Vitrocom, Composite Metal Services LTD, Ilkley, UK) so that its depth was completely filled. Excess water was added to one side of the capillary and the water was allowed to penetrate the sample (Figure 3.4). The sample was heated at 0.5 ^{o}C a minute and the temperatures of each phase transition was measured to an accuracy of 0.2 ^{o}C. For SAXS experiments the lipid and water mixture is contained in a vertical capillary, at high temperatures evaporation from the sample will lead to inaccuracies in phase transition temperatures. Optical microscopy combined with the water penetration technique allows verification of phase transition temperatures at high temperatures to a greater accuracy as water is contained within the flat capillary even at high temperatures. Figure 3.5 shows an example of the inverse hexagonal phase in excess water at 82 ^{o}C.



Figure 3.5 A polarising microscopy image showing characteristic radial fan shapes for an inverse hexagonal phase at 82 ^{o}C in excess water captured using a Nikon full colour CCD camera and Nikon E600Pol at 200x magnification.

3.2.4 Methods: Obtaining rational equilibration times

The position and location of phase boundaries will be affected by the extent of sample equilibration. At synchrotron radiation facilities experimental time is highly sought after and often limited and it is not reasonable to leave a sample to equilibrate for long periods of time. For in house temperature dependent experiments, leaving samples to equilibrate at high temperatures may lead to water loss in the sample. Therefore it is important that a rational decision on sample equilibration is made. Sample equilibration is defined as $\frac{da}{dt} \leq 0.3$ Å for the lamellar phase and less than 1 Å for the Q_{II}^{G} phase for 'in house' experiments and less than ±0.02 Å for synchrotron experiments. The limits for Δa is reduced for synchrotron experiments due to the increased resolution of the detector.

3.2.4.1 Sample equilibration for temperature dependent experiments

For the temperature dependent experiments a compromise needs to be made between sample equilibration and water loss from the sample (within the capillary) at high temperature.

A 24.5 wt % sample was held at 0 °C (L_α) and 25 °C (Q_{II}^G) for 30 minutes and images were taken every minute (Figure 3.6).

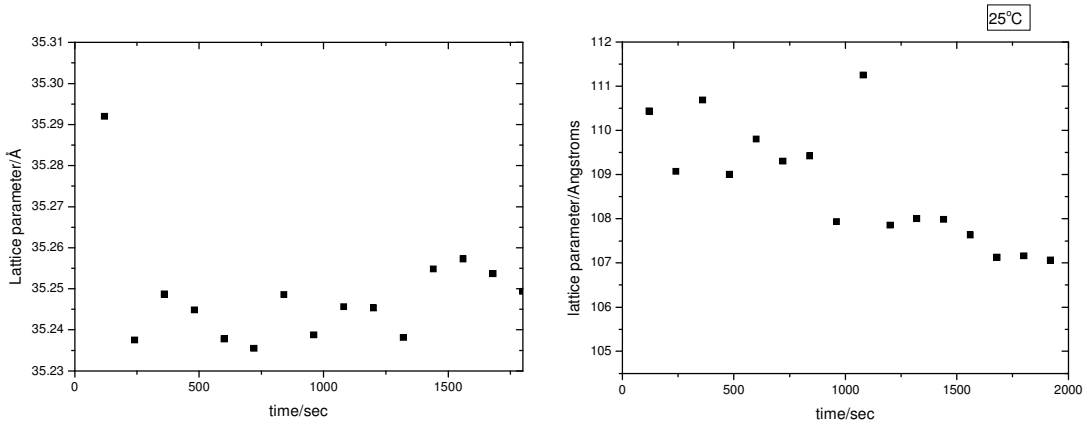


Figure 3.6 Plots of lattice parameter as a function of time to show the change in lattice parameter of the lamellar phase at 0 °C (left) and Q_{II}^G phase at 25 °C (right).

At 0 °C, the lattice parameter stabilises after 2 min and fluctuates around an equilibrium value thereafter which correlates to a fluctuation around the set temperature. At 25 °C the Q_{II}^G lattice parameter stabilises after approximately 15 min when the change in lattice parameter is less than 1 Å. A smaller ΔT will reduce equilibration times as the sample will not make such a large adjustment to the temperature. It will be expected that equilibration time will be reduced during the temperature scan when ΔT = 5 °C or 2 °C.

At higher temperatures, above 35 °C, water lost from the sample into its surroundings can be reduced by shorter equilibration times in the sample. As a compromise between sample equilibration and water evaporation the sample was given 10 min to equilibrate before an image

was taken. It would be important for future experiments to find a way to minimise water loss from the sample at high temperatures so that true equilibrium is attained at all temperatures.

3.2.4.2 Sample equilibration for pressure dependent experiments

Due to time constraints at synchrotron radiation facilities little or no time was previously given for sample equilibration, this section briefly looks at the effect of equilibration time on the lattice parameter and describes how a rational decision can be made for equilibration time.

Equilibration experiments were undertaken on a 22.2 wt% water sample at 20.4 ^{o}C and 38.5 ^{o}C. The change in lattice parameter is plotted as a function of time for both the lamellar and Q_{II}^{G} phases. Figure *3.7* shows the results at 20.4 ^{o}C. Sample equilibration has been attained when $\Delta a \leq$ 0.02 Å.

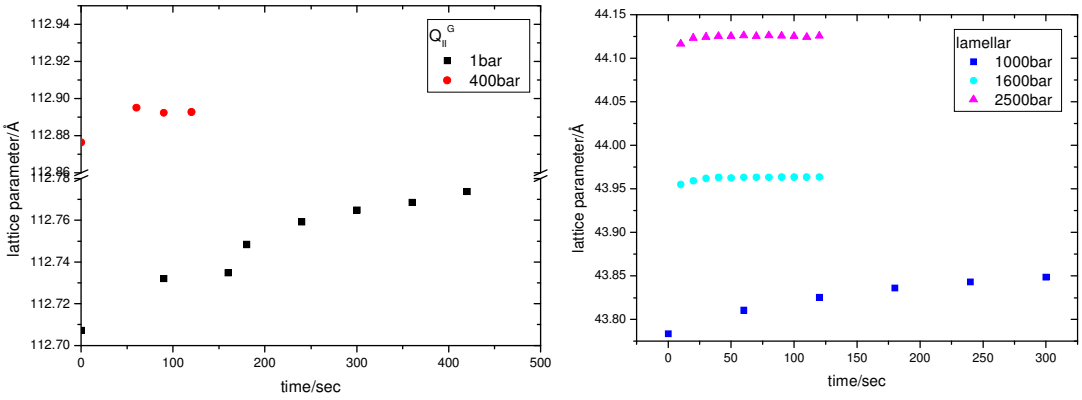


Figure 3.7 Plots of change in lattice parameter with time at different pressures 20.4 ^{o}C for 22.2 wt% water sample. Left – results for Q_{II}^{G} phase at 1 bar (black squares) and 400 bar (red circles). Right - results obtained for the lamellar phase at 1000 bar (blue squares), 1600 bar (turquoise circles) and 2500 bar (magenta triangles).

At atmospheric pressure the Q_{II}^{G} phase has not equilibrated after 10 min. This is due to temperature equilibration rather than pressure equilibration. During these experiments it is important that the sample is left at least 30 min for the temperature bath to reach the desired temperature and the sample to respond to these changes. At 400 bar the Q_{II}^{G} phase has equilibrated after 50 sec.

Considering the lamellar lattice parameter at 1600 bar and 2500 bar, sample equilibration has been achieved within 50 sec. At 1000 bar, the lattice parameter of the lamellar phase in coexistence with the Q_{II}^{G} phase is still changing after 300 sec. Increased water movement throughout the sample means that the sample requires longer equilibration times compared to a pure phase. Despite this, $\Delta a < 0.03$ Å after 150 sec.

The same effect was considered at 38.5 ^{o}C and plots of *a* vs *t* are shown in Figure 3.8.

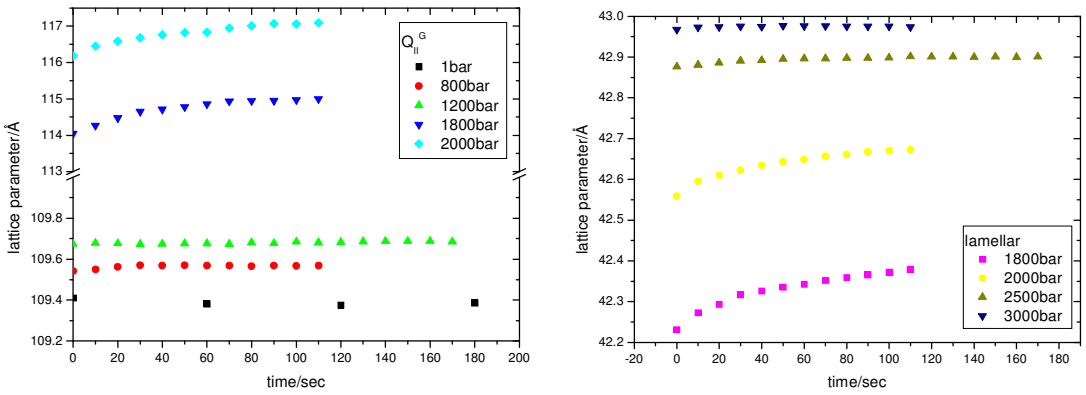


Figure 3.8 Plots to show the change in lattice parameter with time at 20.4 ^{o}C, 22.2 wt% water sample at 38.5 ^{o}C and varying pressures. Left- Q_{II}^{G} phase at 1 bar (black squares); 800 bar (red circles); 1200 bar (green triangles), 1800 bar (inverted blue triangles); 2000 bar (turquoise diamonds). Right- lamellar phase at 1800 bar (magenta squares); 2000 bar (yellow circles); 2500 bar (olive green triangles) and 3000 bar (inverted dark blue triangles).

The data shows that there is less than 0.02 Å change in the lattice parameter after 80 sec for the Q_{II}^{G} phase and less than 0.01 Å change in the lamellar lattice parameter after 90 sec.

As temperature is decreased, equilibration time increases, in addition, when two phases coexist the equilibration time increases. Competition for beam time means that synchrotron experiments are done under considerable time constraints and it was unreasonable for equilibration time to exceed 2 min. A compromise was made between sample equilibration and time constraints and in the majority of cases sample equilibration was attained after 2 min.

If a sample has not fully equilibrated, increasing equilibration time shifts the phase boundaries to lower pressures. To further reduce the error in the position of the phase boundaries the size of the pressure steps were reduced as phase boundaries were approached. The estimated error in the phase boundaries is predicted to be ± 50 bar.

3.2.5. Instrumentation

The beam lines were utilized for these experiments was the Bede Microsource, an in house beamline used for temperature dependent studies and the ID02 and I22 beamlines at ESRF and DLS for the pressure dependent studies, where the diamond pressure cell of R. Winter was used. More details of these can be found in the Materials and Methods section.

3.3 Results

3.3.1 Temperature-composition phase diagram

Figure 3.9 shows the data obtained from SAXS and WAXS experiments undertaken on the in-house Bede beamline. The phases were charaterised from analysis of SAXS and WAXS data and the lattice parameters of the phase were extracted. Figure 3.10 shows the positioning of the phase boundaries using SAXS, WAXS and microscopy data. The boundaries were constructed to the satisfaction of Gibbs Phase rule i.e. for a 2 component system at constant pressure the maximum allowed number of phases at one point is 3.

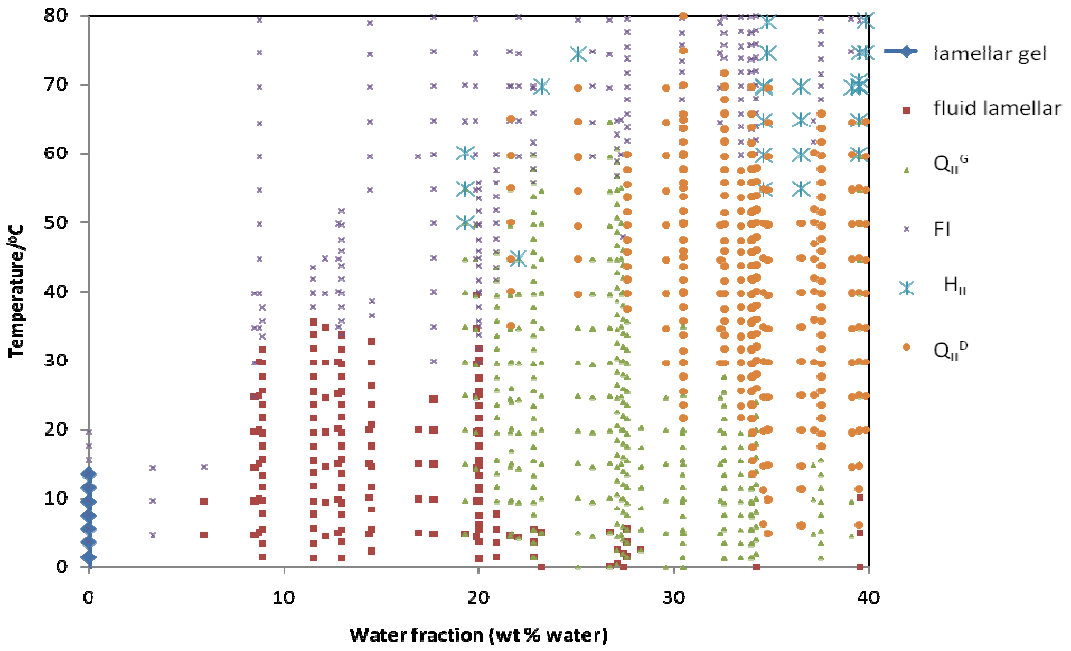


Figure 3.9 Plot showing the phases identified by SAXS and WAXS using the Bede beamline in the water-monolinolein system for varying water contents (0 wt% water – 40 wt% water), and from 0 °C to 80 °C.

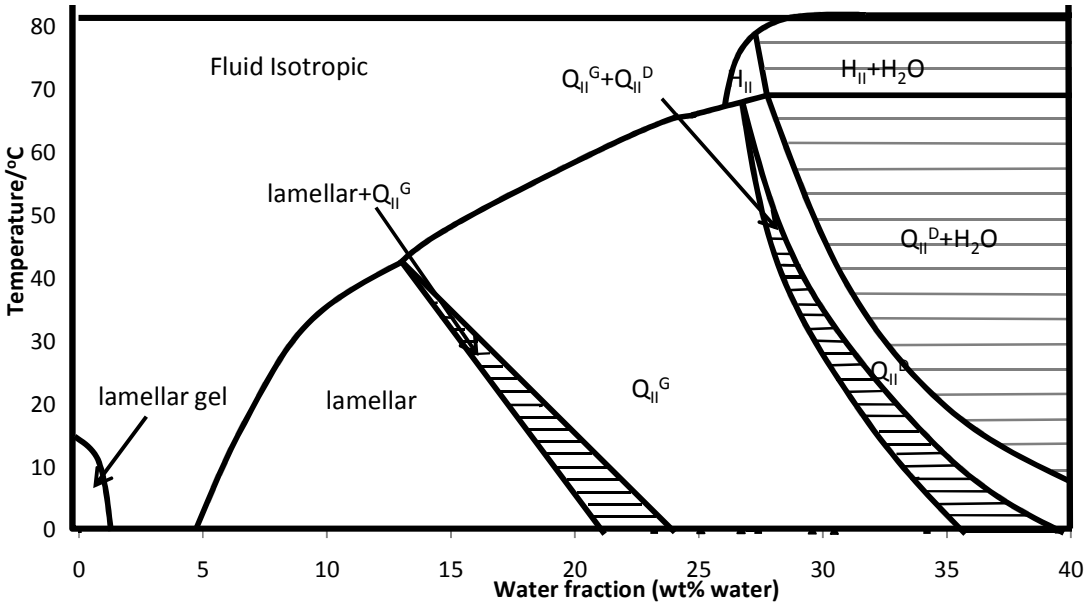


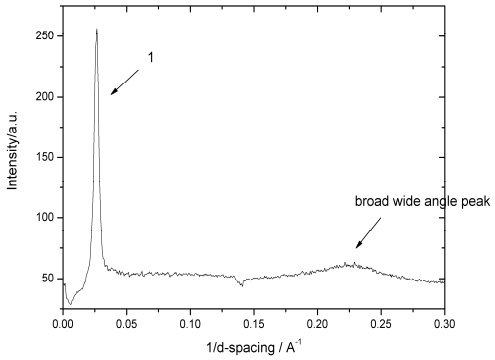
Figure 3.10 Phase diagram for monolinolein and water from 0 wt% water to 40 wt% water and 0 °C to 80 °C. Phase boundaries were positioned according to the location of phases as observed from SAXS, WAXS and optical microscopy.

To discriminate between the lamellar phases it was necessary to use both small and wide angle diffraction, as only one peak was detected in the small angle, Figure 3.11 (c). In the wide angle a broad peak is characteristic of the fluid lamellar phase, a fairly sharp peak at 4.2 Å is characteristic of the gel phase, Figure 3.11 (b).

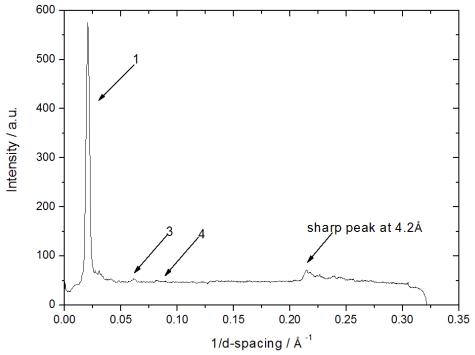
Due to the higher flux and resolution of synchrotron radiation facilities there is evidence of a second order peak of the fluid lamellar phase from the small angle diffraction, Figure 3.11 (d). It can be seen that the intensity of the second peak is very low compared to the first order peak and explains why no diffraction was seen for the second peak on the in house Bede beamline.

The Q_{II}^{G} Phase occupies a large middle region of the phase diagram and has been characterised from in house experiments through 2 Bragg reflections with a ratio of √6 : √8,

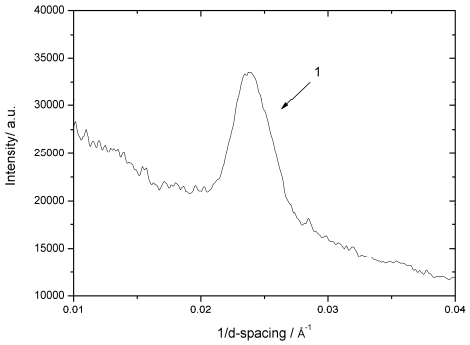
Figure *3.12* (a). These are indexed as the 221 and 220 hkl reflections of the Ia3d crystallographic space group. The resolution of the beam line was low and it was not possible to fully resolve the outer peaks (√20: √22: √24), which appear conjunctively as a broad hump. Higher resolution of synchrotron radiation facilities allows unambiguous assignment of the Q_{II}^{G} where 8 distinct Bragg reflections are observed (√6: √8: √14: √16: √20: √22: √24: √26).



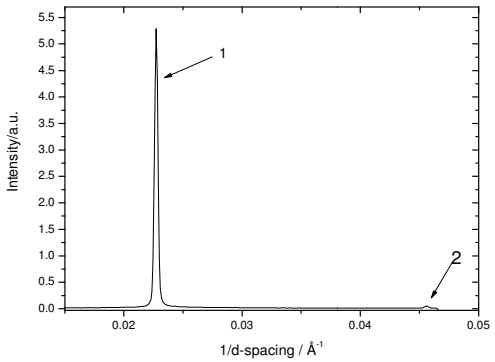
a)



b)



c)



d)

Figure 3.11 Examples of one dimensional radial integrations from X-ray diffraction images with reflections. a) Wide angle diffraction for fluid lamellar phase indicating characteristic broad hump in the wide angle and sharp peak for reflection 1 at small angle taken on the Bede beamline; b)Wide angle diffraction image for gel lamellar phase indicating a characteristic sharp reflection at 4.2Å and equally spaced reflections at small angle taken on the Bede beamline; c) small angle diffraction image for fluid lamellar taken on the Bede beamline, due to the poor resolution of the beamline only one reflection is seen; d) small angle diffraction image for fluid lamellar phase taken at ID02, ESRF, with the first and second reflections for the phase.

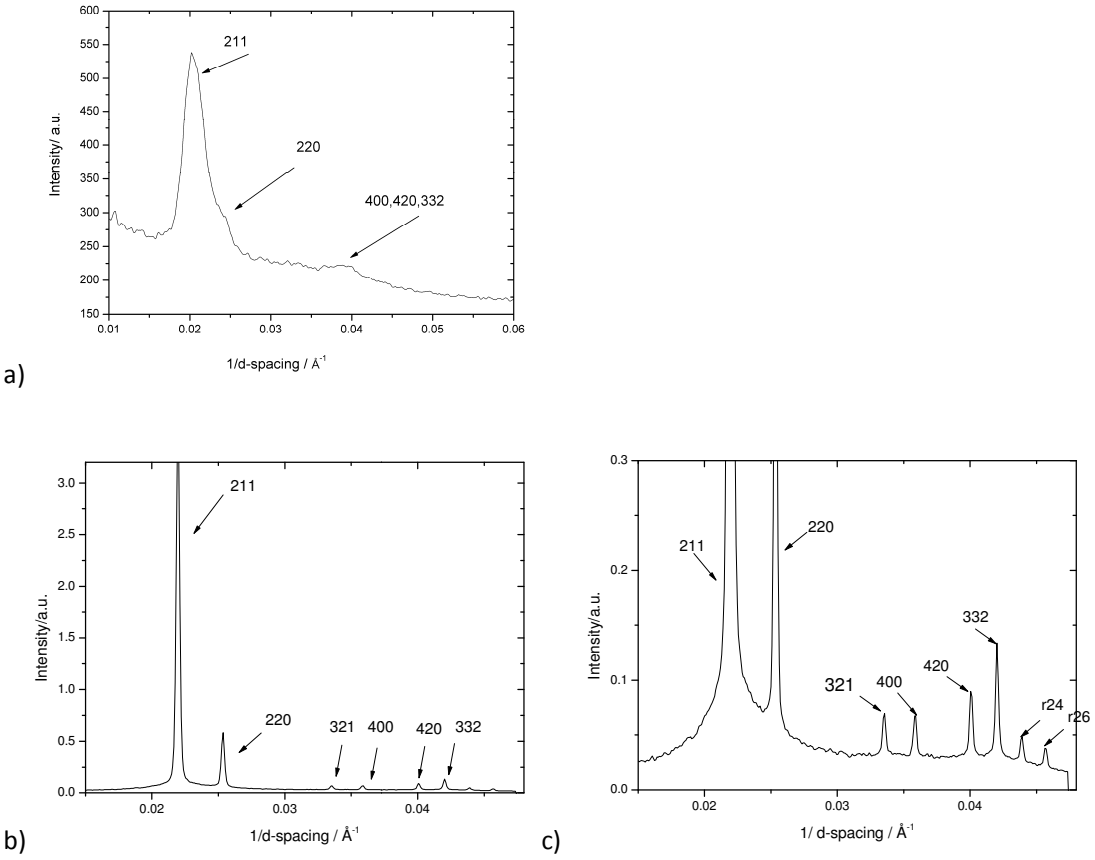


Figure 3.12 Examples of 1-d diffraction images of SAXS data for the Q_{II}^{G} phase obtained on the Bede beamline (a) and from beamline ID02 at the ESRF (b) and (c). All identifiable reflections have been labelled.

As the water content is increased a new phase is identified, Q_{II}^{D}, with Bragg reflections in the ratio of √2: √3: √6: √8,

Figure 3.13 (left), which are characteristic of the Pn3m crystallographic space group and hkl reflections of 110, 111, 211, 220. At high temperatures and high hydrations, i.e. above 70 ^{o}C and 25 wt% water the inverse hexagonal phase is seen with Bragg peaks with ratios of √1: √3: √4 (hk=10,11,20) (Figure 3.13 right). The temperatures of transition between the Q_{II}^{D} and the H_{II} phase were verified using polarising microscopy.

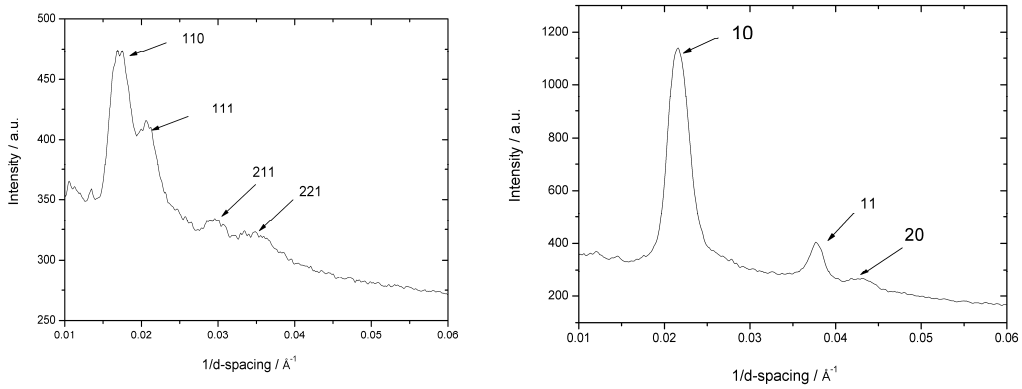


Figure 3.13 Examples of 1-d diffraction images of SAXS data for the Q_{II}^{D} phase (left) and H_{II} phase (right) with respective reflections labelled.

At low hydrations there is insufficient water in the system to stabilise the desired inverse monolayer curvature of the system and the bilayers remain flat. When there is sufficient water in the system the curvature is stabilised by water and bicontinuous cubic phases are formed. Generally speaking, it is predicted that increasing the water content of an amphiphile will lead to an increase in the headgroup area, leading to a transition from the flat bilayer phase to a curved Type I phase. However, in the case of ML, addition of more water favours the formation of Type II phases, where the monolayer curves towards the water. Therefore the phase behaviour is largely governed by the volume occupied by the hydrocarbon chain whose cross sectional area is large compared to the head group.

The Q_{II}^{G} phase is stable in the ML system from 20 *wt%* water to 40 *wt%* water with a lattice parameter of 100-140 Å. At higher temperatures the Q_{II}^{G} phase is stable over a smaller hydration, at 40 ^{o}C from 15-30 *wt%* water with a smaller range of lattice parameters 100-120 Å. As more water is added to the system Q_{II}^{D} becomes preferentially stable. This coincides with the sequence predicted by Schwarz and Gompper [53] where the constant mean curvature model predicts that the bicontinuous cubics will be observed in the following sequence Q_{II}^{G}, Q_{II}^{D} and Q_{II}^{P} phase. The stability of one phase over another is governed by very subtle changes in the bilayer [122].

Qualitatively the effect of hydrating the sample shows similar trends to other Type II systems [13, 97, 99, 112]. As the sample becomes more hydrated there is an increase in lattice parameter. The lattice parameter of the lamellar phase lies between 38-41 Å over a water hydration increase of 10 *wt%*. In comparison, a 10 *wt%* water increase in the Q_{II}^{G} phase increases the lattice parameter by

approximately 20 Å. The Q_{II}^{G} phase has a higher porosity compared to the lamellar phase where water is contained in a network of channels and an increase of 20 Å for a 10 % increase in water hydration implies that the bilayer in ML and water can adopt a wide range of curvatures. Increase in water content leads to a decrease in negative interfacial curvature, Figure 3.10.

The Q_{II}^{G} phase and Q_{II}^{D} phase share a small region of coexistence at approximately 30-37 *wt%* water and have a Bonnet ratio of 1.56 at 25 ^{o}C, where $a(Q_{II}^{G})\approx$ 140 Å and $a(Q_{II}^{D})\approx$90 Å. this is comparable to the predicted Bonnet ratio where $a(Q_{II}^{G})/a(Q_{II}^{D})$ = 1.576 [45] and predicts that the two phases are coexisting with different geometric properties but with the same local properties. Q_{II}^{D} phase forms when more water is present. The interfacial curvature is less than the Q_{II}^{G} phase. The change in lattice parameter as water content is increased (Q_{II}^{D} phase) is negligible as much of its phase region coexists with excess water.

3.3.1.1. Comparisons to previous characterised Phase diagrams

The phase diagram (Figure 3.10) shows similarities to a previous phase diagram characterised by Lutton (Figure 3.14) using polarising microscopy. However, in comparison the phase boundaries are at lower water compositions and the H_{II} phase is seen at higher water compositions in this study.

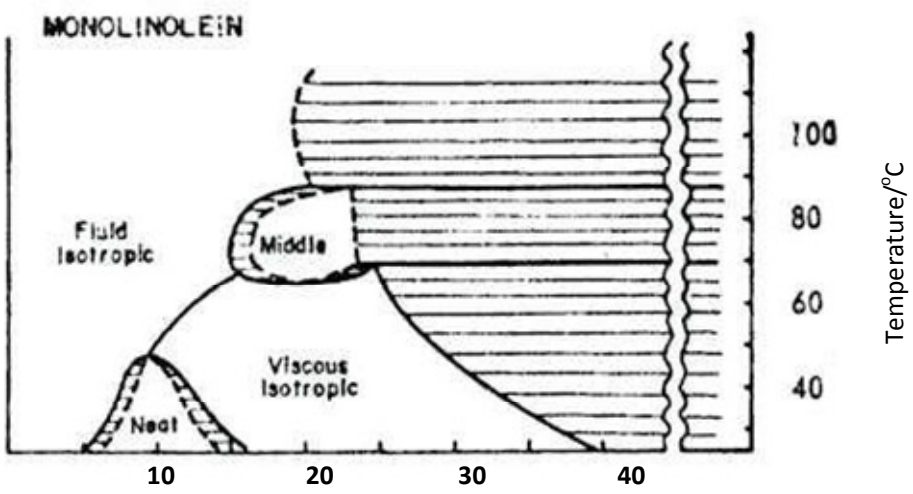


Figure 3.14 Monolinolein / water phase diagram characterised solely by polarising microscopy by Lutton in 1965. [96] Neat refers to lamellar phase, Viscous Isotropic refers to cubic phases and Middle to hexagonal phases.

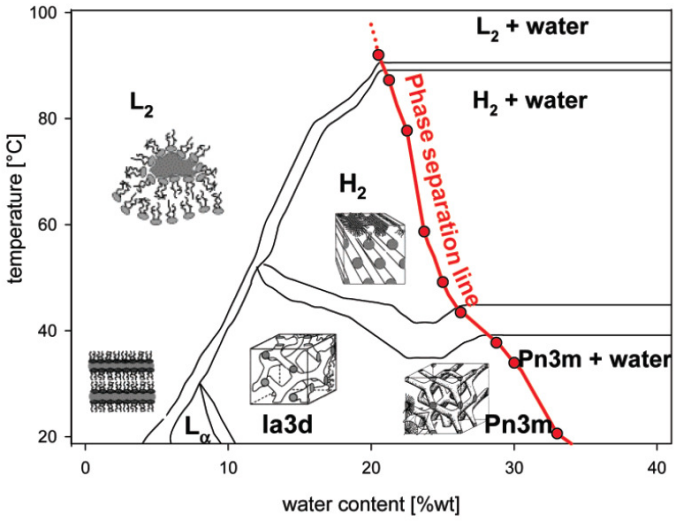


Figure 3.15 Monolinolein (96% pure) and water phase diagram characterised by de Campo [112] using SAXS in the 1990's. Ia3d ~ Q_{II}^G; Pn3m ~ Q_{II}^D. The phase separation line indicates the excess water line.

If Figure 3.10 is compared to the phase diagram characterised by de Campo (Figure 3.15) it can be seen that more highly curved phases (H_{II}) occupy larger regions of the phase diagram forming at lower temperatures and hydration. The difference in phase behaviour can be attributed to differences in the purity of the sample. De Campo utilises a sample with 93.8 % purity whilst the sample used for these experiments was > 99 % pure. The presence of 6 % of impurities has a large effect on the phase behaviour, where impurities [113] have the ability to relieve chain packing frustration and stablilise the H_{II} phase at low temperatures and hydrations. It is interesting to note that the excess water line is also shifted to lower water contents and is due to the stabilisation of the curvature at lower water contents promoted by the presence of impurities.

3.3.1.2. Calculation of excess water points:

In the excess water region the lattice parameter of the mesophase has a strong dependence on temperature but not on its hydration, which makes it possible to find the excess water boundary via two techniques.

1. The excess water boundary can be found by analysis of the lattice parameter as a function of temperature (for a given water sample), the lattice parameter changes from being constant to $\frac{da}{dT} \leq 0$.

2. From analysis of swelling data at constant temperature, the position of the excess water boundary can be found when the gradient $\frac{da}{d\phi}$ changes from $\frac{da}{d\boldsymbol{\phi}} \geq 0$ to $\frac{da}{d\boldsymbol{\phi}} = 0$.

Prior to the excess water point, changes in temperature do not have a significant effect on the lattice parameter; beyond the excess water point the lattice parameter is more sensitive to changes in temperature. As the temperature increases the chain splay of the lipid increases and induces an increased curvature stress on the bilayer. As the temperature is further increased stress will reach a critical point where it is favourable for water to be expelled from the pores and the

reduction of the pore size relieves the stress in the system. The excess water point lies at higher temperatures for a lower hydration sample where the propensity of the system to curve at higher temperatures is facilitated by the smaller amount of water in the sample.

At higher water contents $\frac{da}{dT}$ in the excess water region is non linear (Figure 3.16), this suggests that at high temperatures there is a limit to the amount of chain splay which can be incurred on the lipid and the effect of reduction of the pore size is accelerated at high temperatures.

The calculation of the excess water boundary was undertaken by analysis of the $\frac{da}{dT}$ gradients at a range of water contents from 29 *wt%* water to 50 *wt%* water, and this ensured that any errors associated with water content from sample preparation would be eliminated.

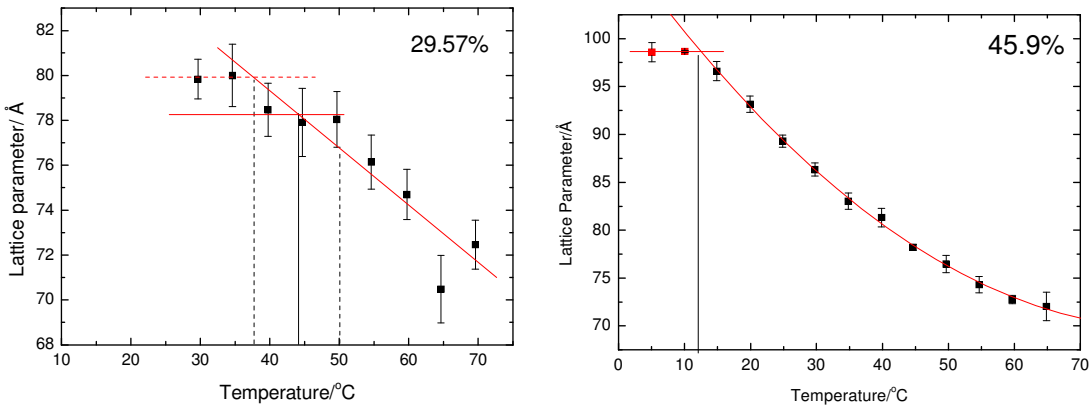


Figure 3.16. Plots of lattice parameter against temperature used to obtain the excess water point for a given water sample. Left- 29.6 wt% water and Right- 45.9 wt% water. Prior to the excess water point there is a negligible change in lattice parameter, after the excess water point (black vertical line) there is a decrease in the lattice parameter. The dotted lines on 29.6 wt% water (left) indicate the error limits of the excess water point.

At 45.9 *wt%* water the change in the gradient at the excess water point is clear. In comparison, at 29.57 *wt%* the position of the excess water boundary has a larger error associated with it. For example the position of the boundary could lie between 38.5 °C and 50 °C. The estimated position and errors in the excess water boundary are stated in Table 3.2. The construction of the excess

water boundary has accounted for these errors. Above 45 °C and below 10 °C, the position of the boundary is more speculative and the boundary has been drawn from an extrapolation of the measured values.

water content/ wt%	Temperature at excess water point / °C
29.6	44.5±6.0
30.4	30±5.0
30.5	32.5± 1.3
33.4	25.5±2.5
37.5	21± 1.3
45.9	11± 1.3

Table 3-2: Summary of the excess water point (with errors) for a given water content sample.

3.3.2 Pressure dependent phase behaviour in limited hydrated monolinolein

The pressure – temperature phase behaviour has been characterised for 7 different water contents between 15.8 *wt%* water and 27 *wt%* water at ambient temperature 7 °C, 11 °C, 24 °C, 31 °C, 37 °C and from 1 bar to 3000 bar at 200 bar intervals. Closer to phase boundaries the pressure intervals were reduced to 50 bar. The data was analysed using the LabVIEW programmes as described in Chapter 2 Materials and Methods and the phase diagrams are reported below. A selection of phase diagrams are shown in

Figure *3.17* for the water content range (15.8 - 24.8 *wt%*). The Q_{II}^{G} phase is observed at low pressure (red open circles) and the lamellar phase (black squares) is seen at high pressure; between the two phases there is a region of coexistence.

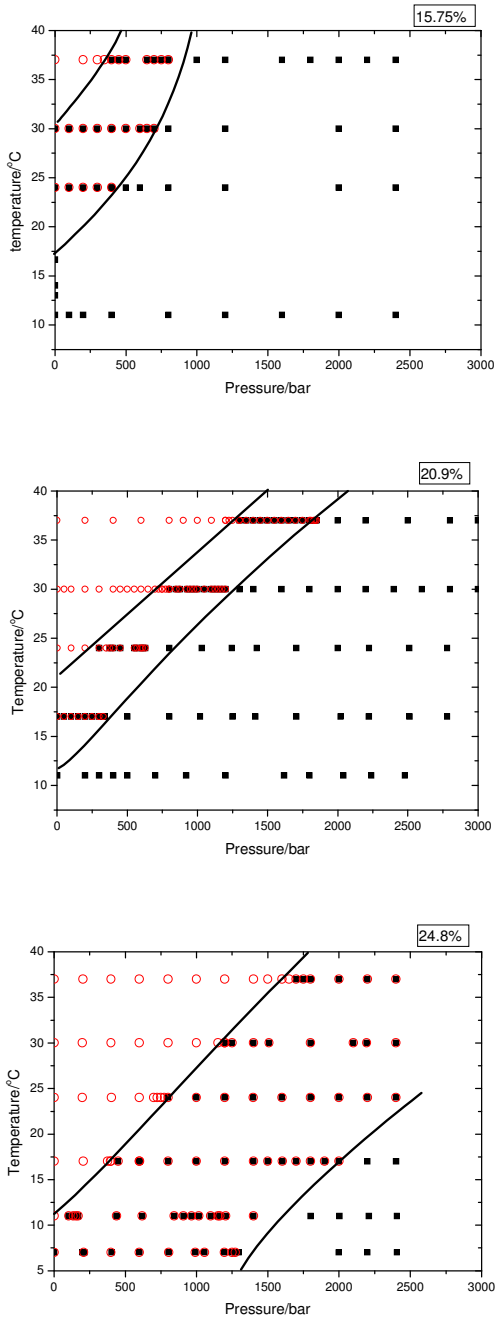


Figure 3.17 Selection of P-T phase diagrams obtained from X-ray diffraction with phases identified at distinct pressures and temperatures and phase boundaries located for 15.75 wt%, 20.9 wt% and 24.8 wt% water samples. Lamellar phase (black squares); Q_{II}^{G} (red circles) (remaining phase diagrams can be found in the Appendix A for reference). When the two symbols are plotted together they indicate phase coexistence.

A 3-D plot of the seven P-T phase diagrams has been generated using Origin 7 to visualise the change in the phase boundaries as the three parameters are varied.

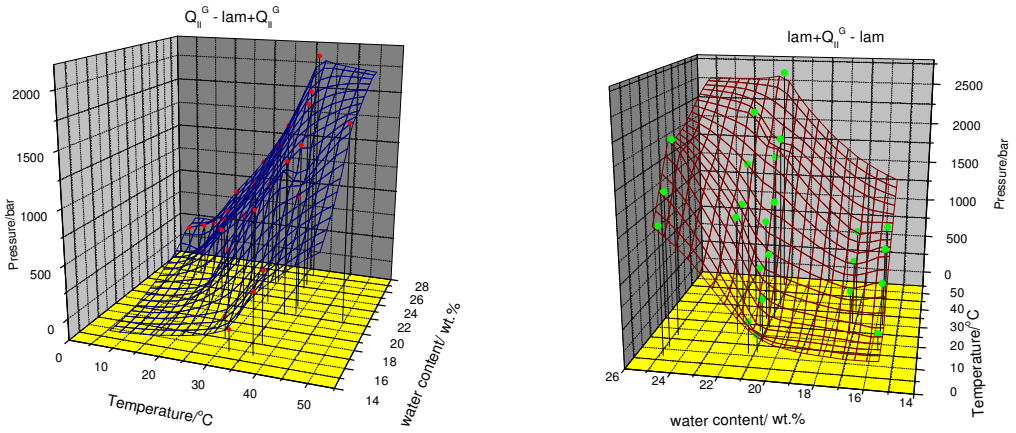


Figure 3.18 3d phase diagram from pressure dependent data obtained at I22 and ID02 beamlines. Left shows the Q_{II}^{G} to lamellar & Q_{II}^{G} phase boundary, and right shows the lamellar to Q_{II}^{G} & lamellar phase boundary.

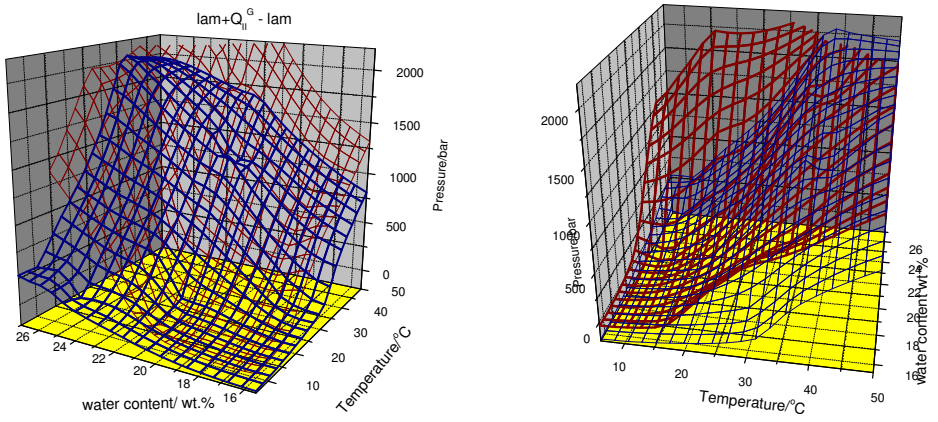


Figure 3.19 3-D phase diagrams for lamellar to Q_{II}^{G} for water contents between 15.8 wt% and 27 wt% water from different viewpoints.

Figure 3.18 and Figure 3.19 show how the phase boundaries for a limited hydrated sample might change with pressure, temperature and water composition. It can be seen that pressure has a linear dependence on the phase boundaries, an increase in pressure will move the phase boundary to higher temperature. The shape and position of the phase boundary in P-T space is determined by its water content.

It is evident that water plays a functional role in phase stability in the monolinolein system where addition of water in the system causes a shift in the phase boundaries to higher pressures and low temperatures and increases the size of the coexistence region. At 30 ^{o}C the region of coexistence for 17.1 *wt%* water is 450 bar and at 26.9 *wt%* water the region of coexistence is more than 1000 bar.

Increasing the pressure leads to a decrease in interfacial curvature as subtle changes in the hydrocarbon chain region cause its volume to decrease. To accommodate for a decrease in curvature and an increase in the pore size radius more water is required to fill the pore. To make water available to the system some of the bilayers will flatten and form a fluid lamellar phase (Figure 3.10), making water available to stabilise the Q_{II}^{G} phase. At low water contents (15.75 *wt%* water), a pressure will be reached where there is insufficient water to the increasing pore size and the whole system will form the lamellar phase. At higher water contents, 26.9 *wt%* water, more water is available in the system and the Q_{II}^{G} phase is stable at higher pressures, where the lamellar phase coexistence makes this possible.

3.3.3 Equilibrium studies in the reverse direction: shift of pressure-temperature phase boundaries

Experiments were undertaken to compare the position of PT phase boundaries for increasing and decreasing pressure. The equilibration time was maintained at 2 min for each change in pressure (in both directions) and diffraction images were taken every 100 bar. Close to the phase boundary the pressure steps were reduced to 50 bar to increase accuracy of phase diagram positions.

The pressure-temperature phase diagram is shown in Figure 3.20 for a 22.2 wt% water sample where the data points have been removed for clarity. Phase boundaries for increasing pressure are

shown in black and decreasing pressure boundaries are shown in grey. It can be seen that there is a shift in the phase boundaries to lower pressure for decreasing pressure equilibrium studies. The maximum displacement is 500 bar and can be attributed to hysteresis in the sample.

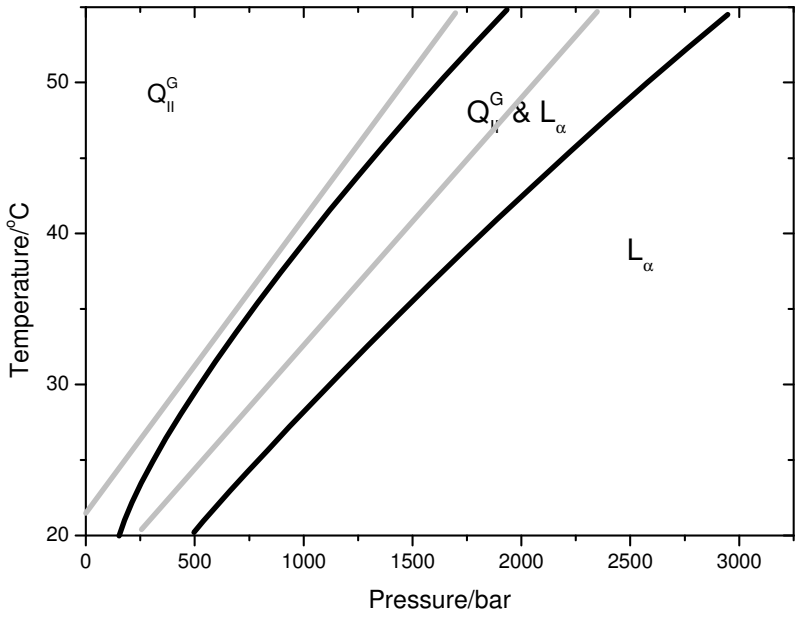


Figure 3.20 P-T phase diagram for 22.2 wt% water: increasing pressure (black boundary) and decreasing pressure (grey boundary).

3.4 Chapter Summary

The full temperature-composition phase diagram has been characterised and discussed, and in addition seven P-T phase diagrams with different water contents ranging from 15.8 -26.9 *wt%* have been characterised. It has been seen that monolinolien with water will form a range of curved and non-curved Type II phases at ambient temperatures. In both temperature and pressure studies, water plays an important role in phase stability.

Errors in this work arise from insufficient sample equilibration time due which will lead to inaccuracies in phase boundary positions. In addition water loss from the sample into its environment at high temperatures will lead to a shift of phase boundaries to lower water contents. It would be important for futures experiments of this kind to attempt to reduce the errors that have been highlighted.

Chapter 4 : Determination of the pivotal surface in the Q_{II}^{G} phase: comparison of the constant mean curvature model and the parallel interface model

Abstract:

Using Q_{II}^{G} lattice parameter data obtained from equilibrium studies on limited hydrated ML samples the existence of the pivotal surface is confirmed. At 25 ^{o}C and atmospheric pressure the pivotal surface lies 8/10 along the length of the lipid from the bilayer midplane which corresponds to carbon 2 of the acyl chain. If temperature is increased the pivotal surface will shift towards the head group, if pressure is increased the pivotal surface will shift towards the bilayer midplane.

At ambient temperatures the stability of the Q_{II}^{G} phase arises from a mixture of packing frustration and curvature stress. As the temperature deviates from ambient temperature frustrations from curvature stress dominate and the bilayer geometry will lie closer to a constant mean curvature interface.

4.1. Introduction:

The stability of the inverse bicontinuous cubic phases arise from a balance of forces and frustration within the bilayer [123]. In order to model the phase behaviour of inverse bicontinuous cubics and predict their locations in phase diagrams accurate calculations of their free energy are needed [53, 122, 124, 125]. To achieve this, the location of the pivotal surface is required, which is defined as the surface, within the bilayer, whose cross-sectional area does not change when the monolayer is bent and is the surface from which the free energy is calculated.

Mathematical models have been established to locate the pivotal surface in inverse cubic phases. In these models the bilayer and the pivotal surface are constrained to either a parallel interface (PIM) or a constant mean curvature interface (CMCM). The parallel interface model has previously been used to locate the position of the pivotal surface at 25 ^{o}C for monoolein (MO) [126], however it was concluded that the precision in measurements of mass, density and lattice parameter limited the unequivocal confirmation of the pivotal surface in bicontinuous cubic phases.

In this chapter, the Parallel Interface model (PIM) and the Constant mean curvature (CMCM) models will be used to confirm the presence of a pivotal surface in the Q_{II}^{G} phase of a limited hydrated monolinolein (ML) sample whose phase behavior has been characterized as a function of temperature, pressure and water volume fraction (Chapter 3). In addition, density measurements of a limited hydrated ML sample were made to reduce the errors and are described in the first part of this chapter. The remaining sections will describe the methodology undertaken to obtain the pivotal surface parameters, A_n and V_n, and discuss the effect of pressure and temperature on the location of the surface.

4.2. Molecular volume of limited hydration monolinolein

In the CMCM and PIM there are five unknowns: ϕ_w, a, A_n, V_n *and* V. ϕ_w, and a (water volume fraction and lattice parameter) are obtained from SAXS measurements of varying water hydrations (Chapter 3) ; A_n and V_n (Area at the pivotal surface and the volume between the pivotal surface and the bilayer midplane) are unknowns that are found in the fitting procedure and V (molecular

volume) is obtained from density values. As there are a limited number of measured lipid densities available, estimates of lipid densities are often used for these calculations. However this will limit the accuracy of A_n and V_n and would not be suitable for our requirements. Therefore, the density of limited hydrated ML was measured as a function of pressure and temperature.

The measurements were achieved using an Anton Paar DMA 512P vibrating densimeter (University of Dortmund) and is described in more detail in Chapter 2, Materials and Methods. Measurements were taken at 11 ^{o}C, 17 ^{o}C, 24 ^{o}C and 37 ^{o}C, from 0-700 bar at 100 bar intervals. Values of molecular volumes at intermediate temperatures and pressures were obtained via extrapolation of the experimental data.

4.2.1 Materials and Methods

Approximately 5 g of sample was required for one experiment. To ensure homogenisation of the sample the lipid water mixtures were made to 23 *wt%* water in approximately 1 g portions. The sample was mechanically mixed, forwards and backwards, by centrifugation and then freeze-thawed at least 30 times. The portions were placed together and the whole sample was centrifuged forwards and backwards 10 times and subjected to a further 10 freeze thaw cycles. The sample was stored under nitrogen and at -20 ^{o}C until further use.

To obtain the precise water content, the sample was removed from the sample cell after the experiment, weighed, and placed on the lyophiliser until no further change in weight was recorded (after 24 hours) and the water content (24 *wt%* water) was obtained.

Samples were loaded using a high pressure filling device, described in Section 2.7.3 and the measurements were taken from an average of 21 consistent data points. Errors were obtained from a standard deviation of these data points.

The density of lipid ρ_l is the inverse of the specific molar volume, V_l , of the lipid (Equation 4.1) .

$$\rho_l = \frac{1}{V_l} = \frac{n_w}{n_l}\left(\frac{1}{\rho} - \frac{1}{\rho_w}\right) + \frac{1}{\rho}$$ Equation 4-1

Where ρ is the measured density of lipid and water, ρ_w is the density of water, n_w is the moles of water and n_l is the moles of lipid.

The molecular volume, V, of the lipid is obtained by multiplying the density by the molecular weight of ML (354.5 g mol^{-1}) and dividing by Avogadro's number.

4.2.2 Results

The density of ML was measured and calculated at 11 °C, 17 °C, 24 °C and 37 °C from 1 bar to 700 bar, and the density and calculated molecular volume are shown in Figure 4.1. A summary of the molecular volume data is given in Table 4.1.

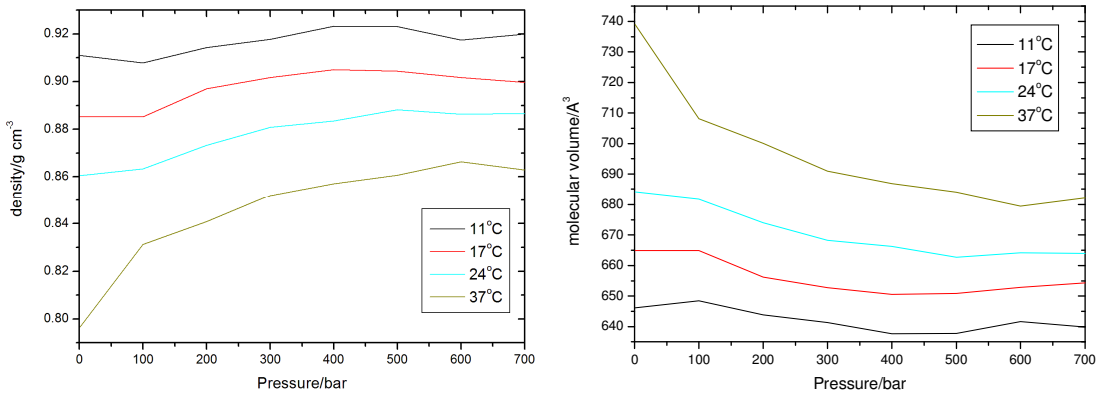


Figure 4.1 Plots of density (left) and molecular volume (right) as a function of pressure at 11 °C, 17 °C, 24 °C and 37 °C for 24 wt% water sample. As temperature increases the density decreases and the molecular volume increases. As pressure is changed there is a smaller effect on the density and molecular volume where density increases as pressure increases and molecular volume decreases as pressure increases.

T / °C (±1oC) → / P / bar (±5bar) ↓	11	17	20	20.4	24	25	31	37
1	646	665	674	673	684	687	705	739
100	648	665			682			708
200	644	656			674		690	700
300	641	653			668			691
400	638	651		659	666			687
500	638	651			663		677	684
600	642	653		657	664			680
700	640	654			664		669	682

*Table 4-1 Experimental molecular volume for a 24 wt% water sample at different pressures and temperatures. The errors arise from standard deviations obtained from 21 values *where no error has been stated for V, the error is less than 0.03 Å^3.*

It can be seen from Figure 4.1 that the molecular volume increases with temperature and decreases with pressure. As temperature is increased, the lipid will have more energy and there will be a greater number of trans-gauche rotamers in the acyl chain which occupy more volume. Conversely when the pressure is increased, the hydrocarbon chains are squeezed together and the volume occupied by the hydrocarbon chains decreases.

At 20 °C the molecular volume for ML is 673 Å^3 and its density is 0.874 g cm^{-3}. At the same temperature MO has a molecular volume of 616 Å^3 [127] and density of 0.942 g cm^{-3} [128]. The molecular volume for ML is greater than MO by 8.5% and is due to the structural difference between the two lipids where ML has an additional cis double bond on carbon 12.

4.2.2.1. Molecular volumes at intermediate temperatures

V and ρ_l were calculated at 5 ^{o}C intervals from 10 ^{o}C to 55 ^{o}C from linear fits (Equation 4.2 and Equation 4.3) to the experimental data (Figure 4.2)**.** An example at atmospheric pressure is shown (Figure 4.2) and a summary of the results are given in Table 4.2.

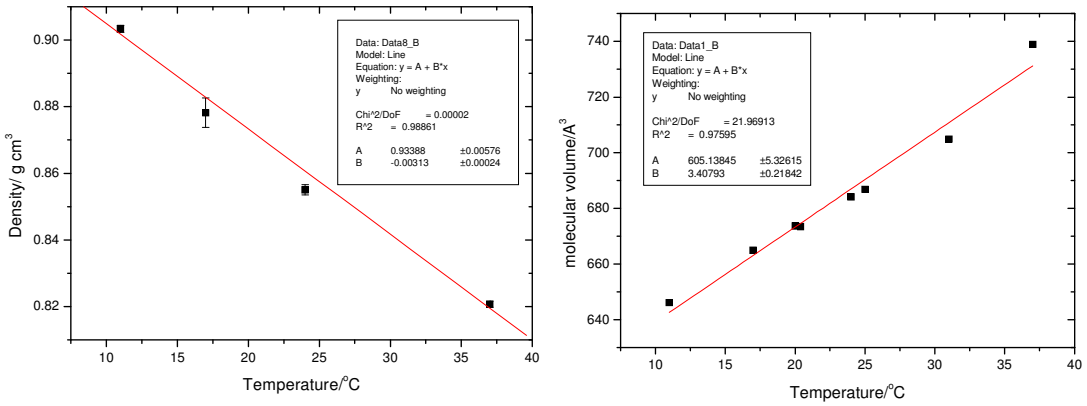


Figure 4.2. To obtain the molecular volume and density at intermediate temperatures the density (left) and molecular volume (right) are plot as a function of temperature. A linear fit is made to the data and from the fit density and pressure at any temperature can be calculated.

$$\rho_l = 0.934\ (\pm 0.006) - 0.0031\ (\pm 0.0002) * T \qquad \text{Equation 4-2}$$

$$V = 605.1\ (\pm 5.3) - 3.4\ (\pm 0.2) * T \qquad \text{Equation 4-3}$$

Temperature/^{o}C	lipid density / g cm^{-3}	Molecular volume / Å^{3}
10	0.92±0.01	639±8
15	0.90±0.01	656±9
20	0.88±0.01	673±10
25	0.86±0.01	690±11
30	0.84±0.01	707±12
35	0.82±0.01	724±13
40	0.80±0.01	742±14
45	0.78±0.01	759±15
50	0.76±0.01	776±16
55	0.74±0.01	730±17

Table 4-2 Summary of lipid density and molecular volume obtained at temperatures between 10 ^{o}C and 55 ^{o}C from linear fits of the experimental data.

4.2.2.2. Molecular volumes at intermediate pressures

In the same way, molecular volume, *V* can be obtained at any pressure from linear fits to experimental data. The linear fits to the data are shown in Appendix B i and a summary of the data is given in Table 4.3.

Pressure Temperature	1 bar	100bar	200bar	300bar	400bar	500bar	600bar	700bar
10 °C	639±8	648±4	642±3	640±2	638±4	637±3	642±3	641±6
15 °C	656±9	659±5	653±3	650±3	647±5	646±3	649±4	648±6
20 °C	673±10	670±5	664±3	659±3	657±5	655±4	656 ±4	656±7
25 °C	690±11	682±6	675±4	669±3	666±6	664±4	665±5	663±8
30 °C	707±12	694±6	686±4	678±4	675±6	673±5	671±5	671±9
35 °C	724±13	705±7	697.±4	688±4	685±7	682±5	678±6	678±10
40 °C	742±14	716±7	708±5	697±4	694±8	691±6	685±6	686±11
45 °C	759±15	728±8	719±5	707±5	704±8	700±6	692±6	693±12

Table 4-3 Summary of molecular volume data at varying pressures and temperatures obtained from linear fits to the experimental data.

The error in the molecular volume is obtained from the difference between the data and the linear fit.

4.2.2.3. Density at intermediate temperatures and pressure

$\frac{\rho_w}{\rho_l}$ is required for calculation of the water volume fraction from the water content (*wt%* water) (Equation 4.5). ρ_w and $\rho_{l,}$ were obtained from experiment and $\frac{\rho_w}{\rho_l}$ calculated at different pressure and temperatures from linear fits to the experimental data. The figures are shown in the Appendix B ii and the results are summarised in Table 4.4.

Temperature Pressure	7 °C	11 °C	17 °C	20.4 °C	22.2 °C	25.6 °C	30 °C	31.5 °C	37 °C
1 bar	1.062	1.101	1.115	1.134	1.144	1.162	1.186	1.193	1.224
100 bar	1.101	1.114	1.132	1.143	1.149	1.160	1.174	1.178	1.196
200 bar	1.097	1.109	1.128	1.138	1.143	1.153	1.167	1.171	1.188
300 bar	1.101	1.111	1.126	1.135	1.140	1.148	1.159	1.163	1.177
400 bar	1.101	1.111	1.126	1.135	1.140	1.148	1.159	1.162	1.177
500 bar	1.104	1.114	1.128	1.136	1.141	1.149	1.160	1.163	1.180
600 bar	1.116	1.124	1.134	1.141	1.144	1.151	1.159	1.162	1.174
700 bar	1.115	1.123	1.136	1.143	1.147	1.154	1.162	1.166	1.180
high pressures	1.116	1.123	1.135	1.142	1.145	1.152	1.161	1.163	1.178

Table 4-4 Summary of $\frac{\rho_w}{\rho_l}$ with less than 2% error on each value, obtained from experimental data for 24 wt% water ML sample with units g cm^{-3}.

4.2.3 Density measurement errors

It would be expected that density change as a function of pressure and temperature will be linear, however the data clearly shows a deviation from linearity at low pressures (Figure 4.1). This is attributed to the presence of a small number of air bubbles in the sample. Complete removal of air bubbles is extremely difficult due to the high viscosity of the limited hydrated sample (see 2.7.3) and the presence of air bubbles will lead to a smaller molecular volume at low pressures. This error is eliminated at higher pressures as the air bubbles will dissolve.

4.2.4 Overview of density experiments

Difficulties in loading highly viscous samples have been overcome and high pressure density measurements were obtained for a 24 *wt%* water ML sample. From linear fits to the experimental data *V* and $\frac{\rho_w}{\rho_l}$ were calculated at any required pressure and temperature.

4.3. Obtaining A_n and V_n from model fitting

Having measured the density of ML and calculated the molecular volume, A_n and V_n can be obtained by fitting the parallel interface model (PIM) and the constant mean curvature (CMCM) to swelling data. The models have been described in the introduction and are given as Equation 4.4 and Equation 4.6 for reference.

Parallel interface model (PIM):

$$a = \frac{V_n}{A_n \times (1-\phi_w)} \left(-2\sigma + \frac{2^{\frac{5}{3}}\sigma^2}{\left(4\sigma^3 + 9\pi\chi(1-\phi_w)^2\left(\frac{V_n}{V}\right)^2 + 3(1-\phi_w)\left(\frac{V_n}{V}\right)\sqrt{\pi\chi\left(8\sigma^3 + 9\pi\chi(1-\phi_w)^2\left(\frac{V_n}{V}\right)^2\right)}\right)^{\frac{1}{3}}} + 2^{\frac{1}{3}}\left(4\sigma^3 + 9\pi\chi(1-\phi_w)^2\left(\frac{V_n}{V}\right)^2 + 3(1-\phi_w)\left(\frac{V_n}{V}\right)\sqrt{\pi\chi\left(8\sigma^3 + 9\pi\chi(1-\phi_w)^2\left(\frac{V_n}{V}\right)^2\right)}\right)^{\frac{1}{3}} \right)$$

Equation 4-4

Where a is the lattice parameter; V_n is the volume between the bilayer midplane and the pivotal surface; A_n is the area at the pivotal surface; ϕ_w is the water volume fraction (calculated from Equation 4.5); σ is the dimensionless surface area; χ is the Euler-Poincare characteristic; V is the molecular volume.

$$\phi_w = \frac{C_w}{C_w + ((1-C_w)*(\frac{\rho_w}{\rho_l})} \qquad \text{Equation 4-5}$$

C_w is the water fraction (*wt%* water) and ρ_w is the density of water and ρ_l is the density of lipid measured experimentally.

Constant mean curvature model (CMCM)

$$a = 2 * \sum_{i=0} \frac{\sigma_i[(\frac{Vn}{V})(1-\phi_w)]^{2i}}{(\frac{An}{V})(1-\phi_w)} \qquad \text{Equation 4-6}$$

where σ_i are are σ_0 = 3.0915; σ_1 = -1.3317; σ_2 = -0.19974; σ_3 = -0.80113 respectively; ϕ_w is the water volume fraction given by Equation 4.5.

4.3.1. Method: fitting to geometric models

The lattice parameter was plotted as a function of water volume fraction and the data fit to Equation 4.4 and 4.6 using the NonLinearModelFit package in Mathematica 7. The full Mathematica code for PIM and CMCM can be found in Appendix B iii.

As the PIM has complex and real solutions the model was evaluated for real solutions only, and A_n and V_n were constrained to assist the fitting process in both models

The data was fit in the following way from 10 °C to 45 °C at 5 °C intervals, and an example of this procedure is shown in Figure 4.3 at atmospheric pressure and 25 °C using the PIM.

1. All of the swelling data at atmospheric pressure and temperature were fitted to the model (Figure 4.3i);

2. The residuals (the difference between the observed and predicted response) (Figure 4.3 ii) were calculated for each data point and the data point with the largest residual was removed;

3. The data was replotted and fit to the model (Figure 4.3 iii);

4. The residuals were plotted and the data point with the largest residual was removed (Figure 4.3 iv);

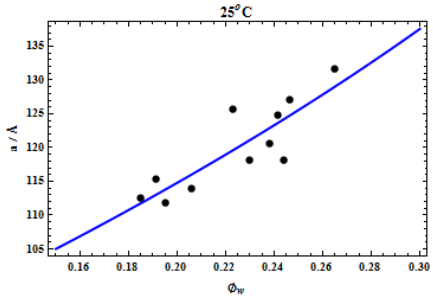
5. The procedure was repeated until all data points had a residual of less than 3 Å for temperature dependent experiments. (Figure 4.3 v-viii).

This fitting procedure was adopted to ensure that the models were being fit to a statistically reliable data set. The anomalous data points are most likely to arise from inhomogeneous samples where the actual ϕ_w differs from the expected ϕ_w. It would be expected that across the temperature range the same water volume fractions are consistently removed. This is not always the case and indicates that within the sample there are likely to be areas with different water contents. Changing the temperature will affect the distribution of water and the correlation of the individual data point to the model at each temperature. As there are a large number of data points it is still possible to obtain reliable values for A_n and V_n despite small differences in water content in the sample.

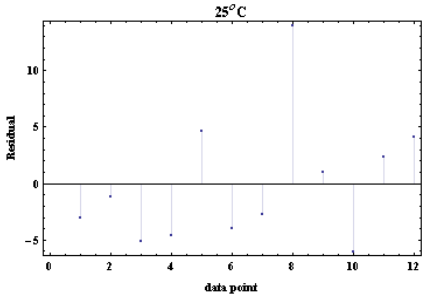
The same procedure was undertaken for the constant mean curvature model using Equation 4.6 between 10 °C to 45 °C at 5 °C intervals.

To fit the pressure dependent data at 24 °C, 30 °C and 37 °C from 1 bar to 600 bar, the same Mathematica code was used. The results of the fitting are shown in Section 4.3.2.

The results obtained at 10 °C for the PIM are not shown as V_n and A_n gave physically unreasonable errors, V_n= 170.5 Å^3 ± 1616.4 Å^3 and A_n=44.5 Å^2 ± 106.2 Å^2. In addition A_n and V_n obtained using the CMCM at 37 °C and 600 bar have large errors and the pivotal surface models do not fit the experimental data under these conditions.

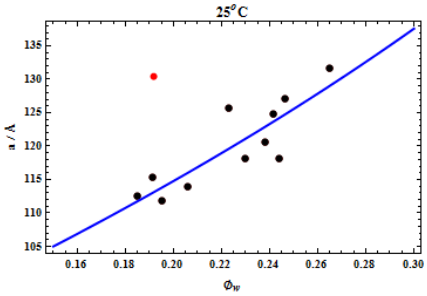


i)

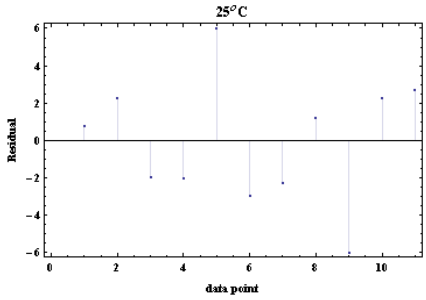


ii)

A_n=43.1 Å^2 ± 8.4 Å^2 V_n = 531 Å^3 ± 300 Å^3

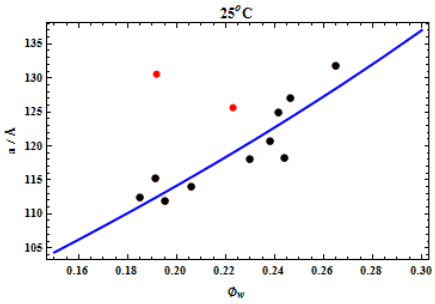


iii)

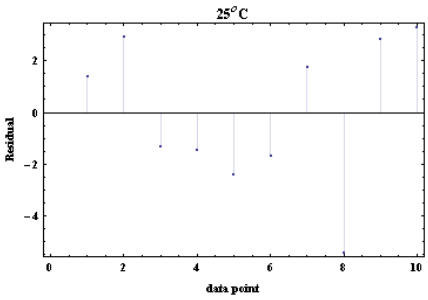


iv)

A_n=39.1 Å^2 ± 3.7 Å^2 V_n =501 Å^3 ± 122 Å^3

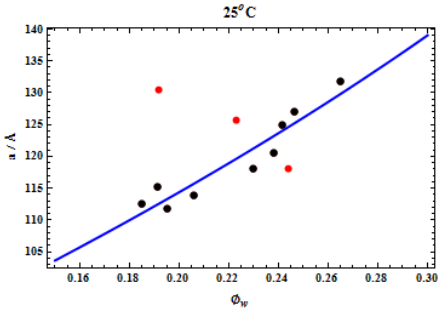


v)

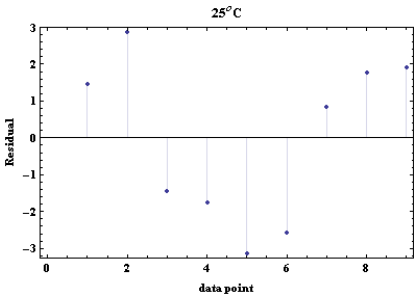


vi)

A_n=39.1 Å^2 ± 3.2 Å^2 V_n =506 Å^3 ± 102 Å^3



vii)



viii)

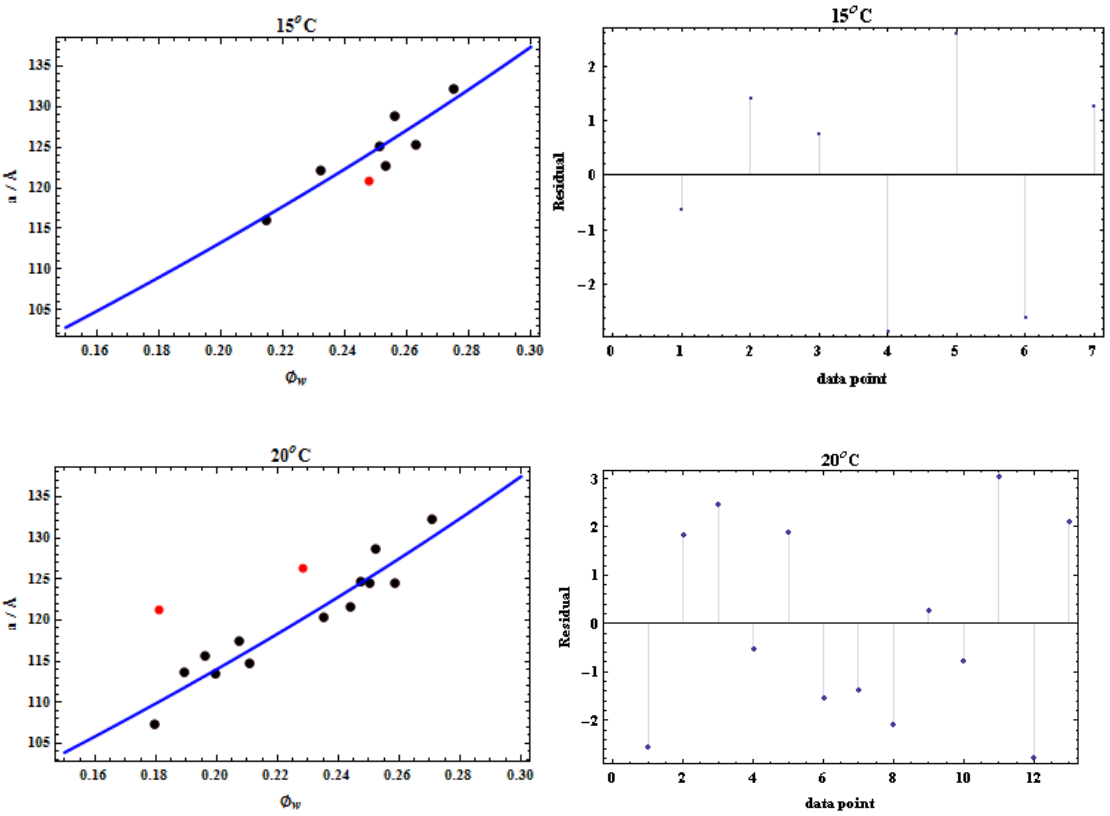
A_n=37.5 Å^2 ± 2.3 Å^2 V_n = 547 Å^3 ± 64 Å^3

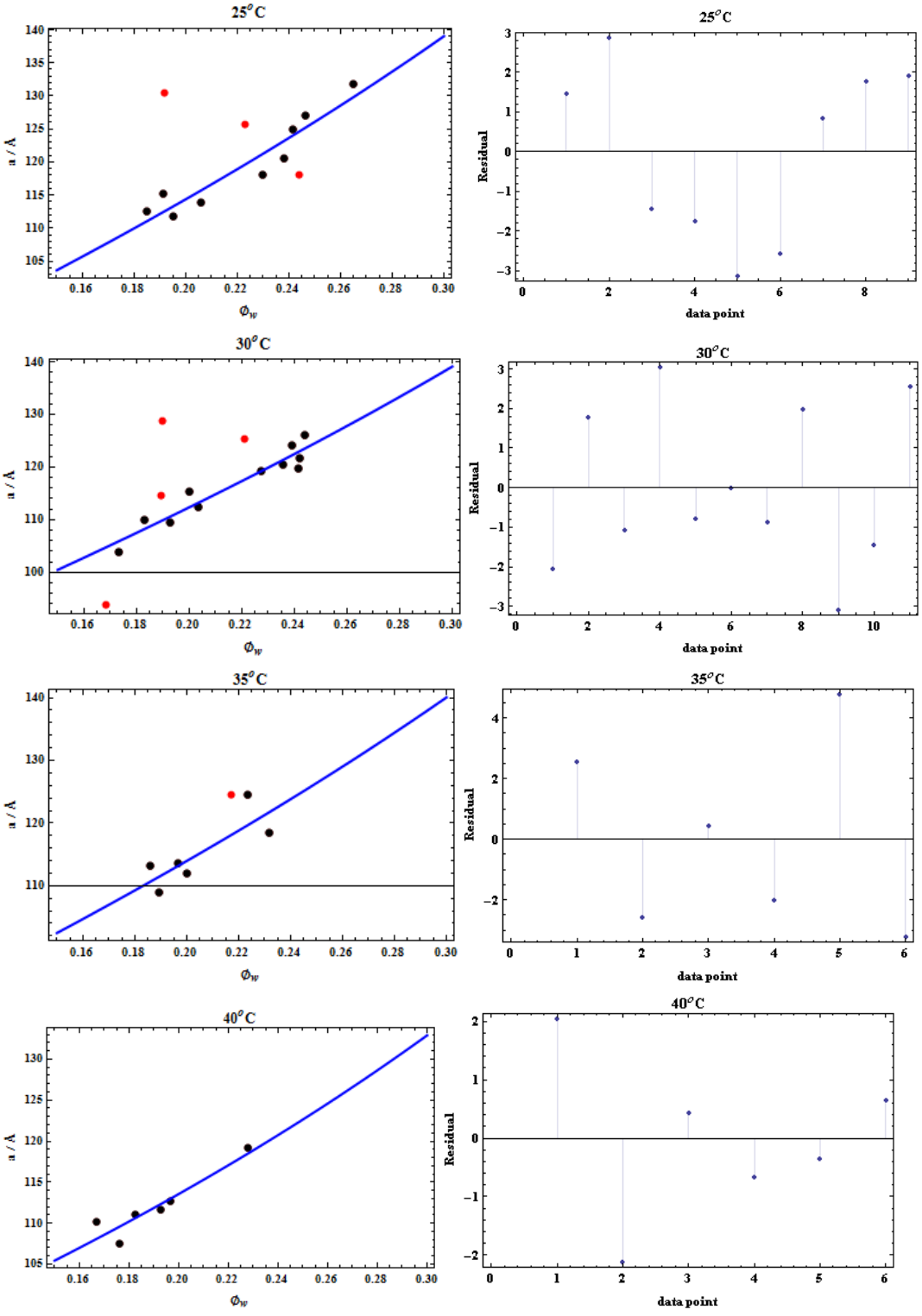
Figure 4.3 Examples of fitting procedure for the parallel interface model at 25 °C and atmospheric pressure. The equation is fit to the data and the residuals obtained and plotted (right). Large residual points are removed, the data are replotted and refitted, and the residuals reanalysed. This methodology is repeated until all the residuals are less than 3 Å.

4.3.2 Results from Model fitting

The results from the model fitting are summarised, with the experimental data and their fits, and shown in Figure 4.4 - Figure 4.11, and a summary of the pivotal surface parameters given in Table 4.6 - Table 4.12. The models were fitted to the black data points whilst the red data points were not included in the fits, and the fit is shown as the blue line.

4.3.2.1 Atmospheric pressure - function of temperature




25°C
a / Å
ϕ_w
25°C
Residual
data point
30°C
a / Å
ϕ_w
30°C
Residual
data point
35°C
a / Å
ϕ_w
35°C
Residual
data point
40°C
a / Å
ϕ_w
40°C
Residual
data point

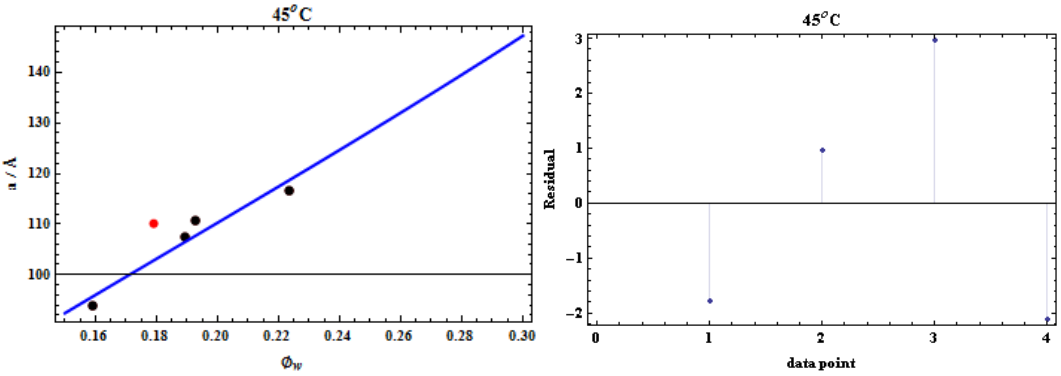
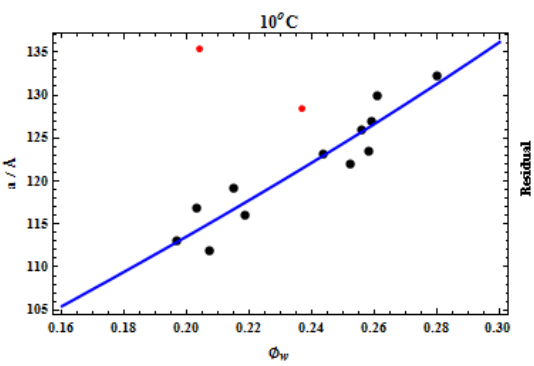
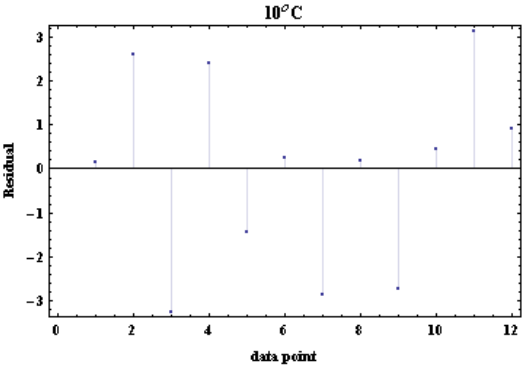


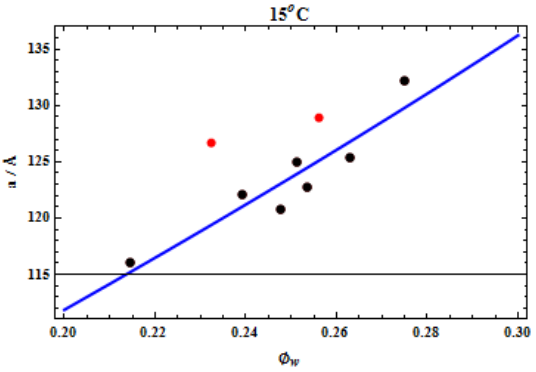
Figure 4.4 Results of PIM fitting to the experimental data at atmospheric pressure from 15 °C to 45 °C obtained on the Bede microsource. On the left are shown model fits (blue line) to the experimental data (black) with data points with residuals larger than 3 removed (red points) to obtain a statistically reliable fit which is reflected in the residual fits for each data point involved in the fitting (right)

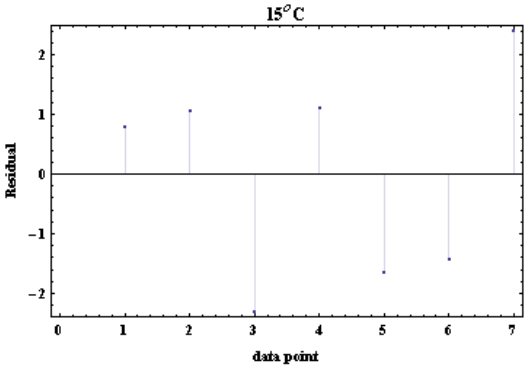
Temperature/°C	V/ Å^3	A_n / Å^2	V_n / Å^3	$\frac{V_n}{V}$ / Å^3
15	656±9	36.2±3.5	519±110	0.77±0.08
20	673±10	37.7±1.7	508±51	0.81±0.10
25	690±11	37.5±2.2	547±64	0.79±0.09
30	707±12	37.1±1.8	608±42	0.86±0.06
35	724±13	38.4±6.4	604±54	0.83±0.21
40	742±14	46.0±4.4	412±183	0.56±0.25
45	759±15	33.8±2.8	771±38	1.02±0.05

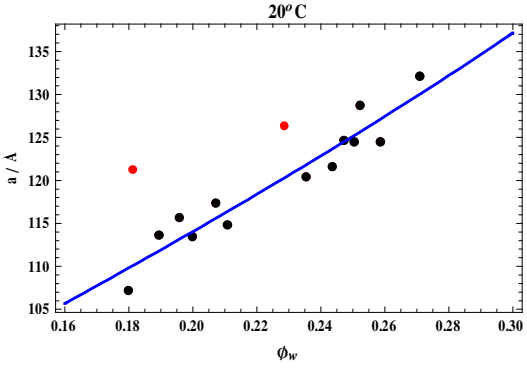
Table 4-5. Summary of molecular parameters obtained at atmospheric pressure. V was obtained from high pressure density measurements whilst A_n and V_n were obtained from fitting the experimental data to the parallel interface model.

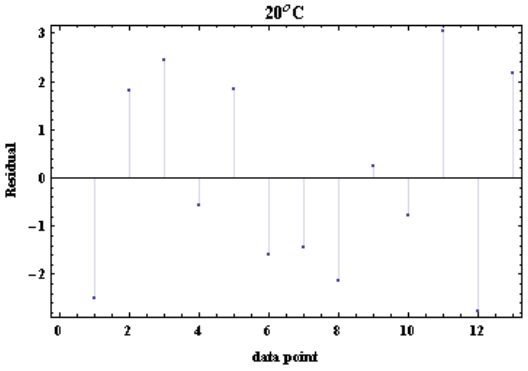

10°C
a / Å
ϕ_w

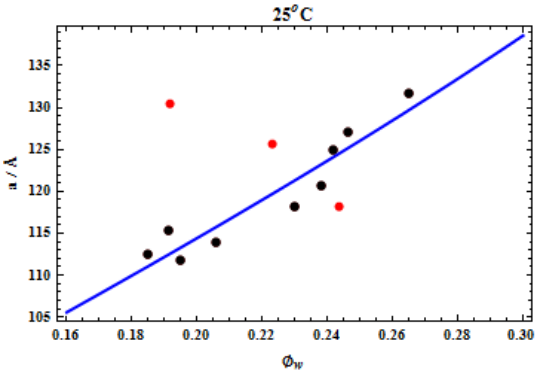

10°C
Residual
data point

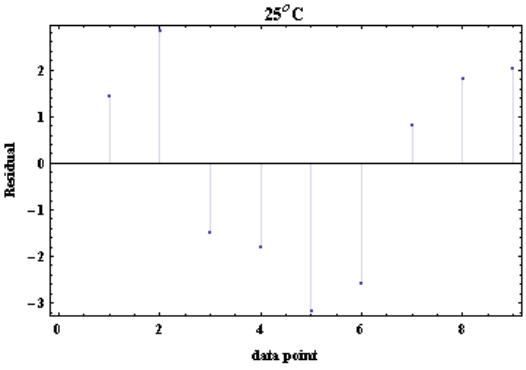

15°C
a / Å
ϕ_w


15°C
Residual
data point


20°C
a / Å
ϕ_w


20°C
Residual
data point


25°C
a / Å
ϕ_w


25°C
Residual
data point

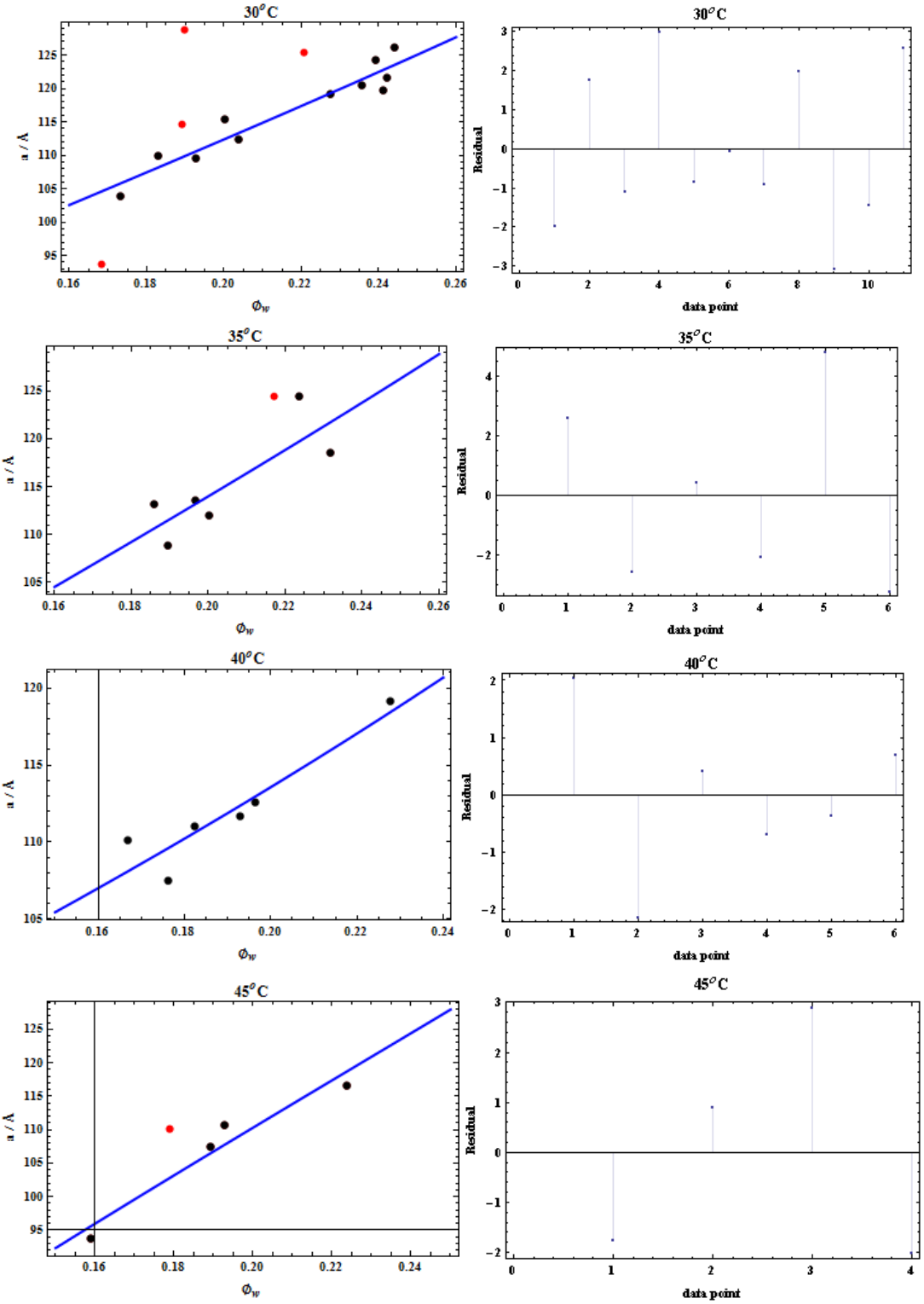


Figure 4.5 Results of CMCM fitting to the experimental data at atmospheric pressure from 10 °C to 45 °C obtained on the Bede microsource. On the left are shown model fits (blue line) to the experimental data (black) with data points with residuals larger than 3 removed (red points) to obtain a statistically reliable fit which is reflected in the residual fits for each data point involved in the fitting (right).

Temperature/^{o}C	V/ Å^3	A_n / Å^2	V_n / Å^3	$\frac{V_n}{V}$ /Å^3
10	639±8	36.5±1.9	462±61	0.72±0.01
15	656±9	36.3±2.7	518±81	0.78±0.12
20	673±10	37.8±1.6	499±48	0.74±0.07
25	690±11	37.8±2.2	536±59	0.78±0.09
30	707±12	37.5±1.7	592±39	0.84±0.05
35	724±13	38.6±6.1	589±142	0.81±0.20
40	742±14	46.0±4.3	408±178	0.36±0.38
45	759±15	34.2±3.1	749±40	0.99±0.05

Table 4-6. Summary of molecular parameters obtained at atmospheric pressure. V was obtained from high pressure density measurements whilst A_n and V_n were obtained from fitting the experimental data to constant mean curvature model .

4.3.2.2 Constant temperature and varying pressures

A summary of fitting the PIM and CMCM to experimental data obtained at constant temperature, 24 ^{o}C, 30 ^{o}C and 37 ^{o}C and various pressures from 1 bar to 600 bar is presented below.

Pressure/bar	V/ Å^{3*}	A_n / Å^2	V_n / Å^3	$\frac{V_n}{V}$ / Å^3
1	684	35.2± 0.7	607±15	0.89±0.02
200	674	34.4±0.4	605±8	0.90±0.01
400	666	35.0±0.6	575±15	0.86±0.02
600	664	40.3±1.5	400±63	0.60±0.10

*Table 4-7. Summary of molecular parameters at 24 ^{o}C and different pressures. V was measured from high pressure experiments and A_n and V_n from fitting experimental data with PIM (*where no error has been stated for V, the error is less than 0.01 Å^3).*

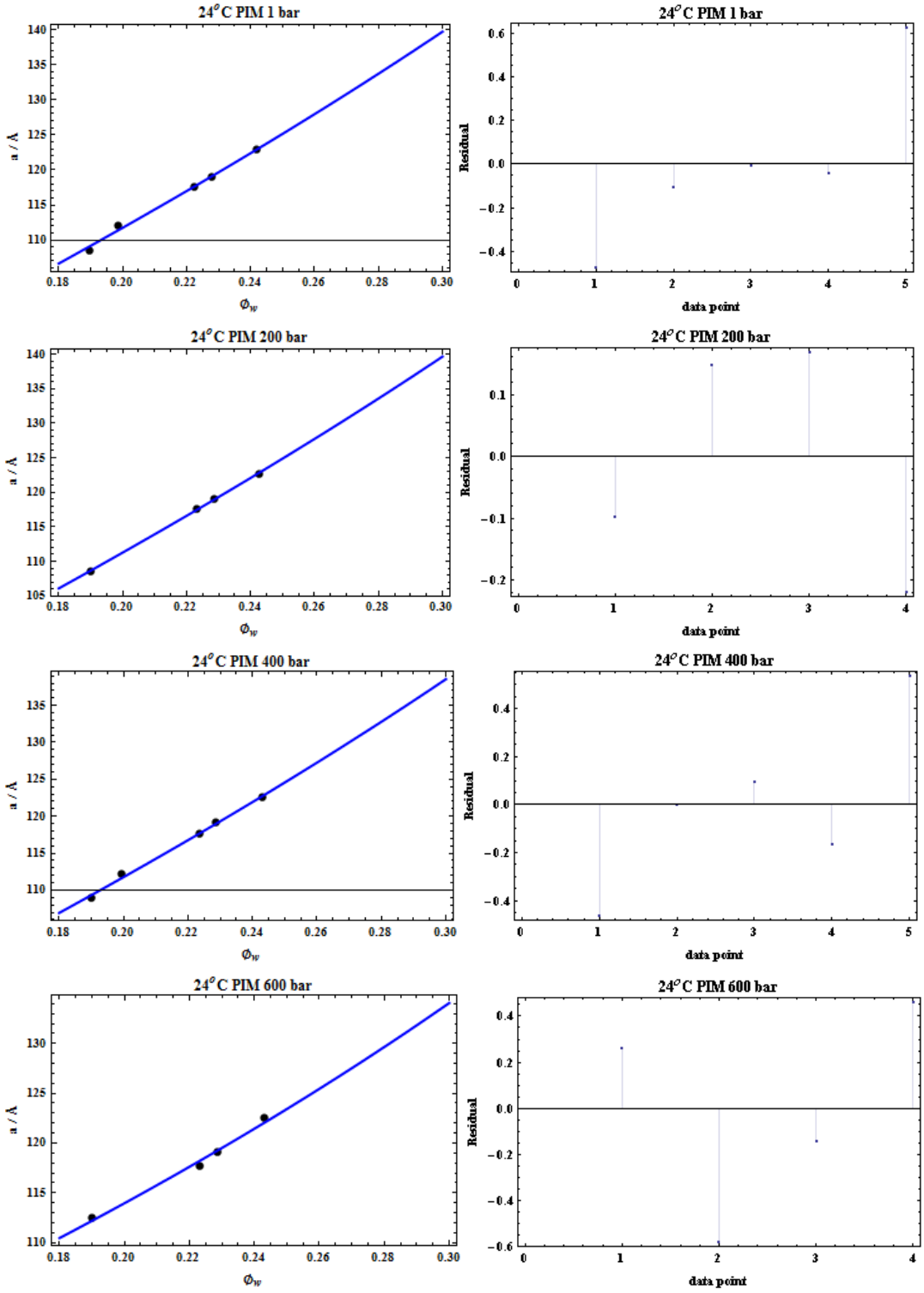


Figure 4.6 Results of PIM fitting to the experimental data at 24 °C from 1 bar to 600 bar obtained on the ID02 beamline for water hydrations from 15 to 25 wt% water. On the left are shown model fits (blue line) to the experimental data (black) and the residual data for each data point (right).

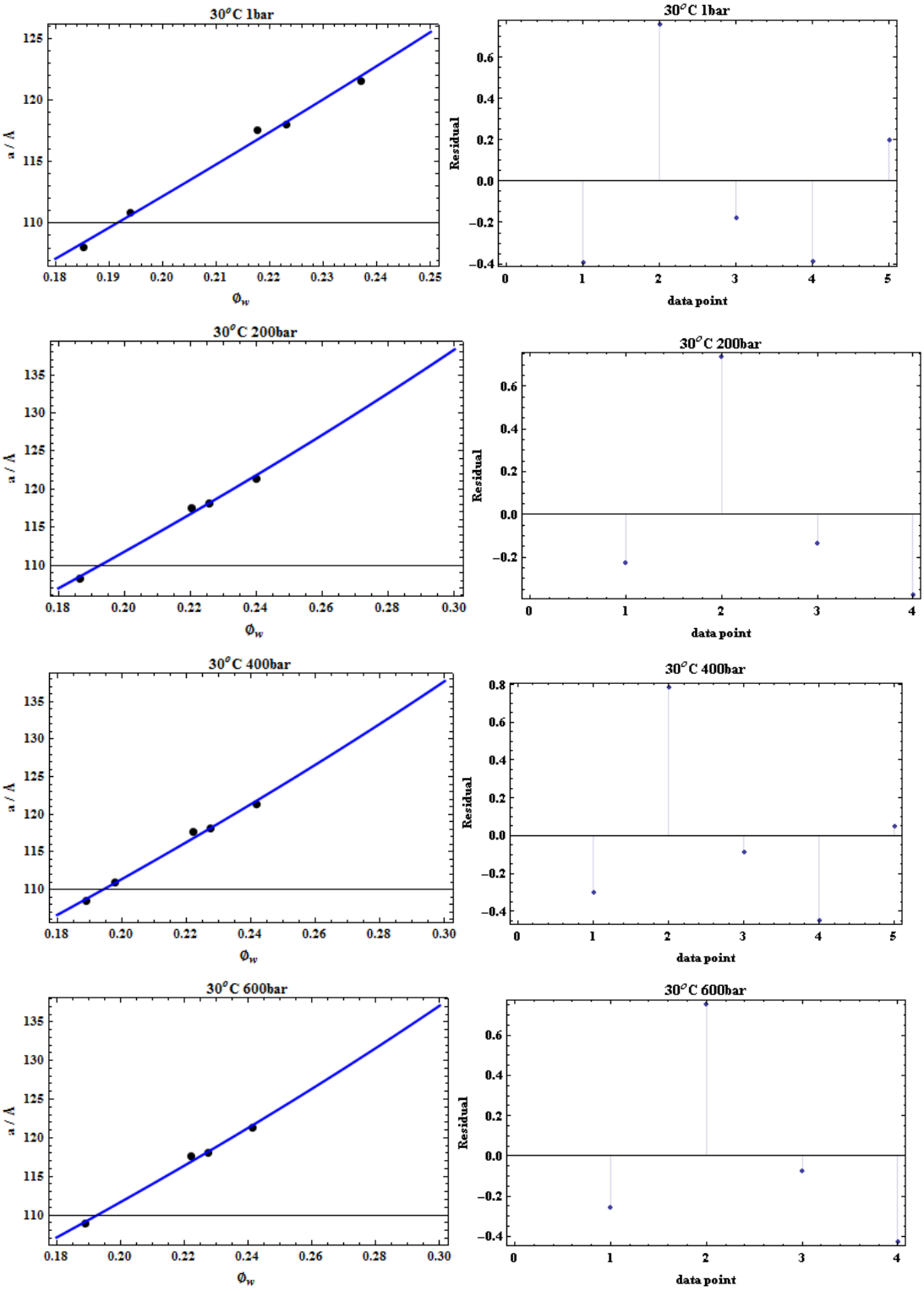
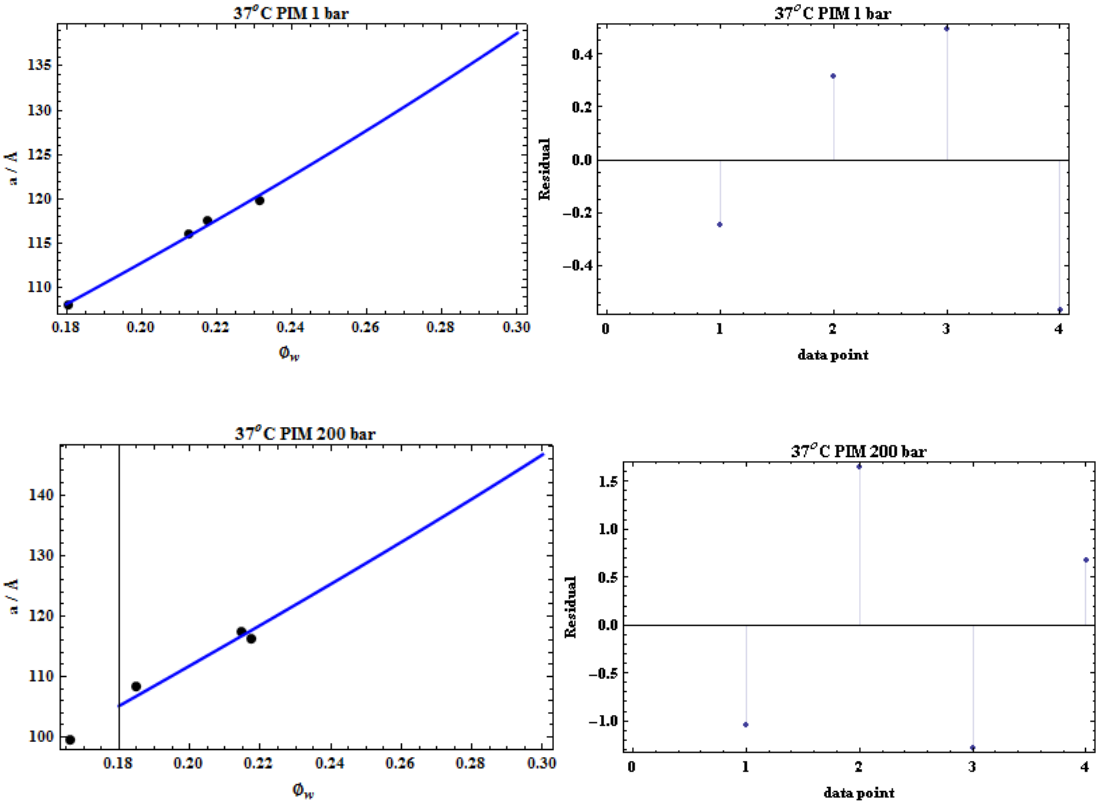


Figure 4.7. Results of PIM fitting to the experimental data at 30 °C from 1 bar to 600 bar obtained on the ID02 beamline for water hydrations from 15 to 25 wt% water. On the left are shown model fits (blue line) to the experimental data (black) and the residual data for each data point (right).

Pressure/bar	V/ Å^3	A_n / Å^2	V_n / Å^3	$\frac{V_n}{V}$ / Å^3
1	707±12	36.4±0.9	625±19	0.88±0.0
200	686±4	36.2±1.1	589±25	0.86±0.04
400	675±6	35.9±0.9	578±20	0.86±0.03
600	671±5	36.2±1.2	558±30	0.83±0.04

Table 4-8. Summary of molecular parameters at 30 ^oC and different pressures. V was measured from high pressure experiments and A_n and V_n from fitting experimental data with PIM.



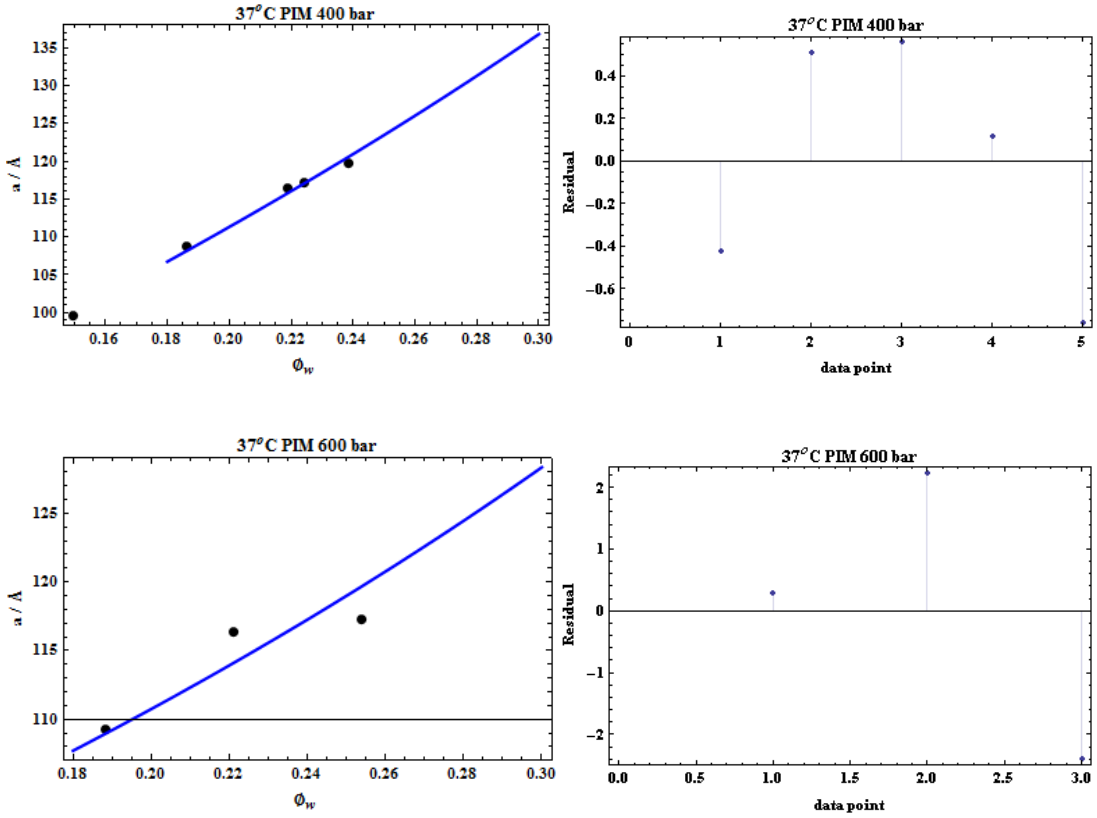


Figure 4.8 Results of PIM fitting to the experimental data at 37 °C from 1 bar to 600 bar obtained on the ID02 beamline for water hydrations from 15 to 25 wt% water. On the left are shown model fits (blue line) to the experimental data (black) and the residual data for each data point (right)

Pressure/bar	V/ Å^3 *	A_n / Å^2	V_n / Å^3	$\frac{V_n}{V}$ / Å^3
1	739	42.1± 2.1	570± 56	0.77±0.08
200	700	35.9±3.8	603±70	0.86±0.10
400	689	36.0±5.2	575±108	0.84±0.16
600	680	39.2±0.4	498±112	0.73±0.16

*Table 4-9 Summary of molecular parameters at 37 °C and different pressures. V was measured from high pressure density experiments and A_n and V_n from fitting experimental data with PIM (*where no error has been stated for V, the error is less than 0.01 Å^3).*

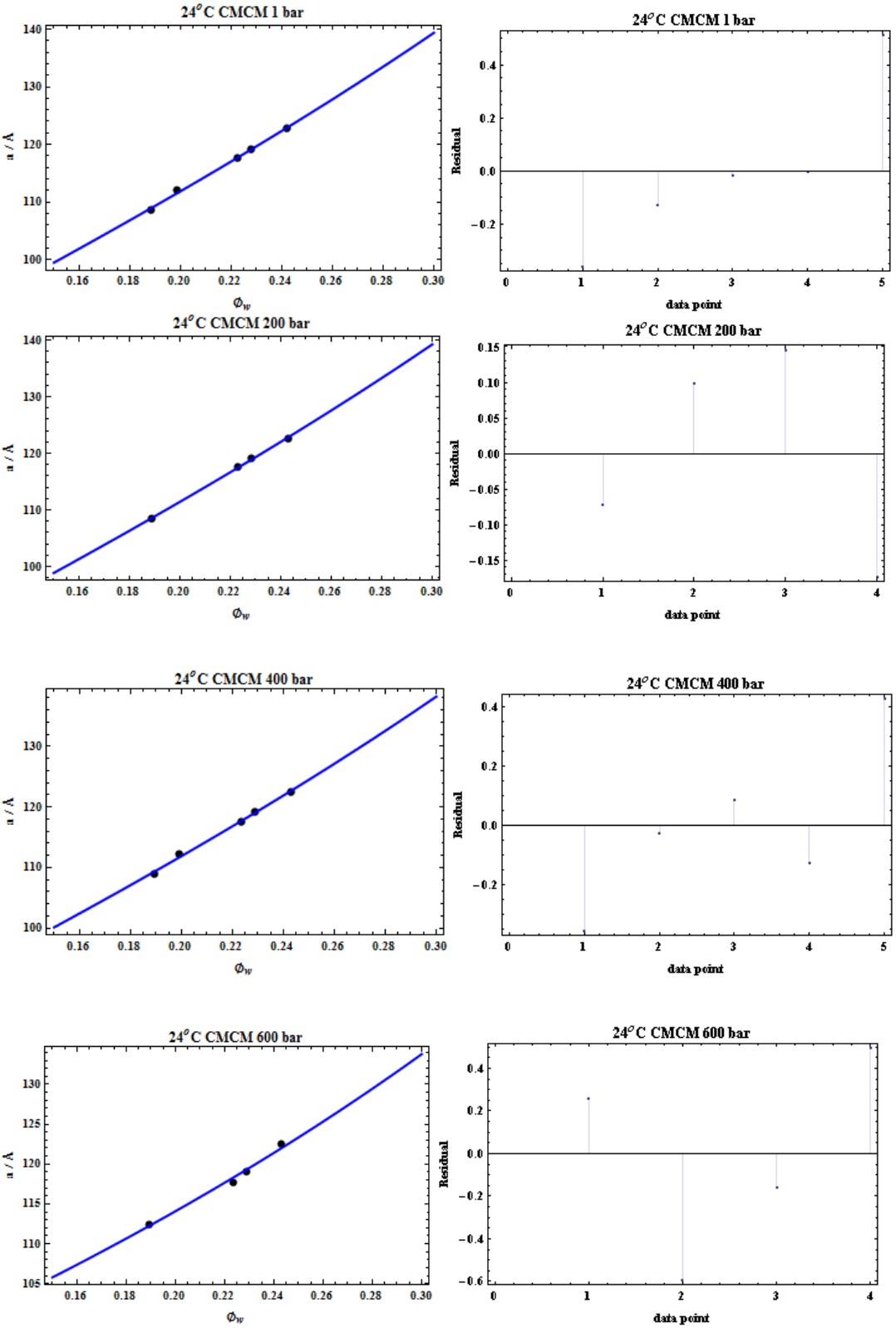
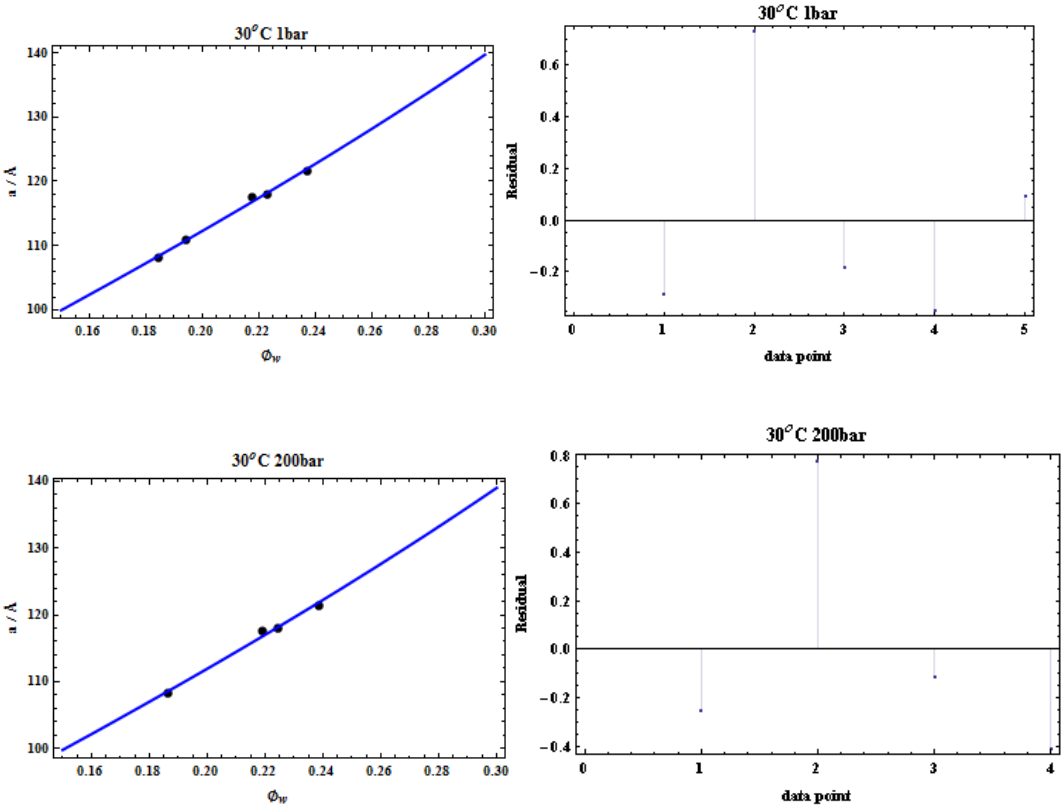


Figure 4.9 Results of CMCM fitting to the experimental data at 24 °C from 1 bar to 600 bar obtained on the ID02 beamline for water hydrations from 15 to 25 wt% water. On the left are shown model fits (blue line) to the experimental data (black) and the residual data for each data point (right).

Pressure/bar	V/ Å^{3} *	A_n / Å^2	V_n / Å^3	$\frac{V_n}{V}$ / Å^{3} *
1	684	35.8± 0.5	586± 11	0.86
200	674	35.1±0.3	583±6	0.86±0.01
400	666	35.6±0.5	555±11	0.83±0.01
600	664	40.7±1.6	380±69	0.57±0.10

*Table 4-10 Summary of molecular parameters at 24 ^{o}C and different pressures. V was measured from high pressure density experiments and A_n and V_n from fitting experimental data with CMCM (*where no error has been stated for V and $\frac{V_n}{V}$, the error is less than 0.01 Å^3).*



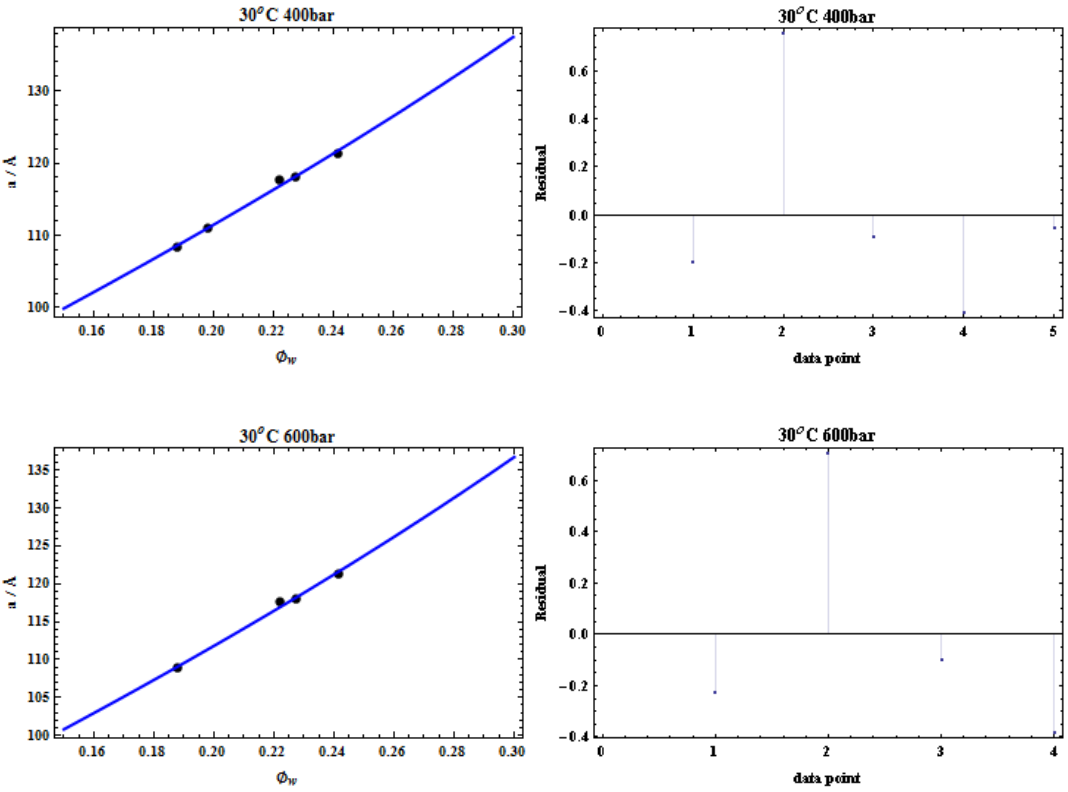


Figure 4.10 Results of CMCM fitting to the experimental data at 30 °C from 1 bar to 600 bar obtained on the ID02 beamline for water hydrations from 15 to 25 wt% water. On the left are shown model fits (blue line) to the experimental data (black) and the residual data for each data point (right)

Pressure/bar	V/ Å^3	A_n / Å^2	V_n / Å^3	$\frac{V_n}{V}$ / Å^3
1	707±12	37.0±0.8	603±16	0.85±0.02
200	686±4	36.1±1.1	582±3.6	0.85±0.03
400	676±6	36.4±0.8	558±18	0.83±0.03
600	671±5	36.8±1.1	536±26	0.80±0.04

Table 4-11 Summary of molecular parameters at 30 °C and different pressures. V was measured from high pressure density experiments and A_n and V_n from fitting experimental data with CMCM.

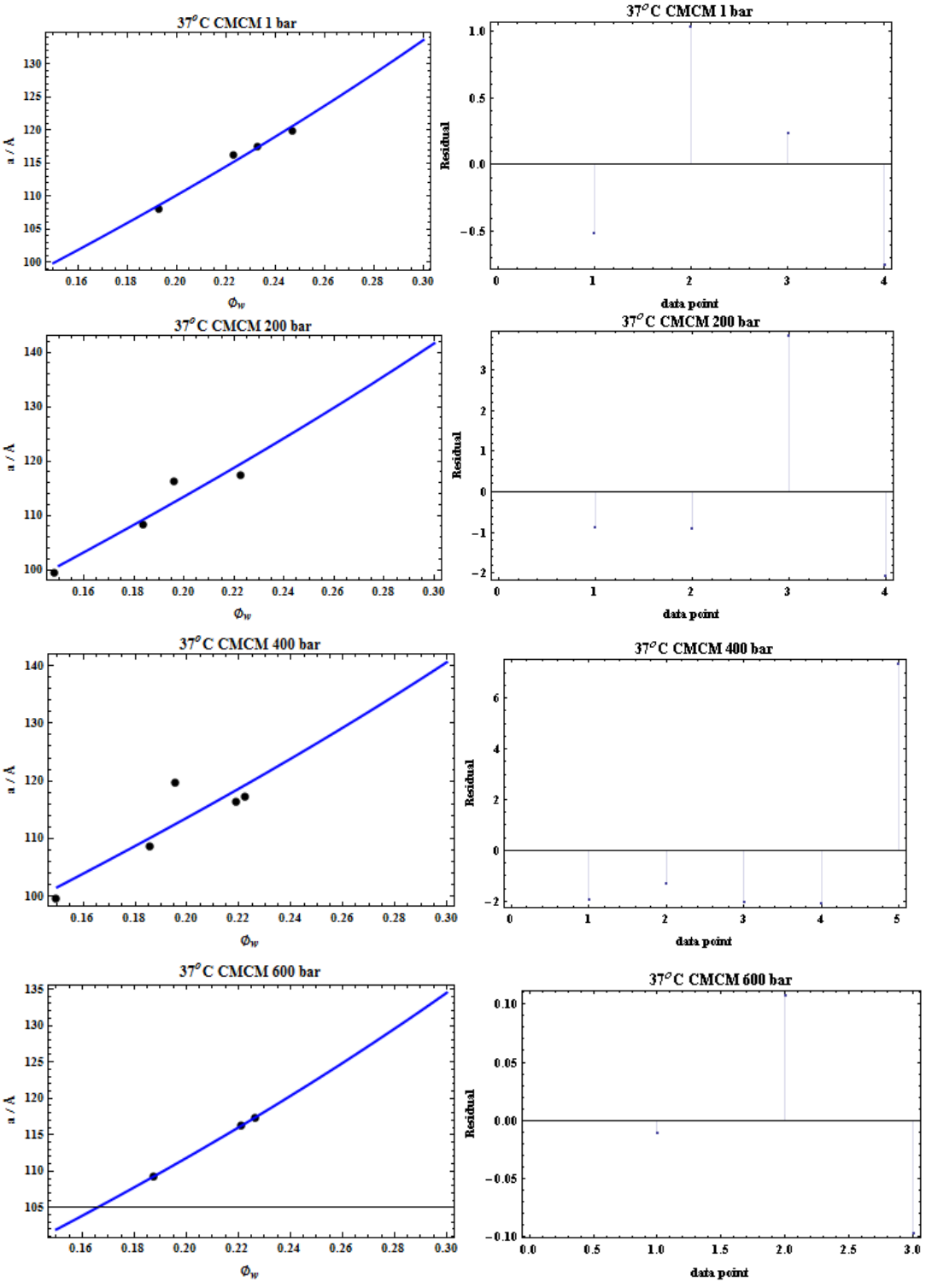


Figure 4.11Results of CMCM fitting to the experimental data at 37 °C from 1 bar to 600 bar obtained on the ID02 beamline for water hydrations from 15 to 25 wt% water. On the left are shown model fits (blue line) to the experimental data (black) and the residual data for each data point (right).

Pressure/bar	V/ Å^{3} *	A_n / Å^2	V_n / Å^3	$\frac{V_n}{V}$ / Å^3
1	739	39.4± 1.3	617± 30	0.83±0.04
200	700	32.0±1.8	694±27	0.99±0.04
400	687	37.2±0.7	573±16	0.83±0.02
600	680	NA	NA	NA

*Table 4-12 Summary of molecular parameters at 37 ^{o}C and different pressures. V was measured from high pressure density experiments and A_n and V_n from fitting experimental data with CMCM (*where no error has been stated for V , the error is less than 0.01 Å^3*).

The experimental data have been fit to the PIM and the CMCM for the pivotal surface where the residuals are <3 Å for temperature dependent data and <0.5 Å for pressure dependent data. The difference in residuals between the two data sets can be attributed to errors in $\boldsymbol{\phi_w}$ and beamline resolution. Temperature dependent data was obtained on the in-house beamline, Bede Microsource, which has a resolution of 1 Å. Pressure dependent data was obtained from ID02 beamline which has a resolution of <0.03 Å. A good correlation between the experimental data and the pivotal surface model can be seen.

It is evident from the model fits to the experimental data (Figure 4.4 - Figure 4.11) that there is a good correlation between the experimental data. The existence of the pivotal surface has been confirmed at varying temperatures and pressures, except at 10 ^{o}C and atmospheric pressure for PIM and 600 bar and 37 ^{o}C for CMCM. Furthermore, the reproducibility of the experimental data can be shown by comparing $\frac{V_n}{V}$ at 1 bar and 30 ^{o}C for temperature dependent and pressure dependent studies (obtained on separate beamlines) where $(\frac{V_n}{V})_P$ = 0.86 ± 0.06 Å^3 and $(\frac{V_n}{V})_T$ = 0.89 ± 0.02 Å^3.

Errors between the experimental data and the pivotal surface models are limited by $\boldsymbol{\phi_w}$ and the molecular volume. Therefore the accuracy in locating the pivotal surface is limited by the precision of density measurements.

4.3.3. Discussion: The pivotal surface in fixed hydration Q_{II}^{G} phase:

$\frac{V_n}{V}$, the location of the pivotal surface and A_n, the area at the pivotal surface have been obtained from fitting experimental data to the mathematical models. In this section, the effect of pressure and temperature will be discussed.

4.3.3.1. Temperature effects on the location of the pivotal surface

$\frac{V_n}{V}$ is plotted as a function of temperature; a linear fit is undertaken and the effect of temperature on $\frac{V_n}{V}$ is discussed.

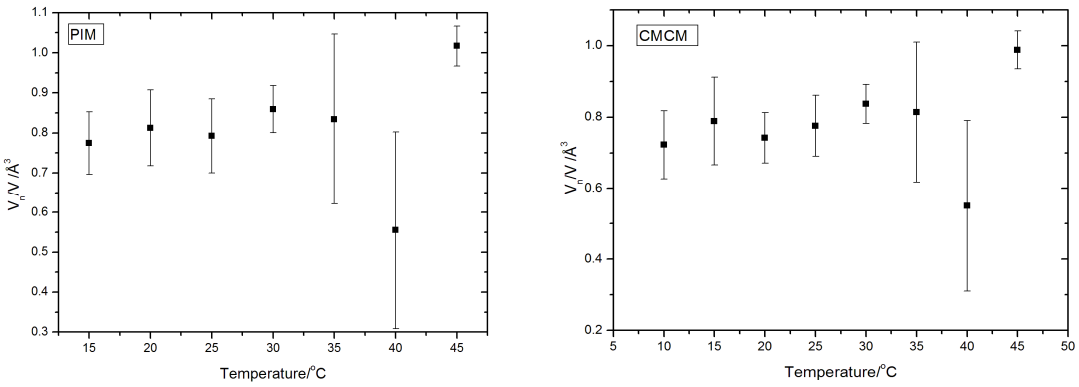


Figure 4.12 Plots of $\frac{V_n}{V}$ against temperature to show how the position of the pivotal surface may change with temperature for PIM (left) and CMCM (right). As the temperature increases the pivotal surface moves towards the headgroup.

At 25 °C the pivotal surface lies approximately 8/10's along the length of the lipid (measured from the bilayer mid plane) (Figure 4.12) where V_n^{PIM} = 547.1 Å^3 ± 63.9 Å^3 and V_n^{CMCM} = 535.6 Å^3 ± 59.1 Å^3. For a fluid phase, a CH_3 unit occupies approximately 54 Å^3 and a CH_2 approximately 27 Å^3 [129]. At 25°C the pivotal surface is estimated to lie on carbon 2 of the acyl chain. In comparison the

pivotal surface for MO has been located between carbon 3 and carbon 4 where the addition of a *cis* double bond in the hydrocarbon chain will shift the pivotal surface away from the bilayer midplane.

As temperature is increased from 15 °C to 35 °C, the location of the pivotal surface moves away from the bilayer mid plane, towards the headgroup. Below 35 °C the error is approximately 10 % and above 35 °C the error increases to 40 %. At 45 °C $\frac{V_n}{V}$ is larger than 1 which is physically unreasonable. Due to the large errors in $\frac{V_n}{V}$ at high temperatures linear fits were undertaken on the data up to and including 35 °C to obtain a more quantitative description of temperature effects on the location of the pivotal surface. (Figure 4.14)

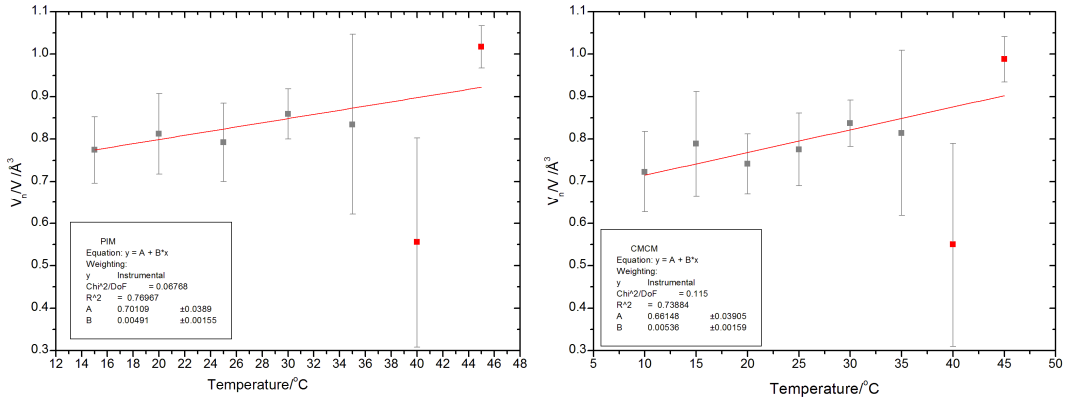


Figure 4.13 Linear fits of $\frac{V_n}{V}$ against temperature at atmospheric pressure which show < 1 % K^{-1} change.

Linear fits to $\frac{V_n}{V}$ against temperature from 10 °C to 35 °C at atmospheric pressure, for PIM and CMCM, show that there is < 1 % K^{-1} shift towards the head group where $\left(\frac{d}{dp}\left(\frac{V_n}{V}\right)\right)_{PIM}$ = 0.00491 Å^3 ± 0.0016 Å^3 and $\left(\frac{d}{dp}\left(\frac{V_n}{V}\right)\right)_{CMCM}$ = 0.00538 Å^3 ± 0.0016 Å^3.

4.3.3.2. Pressure effects on the location of the pivotal surface

The effect of pressure on the location of the pivotal surface can be determined by plotting $\frac{V_n}{V}$ as a function of pressure. Figure 4.14 shows data obtained at 30 °C.

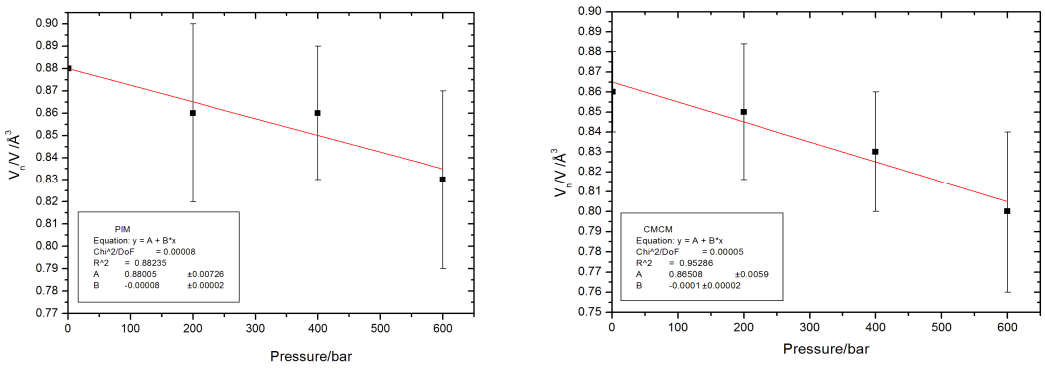


Figure 4.14. Plots of V_n/V against pressure, obtained from model fitting showing the change in position of the pivotal surface with pressure. PIM (left) and CMCM (right). As the pressure increases there is an approximately 0.01 % bar^{-1} decrease in its location.

Linear fits to the data show that for both models there is an approximate shift of 0.01 % bar^{-1} (11.8 % Kbar^{-1}) towards the bilayer midplane. $\left(\frac{d}{dT}\left(\frac{V_n}{V}\right)\right)_{PIM}$ = -0.00008 Å^3 ± 0.00002 Å^3 and $\left(\frac{d}{dT}\left(\frac{V_n}{V}\right)\right)_{CMCM}$ = -0.0001 Å^3 ± 0.00002 Å^3.

The pivotal surface will shift as a reaction to changes in the lipid structure caused by a change by an external thermodynamic parameter. Increasing in temperature increases V_n and the pivotal surface shifts towards the bilayer midplane; increasing the pressure will lead to a decrease in V_n leading to the pivotal surface shifting towards the head group area.

4.3.3.2. Temperature effects on the cross-sectional area at the pivotal surface

A_n obtained from fitting geometric models to experimental data is plotted as a function of temperature (Figure 4.15).

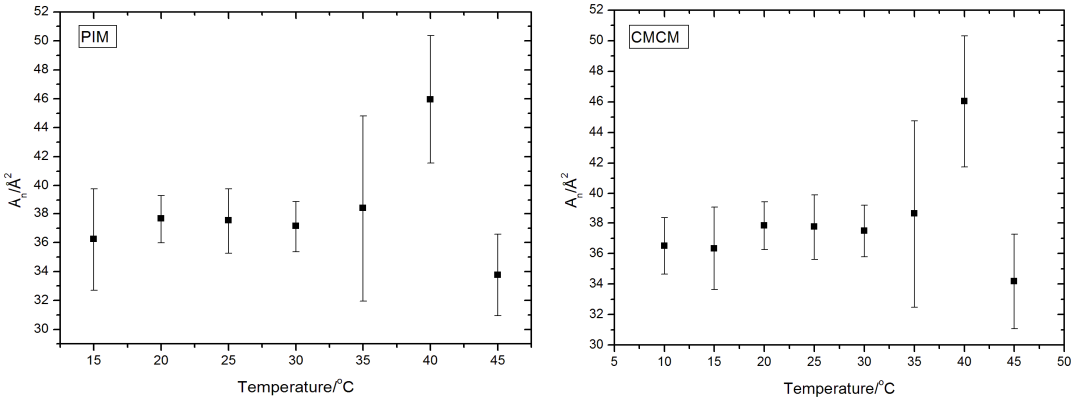


Figure 4.15. Plots of A_n as a function of temperature for PIM (left) and CMCM (right).

At 25 °C and atmospheric pressure A_n = 37.5 Å^2 $\pm$ 1.2 Å^2 for the PIM and is comparable to the values obtained for monoolein at the same temperature, pressure and geometric model, where A_n = 32.6 Å^2 $\pm$ 1.2 Å^2 [55]. Below 35 °C, errors in A_n are approximately 5 %, which increase to 10 % above 35 °C. At 40 °C, A_n is reportedly 10 Å^2 larger than at 35 °C and it is unlikely that over 5 °C the area will increase so dramatically. Data at 40 °C and 45 °C are not included in the linear fits (Figure 4.16.)

Linear fits to A_n vs T (Figure 4.16) give $(\frac{d\,A_n}{dT})_{PIM}$ = 0.01 Å^2 ± 0.05 Å^2 and $(\frac{d\,A_n}{dT})_{CMCM}$ = 0.06 Å^2 ± 0.03 Å^2. The error from the fit for the PIM indicates that there is no significant temperature effect on the cross-sectional area of the pivotal surface, however for the CMCM A_n increases approximately 0.2 % K^{-1}. This can be explained by discussing the difference in the lipid structure for the two geometries. When the pivotal surface adopts a constant mean curvature interface the individual acyl chains will bend and stretch. If the bilayer bends as a consequence of an increase in temperature, the acyl chains will occupy a larger volume in order to maintain the

constant mean curvature configuration. If the surface is constrained to a parallel interface all the lipids will be uniform in length and at a given position in the lipid the cross sectional area will be the same. In order to maintain a parallel interface, modifications to the curvature will occur at the interfacial region. As temperature increase**s,** $(\frac{d\,A_n}{dT})_{CMCM}$ **>** $(\frac{d\,A_n}{dT})_{PIM}$ because V_n increases in order to maintain the constant mean curvature geometry. Further experiments will be required to to reduce the errors in A_n and to make stronger conclusions.

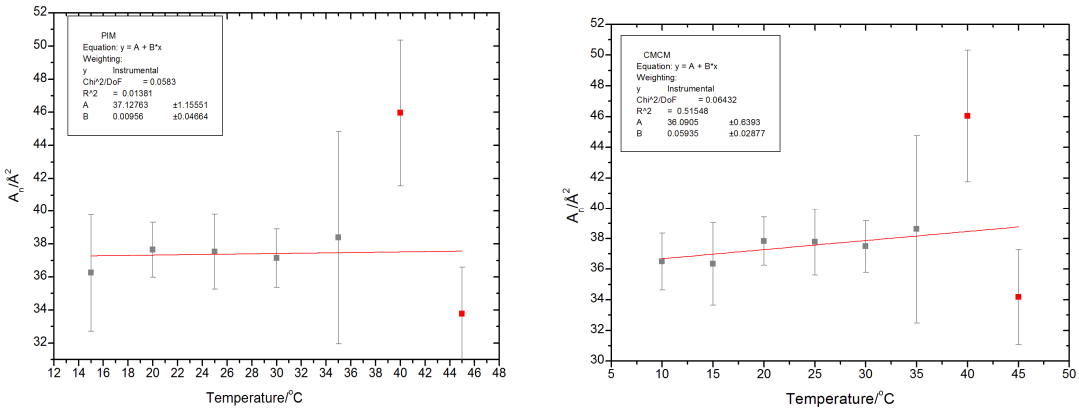


Figure 4.16. Linear fits to A_n as a function of temperature for PIM (left) and CMCM (right). Showing that for PIM the gradient change is insignificant and in CMCM A_n increases approximately 0.2 % K^{-1}.

4.3.3.3. Pressure effects on the cross-sectional area at the pivotal surface

If pressure is induced on the system, changes to A_n are less than 1 Å^2 over 600 bar and are within the error of model fitting (Figure 4.17), so it is difficult to observe any consistent trends in the pressure dependent behaviour. However, it may be predicted from the temperature dependence of A_n and temperature and pressure dependence on $\frac{V_n}{V}$ that increasing pressure will lead to a decrease in the cross-sectional area. The data (Figure 4.17) agrees with this prediction at low pressures.

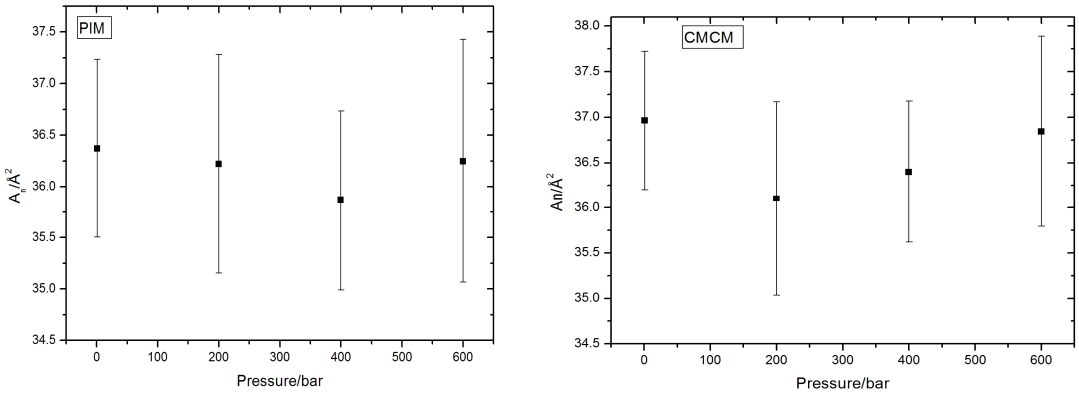


Figure 4.17. Plots of A_n as a function of temperature for PIM (left) and CMCM (right).

4.3.4. Comparisons between the CMCM and PIM as descriptions for the pivotal surface geometry

In this section the errors in A_n and V_n, and the average residuals from the fitting will be compared and discussed. By comparing the results obtained from the CMCM and the PIM, it will be possible to make assertions about the pivotal surface and the bilayer geometry**.**

4.3.4 .1. Atmospheric pressure, as a function of temperature

A_n and V_n obtained from fitting experimental data with PIM and CMCM are directly compared. V_n is larger and A_n is smaller in CMCM compared to PIM (Figure 4.18). If the bilayer adopted a constant mean curvature surface there will be variation in the chain length and it is possible that the average volume occupied by the acyl chain will be larger in CMCM compared to PIM where lipid length will be uniform. However, due to the error on the values it should be concluded that there is no significant difference in A_n and V_n for the two models.

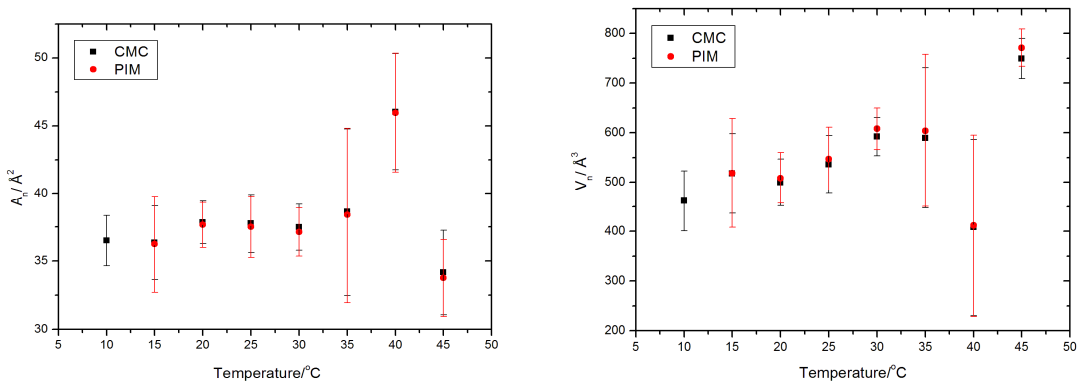


Figure 4.18. Direct comparison of A_n (right) and V_n (left) as a function of temperature and atmospheric pressure for PIM and CMCM. V_n is consistently larger in the CMCM and A_n is consistently smaller, compared to PIM.

The fitting parameters from the two models are comparable (within the accuracy of the experimental data) and suggests that the bilayer lies somewhere between a parallel interface and a constant mean curvature surface. If the bilayer were to adopt an extreme geometry the energetic cost will be too large and the bilayer will change its configuration to reduce these costs and adopt properties of both a parallel interface and a constant mean curvature interface.

The residuals from the fitting procedure were averaged at each temperature and compared (Figure 4.19); the smaller the average residual, the better the correlation between experiment and model. The analysis shows that there is a good correlation between the experimental data and the models where the average residual is less than 2.2 Å confirming the existence of the pivotal surface in a limited hydrated Q_{II}^{G} phase.

At ambient temperatures, 20 °C – 30 °C it can be seen that the average residual is approximately the same for the two models, where the average residual is 1.7 Å at 25 °C. Therefore at ambient temperatures the pivotal surface is described equally well by the two models. At all other temperatures the average residual is smaller for the CMCM which suggests that the pivotal surface lies closer to a constant mean curvature interface than a parallel interface. At higher temperatures the hydrocarbon chain will have more energy and the lateral pressure in the hydrocarbon chain increases leading to an increased propensity for curvature in the bilayer. In a parallel interface configuration the bilayer will experience large amounts of curvature stress and it becomes energetically more favourable for the bilayer to lie closer to the constant mean curvature interface.

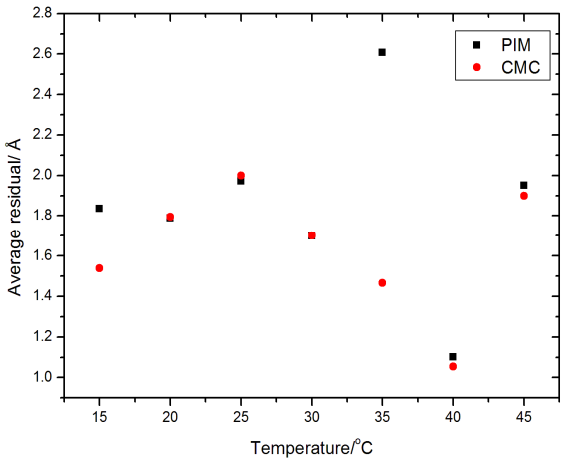


Figure 4.19. Plot to show the average residuals obtained from fitting experimental data to PIM and CMCM as a function of temperature at atmospheric pressure. Generally the CMCM has a smaller average residual compared to PIM.

4.3.4.2. Constant temperature (30 °C) and as a function of pressure

V_n and A_n at constant temperature can be directly compared (Figure 4.20). V_n is less in CMCM than the PIM, conversely A_n is larger in CMCM compared to PIM. The errors in A_n and V_n are consistently smaller in the CMCM where, for example, at 400 bar there is 3.5% error in $(V_n)_{PIM}$ and 3.2% error in $(V_n)_{CMCM}$. However, when accounting for errors in V_n and A_n, the values obtained from the CMCM and PIM are equal and the differences between the percentage error in $(V_n)_{PIM}$ and $(V_n)_{CMCM}$ are so small that they are be assumed to be insignificant.

These errors are approximately an order of magnitude smaller than the errors obtained for A_n and V_n under constant pressure conditions and are attributed to experimental errors. One error, already discussed is due to discrepancies between the expected water content and the actual water content of the sample. This error has been eliminated in the pressure dependent data as the actual water content was calculated from lattice parameter data at atmospheric pressure (described in Chapter 3). Additional errors can be attributed to differences in resolution of the beamline where the Bede microsource (temperature dependent studies) has a resolution of ± 1 $Å^{-1}$ and the ID02 beamline, ESRF, has a resolution of ± 0.03 $Å^{-1}$.

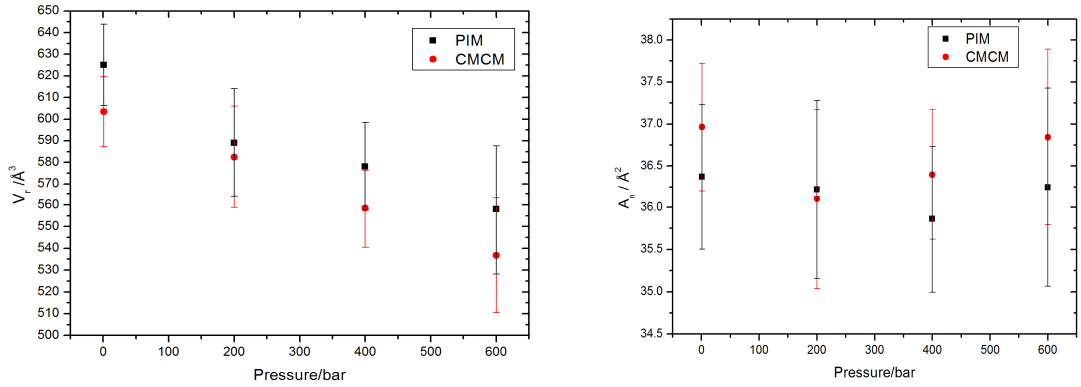


Figure 4.20 Direct comparison of A_n (right) and V_n (left) as a function of pressure for PIM (black squares) and CMCM (red dots) at 30 ^oC.

Comparison of the average residual at each pressure, Figure 4.21, shows an average residual of less than 0.4 Å highlighting the good correlation between experimental data and the pivotal surface models. It can also be seen that the average residual is less for the CMCM compared to the PIM (except 200 bar) and suggests that the bilayer geometry in the Q_{II}^G phase is closer to a constant mean curvature surface than a parallel interface at higher pressures.

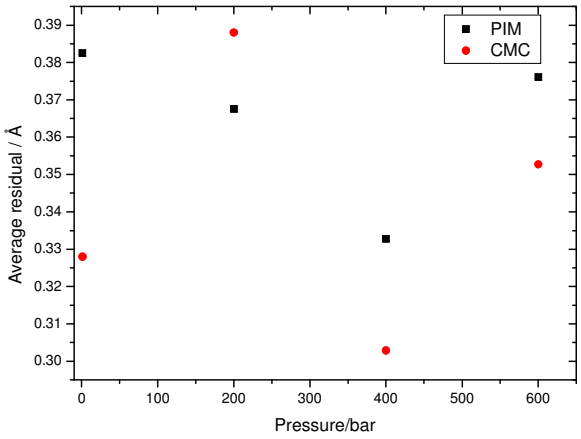


Figure 4.21 Plot to show the average residuals obtained from fitting experimental data to PIM and CMCM as a function of pressure at 30 ^oC. Generally the CMCM has a smaller average residual compared to PIM.

4.3.5 Summary

V_n and A_n have been obtained from fitting experimental data to pivotal surface models, PIM and CMCM and it has been shown that the pivotal surface exists in a limited hydrated Q_{II}^G phase at ambient temperatures where the accuracy of A_n and V_n are limited by the precision of the density measurements. Its existence is not as apparent at higher temperatures where larger discrepancies between the model and experimental data are seen.

Error analysis of A_n and V_n have shown that the PIM and CMCM are equally good descriptions of the bilayer at average temperatures and the bilayer is likely to adopt geometric properties from both models. However, as deviations are made from room temperature, and at higher pressures, the CMCM is a more appropriate description for the lipid bilayer.

At 25 ^{o}C and atmospheric pressure the pivotal surface is located on the 2nd carbon of the acyl chain. As temperature increases the pivotal surface will move towards the bilayer midplane and as pressure increases the pivotal surface moves towards the headgroup. The effect of temperature on the position of the pivotal surface is equal in the CMCM and PIM, however A_n has a greater temperature dependence in the CMCM than the PIM. At present it has not been possible to ascertain the trends in the pressure dependent behaviour of A_n.

4.4. Pressure and temperature effects on the lipid geometry and properties of the pivotal surface: overview

In the final section of this chapter an overview of pressure and temperature effects on the lipid geometry will be given. All the results shown in this section have been obtained from experimental data obtained at beamline ID02, at 24 ^{o}C, 30 ^{o}C, and 37 ^{o}C between 1 bar and 400 bar. A_n and V_n have been obtained from the model fitting to swelling data (Table 4.7-4.12) and V has been obtained from high pressure experiments (Section 4.1). The lipid length, l, and area at the headgroup (A_{HG}) have been calculated using Equation 4.7-4.8.

$$A_{HG} = \frac{2V}{\phi_l a^3}(\sigma\, a^2 + 2\pi\chi l^2)$$ Equation 4-7

where A_{HG} is the area at the headgroup and, V is the molecular volume.

$$1 - \emptyset_w = 2\,\sigma\,\left(\frac{l}{a}\right) + \frac{4}{3}\,\pi\,\chi\,\left(\frac{l}{a}\right)^3$$ Equation 4-8

where ϕ_w is the water volume fraction; σ is the dimensionless unit area; l is the length of the lipid; a is the lattice parameter (experimentally obtained); χ is the Euler characteristic.

Discussion will focus on the constant mean curvature model for illustrative purposes. Results for the PIM have been included in the Appendix B iv for reference. The data obtained as a function of pressure and temperature were fitted to a plane using Mathematica 7 and plotted in 3-D for clarity.The code can be found in Appendix B v and general statements will be made regarding the effect of pressure and temperature on structural properties.

4.4.1 Effects of temperature and pressure on the lipid geometry: lipid length and headgroup area

The structural properties of a lipid can be described through the lipid length and the area at the headgroup; these were calculated for a fixed hydration sample (ϕ_w = 0.227). It is shown that temperature and pressure will have opposing effects on the lipid (Figure 4.22 and Figure 4.23). Increasing the temperature leads to a decrease in lipid length and increase in A_{HG} and a decrease in pressure will have the same effect on lipid length and A_{HG}.

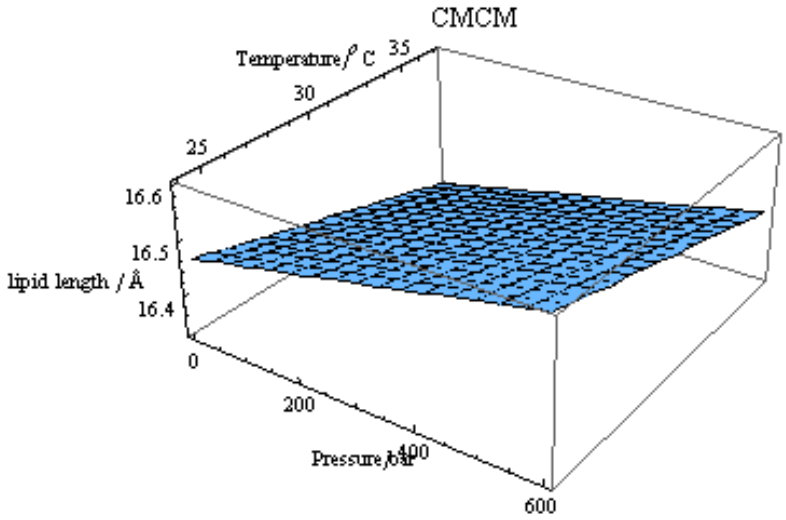


Figure 4.22 Plots of lipid length as a function of pressure (1 bar to 600 bar) and temperature (24 ^{o} C to 37 ^{o}C) show that an increase in pressure leads to an increase in the lipid length and increasing the temperature leads to a decrease in lipid length.

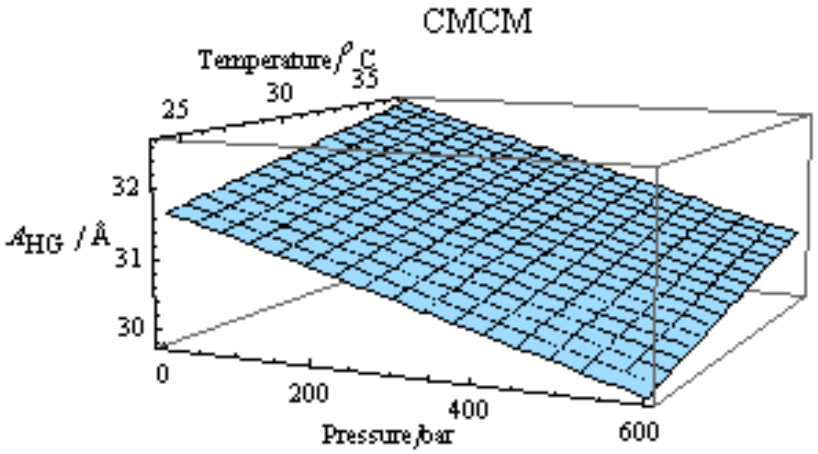


Figure 4.23 Plots of A_{HG} as a function of pressure (1 bar to 600 bar) and temperature (24^{o} C to 37^{o} C) show that as temperature is increased A_{HG} increases and as pressure increases A_{HG} decreases.

An increase in temperature will lead to an increase in the energy in the hydrocarbon chain and the number of trans-gauche rotamers in this region. The volume occupied by the chain will increase as a consequence of a greater number of repulsions between the acyl chains (Figure 4.24). The bilayer

will have an increased propensity to curve and the head groups are pushed together, however this is unfavourable due to repulsive head group - head group interactions and the head groups ultimately increase their area (Figure 4.23). When pressure is increased, the whole lipid is squeezed. A_{HG} decreases and the volume occupied by the hydrocarbon chain reduces and the overall length of the lipid increases. The effects are summarised in Figure 4.24.

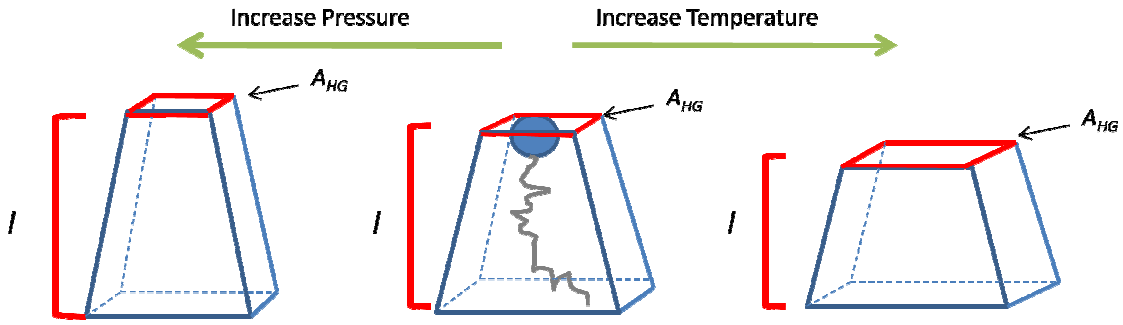
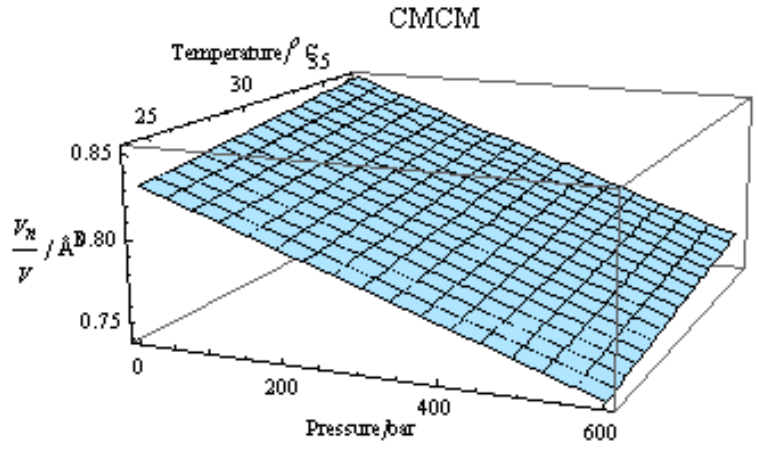


Figure 4.24 Cartoon showing the effects of increasing pressure and temperature on the lipid length and A_{HG}. Increasing pressure will lead to an increase in lipid length and a decreases in A_{HG}. Increasing temperature will lead to a decrease in lipid length and an increase in A_{HG}.

4.4.2 Effects of temperature and pressure on the properties of the pivotal surface

3-D surface plots of $\frac{V_n}{V}$ and A_n as a function of pressure and temperature are shown in Figure 4.25 and summarised below in Figure 4.25.

i)



ii)

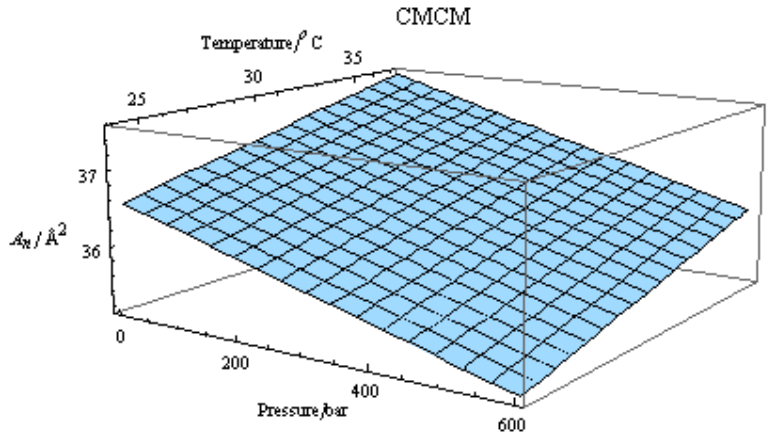


Figure 4.25 Surface plots showing the effect of pressure and temperature on i) the location of the pivotal surface, and ii) A_n.

Increasing the temperature and pressure has inverse effects on the location and cross-sectional area of the pivotal surface. The pivotal surface will move towards the head-group when temperature is increased and towards the bilayer midplane when the pressure is increased (Figure 4.25 i). It can be conjectured that the area of incompressibility will react to changes in the lipid structure where increasing the volume at the acyl chain region will have the effect of pulling the pivotal surface closer to this region.

It can be seen that the cross-sectional area of the pivotal surface increases with temperature and decreases with increasing pressure and is attributed to changes in the hydrocarbon chain area (Figure 4.25 i). Increasing temperatures leads to a larger number of trans-gauche rotamers in the hydrocarbon area and the chain occupies more space, leading to an increase in A_n. Conversely, if the chains are compressed when pressure is increased and A_n decreases. The characteristics have been summarised in a cartoon in Figure 4.26.

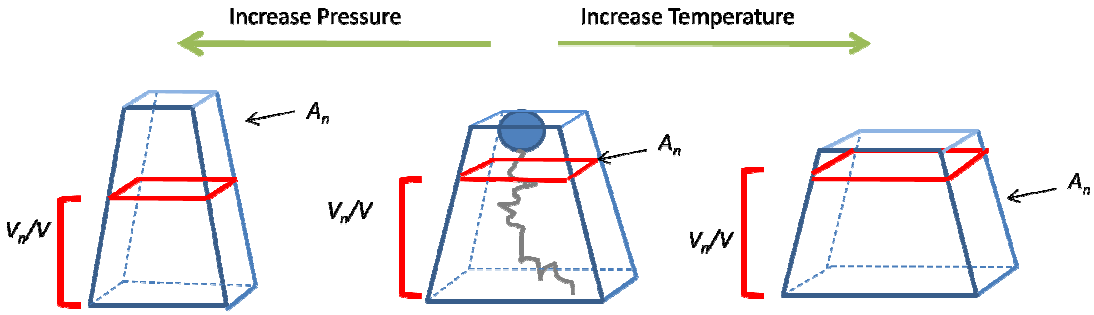


Figure 4.26 Cartoon showing the effects of increasing pressure and temperature on the pivotal surface location and $A_{HG.}$ Increasing pressure shifts the pivotal surface towards the interfacial region and reduces the area of the pivotal surface, and increasing temperature will shift the pivotal surface towards the bilayer midplane, increasing its cross sectional area.

4.5 Chapter summary

The measurement of high pressure density values for ML and measurements of the lattice parameter at varying limited hydration have unequivocally shown that the pivotal surface exists in a limited hydrated fixed hydration Q_{II}^{G} phase in ML at ambient temperatures and elevated pressures.

The Q_{II}^{G} phase is stable due to fine balances between packing frustration and curvature stress where the energetic contributions from packing frustration are less than the contributions from curvature elastic stress. It is likely that this is also the case for the other inverse bicontinuous cubic phases, Q_{II}^{D} and Q_{II}^{P} and it would be worthwhile undertaking the same analysis on a system which contains all 3 inverse bicontinuous phases, such as monoelaidin. From this it would be possible to predict the contributions of packing frustration and curvature elastic stress to the overall energy of each of the inverse bicontinuous phases.

In the future more precise measurements of density and mass as well as more refined models which account for the geometric competition between the two extremes and other local interactions within the bilayer will be required for more accurate descriptions of the pivotal surface.

Chapter 5 : Structural transformations in lamellar to cubic phase transitions.

Abstract:

Pressure-jump time resolved X-ray diffraction was used to probe the dynamics of the lamellar to Q_{II}^{G} phase transition in a limited hydrated ML sample. This chapter focuses on a discussion of the structural changes during the lamellar to Q_{II}^{G} phase transition in a 22.1 wt% water ML sample at 26 ^{o}C.

Evidence for an intermediate structure is presented, whose rate of formation and diffusion determines the rate of formation for the initial Q_{II}^{G} phase which is directly affected by the extent of change in the external thermodynamic parameter (pressure). It is seen that the Q_{II}^{G} phase will initially form with a stretched bilayer and the drive to reduce the elastic energy in the system will lead to the formation of other Q_{II}^{G} unit cells and eventually drive the phase to equilibrium.

5.1. Introduction

It has been generally accepted that the lamellar to inverse bicontinuous phase transitions proceeds via the stalk mechanism which is used to describe fundamental membrane processes such as endo and exocytosis [58, 71, 73, 74]. Increasing our understanding of lamellar to cubic phase transitions are key to understanding fundamental cellular processes. The complexity of the cell makes it difficult to decipher the role of lipids in these processes and model membranes consisting of pure water/lipid mixtures allow a finer control of sample environments. Evidence for the stalk mechanism has been seen in model membranes where experiments have shown point protrusions, stalk structures and ILAs (inter-lamellar attachements) [84, 85, 130].

The success of the pressure jump time-resolved X-ray diffraction technique to probe transformation pathways of liquid crystalline phase transitions has been well documented [48, 58, 131-135] and is the experimental tool chosen for our experiments. Increased time resolution of detectors makes it possible to detect phase transitions on the millisecond time scale.

There have been a limited number of experiments undertaken on the lamellar to inverse bicontinuous phase transition in pure lipid systems. One such study involved monoelaidin (ME) [69] in excess water for the lamellar to Q_{II}^{D} phase transition. It was shown that the lattice parameter of the lamellar phase decreases immediately after the pressure jump and coexists with a swollen intermediate Q_{II}^{D} phase, furthermore the equilibrium cubic phase forms with an initially large lattice parameter which decreases with time. Studies on limited hydrated pure lipid systems have been undertaken for the lamellar to inverse bicontinuous cubic phases [68, 100, 136] where no structural intermediates are detected. However, like the excess water experiments the cubic phase forms with an initially large lattice parameter which decreases with time.

Whilst it is most biologically relevant to undertake time-resolved studies of lyotropic phase transitions under excess water conditions there are several advantages of investigating the lamellar to inverse bicontinuous cubic phase transition under limited hydration conditions.

1. The exact water content in the sample is known and a deeper understanding of water movement in the sample can be ascertained.

2. No swollen cubic phases are observed and it can be assumed that all water and lipid is divided between the lamellar and Q_{II}^{G} phases.

3. In the monolinolein and water system the fluid lamellar to Q_{II}^{G} phase transition can be accessed at pressures and temperatures within instrumentation limits.

In this chapter pressure jumps with varying end pressures have been undertaken and analysed at 26 ^{o}C for a ML- water sample with water content of 22.1%. Analysis of pressure jump data shows that the transition goes via a nucleation-growth mechanism with evidence for a structural intermediate, not observed under diffraction conditions. Furthermore, it will be argued that the bilayer of the Q_{II}^{G} phase is compressed after its initial formation and relaxation of its elastic energy drives the Q_{II}^{G} phase to equilibrium.

5.2. Materials and Methods

Monolinolein was purchased from Larodan Fine Chemicals (Malmo, Sweden) and used without further purification. The samples were prepared in bulk, of approximately 500 mg to 22.1 wt% water. To ensure sample homogeneity the lipid water mixtures were subjected to mechanical mixing and over 20 freeze-thaw cycles before and after transport. Prior to use they were stored at -20 ^{o}C and placed into teflon based sample containers immediately before the experiment. These teflon sample containers consist of a ring of teflon, with thicknesses of 1 mm to 1.5 mm and a 3 mm diameter hole to contain the sample; mylar windows are fixed to the teflon with double sided adhesive tape to contain the sample.

Samples were loaded into a hydrostatic pressure cell, designed by R. Winter at the University of Dortmund (see Chapter 2 Materials and Methods), and subjected to 10 pressure cycles from 1 bar to 2000 bar to ensure sample homogeneity. After a change in temperature, 30 min was allowed for the sample to equilibrate. Pressure jumps were designed after consideration of the pressure –

temperature phase diagram (Chapter 3), after every pressure jump the sample pressure was reduced to 1 bar, left for 2 min and then returned to the starting pressure. The P-jump was triggered by a TTL pulse on the acquisition of the 3rd image at time t = 0 sec.

All pressure jump experiments were undertaken at the ID02 beamline, European Synchrotron Radiation Facility, Grenoble, France. 11 pressure jumps were undertaken with varying end pressures at 26 °C for a fixed hydration sample with 22.1 wt% water. A summary of the pressure jumps are given in Table 5-1.

Jump	Temp / °C	Pressure Jump / bar	P_{amp} / bar
1	25.9	1800-310	-965
2	26	1800-310	-965
3	26	1800-310	-965
4	26	1800-310	-965
5	26	1800-400	-875
6	26	1800-480	-795
7	26	1800-525	-750
8	26	1800-570	-705
9	26	1800-440	-835
10	26	1800-355	-920
11	26	1800-590	-685

Table 5-1 Summary of pressure jumps for 22.1 wt% water sample at 26 °C for lamellar to Q_{II}^{G} transition.

Previous work has shown that the transition rate is dependent on the pressure difference between the equilibrium phase boundary and end pressure of the jump rather than the total magnitude of the pressure jump. This pressure difference is designated the pressure jump amplitude (P_{amp}). A negative pressure jump amplitude indicates a change from high pressure to low pressure and conversely, a positive pressure jump amplitude describes the reverse process, a jump from low pressure to high pressure.

Analysis of the pressure jump data was undertaken using a programme written by Dr. N. Brooks, Imperial College London (see Materials and Methods chapter for further information) to extract lattice parameter and absolute intensities from each diffraction pattern. The diffracted intensity was obtained for the incoming and outgoing phases for each jump using the custom written analysis programme. The pressure cell diamond windows contribute significant background scattering to diffraction patterns and will vary depending on window orientation which may change during sample loading, hence it is not possible to account for background by simply subtracting a measured background image. To systematically account for background scattering, peaks are removed by discounting data with a gradient magnitude above a threshold value, the remaining pattern is fitted to a 4^{th} order polynomial and this fit is subtracted as a background. The peak intensity was obtained by integrating the total intensity under each peak. The intensity of the first peak was normalised to account for the sample thickness to obtain the absolute intensity in units of $rad^2\ m^{-1}$. The lattice parameter was obtained from the pixel position after calibration with silver behenate, further details can be found in Chapter 2.

The amount of intermediate phase during the lamellar to Q_{II}^{G} transition can be obtained by analysis of the total intensity at a given time. It is assumed that when every part of the sample diffracts, according to diffraction conditions, the total intensity at a given time will equal 1. If some part of the sample i.e. intermediates do not diffract then the total intensity is < 1. Therefore the volume fraction of the ILAs (interlamellar attachments), can be calculated from the total intensity at time t from Equation 5.1.

$$\phi_{intermediate} = 1 - \phi_{total} = 1 - \phi_{lam} + \phi_{QIIG} \qquad \text{Equation 5-1}$$

Where $\phi_{lam} = (\frac{I_t}{I_{t=0}})_{lam}$ and $\phi_{QIIG} = (\frac{I_t}{I_{t=\infty}})_{Q_{II}^{G}}$ for a lamellar to Q_{II}^{G} phase transition.

The water volume fraction of the Q_{II}^{G} phase can be calculated using Equation 5.2, from the parallel interface model, and the measured lattice parameters, a.

$$a = \frac{V_n}{A_n \times (1-\phi_w)} \left(-2\sigma + \frac{2^{\frac{5}{3}}\sigma^2}{\left(4\sigma^3 + 9\pi\chi(1-\phi_w)^2\left(\frac{V_n}{V}\right)^2 + 3(1-\phi_w)\left(\frac{V_n}{V}\right)\sqrt{\pi\chi\left(8\sigma^3 + 9\pi\chi(1-\phi_w)^2\left(\frac{V_n}{V}\right)^2\right)}\right)^{\frac{1}{3}}} + \right.$$

$$\left. 2^{\frac{1}{3}}\left(4\sigma^3 + 9\pi\chi(1-\phi_w)^2\left(\frac{V_n}{V}\right)^2 + 3(1-\phi_w)\left(\frac{V_n}{V}\right)\sqrt{\pi\chi\left(8\sigma^3 + 9\pi\chi(1-\phi_w)^2\left(\frac{V_n}{V}\right)^2\right)}\right)^{\frac{1}{3}} \right)$$

Equation 5-2

where ϕ_w is the water volume fraction, V is the molecular volume, σ is the dimensionless surface area, A_n is the area at the pivotal surface, a is the lattice parameter and χ is the Euler characteristic , V_n is the volume between the bilayer midplane and the pivotal surface. V_n, A_n, V are assumed to be the value at the pressure and temperature of the end of the jump as the extent of their change during the phase transformation is unknown.

Having obtained ϕ_w, the change in lipid length and A_n during the phase transition can be calculated using Equations 5.3 and 5.4-5.6 respectively.

$$\emptyset_l = 2\,\sigma\left(\frac{l}{a}\right) + \frac{4}{3}\,\pi\,\chi\left(\frac{l}{a}\right)^3 \qquad \text{Equation 5-3}$$

$$A_n = \frac{v_n}{\xi}\left(\frac{1+K\,\xi^2}{1+\frac{1}{3}K\,\xi^2}\right) \qquad \text{Equation 5-4}$$

Where

$$K = \frac{2\pi\chi}{\sigma a^2} \qquad \text{Equation 5-5}$$

And

$$\frac{V_n}{V} \times \emptyset_l = 2\,\sigma\left(\frac{\xi}{a}\right) + \frac{4}{3}\,\pi\,\chi\left(\frac{\xi}{a}\right)^3 \qquad \text{Equation 5-6}$$

5.3. Overview

An example of a pressure jump is shown in Figure 5.1 which shows a stack plot (generated in Axcess) of the lattice parameter and absolute intensity data for a lamellar to Q_{II}^{G} phase transition in a limited hydrated monolinolein sample at 26 ^{o}C for P_{amp}= -835 bar is shown. Data for the other pressure jumps can be found in Appendix C.

Observed qualitative trends are consistent between all pressure jumps. It can be seen that immediately after the pressure jump is triggered, t = 0, there is an increase in the lamellar lattice parameter of approximately 0.2 Å (Figure 5.1, ii), thereafter, there is a decrease in both lamellar lattice parameter and intensity (Figure 5.1, ii, iii).

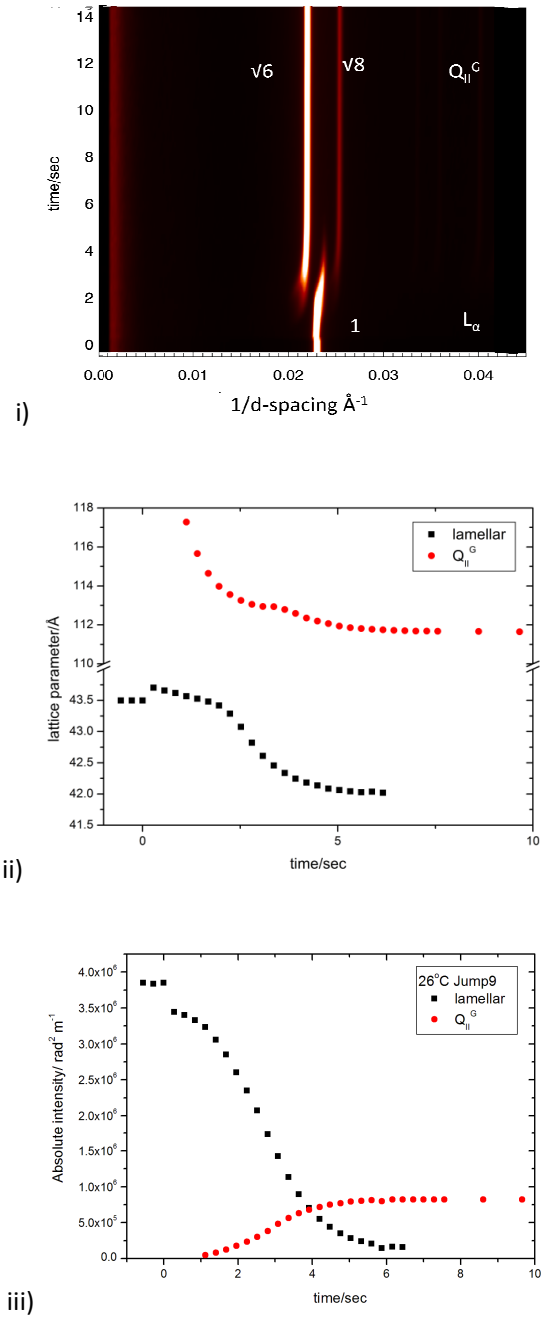


Figure 5.1. Analysis for Pressure jump 9 at 26 ^{o}C for 22.1 wt% water sample where P_{amp}=-895 bar. i) shows a stack plot of the jump with labelled reflections for the lamellar phase (1) and Q_{II}^{G}(√ 6 and √ 8). ii). Plots showing lattice parameter for lamellar (black squares) and Q_{II}^{G} (red circles). iii) Plots showing the absolute intensity change for lamellar (black squares) and Q_{II}^{G} (red circles) as a function of time.

The increase in lattice parameter of 0.2 Å can be attributed to the formation of structural intermediates such as interlamellar attachments. Whilst it may seem likely that the formation of inter lamellar attachments will pull the bilayer together thus reducing the lattice parameter, in reality formation of ILA's will cause the bilayer to swell increasing d-spacing. Lipids rearrange to fill the inter-bilayer space and water is locally displaced leading to an increase in water layer thickness and hence bilayer d-spacing [137].

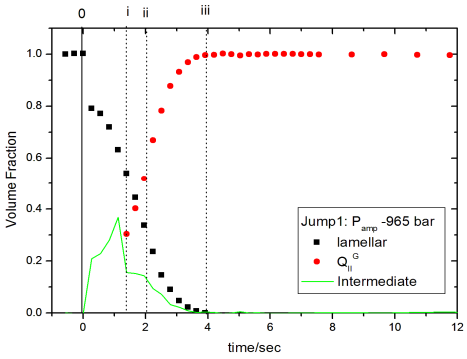
Immediately after the jump there is a decrease in the amount of substance in the lamellar phase (

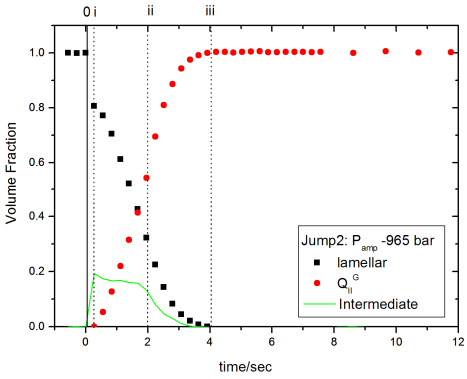
Figure *5.1* iii black squares) when ILAs form. The intensity of the lamellar phase decreases as the concentration of (ILA's) increases, whilst the sample maintains its lamellar integrity. The formation of non – correlated ILA's will cause a variation in the bilayer spacing. The reciprocal lattice points will be dispersed and there will be a poorer interception with the Ewald Sphere reducing the observed intensity. Analysis of the total intensity (Equation 5.1) during the transformation will give information about the amount of intermediate at a given time.

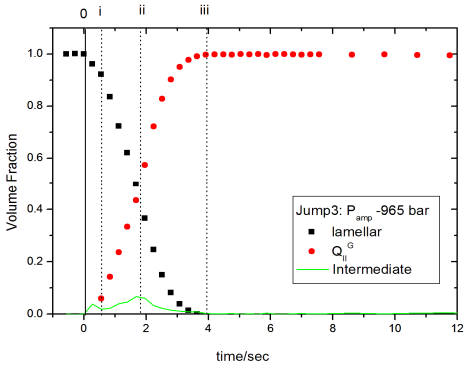
The Q_{II}^{G} phase appears approximately 1 sec after the pressure jump with a lattice parameter of 117 Å (Figure 5.1ii)**;** the relatively broad peaks (Figure 5.1 i) signify a lattice with varying water contents. Once the Q_{II}^{G} phase has formed, there is a greater decrease in the lattice parameter and decrease in intensity of the lamellar phase (Figure 5.1 ii, iii). Between 1 sec and 6 sec the lamellar phase and Q_{II}^{G} phase coexist. During this period the proportion of lamellar phase decreases and the Q_{II}^{G} phase grows; with the lattice parameter in both phases decreasing. A decrease in lattice parameter in the lamellar phase indicates dehydration in the system during Q_{II}^{G} phase formation.

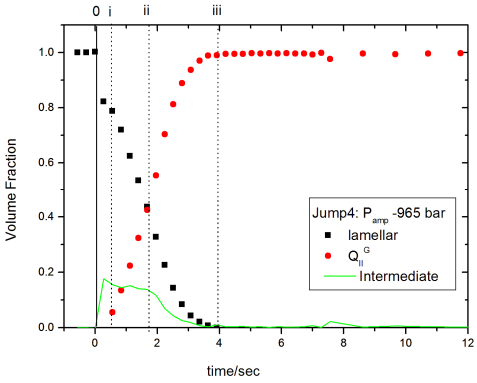
5.3.1. Discussion: Structural behaviour of the intermediate and the Q_{II}^{G} phase

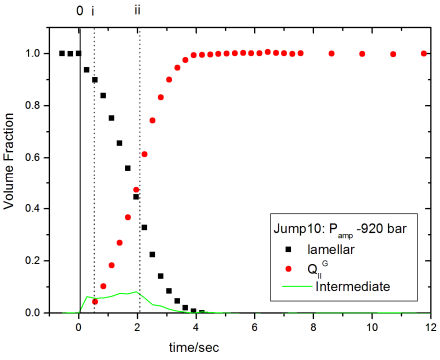
Using the absolute intensity data the volume fraction of the lamellar phase, Q_{II}^{G} phase and the intermediate were calculated using Equation 5.1 during each pressure jump. The results are shown in Figure 5.2 from the longest P_{amp} to the smallest P_{amp}.

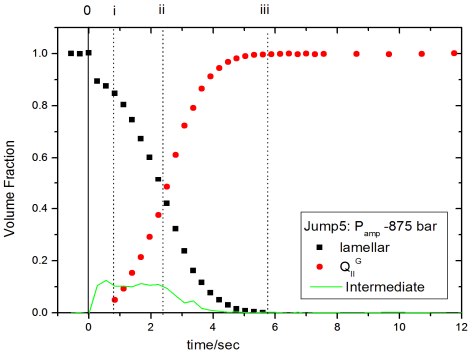

0
i
ii
iii
Volume Fraction
time/sec
Jump1: P_amp -965 bar
lamellar
Q_II^G
Intermediate

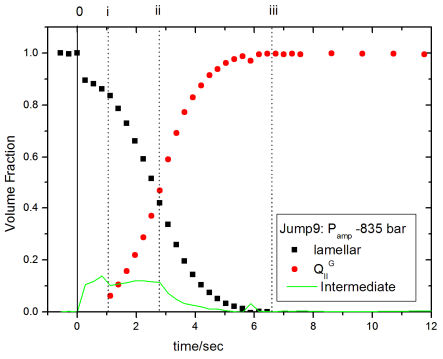

0
i
ii
iii
Volume Fraction
time/sec
Jump2: P_amp -965 bar
lamellar
Q_II^G
Intermediate

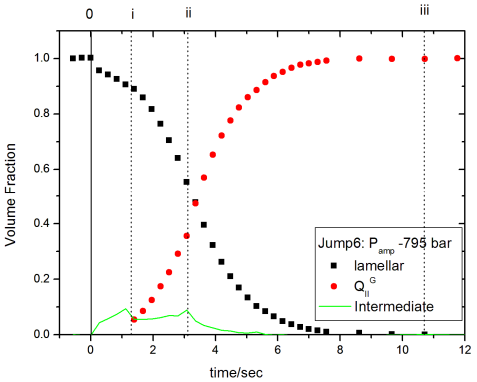

0
i
ii
iii
Volume Fraction
time/sec
Jump3: P_amp -965 bar
lamellar
Q_II^G
Intermediate


0
i
ii
iii
Volume Fraction
time/sec
Jump4: P_amp -965 bar
lamellar
Q_II^G
Intermediate


0
i
ii
Volume Fraction
time/sec
Jump10: P_amp -920 bar
lamellar
Q_II^G
Intermediate


0
i
ii
iii
Volume Fraction
time/sec
Jump5: P_amp -875 bar
lamellar
Q_II^G
Intermediate


0
i
ii
iii
Volume Fraction
time/sec
Jump9: P_amp -835 bar
lamellar
Q_II^G
Intermediate


0
i
ii
iii
Volume Fraction
time/sec
Jump6: P_amp -795 bar
lamellar
Q_II^G
Intermediate

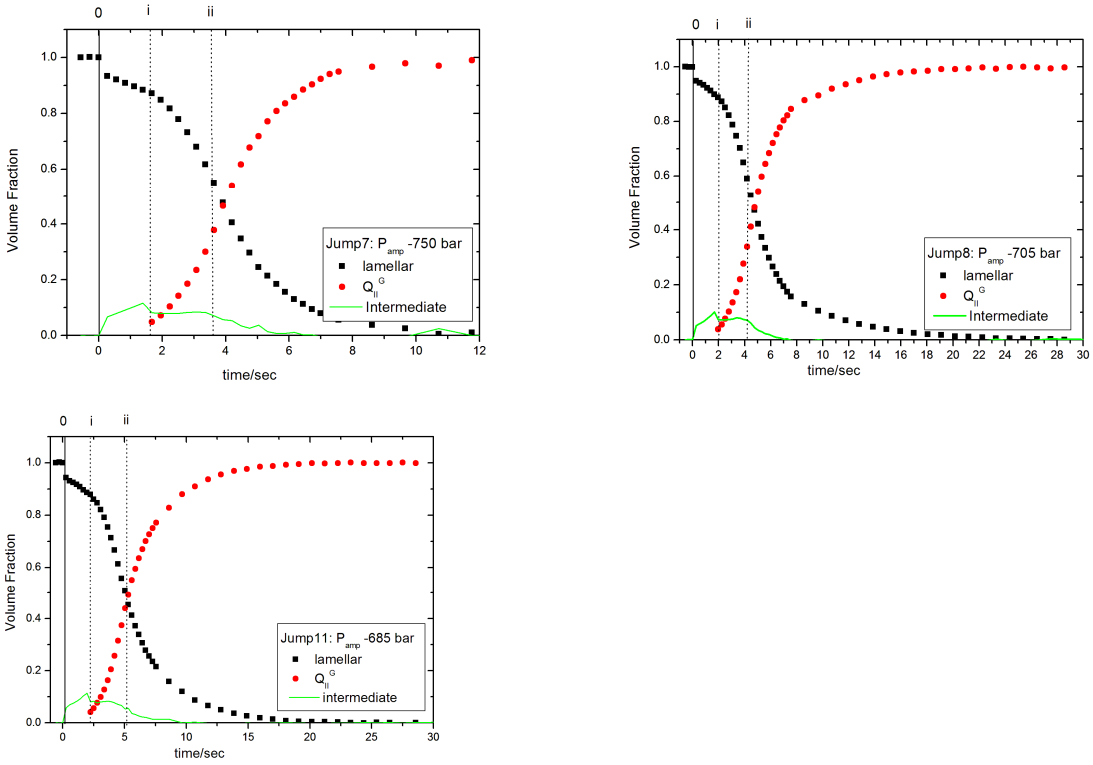


Figure 5.2 Plots showing the relative volume fraction of the lamellar phase (black squares); Q_{II}^{G} phase (red circles); $\varphi_{intermediate}$ (green line) during the lamellar to Q_{II}^{G} phase transition from analysis of absolute intensity data for lamellar to Q_{II}^{G} transition at 26 ^{o}C for 22.1 wt% water. Plots are shown in order of decreasing P_{amp} where Jumps 8 and 11, the shortest jumps have not gone to completion i.e. at the end of the jump phase coexistence between the lamellar and Q_{II}^{G} phase is seen.

Immediately after the pressure jump (at 0) the volume fraction of the intermediate is seen and the lamellar lattice parameter increases by ~ 0.2 *Å*. This indicates that ILAs form immediately after the pressure jump is triggered (Figure 5.2). Hereafter, between 0 and (i) the number of ILAs increases (Figure 5.2) until a critical amount is formed (typically between 5 and 35 % of the total volume fraction). The critical amount is dependent on the formation, diffusion and arrangement of ILAs prior to the formation of the Q_{II}^{G} phase where ILAs are required to arrange in a specific configuration. Once the ILAs are in a favourable configuration for Q_{II}^{G} formation the volume fraction of ILA decreases as they transform into water channels ubiquitous to the Q_{II}^{G} phase (Figure 5.2 ii) and diffraction from Q_{II}^{G} phase is seen. It has been shown that a hexagonal array of ILAs is

more favourable than a square lattice [65], therefore it is possible that ILAs will pack into an hexagonal array (Figure 5.3) which distort to form water channels ubiquitous to the Q_{II}^{G} phase. However, the packing of ILAs prior to Q_{II}^{G} phase formation is still unclear and further experiments are required to verify this. The results show (Figure 5.2) that as little as 0.5 % of ILAs are required for Q_{II}^{G} formation.

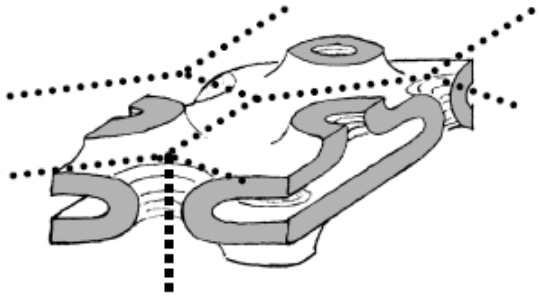


Figure 5.3 This cartoon shows a hexagonal array of ILAs which form water channels with 120^{o} angle. It is possible that ILAs will pack hexagonally and distort prior to the formation of the Q_{II}^{G} phase. However, the exact configuration of ILAs prior to Q_{II}^{G} phase formation is still unknown.

The results in Figure 5.2 show that increasing the pressure jump amplitude leads to faster formation of the Q_{II}^{G} phase, therefore random formation and diffusion of ILAs, prior to Q_{II}^{G} phase formation, is dependent on the pressure jump amplitude.

Once the Q_{II}^{G} phase has formed (Figure 5.2. i), the volume fraction of the intermediate phase remains fairly constant (Figure 5.2 ii) and the rate of ILA formation equals the rate of Q_{II}^{G} phase formation. Once the lamellar phase has decreased to approximately half its amount (ii), the ILA concentration begins to decrease and approaches zero (iii) and the rate of Q_{II}^{G} phase formation increases. Once the Q_{II}^{G} phase has formed, the rate of cubic phase growth is no longer dependent on the formation and diffusion of ILAs.

5.3.2. Structural behaviour of the Q_{II}^{G} phase

From the Q_{II}^{G} lattice parameter data structural analysis of the phase can be undertaken to deduce the driving force for Q_{II}^{G} phase formation after initial Q_{II}^{G} unit cells are formed. Using Equations 5.2-5.6 the water volume fraction, lipid length and A_n can be calculated from the lattice parameter.

Using Equation 5.2 the water volume fraction of the Q_{II}^{G} phase during the transition was calculated. The parameters, V, V_n and A_n have been calculated in Chapter 4 at P_{end} and it is assumed that they are constant throughout the transformation.

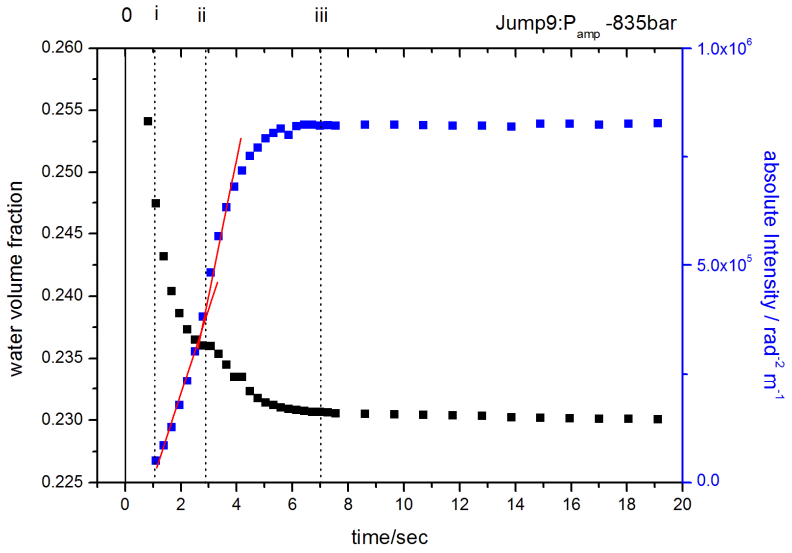


Figure 5.4 Plot showing the water content (left axis, black squares) and Intensity change (right axis-blue squares) for the Q_{II}^{G} phase during the lamellar to Q_{II}^{G} phase transition for pressure jump 9 at 26 ^{o}C with P_{amp}=-835 bar. The lines indicate different stages in the transition: 0 the start of the pressure jump; i when the Q_{II}^{G} phase is first detected; ii a change in rate of Q_{II}^{G} phase formation and the start of a plateau in the water volume fraction and iii when all the lamellar and intermediate has disappeared.

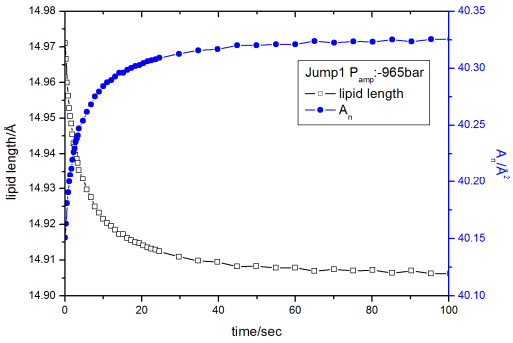
The water volume fraction and absolute intensity change of the Q_{II}^{G} phase is shown for Jump 9 (Figure 5.4), P_{amp} =-835 bar, (the other jumps are shown in the Appendix C). It can be seen that the

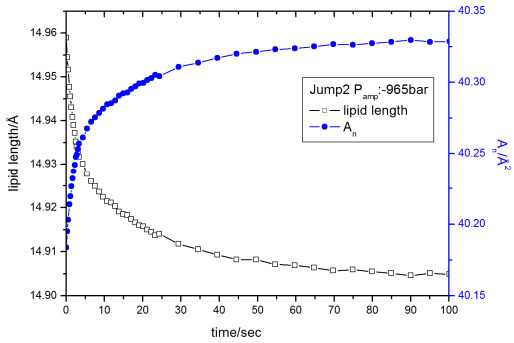
Q_{II}^{G} phase forms with a large water volume fraction. As the intensity of the Q_{II}^{G} phase increases the water volume fraction decreases until it reaches equilibrium. As it has been assumed that *V, V_n* and A_n are constant throughout the transformation the system is effectively constrained, the large water volume fraction for the Q_{II}^{G} phase during the phase transitions indicates that the bilayer is stretched and there is insufficient curvature in the system where the Q_{II}^{G} phase forms with a decreased curvature and larger pore size. This is possible due to the increased local water concentration from formation of ILAs.

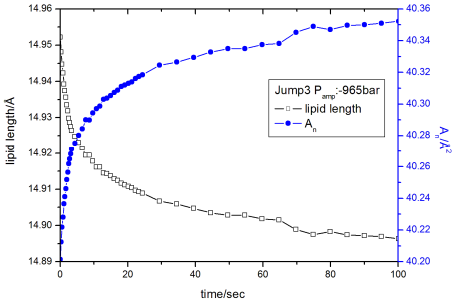
Analysis of the amount of water in the sample at a given time shows a slight plateau in the Q_{II}^{G} phase water content, indicated by region ii Figure 5.4. This plateau coincides with the plateau in intermediate volume fraction (Figure 5.2 i-ii). During this period, the rate of growth of the Q_{II}^{G} structure is at its maximum (shown as red line) and the transformation is now being driven by a necessity to increase its curvature by forming more water channels and more unit cells.

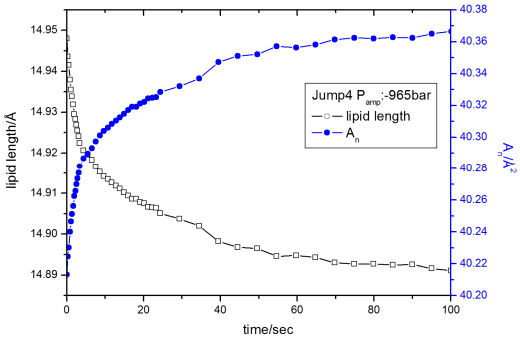
When the bilayer is stretched and the curvature is low it can be predicted that the lipids will have a long lipid length and a small cross sectional area (analogous to the structure at low temperature or high pressure see Chapter 4). The elastic energy in the system is large and the bilayer will tend to relax to alleviate this energetic cost. It does this by increasing the cross sectional area of the lipid and decreasing the lipid length, and increasing the interfacial curvature. This can be achieved by the growth of more unit cells and an increase in density of water channels with larger negative interfacial curvature.

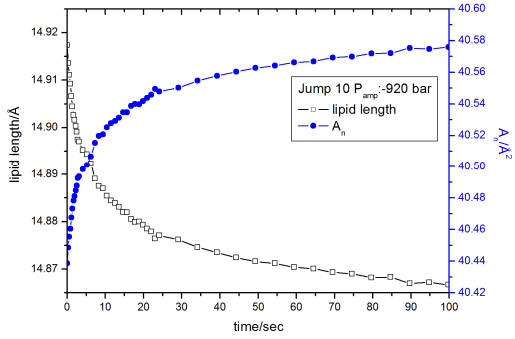
This can be confirmed by calculating the lipid length and the area at the pivotal surface (A_n) once all the lamellar phase and intermediate has disappeared (Equations 5.3-5.6). At this point it is assumed that all the water is within the Q_{II}^{G} phase which has been designated t = 0 for clarity. The results of the calculations are shown in Figure 5.5 for all pressure jumps at 26 ^{o}C with decreasing pressure jump amplitude where the change in lipid length is shown in grey and A_n is shown in blue.

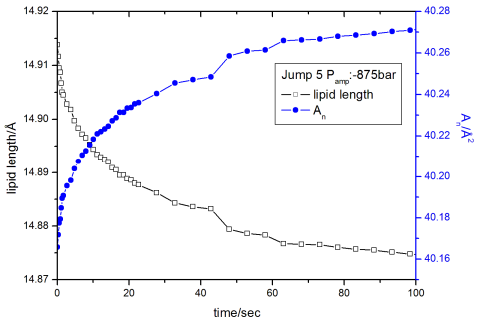

Jump1 P$_{amp}$:-965bar
lipid length
A$_n$
lipid length/Å
A$_n$/Å^2
time/sec

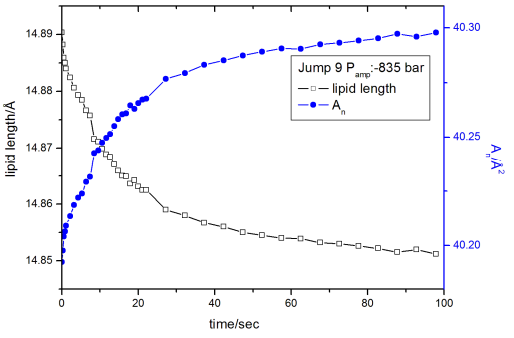

Jump2 P$_{amp}$:-965bar
lipid length
A$_n$
lipid length/Å
A$_n$/Å^2
time/sec

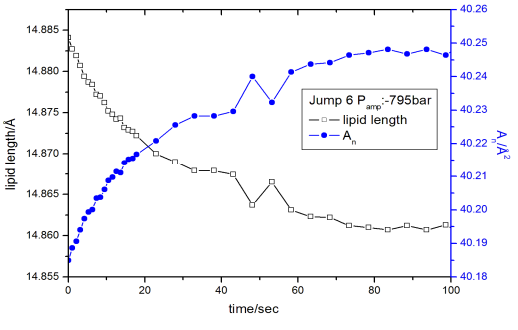

Jump3 P$_{amp}$:-965bar
lipid length
A$_n$
lipid length/Å
A$_n$/Å^2
time/sec


Jump4 P$_{amp}$:-965bar
lipid length
A$_n$
lipid length/Å
A$_n$/Å^2
time/sec


Jump 10 P$_{amp}$:-920 bar
lipid length
A$_n$
lipid length/Å
A$_n$/Å^2
time/sec


Jump 5 P$_{amp}$:-875bar
lipid length
A$_n$
lipid length/Å
A$_n$/Å^2
time/sec


Jump 9 P$_{amp}$:-835 bar
lipid length
A$_n$
lipid length/Å
A$_n$/Å^2
time/sec


Jump 6 P$_{amp}$:-795bar
lipid length
A$_n$
lipid length/Å
A$_n$/Å^2
time/sec

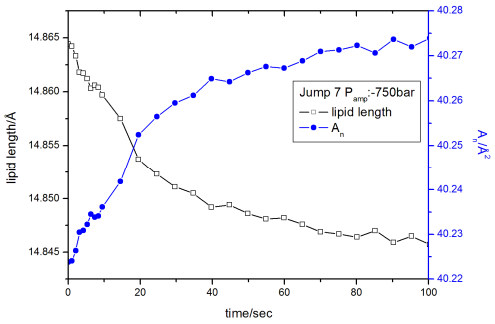


Figure 5.5 Plots showing lipid length and A_n once the lamellar phase and Q_{II}^G phase has disappeared (time = 0, corresponds to line (iii) in Fig. 5.4) for the Q_{II}^G phase. They show that the lipids will decrease in length and increase the area at the pivotal surface as the Q_{II}^G phase approaches equilibrium. The jumps are shown in decreasing pressure jump amplitude order and jumps 8 and 11 are not shown as the lamellar phase is still present at the end of the jump.

Once all the lamellar and intermediate have disappeared at time t = 0 the results in Figure 5.5 show that the lipid length decreases and the area the pivotal surface increases as the Q_{II}^G phase approaches equilibrium. This agrees with the postulate that the bilayer of the Q_{II}^G phase is initially stretched and the lipids are compressed after its initial formation. As the Q_{II}^G phase approaches equilibrium the elastic energy reduces by increasing A_n and the negative interfacial curvature of the bilayer by increasing the density of its water channels.

5.4. Chapter Summary

In this chapter the analysis of 11 pressure jumps at 26 ^oC for a limited hydrated ML water system with varying end pressures have shown that the lamellar to Q_{II}^G phase transition follows a nucleation-growth mechanism where the rate of Q_{II}^G phase formation is limited by the random nucleation and diffusion of ILAs. It has been seen that ILAs will form sporadically throughout the transition until all the lamellar phase has been consumed. ILAs are required to adopt a specific packing prior to the formation of the Q_{II}^G phase which forms with a stretched bilayer due to the increased local water concentration within the ILA. There is a large elastic energy cost associated with a stretched bilayer and the lipids will favour an increase in cross-sectional area and negative interfacial bilayer curvature to reduce the energetic cost. This is made possible by creating more water channels in the system and drives Q_{II}^G phase formation and equilibration.

Chapter 6 : Kinetics of the lamellar to Q_{II}^{G} phase transition - model fitting to experimental data

Abstract:

Pressure-jump time resolved X-ray diffraction was used to probe the lamellar to Q_{II}^{G} (forward and reverse) phase transition in ML under limited hydration conditions at various temperatures. In this chapter kinetic models are used to fit experimental data for the incoming and outgoing phases and the rate constant, *k* (s^{-1}), for the transition is obtained. The pressure jump amplitude dependence on k is plotted and discussed to rationalise the relevance of the chosen kinetic models for fitting experimental data.

6.1. Introduction

Quantification of liquid crystalline phase transitions has often been difficult to obtain due to the lack of reproducible kinetic data and the difficulty in obtaining experimental time at synchrotron X-ray beamlines. Kinetic processes in liquid crystalline phase transitions have traditionally been described using single exponential decays with little physical interpretation of the model. Often, large errors in parameters suggest that models should be more carefully considered. While previous work has formed an excellent base to this field [28, 68, 69, 138-140], it is extremely important for advancement in this area that kinetic data is fit to physically relevant and interpretable models.

It has been shown in Chapter 5 that the lamellar to Q_{II}^{G} phase transition is likely to follow a nucleation-growth mechanism, and in this chapter the Avrami model, a nucleation- growth model, will be used to fit the absolute intensity for the lamellar to Q_{II}^{G} phase transition at constant temperature. The relevance of the Avrami model to the experimental data will also be discussed.

The Avrami model was originally developed to describe solid crystallisation and later applied to polymer crystallisation. In addition, it has been used to describe lamellar–to-lamellar transitions [139, 141] and smectic-to-nematic transitions in thermotropic liquid crystals [142]. The model describes a process where nucleation sites form throughout the initial structure when an external driving force, either a change in pressure or temperature is applied to the system. For the lamellar to Q_{II}^{G} phase transition the nucleation sites will be ILAs and the number of ILAs formed are dependent on the magnitude of the driving force (Chapter 5). The nuclei will increase in size to form a grain (a specific arrangement of a number of ILAs) which will grow into a domain or a Q_{II}^{G} unit cell. The Avrami model states that work is required for the nuclei (ILA) to form a grain (cluster of ILAs), once there is sufficient energy the grain will grow without further energy input and form a domain (Q_{II}^{G} unit cells).

When most of the ILAs have been converted into the water channels there may be a deviation from the linearised Avrami equation as the driving force for the reaction changes (Chapter 5). If the Avrami model is applicable to the lamellar to Q_{II}^{G} phase transition then fitting the experimental data will give information about the formation of the nuclei i.e. spontaneous or sporadic and the dimensionality of the domain growth.

The total increase of the new phase is the product of the increase in mass of a new domain multiplied by the total number of growing domains within the phase.

$$\frac{\partial I_t}{\partial t} = N_c k_c A_c \left(\frac{I_{max} - I_t}{V_t}\right) \qquad \text{Equation 6-1}$$

where I_t is the amount of the new phase at a given time; N_c is the number of domains; k_c is the rate constant for a single domain growth (m s^{-1}) ; A_c is the area of the domain involved in growth; I_{tot} is the maximum amount of phase that can grow and V_t is the total volume (m^3).

The number of domains per unit volume is given by:

$$\rho_c = \frac{N_c}{V_T} \qquad \text{Equation 6-2}$$

Equation 6-1 can then be rearranged to:

$$\frac{\partial I_t}{I_{max} - I_t} = \rho_c k_c A_c \partial t \qquad \text{Equation 6-3}$$

If the domain growth is spherical and linear with time then

$$A_c = 4\pi (gt)^2 \qquad \text{Equation 6-4}$$

where *g* is the growth rate constant for a domain's radius, length or height (s^{-1})

Equation 6-3 becomes:

$$\frac{\partial I_t}{I_{max} - I_t} = \rho_c k_c \, 4\pi \, (gt)^2 \partial \, t \qquad \text{Equation 6-5}$$

$$\int_0^{I_t} \frac{\partial I_t}{I_{max} - I_t} = \rho_c k_c \, 4\pi \, g^2 \int_0^t t^2 \, \partial \, t \qquad \text{Equation 6-6}$$

$$ln \frac{I_{max}}{I_{max} - I_t} = \frac{4}{3} \rho_c k_c \, \pi \, g^2 \, t^3 \qquad \text{Equation 6-7}$$

$$\frac{I_t}{I_{max}} = 1 - e^{-\frac{4}{3} \rho_c k_c \, \pi \, g^2 \, t^3} \qquad \text{Equation 6-8}$$

$$\frac{I_t}{I_{max}} = 1 - e^{-k \, t^3} \qquad \text{Equation 6-9}$$

where k is the rate constant (m^{-2} s^{-3}).

Depending on the nucleation and growth of the domain A_c and ρ_c will differ. For spontaneous nucleation i.e. when most of the nucleation sites form at the beginning of the reaction

$$\rho_c = \frac{N_c}{V_T} \qquad \text{Equation 6-10}$$

For sporadic nucleation when the nucleation sites form throughout the transformation

$$\rho_c = \frac{N_c}{V_T} = jt \qquad \text{Equation 6-11}$$

Where j is the nucleation rate constant (m^{-3} s^{-1}) and t is the time.

Consequently different nucleation-growth processes will lead to different variations of the Avrami equation. The full derivations will not be shown here but a summary is given in Table 6. 1

Nucleation-growth process	A_c	Avrami equation	Rate constant, k
Spontaneous-spherical	$4\pi\,(gt)^2$	$\frac{I_t}{I_{tot}} = 1 - e^{-k\,t^3}$	$\frac{4}{3}\,\rho_c k_c\ \pi\, g^2$
Sporadic- spherical	$4\pi\,(gt)^2$	$\frac{I_t}{I_{tot}} = 1 - e^{-k\,t^4}$	$\rho_c k_c\ \pi\, j$
Spontaneous-plate like	$4hgt$	$\frac{I_t}{I_{tot}} = 1 - e^{-k\,t^2}$	$2h\rho_c k_c g$
Sporadic-plate like	$4hgt$	$\frac{I_t}{I_{tot}} = 1 - e^{-k\,t^3}$	$\frac{4}{3}\,\rho_c k_c\ \pi\, j\, g$
Spontaneous-rod like	$4\pi\, r^2$	$\frac{I_t}{I_{tot}} = 1 - e^{-k\,t}$	$-2\,\pi\, r^2 \rho_c k_c$
Sporadic-rod like	$4\pi\, r^2$	$\frac{I_t}{I_{tot}} = 1 - e^{-k\,t^2}$	$\pi\, r^2\, j k_c$

Table 6-1 Summary of the different types of nucleation-growth processes and the consequent Avrami equations.

The Avrami equation can then be written in its generalised form:

$$\frac{I_t}{I_{max}} = 1 - e^{-k\,t^n} \qquad \text{Equation 6-12}$$

Where n is the dimensionality of the domain growth and gives information about the nucleation-growth process. Therefore, from kinetic data it is possible to use the Avrami model to extract information about domain nucleation and growth.

In this chapter the validity of the Avrami model for describing lamellar to Q_{II}^{G} phase transitions is discussed after using the model to fit over 40 pressure jumps with different pressure jump amplitudes at varying temperatures for forward and reverse transitions. Reproducibility of experimental data has already been shown at 26 ^{o}C for a 22.1 wt% water ML sample in Chapter 5. The case for the Avrami model will be argued by determining trends for ln k vs P_{amp} and the chapter will finish with a discussion of the physical meaning of the fitting parameters obtained from Avrami model.

6.2. Materials and methods

Please refer to Chapter 5. 2 for the materials and methods.

Approximately 40 pressure jumps were undertaken with varying end pressures at 3 different temperatures 26 ^{o}C, 31.5 ^{o}C, and 38.5 ^{o}C in the forward direction i.e. from the lamellar to Q_{II}^{G} transition for a 22.1 wt% sample. A second sample made to 18 wt% water was subjected to jumps with varying end pressures at 18 ^{o}C (forward transition, lamellar to Q_{II}^{G}) and 11.8 ^{o}C (reverse transition, Q_{II}^{G} to lamellar). The jumps are shown in Tables 6.2-6.6 in sequential order, where the jumps summarised in Table 6.2 were described in Chapter 5 and the jumps summarised in Table 6.3-6.6 are additional jumps. P_{amp} has been previously defined and negative P_{amp} indicates a jump in the forward transition direction for the lamellar to Q_{II}^{G} transition and positive P_{amp} indicates a jump in the reverse direction for the Q_{II}^{G} to lamellar transition. Asterisked jumps indicate jumps which were unsuccessful. All pressure jump experiments were undertaken at ID02 beamline, European Synchrotron Radiation Facility, Grenoble, France.

Jump	Temp/^{o}C	P_{start}-P_{end}/ bar	P_{amp} /bar
1	25.9	1800-310	-965
2	26	1800-310	-965
3	26	1800-310	-965
4	26	1800-310	-965
5	26	1800-400	-875
6	26	1800-480	-795
7	26	1800-525	-750
8	26	1800-570	-705
9	26	1800-440	-835
10	26	1800-355	-920
11	26	1800-590	-685

Table 6-2 Summary of pressure jumps undertaken for 22.1 wt% water sample at 26 ^{o}C for the lamellar to Q_{II}^{G} transition.

Jump	Temp/^{o}C	P_{start}-P_{end}/ bar	P_{amp}/bar
1	31.5	2000-767	-908
2	31.5	2000-342	-1333
3	31.5	2000-342	-1333
4	31.5	2000-342	-1333
5	31.5	2000-513	-1162
6	31.5	2000-682	-993
7	31.5	2000-851	-824
8*	31.5	2000-935	-740
9	31.5	2000-978	-697
10	31.5	2000-895	-780
11	31.5	2000-598.2	-1076.8
12	31.5	2000-938	-737

Table 6-3 Summary of pressure jumps undertaken for the 22.1 wt% water sample at 31.5 ^{o}C for Q_{II}^{G} to lamellar phase.

Jump	Temp/^{o}C	P_{start}-P_{end}/ bar	P_{amp}/bar
1	38.4	2400-400	-1825
2	38.4	2400-400	-1825
3	38.4	2400-580	-1645
4	38.4	2400-910	-1315
5	38.4	2400-1004	-1221
6	38.4	2400-1087	-1138
7	38.5	2400-1171	-1054
8	38.5	2400-1213	-1012
9	38.5	2300-831	-1394
10	38.5	2300-1069	-1156
11	38.5	1200-1193	-1032
12	38.5	2300-556	-1669

Table 6-4 Summary of pressure jumps undertaken for a 22.1 wt% water sample at 38.5 ^{o}C for the lamellar to Q_{II}^{G} transition.

Jump	Temp/^{o}C	P_{start}-P_{end}/ bar	P_{amp} /bar
1*	18.1	2580-530	-170
2	18.1	1500-380	-320
3	18.1	800-170	-530
4*	18.1	800-460	-240
5	18.1	800-330	-370
6	18.1	800-410	-290
7	18.1	820-320	-380
8	18.1	800-210	-490

Table 6-5 Summary of pressure jumps undertaken for an 18 wt% sample at 18.1 ^{o}C for the lamellar to Q_{II}^{G} transition.

Jump	Temp/°C	P_{start}-P_{end}/ bar	P_{amp} /bar
1	11.8	20-610	60
2	11.8	40-1300	750
3	11.8	30-970	420
4	11.8	60-1110	560
5	11.8	60-1300	750
6	11.8	60-870	320

Table 6-6 Summary of pressure jumps undertaken for 18 wt% water sample at 11.8 °C for the Q_{II}^{G} to lamellar transition.

(*) denotes jumps which did not go to completion.

6.2.1 Data analysis

The kinetics of the lamellar to Q_{II}^{G} phase transitions and the Q_{II}^{G} to lamellar phase transitions are tracked by observing changes to the intensity of the incoming and outgoing phases. The absolute intensity can be used as a measure of how much material is contributing to the observed diffracted intensity at time *t*. It is assumed that the X-ray form factor will not change as a consequence of a change in water hydration in the Q_{II}^{G} phase during the transition (typically ~2 wt% water). The relative intensity was obtained from diffraction patterns using a programme written by Dr. N. Brooks, Imperial College London and the absolute intensities were obtained by dividing the relative intensities by the sample thickness (see Chapter 2 and Chapter 5 for further information).

The Avrami model was modified (Equation 6.13) for fitting the incoming and outgoing phases to obtain 3 parameters; I_{max} for the incoming phase and I_{min} for the outgoing phase; k (s^{-1}) the rate constant and n the dimensionality of domain growth. I_{max} and I_{min} were included in the fitting parameters to increase the accuracy of the fit.

$$I_t = I_{max}(1 - e^{-(kt)^n})$$ Equation 6-13

I_t is the absolute intensity at time *t*.

Typically, the shape of the Avrami curve is s-shaped where the growth of the new phase is slow at the beginning and end of the reaction and fast in the middle (Figure 6.1 left). The equation can be linearised (Equation 6.14), giving a straight line when $ln\left(-ln\left(1-\frac{I_t}{I_0}\right)\right)$ is plotted against ln t (Figure 6.1), when the experimental data fit to the Avrami model.

$$ln\left(-ln\left(1-\frac{I_t}{I_0}\right)\right) = n\,ln\,k + n\,ln\,t$$ Equation 6-14.

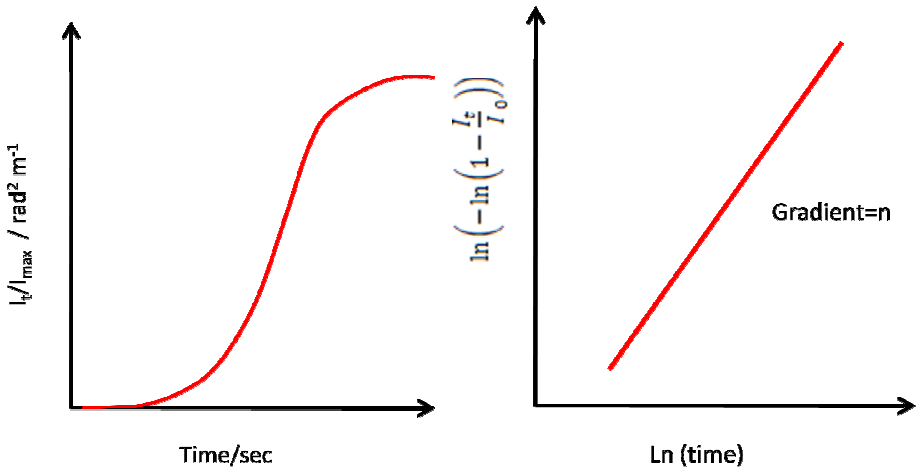


Figure 6.1. Cartoons of the Avrami model (left) showing an s-shaped curved and the linearised Avrami model (right).

In the first instance, absolute intensity data were linearised using Equation 6.2 to ascertain whether the Avrami model was a reasonable description of the experimental data. If a straight line was observed absolute intensity data were fitted to Equation 6.1. If a straight line was not seen the data were fitted to monoexponential decay (Equation 6.3):

$$I_t = I_0 + A_0\, e^{-t/k} \qquad \text{Equation 6-15.}$$

where k is the rate constant with units s^{-1}, A_0 is the pre-exponential factor, and I_0 is the intensity at time 0.

To test the model correlation to the data, absolute intensities were linearised and plotted against time (Equation 6.4).

$$ln\ (I_t - I_0) = ln\, A_0 - \frac{t}{k} \qquad \text{Equation 6-16}$$

The parameter, k, in both the Avrami and exponential decay model is the rate constant (s^{-1}) and can be directly compared. Due to the number of jumps, a few examples of the fitting have been included as part of the discussion and the remaining fits can be found in the Appendix D. Mathematica 7.0 was used for all model fitting.

6.2.2. Lamellar to Q_{II}^G phase transition - Avrami model

The relative intensities for the incoming (Q_{II}^G) and outgoing phases (lamellar) phases for 22.1 wt% water at 26 °C, 31.5 °C and 38.5 °C were linearised for the Avami model (Equation 6.1) and are shown in Figure 6.2 with the jumps shown in order of decreasing P_{amp}. A straight line for the majority of Q_{II}^G growth (left) is seen indicating that it is reasonable to fit the Avrami model to absolute intensity data for Q_{II}^G phase growth. When the gradient = 0 the amount of Q_{II}^G phase has reached a maximum. For lamellar phase decay (right) it can clearly be seen that the initial part of

the reaction does not follow Avrami kinetics and an alternative model is required to fit the lamellar phase which will be discussed in detail in Section 6.2.3.

During Q_{II}^{G} phase growth there is a clear positive linear trend for the Avrami model; however for jumps with smaller pressure jump amplitude there is a change in the gradient where the gradient decreases part way through the transformation. This is apparent for pressure jumps P_{amp} =-795 bar to – 685 bar at 26 ^{o}C; P_{amp} =-908 bar to -697 bar at 31.5 ^{o}C and P_{amp} =-1032 bar to -1012 bar at 38.5 ^{o}C. This indicates that the Q_{II}^{G} phase growth follows a two step process which each independently follow the Avrami model. The second part of the reaction has a smaller gradient and a smaller dimensionality, *n*, (the significance of dimensionality is discussed later). To maintain consistency for jumps which show a two step process the model was fit to the whole data set, effectively taking an average of the two steps.

Absolute intensity data for Q_{II}^{G} phase growth at 18 ^{o}C, 26 ^{o}C, 31.5 ^{o}C and 38.5 ^{o}C for each of the jumps was fit to the modified Avrami equation (Equation 6.1) using Mathematica 7. Residuals for each fit were obtained and plotted. Examples of the kinetic fitting at 26 ^{o}C, 31.5 ^{o}C and 38.5 ^{o}C are shown in Figure 6.3 – Figure 6.4 and the remaining kinetic fits are shown in the Appendix D. A summary of the fitting parameters is given in Section 6.3.1.

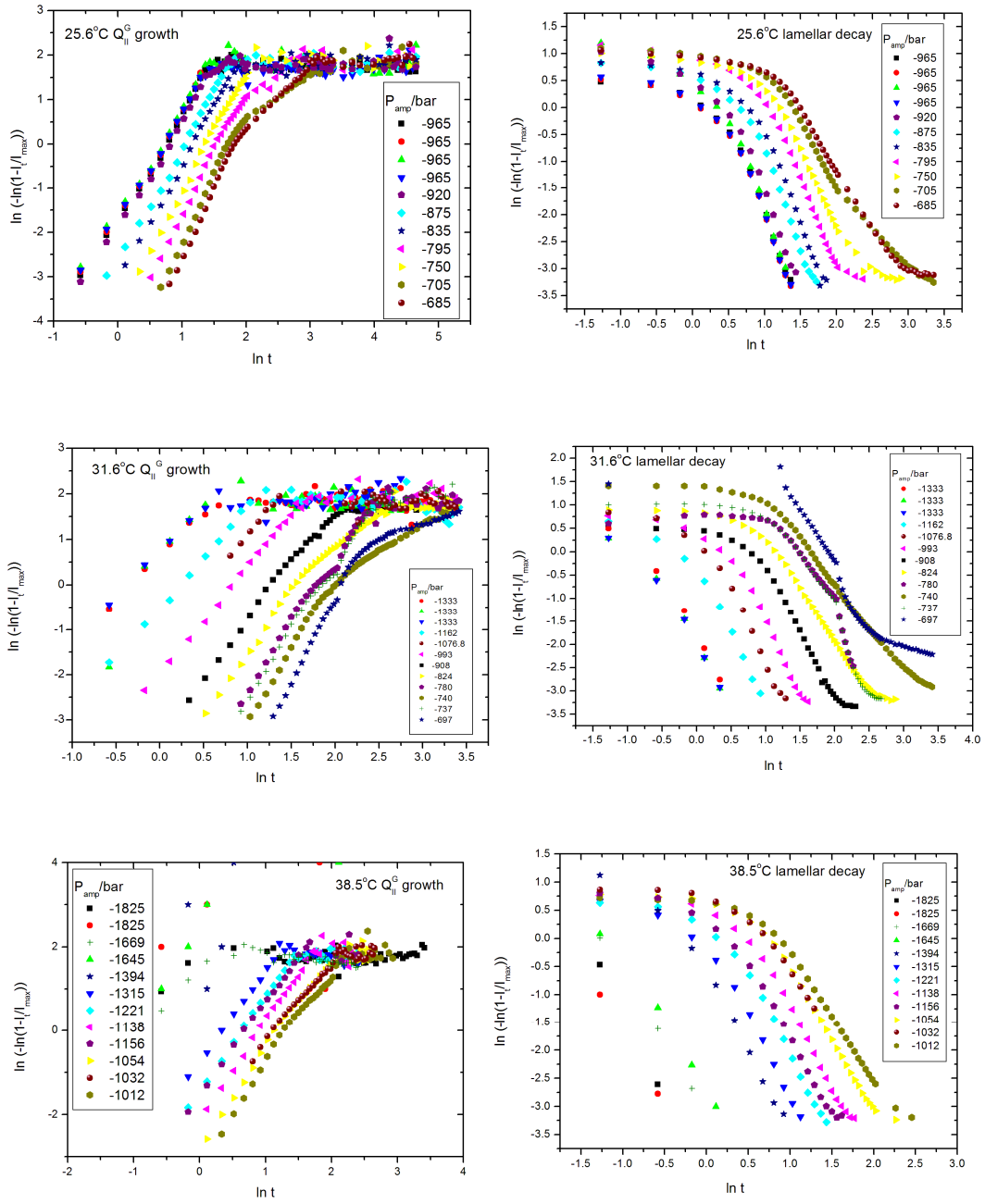


Figure 6.2. The Q_{II}^{G} growth data (left) and lamellar decay data (right) at 26°C were linearised according to the Avrami model and plotted against ln (time). It shows that all of Q_{II}^{G} can be described by the Avrami model which is not the case for the lamellar phase decay.

Figure 6.3 shows a good correlation between the Avrami model and the experimental data, with random positive and negative residuals indicating that the Avrami model is a good description of the physical processes in the phase transition. However, residuals with systematic cyclic patterns are consistently seen for shorter pressure jumps (Figure 6.4) which indicates that the Avrami model may not be a good fit to all pressure jumps. After linearization of the Avrami model it is apparent that shorter pressure jumps at all temperatures show a two step process. Whilst the underlying mechanism for phase transitions remains unchanged, and are based on the a nucleation-growth mechanism , it is clear that the model may need to include a modification to account for deviations seen for shorter pressure jump amplitudes where the kinetics are slower. Despite this it can be concluded that the Avrami model is a reasonable description of Q_{II}^{G} phase growth as differences between the experimental data and model are less than 2.5 % and R^2 values from fitting are consistently greater than 0.998.

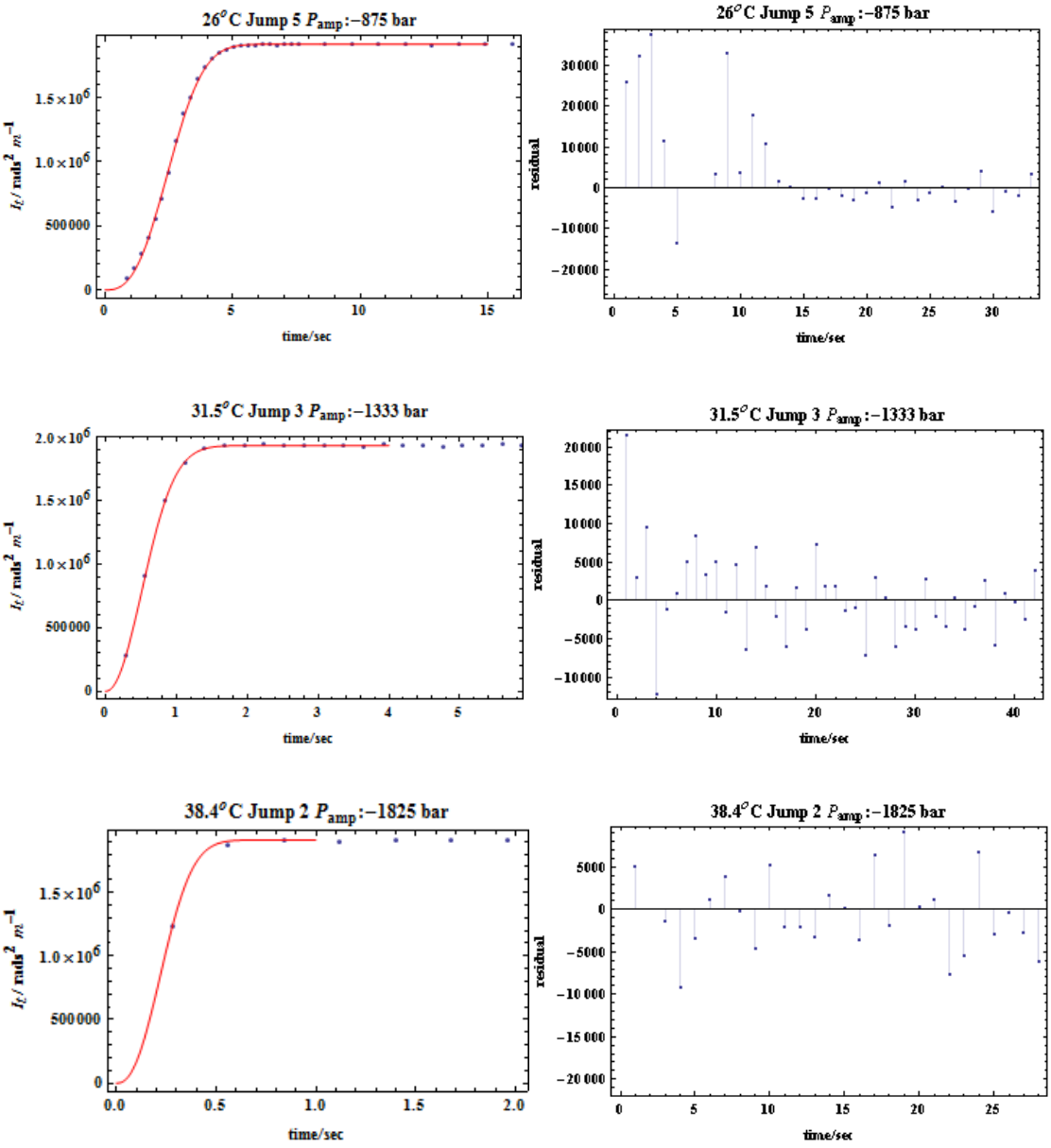


Figure 6.3 Examples of Avrami model fitting to Q_{II}^{G} phase growth for various pressure jumps at 31.5°C and 38.5°C. The residuals obtained from these fits show a positive and negative values with no systematic pattern and errors less than 1% indicating that the Avrami model is a good description of the Q_{II}^{G} phase growth in the lamellar to Q_{II}^{G} phase transition.

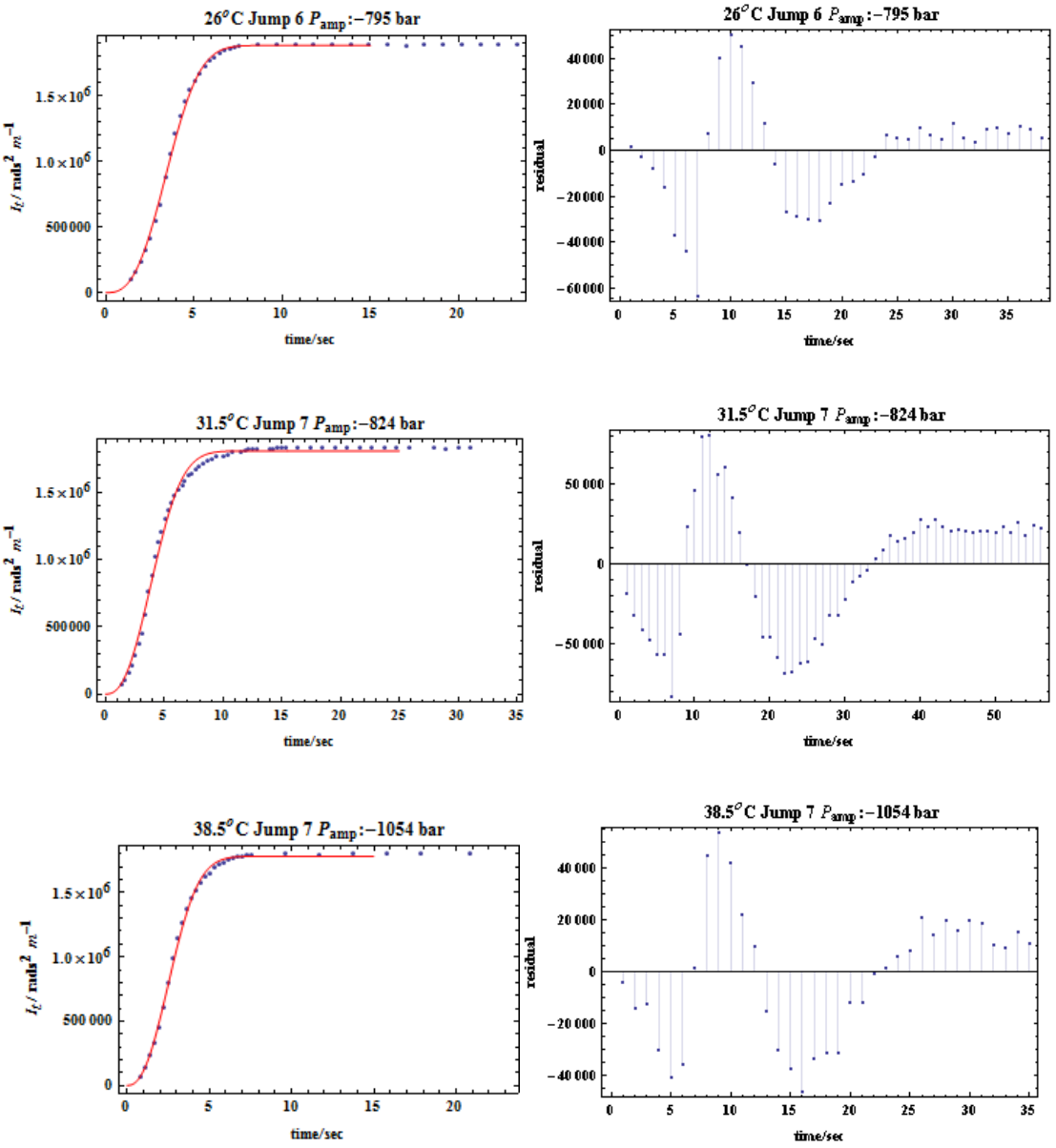


Figure 6.4 Examples of Avrami model fitting to Q_{II}^{G} phase growth for various pressure jumps at 26 °C, 31.6 °C and 38.4 °C. The residuals obtained from these fits show a positive and negative residuals values with a slight cyclic pattern. However errors from the fitting are less than 2.5% and indicating that the Avrami model is a reasonable description of the Q_{II}^{G} phase growth in the lamellar to Q_{II}^{G} phase transition for smaller pressure jumps.

6.2.3 Exponential decay for lamellar phase decay:

It has been shown in the previous section that lamellar phase decay does not linearize to the Avrami model and therefore this model would be unsuitable to describe the kinetic process. For example, the initial part of lamellar decay does not show a straight line (Figure 6.2 right). It should be noted here, that even though the Avrami model describes a growth process, the model can be extended to describe a decay process where the dimensionality, n, is negative and relates to a decrease in surface area of the domain as the phase disappears.

To obtain rate constant values for the lamellar decay process the data was fit to the exponential decay model (Equation 6.3) to quantify the change in the lamellar phase as a function of time after inital nucleation of the new phase had taken place. The region of fitting was determined from linearization of the Avrami model where the region showing a straight line was fit to the exponential decay model. Examples of the fits at 26 ^{o}C, 31.5 ^{o}C and 38.5 ^{o}C are shown in Figure 6.5, where exponential decay fitting gives a good fit to the data. Residual data show that there is less than 4 % difference between the model and the experimental data.

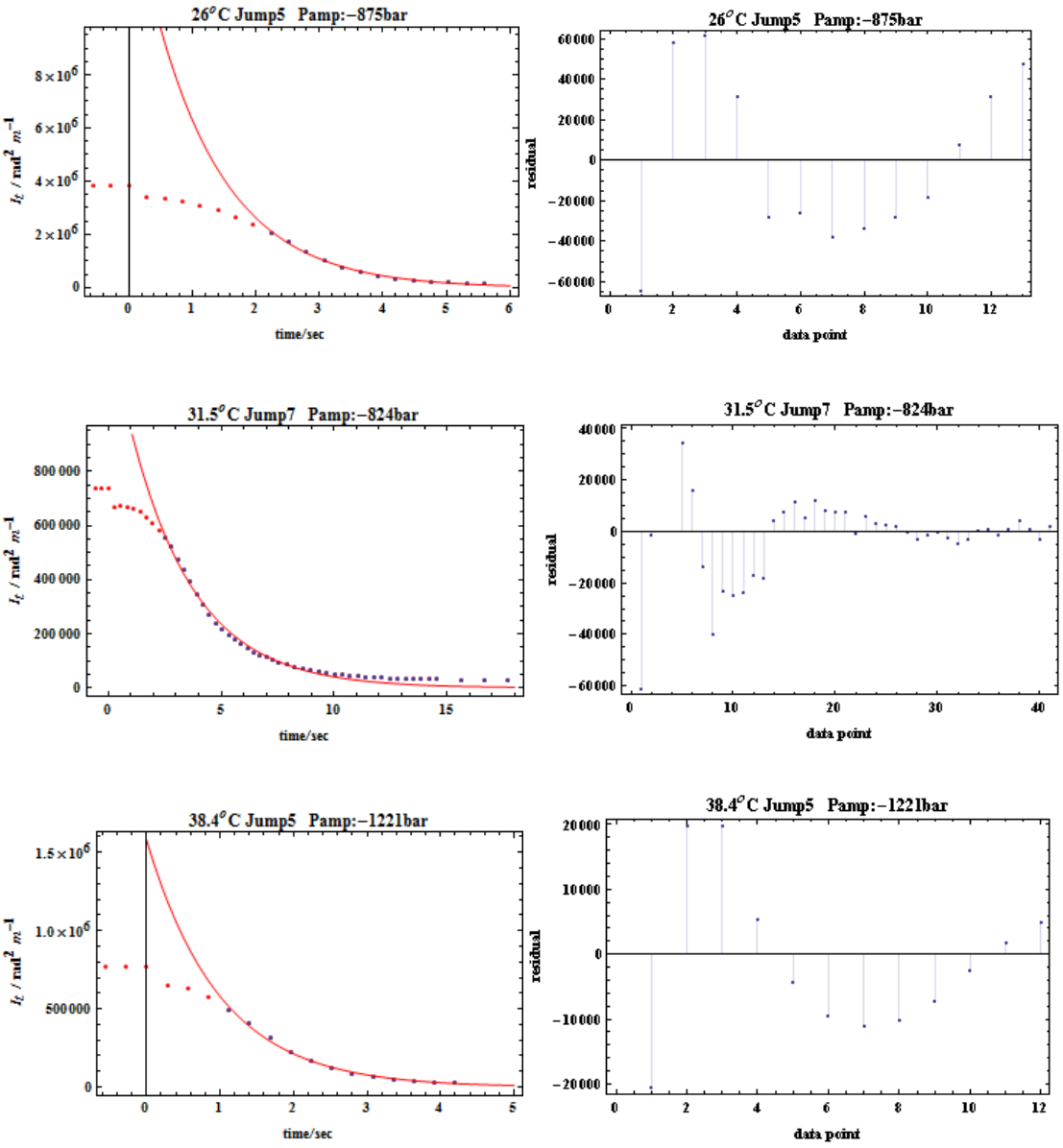


Figure 6.5 Exponential decay fits to the latter part of lamellar phase decay. Examples of the fit are shown at 26 °C, 31.5 °C and 38.5 °C for 25 wt% water with the residuals from the model fitting. The fits indicate a good correlation between the model and the experimental data with residuals less than 4% of the experimental data.

The exponential decay model was used for analysis of the latter part of lamellar phase decay for lamellar to Q_{II}^{G} phase transition at all temperatures. Deviations from the Avrami model

immediately after the pressure jump suggest that the nucleation process is too complex to be described by this model and more sophisticated models may need to be developed to account for the nucleation processes. All the fitting data has been shown in the Appendix D and a summary of the rate constant k, obtained from the fitting is given in Section 6.3.1.

6.2.4. Avrami fitting for the Q_{II}^{G} to lamellar phase transition:

Unlike the forward process (lamellar to Q_{II}^{G}) the Avrami model was used to fit the incoming and outgoing phases for Q_{II}^{G} to lamellar transitions. Figure 6.6 and Figure 6.7 shows examples of Avrami fit at 11.8 ^{o}C for 18 wt% water sample for the lamellar phase growth and Q_{II}^{G} phase decay respectively.

Systematic cyclic patterns are seen consistently for the residuals obtained from Avrami fitting to the lamellar and Q_{II}^{G} phase absolute intensities indicating that experimental data does not fit well to this model. Despite this, R^2 from the fits are consistently greater than 0.998 and residuals are less than 2 % throughout the course of the transition for the outgoing phase Q_{II}^{G}. Even though the residuals obtained from the experimental fit show systematic cyclic patterns the small errors in the parameters and excellent values for R^2 suggest that the Avrami model may be suitable for fitting absolute intensities for the Q_{II}^{G} to lamellar phase transition.

This analysis has shown that the reverse transition is less complex than forward transitions where it has not been possible to fit the Avrami model to the decay of the lamellar phase immediately after the jump.

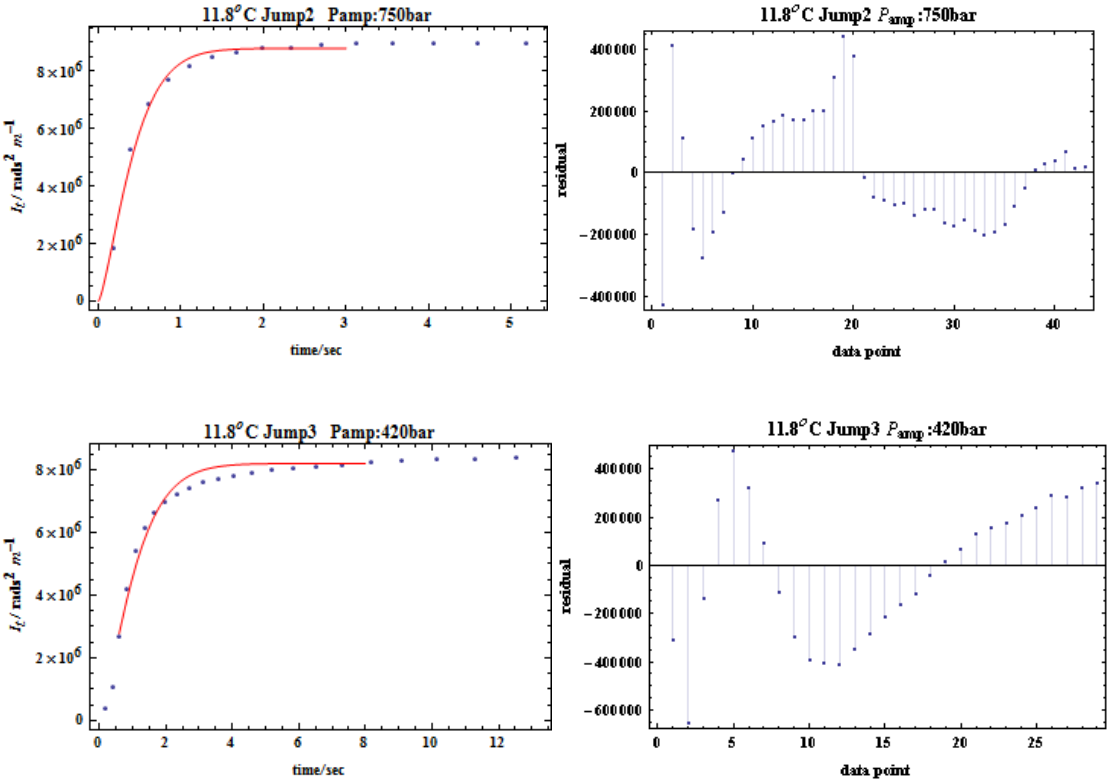


Figure 6.6. The Avrami model was fitted to the lamellar phase growth for the reverse transition. It shows that there is a reasonable fit to the data where the residuals indicate an approximate error of 5 % between the model and the data. Examples are shown at 11.8 °C for Jump1 (top) and Jump2 (bottom) where P_{amp} = -1825 bar and -750 bar respectively for a 18 wt% water sample.

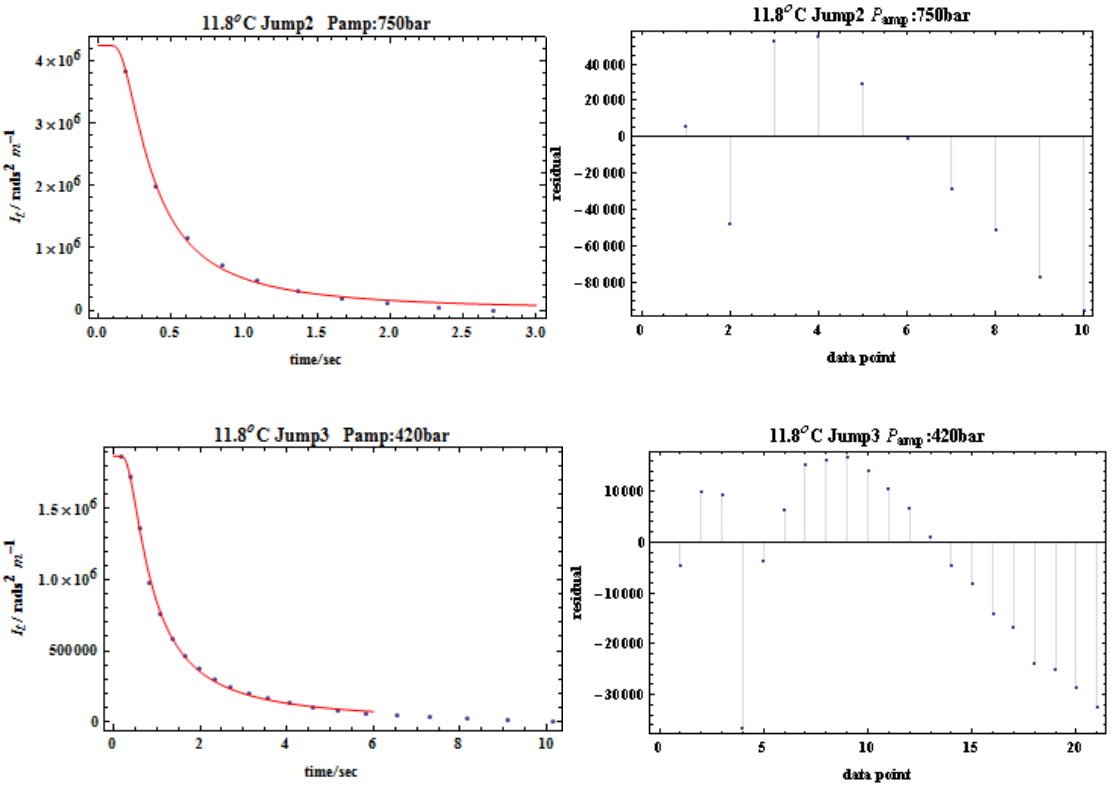


Figure 6.7. The Avrami model was fit to the Q_{II}^{G} phase decay for reverse transitions at 11.8 °C and 18 wt% water sample. Examples of Avrami fitting are shown for Jump1 (top) and Jump2 (bottom) where P_{amp} = -1825 bar and -750 bar respectively. Analysis of the residual fit indicate that there is appriximately 2% error between the Avrami model and the experimental data.

6.3. Effect of Pressure Jump amplitude on the rate constant

Previous studies have shown that an increase in pressure jump amplitude leads to an increase in the rate of the phase transition [28, 135]. Furthermore it has been shown that the pressure jump amplitude (P_{amp}) has a linear dependence on ln k [69]. This section will show that a similar trend is seen for the monolinolein system and reflects the reliability of the data and kinetic models chosen for fitting.

6.3.1. Results: Summary of fitting parameters

k (s^{-1}), the rate constant, quantifies the rate of the phase transition and can be obtained from the Avrami and exponential decay models where in each model k has the same physical meaning. Analysis undertaken with the Avrami model will give an additional parameter, n, which describes the dimensionality of the domain growth (positive) or decay (negative). Fitting parameters k and n are summarised in Table 6.6 with R^2 from the data fitting. The results are shown from the largest P_{amp} to the smallest P_{amp} at each temperature.

P_{amp}/bar	jump	(Q_{II}^G) k / s^{-1}	n	R^2	(lam) k / s^{-1}	R^2
-965	1	0.463±0.002	2.491±0.041	0.99989	1.010± 0.056	0.994698
-965	2	0.474±0.003	2.464±0.049	0.999843	1.029± 0.059	0.994911
-965	3	0.487±0.003	2.419±0.051	0.999826	1.067± 0.060	0.995385
-965	4	0.480±0.003	2.436±0.049	0.99984	1.036± 0.056	0.994958
-920	10	0.440±0.002	2.516±0.041	0.999885	0.915± 0.054	0.993261
-875	5	0.347±0.001	2.741±0.038	0.999901	0.813± 0.0312	0.995975
-835	9	0.309±0.001	2.805±0.042	0.999869	0.619± 0.029	0.992214
-795	6	0.252±0.001	2.836±0.055	0.999722	0.553± 0.015	0.996536
-750	7	0.214±0.002	2.904±0.069	0.999481	0.429±0.014	0.994226
-705	8	0.178±0.002	2.850±0.102	0.998646	0.273± 0.011	0.990466
-685	11	0.160 ±0.002	2.814±0.109	0.998345	0.259±0.009	0.994626

Table 6-7 Results from Avrami fitting (Q_{II}^G phase growth) and exponential decay (lamellar phase decay) at 26 ^oC for a 22.1 wt% water sample. k, the rate constant and n, the dimensionality, are obtained from Avrami fitting and k, the rate constant is obtained from exponential decay fitting. R^2 values from the fitting are shown.

P_{amp}/bar	Jump	(Q_{II}^{G}) k/ s^{-1}	n	R^2	(lam) k/ s^{-1}	R^2
-1333	2	1.390±0.004	2.071±0.023	0.999991	2.100±0.131	0.997669
-1333	3	1.435±0.006	2.031±0.017	0.999991	NA	
-1333	4	1.455±0.005	2.090±0.023	0.999984	2.227±0.107	0.999697
-1162	5	0.788±0.003	2.179±0.023	0.999973	1.666±0.032	0.998039
-1076.8	11	0.583 ±0.002	2.352±0.024	0.999966	1.179±0.050	0.996021
-993	6	0.435±0.001	2.423±0.022	0.999963	0.988±0.023	0.998715
-908	1	0.305±0.002	2.415±0.040	0.999817	0.567±0.015	0.996021
-824	7	0.211±0.002	2.454±0.064	0.999361	0.349±0.010	0.993161
-780	10	0.164±0.002	2.479±0.084	0.999098	0.186±0.012	0.992704
-740	8*	0.131±0.003	2.134±0.106	0.996707	0.160±0.007	0.984982
-737	12	NA	NA		0.208±0.009	0.997669
-697	9	NA	NA		NA	NA

Table 6-8 Results from Avrami fitting (Q_{II}^{G} phase growth) and exponential decay (lamellar phase decay) at 31.5 ^{o}C for a 22.1 wt% water sample. k, the rate constant and n, the dimensionality, are obtained from Avrami fitting and k, the rate constant, is obtained from exponential decay fitting. R^2 values from the fitting are shown.

P_{amp}/bar	jump	(Q_{II}^{G}) k/ s^{-1}	n	R^2	(lam) k/ s^{-1}	R^2
-1825	1	2.954±0.020	2.140±0.053	0.99997	3.317±0.835	0.99001
-1825	2	3.615±0.018	2.355±0.228	0.99999	4.350±0.334	0.99914
-1825	3	1.969±0.013	2.166±0.040	0.99996	3.342±0.072	0.99983
-1669	12	2.254±0.011	2.490±0.034	0.99994	4.323±0.199	0.99969
-1394	9	0.880±0.002	2.215±0.019	0.99993	1.572±0.068	0.99747
-1315	4	0.714±0.002	2.202±0.018	0.99998	1.259±0.049	0.99762
-1221	5	0.533±0.001	2.324±0.019	0.99997	1.000±0.0343	0.99731
-1156	10	0.507±0.002	2.231±0.024	0.99984	NA	NA
-1138	6	0.409±0.002	2.421±0.034	0.9999	0.804±0.016	0.99866
-1054	7	0.318±0.002	2.370±0.049	0.99973	0.566±0.012	0.99795
-1032	11	0.327±0.003	2.247±0.051	0.99958	NA	NA
-1012	8	0.272±0.002	2.276±0.053	0.99944	-0.355±0.205	0.20534

Table 6-9 Results from Avrami fitting (Q_{II}^{G} phase growth) and exponential decay (lamellar phase decay) at 38.5 ^{o}C for a 22.1 wt% water sample. k, the rate constant and n, the dimensionality, are obtained from Avrami fitting and k, the rate constant, is obtained from exponential decay fitting. R^2 values from the fitting are shown.

P_{amp}/bar	jump	(Q_{II}^{G}) k/ s^{-1}	n	R^2	(lam) k/ s^{-1}	R^2
-530	3	0.503±0.004	2.176±0.051	0.999798	1.177±0.052	0.996505
-490	8	0.382±0.004	2.110±0.052	0.999717	0.876±0.022	0.998819
-380	7	0.145±0.004	1.571±0.070	0.998209	0.235±0.003	0.999163
-370	5	0.154±0.004	1.551±0.072	0.99797	0.211±0.004	0.998274
-320	2	0.054±0.001	1.264±0.045	0.998187	0.063±-0.001	0.998491
-290	6	0.105±0.004	1.495±0.094	0.996029	0.128±0.006	0.991393
-240	4	0.203±0.002	2.409±0.103	0.998565	0.172±0.032	0.970475
-170	1	0.014±0.001	0.836±0.039	0.995919	0.070±0.037	0.994544

Table 6-10 Results from Avrami fitting (Q_{II}^{G} phase growth) and exponential decay (lamellar phase decay) at 18.1 ^{o}C for a 18 wt% water sample. k, the rate constant and n, the dimensionality, are obtained from Avrami fitting and k, the rate constant is obtained from exponential decay fitting. R^2 values from the fitting are shown.

P_{amp}/bar	jump	Q_{II}^{G} k/s^{-1}	n	R^2	(lam) k/ s^{-1}	n	R^2
750	2	3.262±0.222	-1.738±0.093	0.998676	2.166±0.060	1.356±0.076	0.999515
750	5	3.273±0.244	-1.723±0.099	0.998477	2.244±0.071	1.241±0.073	0.99948
650	7	2.923±0.157	-1.576±0.063	0.998586	1.721±0.063	1.056±0.062	0.999277
560	4	2.275±0.076	-1.537±0.047	0.998698	1.489±0.048	1.411±0.089	0.999177
420	3	1.393±0.023	-1.528±0.025	0.99941	0.854±0.031	1.325±0.087	0.998472
320	6	1.712±0.267	-1.061±0.087	0.977824	0.541±0.017	1.056±0.056	0.998689
220	8	4.8341±6.657	-0.646±0.112	0.937311	0.337±0.010	1.100±0.052	0.998424
60	1	0.435±0.005	-1.196±0.012	0.999615	0.241±0.007	1.151±0.048	0.998385

Table 6-11 Results from Avrami fitting to Q_{II}^{G} phase decay and lamellar phase growth for a series of pressure jumps undertaken at 11.8 ^{o}C for a 18 wt% water sample. k, the rate constant and n, the dimensionality, are obtained from Avrami fitting and R^2 values from the fitting are shown.

(NA denotes examples where the model was unable to fit the data)

The fitting parameters obtained from kinetic model fitting to absolute intensity data for the incoming and outgoing phases give physically reasonable values with low errors.

6.3.2. Pressure jump amplitude effect on the rate constant

The effect of P_{amp} on the rate constant is found by plotting ln *k* against P_{amp}. From linear fits to the data ln *k'* and $\frac{d\,lnk}{dp}$ can be obtained. To obtain accurate fits, residual analysis was undertaken on linear fits to the data to obtain an even distribution of positive and negative residuals with values close to zero. If this was not seen then data with large residuals were 'masked' and the data refitted.

The analysis was undertaken on the incoming (Q_{II}^{G}) and outgoing phases (lamellar) for 22.1 wt% water sample at 26 ^{o}C, 31.5 ^{o}C, and 38.5 ^{o}C.

6.3.3 Ln k vs P_{amp} dependence: 22.1 wt% Water

Ln *k* obtained from kinetic model fitting was plotted against the P_{amp}. The resulting plot for Q_{II}^{G} phase growth at 26 ^{o}C shows a linear trend (Figure 6.8), where the rate of reaction increases for a large external driving force. A linear fit to the data shows that jumps undertaken at large and small pressure jumps amplitudes have large residuals (Figure 6.8 bottom left). Therefore, data points at large and small pressure jumps were masked and the linear fit reapplied. The results give residuals close to zero with an even positive and negative distribution (Figure 6.8 bottom right).

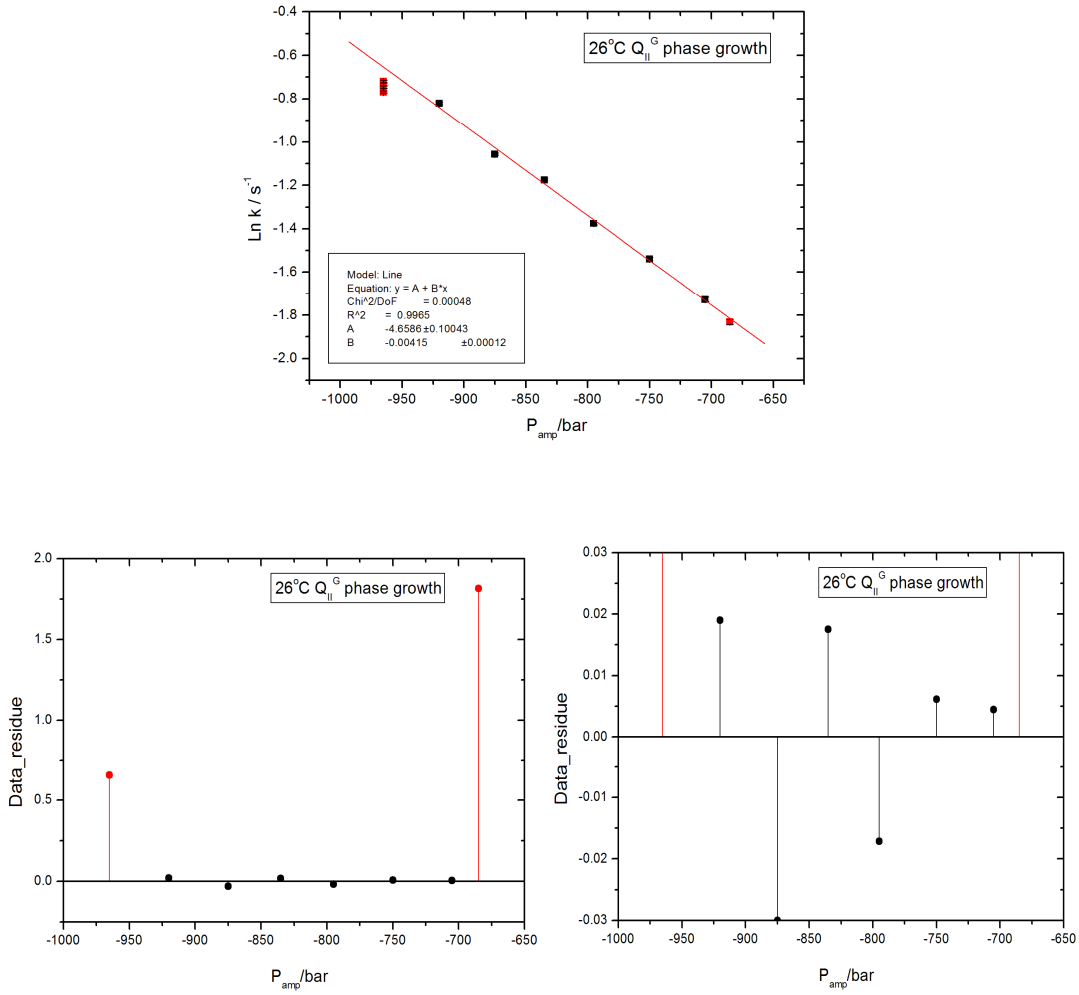


Figure 6.8 Linear fit to Ln k vs P_{amp} data obtained from experimental data to the kinetic models for Q_{II}^{G} phase growth at 26 ^{o}C. To obtain a good linear fit the residuals from the linear fit are analysed. Data points were removed to obtain an even distribution of positive and negative residuals close to zero. Bottom left shows residual data for the full data set and bottom right shows residual data after some data points have been removed.

The same procedure was undertaken for pressure jumps undertaken at 31.5 ^{o}C and 38.5 ^{o}C for Q_{II}^{G} phase growth. The results of the fit and the residuals are shown in Figure 6.9. At 31.6 ^{o}C the ln *k* at small pressure jumps were removed after analysis of the residuals and at 38.5 ^{o}C all of the data were included in the linear fit which gave an even distribution of small residuals.

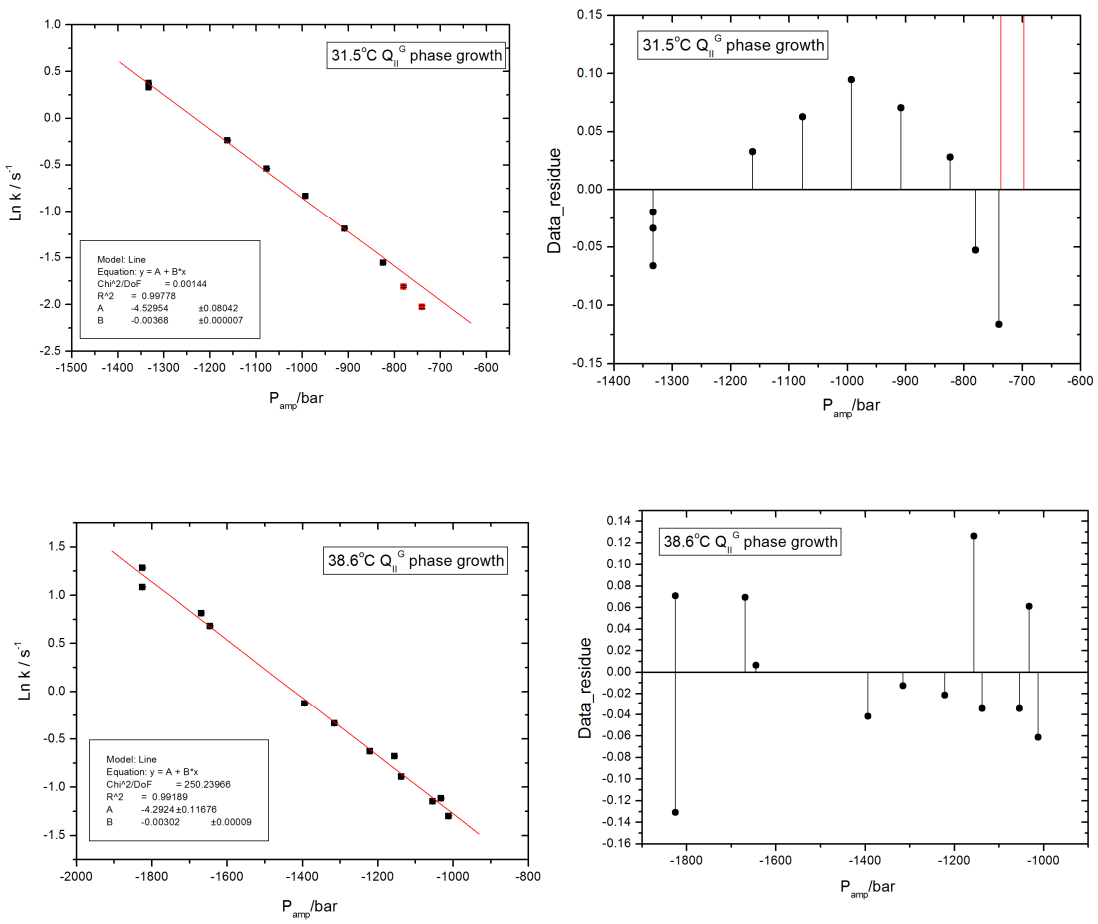


Figure 6.9 Linear fit to ln k vs P_{amp} data for Q_{II}^{G} growth at 31.5 °C (top) and 38.5 °C (bottom) The residual fits are shown on the right and indicate that removal of relevant data points increases the accuracy of the linear fit.

It was discussed previously (Section 6.2.1) that short pressure jumps exhibit a two step process with different rate constants. To keep the fitting of the data consistent, the Avrami model was fitted to the whole data set for all the jumps assuming a one step process. Averaging the two processes in slower jumps may lead to an increase or decrease in the rate constant compared to the faster jumps and account for deviations from the linear trend at low pressure jump amplitudes (31.5 °C) and at low and high pressure jump amplitudes (26 °C).

The standard deviations for k was calculated from repeat jumps at 26 °C, 31.6 °C and 38.5 °C giving errors of 0.01 s^{-1}, 0.04 s^{-1} and 0.8 s^{-1} respectively; the precision of the experiment decreases with increasing temperature.

The pressure dependence on the rate constant was also undertaken for the lamellar phase decay at 26 ^{o}C , 31.5 ^{o}C , 38.5 ^{o}C for 22.1 wt% water sample where the rate constant, *k* was obtained from fitting absolute intensities to the exponential decay model. Linear fits and the residual data from the fits are shown in Figure 6.10 for 26 ^{o}C (top), 31.5 ^{o}C (middle) and 38.5 ^{o}C (bottom).

As the pressure jump amplitude increases the rate constant for the disappearance of the lamellar phase increases. Compared to the Q_{II}^{G} phase growth the residuals from linear fit to ln *k* vs P_{amp} are larger. However, the residuals are still within experimental error and the number of jumps analysed give a statistically reliable fit.

A summary of ln *k'* and $\frac{d\,lnk}{dp}$ at each temperature for 22.1 wt% water ML sample is given in Table 6.11 where the parameters were obtained from linear fits to rate constant data. The linear dependence of ln *k* on the pressure jump amplitude correlates with trends seen in previous experiments and confirms the reliability of the experimental data and the models chosen to fit the data to obtain the rate constant.

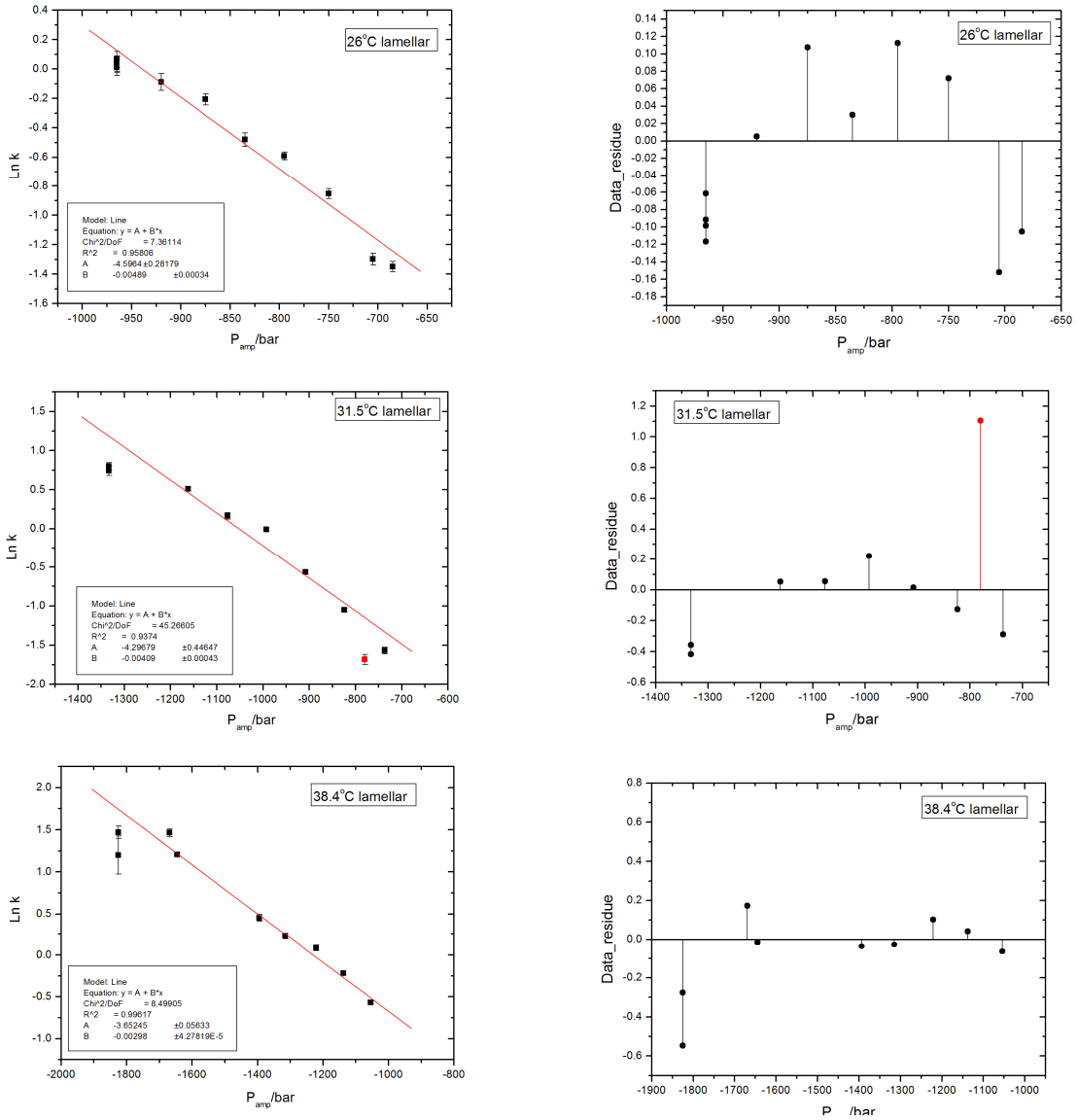


Figure 6.10 Linear fits were undertaken on ln k vs P_{amp} (left) for the lamellar phase decay at 26 °C, 31.5 °C (middle) and 38.4 °C where k was obtained from exponential decay fits to the data. Analysis of residuals allows a rational way of deciding to mask some data to obtain accurate linear fits to the data. The residuals are shown on the right.

	Q_{II}^{G} growth		Lamellar decay	
Temperature/°C	**ln *k'***	**$\frac{d\ lnk}{dp}$ bar^{-1}**	**ln *k'***	**$\frac{d\ lnk}{dp}$bar^{-1}**
26	-4.66±0.10	-0.00415±0.00001	-4.60 ± 0.28	-0.00489± 0.00034
31.5	-4.53±0.08	-0.00368±0.00007	-4.30± 0.45	-0.00409±0.00043
38.5	-4.29±0.12	-0.00302±0.00009	-3.65±0.056	-0.00295+0.00004

Table 6-12 Summary of ln k' and $\frac{d\ lnk}{dp}$ obtained from linear fit to ln k vs P_{amp} for 25.4 wt% water for a lamellar to Q_{II}^{G} phase transition at different temperatures.

6.3.4. Pressure dependence on the rate constant: 18 wt% water

Ln *k* values obtained from the kinetic model fitting were plotted as a function of P_{amp} for an 18 wt% water sample at 18.1 °C for the forward reaction and 11.8 °C for the reverse reaction. Linear fits were made to the data to obtain an even distribution of positive and negative residuals close to zero. The linear fits are shown in Figure 6.10. Summaries of ln *k'* and $\frac{d\ lnk}{dp}$ are given in Table 6.12 and Table 6.13.

6.3.4.1. Lamellar to Q_{II}^{G} transition at 18.1 °C

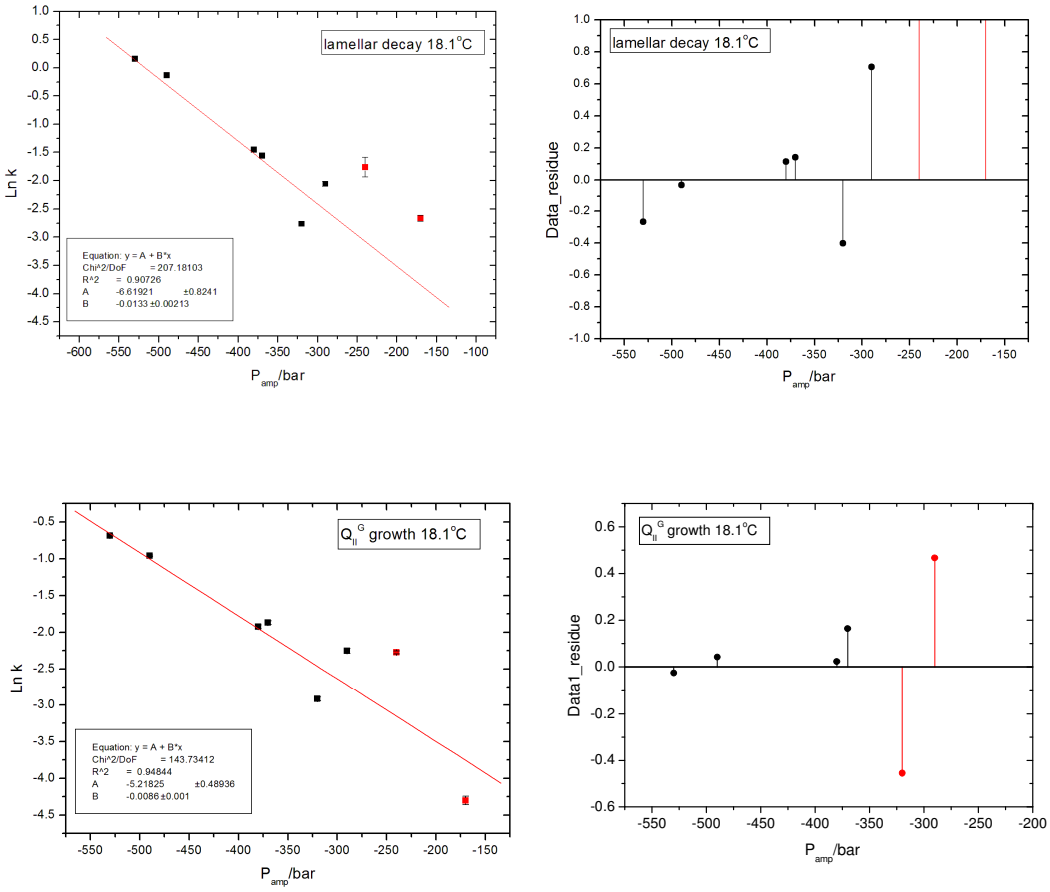


Figure 6.11 Linear fit to ln k vs P_{amp} data obtained from experimental data to the kinetic models for Q_{II}^{G} phase growth (bottom) and lamellar phase decay (top) at 18 °C for a 18 wt% water sample. To obtain a good linear fit the residuals from the linear fit are analysed. Data points were removed to obtain an even distribution of positive and negative residuals close to zero. Right shows the residuals for each data point.

Residuals obtained from the linear fit to ln *k* vs P_{amp} increase as P_{amp} decreases and can be attributed to a deviation of the experimental data from the kinetic models for slower phase transitions.

	Q_{II}^{G} growth		Lamellar decay	
Temperature/^{o}C	ln k'	$\frac{d\ lnk}{dp}$ bar^{-1}	ln k'	$\frac{d\ lnk}{dp}$ bar^{-1}
18.1	-5.22±0.49	-0.0086±0.001	-6.62 ± 0.82	-0.0133± 0.0021

Table 6-13 Parameters from linear fit of ln k vs P_{amp} for 18 wt% water sample for Q_{II}^{G} growth and lamellar decay.

6.3.4.2 Q_{II}^{G} to lamellar transition at 11.8 ^{o}C

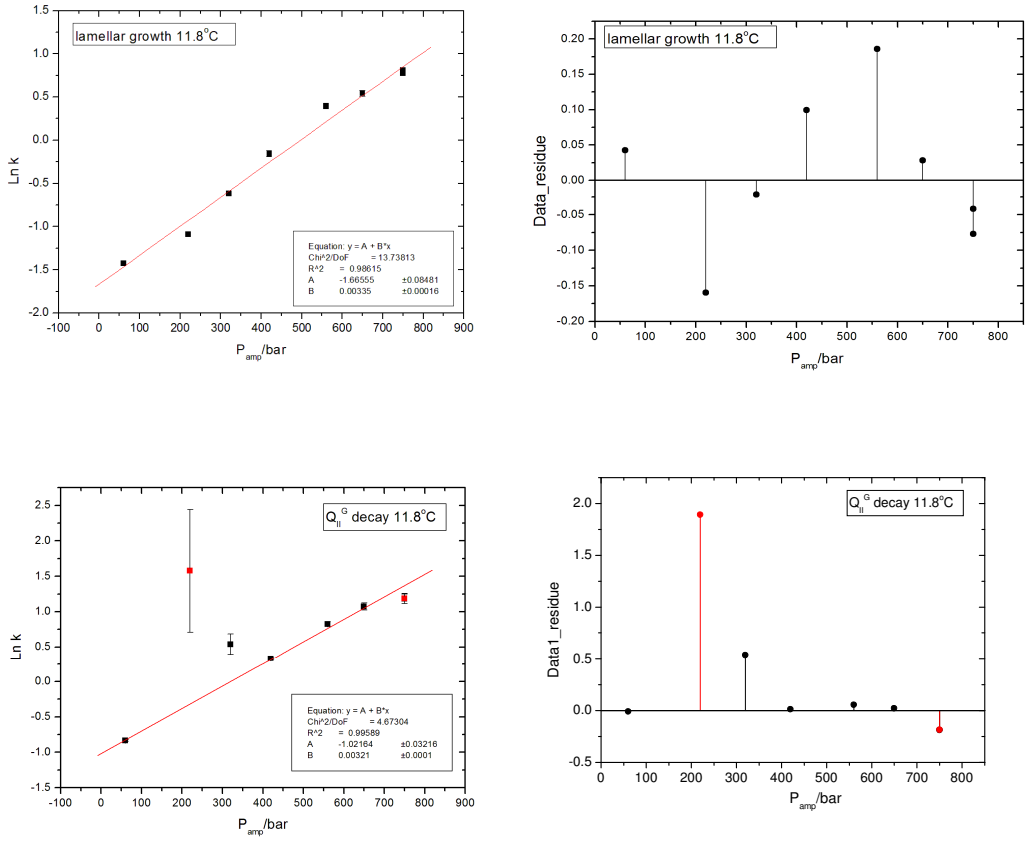


Figure 6.12 Linear fit to ln k vs P_{amp} data obtained from experimental data to the kinetic models for Q_{II}^{G} phase decay (bottom) and lamellar phase growth (top) at 11.8 ^{o}C for a 18 wt% water sample. To obtain a good linear fit the residuals from the linear fit are analysed. Data points were removed to obtain an even distribution of positive and negative residuals close to zero. Right shows the residuals for each data point.

	Q_{II}^{G} decay		Lamellar growth	
Temperature/^{o}C	**ln *k'***	**$\frac{d\,lnk}{dp}$ bar^{-1}**	**ln *k'***	**$\frac{d\,lnk}{dp}$ bar^{-1}**
11.8	-1.02±0.03	0.0032±0.0001	-1.67 ± 0.08	0.0034± 0.0002

Table 6-14 Parameters from linear fit of ln k vs P_{amp} for 18 wt% water sample for Q_{II}^{G} decay and lamellar growth at 11.8 ^{o}C.

6.4. Physical meaning of dimensionality, *n* for nucleation growth mechanisms

The parameter *n*, obtained from Avrami model fitting, encodes information about the growth of the domains. From analysis of Q_{II}^{G} growth at 26 ^{o}C, 31.6 ^{o}C and 38.4 ^{o}C (Figure 6.13) *n* lies between 2 and 3 describing a domain growth between a surface and a volume i.e. disc like (surface) or sphere like (volume). *n* also describes ILA nucleation: sporadic nucleation during which sites forming throughout the transformation. In this instance n will be closer to 3 and spontaneous nucleation describes the nucleation sites appearing simultaneously at the beginning of the transformation and *n* will typically be close to 2. It is likely that nucleation sites form spontaneously *and* sporadically, with some nucleation sites forming at the beginning of the reaction *and* as the transition progresses. This will also explain why non integer values for n are obtained for these processes.

Plotting the dimensionality *n* against P_{amp} (Figure 6.13) at 26 ^{o}C, 31.6 ^{o}C, and 38.5 ^{o}C shows that there is a decrease in dimensionality as pressure jump amplitude increases and can be attributed to either a change in domain growth dimensionality or to a shift from a sporadic nucleation to a spontaneous nucleation.

It has been shown that increasing $P_{amp,}$ increases the rate of Q_{II}^{G} phase formation (Chapter 5) and it is likely that a larger number of nucleation sites form immediately after the pressure jump is triggered when the external parameter is increased. The underlying mechanism for lamellar to Q_{II}^{G}

phase transition will remain the same and the dimensionality of domain growth is constant regardless of the change in P_{amp}.

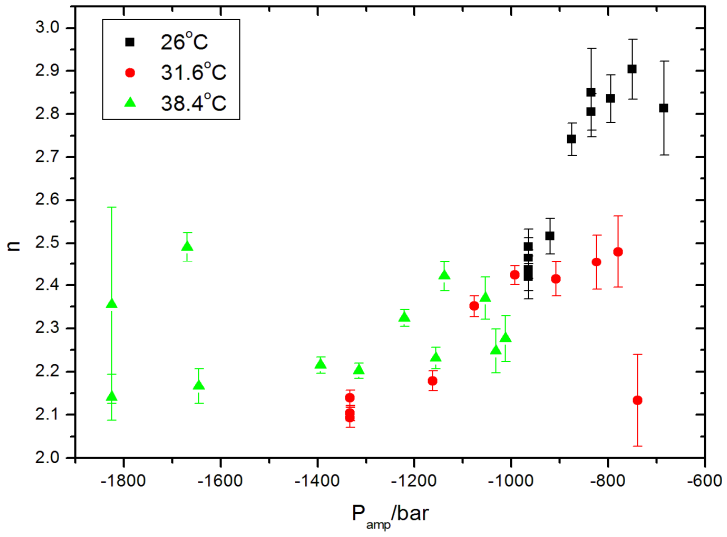


Figure 6.13 Plot of the dimensionality as a function of pressure jump amplitude for 22.1 wt% water at three different temperatures obtained from Avrami model fitting to the data showing the dimensionality of domain growth lies between 2 and 3.

Figure 6.13 shows that *n* is temperature dependent. Where n is larger at lower temperatures and smaller at higher temperature, suggesting that more ILAs form spontaneously at higher temperatures than at lower temperatures. Furthermore, from linear fits to *n* vs P_{amp} at 26 °C, 31.6 °C, and 38.4 °C (Figure 6.14) it is possible to deduce that the pressure dependence on n is greater at lower temperatures where increasing the pressure jump amplitude leads to an increased number of ILAs immediately after the pressure jump is triggered. At high temperatures, where most of the ILAs form spontaneously a change in pressure jump amplitude does not have an additional affect on ILA formation at the start of the reaction.

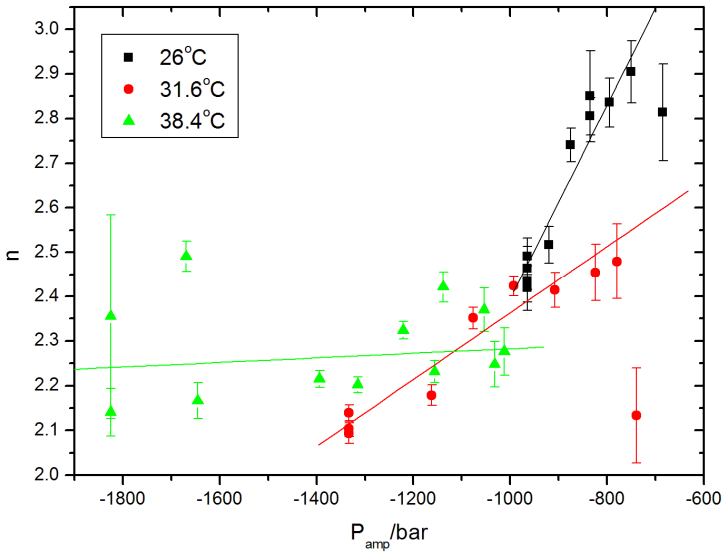


Figure 6.14 Plot of the dimensionality as a function of pressure jump amplitude with linear fits to the data at each individual temperature for 22.1 wt% water shows that n is pressure and temperature dependent.

The modulus of dimensionality, *n*, obtained from Avrami model fitting to the experimental absolute intensities was plotted as a function of pressure for the reverse process at 11.8 °C (Figure 6.15) for the incoming (lamellar) and outgoing (Q_{II}^{G}) phases.

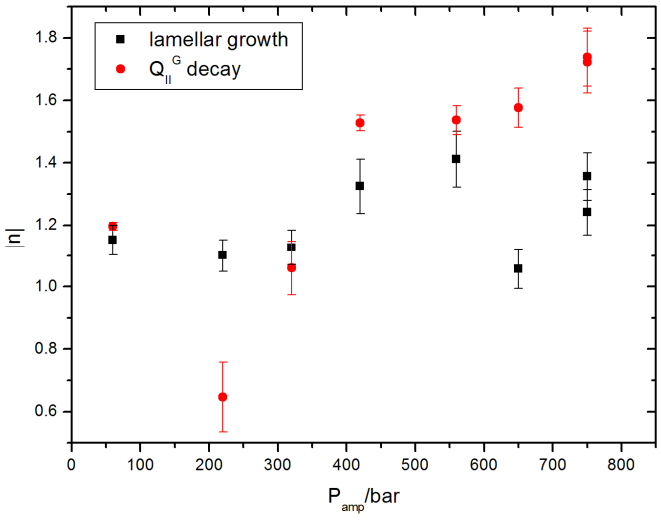


Figure 6.15 |n| vs P_{amp} plot for reverse transition at 11.8 °C for an 18 wt% water sample shows a dimensionality close to 1.

Figure 6.15 shows that the dimensionality, $|n|$, of the incoming and outgoing phases is close to 1 describing spontaneous nucleation and a linear domain decay or growth. There is also a decrease in dimensionality with decreasing P_{amp} which reaches a limiting value at approximately 300 bar. These trends are inconsistent with the trends observed for the forward reaction and is due to different mechanistic pathways which the forward and reverse transitions follow. It is evident from Avrami model fitting to the experimental data that the reverse process can be described by a nucleation – growth mechanism, however details of the mechanistic steps for the reverse process are still unclear and require more theoretical and experimental work.

6.5 Chapter Summary

In this chapter it has been argued that the transition kinetics of the lamellar to Q_{II}^{G} phase transition can be followed by the Avrami model which describes a nucleation growth mechanism. Model fitting to the experimental data and subsequent analysis of residual data has shown that this is a reasonable argument for the majority of pressure jumps. However, it is seen that the Avrami model may break down for phase transitions with slower kinetics. In addition, it is not a reasonable description of lamellar phase decay for the forward reaction where the nucleation process may be too complex to be described by this model.

Despite this, fitting absolute intensity data to the Avrami model and the exponential decay has given physically reasonable results for k, the rate constant, with good errors and excellent R^2 values to the fitting. Furthermore, it has been shown that ln k has a linear dependence with P_{amp} which agrees with previous experiments. Observations of the dimensionality, n, agree with qualitative deductions made in Chapter 5.

The reliability and reproducibility of the experimental data has been unequivocally shown, making it possible to make quantitative discussions about the lamellar to Q_{II}^{G} phase transition (discussed in Chapter 7). However, the limitations in the Avrami model for monitoring slower kinetic transformations will need to be addressed.

Chapter 7 Quantitative model for the kinetics of the lamellar to Q_{II}^{G} phase transition

Abstract:

Kinetic data describing the lamellar to Q_{II}^{G} phase transition in ML under limited hydrated conditions was analysed using the Squires model. It is shown that the model has potential in successfully describing mechanisms of transformations between mesophases of different geometries.

Using estimates of the spontaneous mean curvature and curvature elastic modulus the mean curvature of the transition state is calculated to lie between -0.0155 ± 0.0004 and -0.0141 ± 0.0002 $Å^{-1}$ for an 18.1 wt% water sample at 11.8 ^{o}C. Furthermore, the equivalent of 4.5 % of a Q_{II}^{G} phase undertakes the phase transition cooperatively. In addition, analysis of kinetic data for a 22.1 wt% water sample shows that energy is required to reach the transition state and there is an increase in volume to the transition state from the lamellar phase.

7.1 Introduction

A long standing problem in quantifying lyotropic phase transitions has been the availability of reproducible data, which has generally been attributed to difficulties in controlling sample homogeneity and water content as well as to constraints on experimental time at synchrotron radiation facilities. These issues have been overcome and reproducible kinetic data from a limited hydration monolinolein sample at varying temperatures have been obtained (Chapter 5 and 6). Furthermore, the amount of data makes it possible to quantitate the transition using a model recently published by Squires et al [93].

The model has been outlined in the introduction and provides an insight into transition pathways for lipid systems between phases of different geometries. Due to the limited availability of experimental data for the lamellar to Q_{II}^{G} phase transition the Squires model was previously applied to phase transitions of the same geometry (Q_{II}^{G} to Q_{II}^{D} phase transition) in 30 wt% water monoolein. Applying the model to the experimental data gave physically reasonable values for the cooperative unit N_{coop} and the enthalpy of transition, $H^{\#}$ reflecting the potential success of this model to describe lyotropic phase transitions.

In this chapter the model will be used to interpret kinetic data for an 18 wt% water monolinolein sample for the lamellar to Q_{II}^{G} phase transition. The implications of these results are potentially far reaching where the lamellar to Q_{II}^{G} phase transition has been compared to fundamental cellular processes such as membrane fusion and fission.

7.1.1 The model

Transition parameters such as $H^{\#}$, mean curvature of the transition state and N_{coop}, the cooperative unit, can be determined from the Squires model, furthermore the activation energy of the transition can be obtained from analysis of phase transformation kinetics which have been discussed in Chapter 6.

The equations used to obtain the transition parameters are described in Chapter 1 and are summarised here for reference (Equations 7.1 -7.6).

Mean curvature of transition state, $H^{\#}$:

$$\frac{\frac{d\ ln\ k_{L-G}}{dP}}{\frac{d ln\ k_{G-L}}{dP}} = \frac{(H^{\#} - H_L)}{(H^{\#} - H_G)} \qquad \text{Equation 7-1}$$

L-G signifies the lamellar to Q_{II}^{G} phase transition and G-L refers to the reverse process, Q_{II}^{G}-lamellar phase transition. $\frac{d\ lnk}{dp}$ is obtained from linear fits of ln *k* plot against P_{amp}, where *k* was obtained from fitting to the experimental data. The results are summarised in Chapter 6.3.2. $H^{\#}$ is the mean curvature of the transition state. H_L is the mean curvature of the lamellar phase (0 $Å^{-1}$) and H_G is the mean curvature of the Q_{II}^{G} phase at the pivotal surface, obtained using Equations 7.2-7.4.

$$H_G = \frac{K\,\xi}{1+K\,\xi^2} \qquad \text{Equation 7-2}$$

K is the surface averaged Gaussian curvature given by Equation 7.3

$$< K > = \frac{2\pi\chi}{\sigma_0\, a^2} \qquad \text{Equation 7-3}$$

where χ is the Euler characteristic, (-8 for the G surface) and σ_0 is the dimensionless surface area of the unit cell (equal to 3.091), a is the lattice parameter.

ξ is the distance from the bilayer mid plane to the pivotal surface and is obtained from Equation 7.4:

$$\phi_w = \frac{v}{v_n} \left(2\,\sigma_0\,\frac{\xi}{a} + \frac{4}{3}\,\pi\,\chi\,\left(\frac{\xi}{a}\right)^3 \right) \qquad \text{Equation 7-4}$$

ϕ_w is the water volume fraction of the sample; V is the total molecular volume, V_n is the volume between the minimal surface and the neutral surface.

Relative curvature, α

$$\alpha = \frac{H^{\#} - H_L}{H_G - H_L} \qquad \text{Equation 7-5}$$

The number of molecules in a cooperative unit N_{coop}

$$N_{coop} = \frac{\left(\frac{d}{dp} ln(k_{L-G}) - \frac{d}{dp} ln(k_{G-L})\right)}{C_p \frac{4\kappa A_n}{RT} N_A \,(H_G - H_L)} \qquad \text{Equation 7-6}$$

where A_n is the area at the pivotal surface calculated at P_{end} (Chapter 4); R is the gas constant; N_a Avogadros number; $C_p = \frac{d\,H_0}{dp}$ where H_0 is the spontaneous mean curvature; κ is the curvature elastic modulus. Values for C_p and κ are not available for monolinolein, therefore values previously obtained for monoolein will be used as a first approximation [93, 143]. Due to small differences in the structure of MO and ML it is assumed that κ and C_p will be in the same order of magnitude for

the two lipids. It can be further predicted that $\kappa_{ML} < \kappa_{MO}$. Further experiments will be required to obtain more accurate values for κ and C_p for ML.

To obtain the transition parameters, kinetic data for the forward and reverse processes at constant temperature are required. Pressure jump time-resolved experiments undertaken on an 18 wt% water sample (Tables 6.4-6.5) in the forward and reverse directions can be applied to the Squires model. However, forward direction (lamellar to Q_{II}^G) pressure jumps were undertaken at 18.1 °C and reverse (Q_{II}^G to lamellar) pressure jumps at 11.8 °C. Therefore, $\frac{d\ln k_{L-G}}{dP}$ at 18.1 °C is corrected to 11.8 °C in order to compare the forward and reverse transition kinetics.

7.2. Temperature correction for reverse transitions

$\frac{dlnk}{dP}$ was obtained from linear fitting (Section 6.3.3) for the incoming (Q_{II}^G) and outgoing (lamellar) phases at 26 °C, 31.5 °C and 38.5 °C in a 22.1 wt% water sample and plotted as a function of temperature (Figure 7.1). The results were extrapolated to obtain $\frac{dlnk}{dP}$ at 18 °C and 11.8 °C, and a 'temperature factor' calculated (Table 7.1). The 'temperature factor' was used to correct for the effect of temperature on $\frac{dlnk}{dP}$ for the forward and reverse transitions in the 18 wt% water sample (Table 7.2).

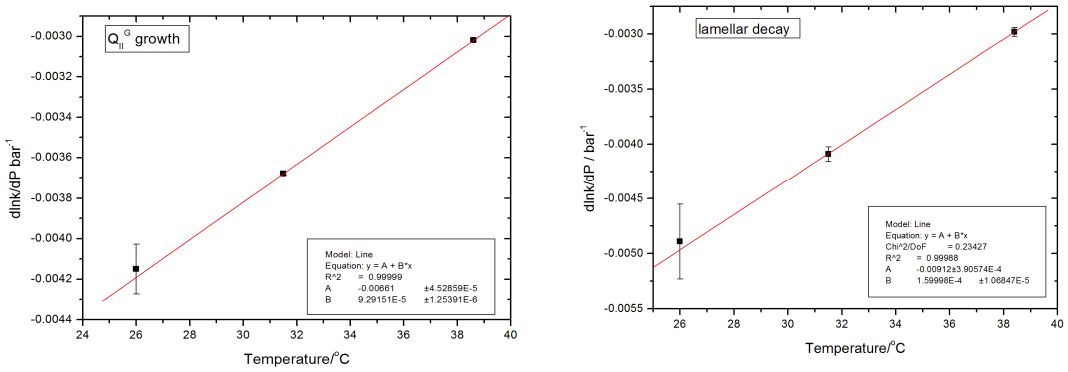


Figure 7.1 dlnk/dP vs temperature plots for lamellar to Q_{II}^G transition for Q_{II}^G phase growth (left) and lamellar phase decay (right) for 22.1 wt% water sample. The data was extrapolated to 18 °C and 11.8 °C to obtain dlnk/dP at these temperatures for the incoming and outgoing phases.

Figure 7.1 shows a linear temperature dependence of $\frac{dlnk}{dP}$ with R^2 > 0.996. The good linear fit to $\frac{dlnk}{dP}$ reaffirms the reliability of the experimental data and the fitting models. For temperature correction it is assumed that differences in water content do not affect on $\left(\frac{dlnk}{dP}\right) \times \frac{1}{dT}$.

Temp./^{o}C	**(Q_{II}^G) $\frac{dlnk}{dP}$ bar^{-1}**		**(lam) $\frac{dlnk}{dP}$ bar^{-1}**
18	-0.00493±0.00003		-0.0062±0.0002
11.8	-0.00551±0.00002		-0.0072±0.0003
Temperature factor	1.1176±0.0108		1.1613±-0.0832

Table 7-1 $(\frac{dlnk}{dP})^{18^oC}$ *and* $(\frac{dlnk}{dP})^{11.8^oC}$ *for the lamellar and* Q_{II}^G *phases for a forward reaction obtained from extrapolating linear fits of* $\frac{dlnk}{dP}$ *vs Temparature for 22.1 wt% water sample. From these values a temperature factor was obtained which can be used to correct for differences in temperature between the forward and reverse processes.*

$(\frac{dlnk}{dP})_{G-L}^{11.8^oC}$ and $(\frac{dlnk}{dP})_{L-G}^{18.1^oC}$ were obtained from linear fits to ln *k* vs P_{amp} data, (Figure 7.2), previously presented in Chapter 6 for the lamellar and Q_{II}^G phases for phase transitions in the forward and reverse directions. The values are summarised in Table 7.2. The temperature factor for the lamellar and Q_{II}^G phases was used to correct $(\frac{dlnk}{dP})_{L-G}^{18^oC}$ to $(\frac{dlnk}{dP})_{L-G}^{11.8^oC}$ which was then used to obtain the transition parameters, $H^{\#}$ and N_{coop} using Equations 7.1-7.6.

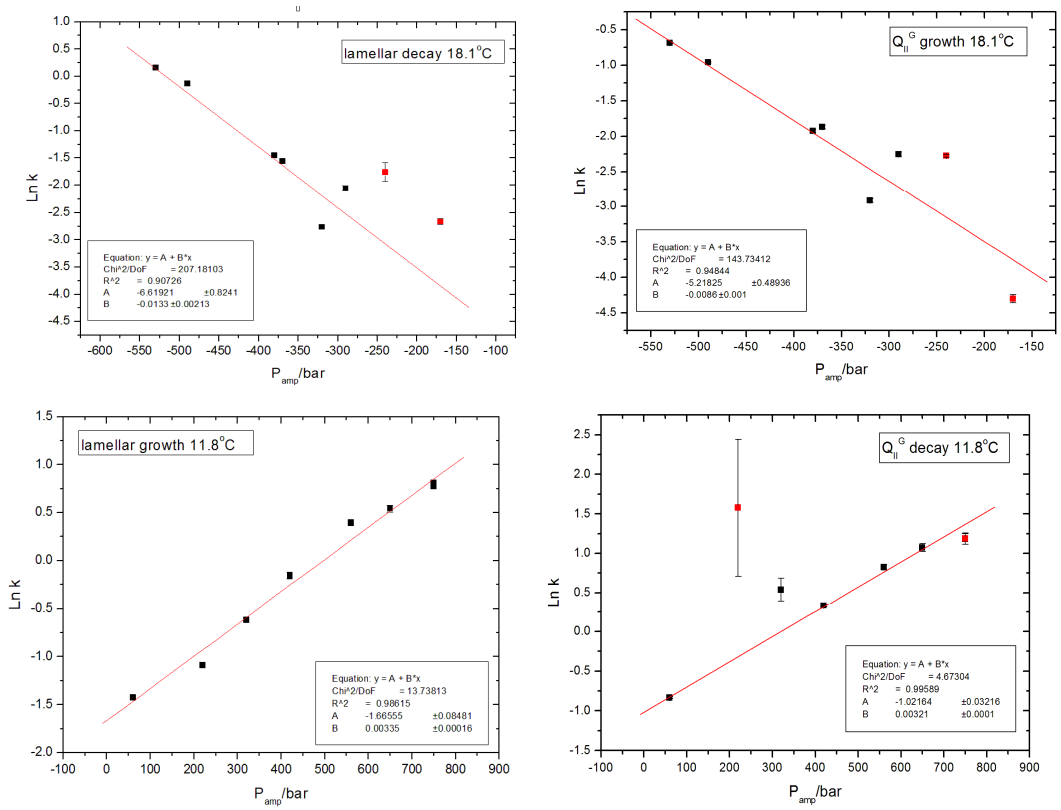


Figure 7.2 Linear plots of Ln k vs P_{amp} where k is obtained from fitting experimental absolute intensity for incoming and outgoing phases for 18 wt% water ML sample. The forward transition (lamellar to Q_{II}^{G}) is shown at the top at 18.1 °C and the reverse transition Q_{II}^{G} to lamellar at 11.8 °C is shown at the bottom.

	lam-Q_{II}^{G} **18°C**	***Q_{II}^{G}-lam*** ***11.8°C***	***lam-Q_{II}^{G}*** ***11.8°C***
	$(\frac{dlnk}{dP})_{L-G}^{18^oC}$ / bar^{-1}	$(\frac{dlnk}{dP})_{G-L}^{11.8^oC}$ / bar^{-1}	$(\frac{dlnk}{dP})_{L-G}^{11.8^oC}$ / bar^{-1}
lam	-0.0133±0.0021	**0.00335±0.00016**	**-0.0155±-0.0034**
Q_{II}^{G}	-0.0086±0.001	**0.00321±0.0001**	**-0.0096±0.0010**

Table 7-2 Summary of dlnk/dp at 18 °C and 11.8 °C for the lamellar and Q_{II}^{G} phases obtained from experimental data and corrected dlnk/dp for the forward transitions from 18 °C to 11.8 °C. The values shown in bold are used for determine transition parameters.

7.3. Curvature of transition state ($H^{\#}$)

From discussions in Chapter 5 it has been postulated that the most likely structure for the transition state is the ILA. Whilst the ILA is believed to be an important structural element of the forward process there is little evidence for its role in the reverse process. The Squires model assumes that the forward and reverse transitions will pass through a common transition state i.e. the ILA.

The curvature of the transition state ($H^{\#}$) and the relative curvature (α) can be calculated from Equations 7.1 and 7.5 and using $(\frac{dlnk}{dP})^{Lamellar}$ and $(\frac{dlnk}{dP})^{QIIG}$ obtained from experimental data in the forward and reverse transitions at 11.8 ^{o}C which are summarised in Table 7.2. The curvature of the Q_{II}^{G} phases and lamellar phases have been calculated: H_G = -0.0188 Å $^{-1}$ (Equation 7.2) and H_L = 0 Å^{-1}.

Using Equation 7.1 $H^{\#}_{lam}$ is -0.0155 ±0.0004 Å^{-1} and $H^{\#}_{QIIG}$ is -0.0141 ± 0.0002 Å^{-1} . The relative curvature of the transition state is calculated from Equation 7.5 giving α_{lam} = 0.82 ± 0.02 and α_{QIIG} = 0.75 ± 0.01.

Values obtained for the transitions parameters, $H^{\#}$ and α for lamellar and Q_{II}^{G} phase are within the same order of magnitude. $H^{\#}$ obtained from lamellar phase analysis is larger than Q_{II}^{G}. A smaller error in $H^{\#}_{QIIG}$ compared to $H^{\#}_{lam}$ suggests that the former is the more accurate value. It is likely that this is a consequence of kinetic fitting to only part of the lamellar decay process when determining the rate constant. Conversely, the Avrami model was used to fit all of the Q_{II}^{G} phase transition data for the forward and reverse transitions.

The relative curvature, α, of the transition state was calculated from $H^{\#}$ and gives a relative curvature greater than 0.5. The curvature of the transition state lies closer to the product (Q_{II}^{G} phase) than the initial state (lamellar phase). This agrees with what is known about the transition state where the bilayers in the ILA are curved and only a small change in bilayer curvature will transform the ILAs into water channels ubiquitous to the Q_{II}^{G} phase.

7.4. The cooperative unit

The size of the cooperative unit can be calculated by using Equation 7.7.

$$N_{coop} = \frac{(\frac{d}{dp} ln(k_{l-G}) - \frac{d}{dp} ln(k_{G-l}))}{C_p \frac{4\kappa A_n}{RT} N_A (H_G - H_l)}$$ Equation 7-7

Where A_n^{CMC} = 36.79 ± 0.98 Å^2 at 11.8 °C and atmospheric pressure (Chapter 4); N_a is Avogadro's number 6.02214 × 10^{23} mol^{-1}; T is 11.8 °C or 284.85 K; H_{QIIG} at the neutral surface is -0.0188 Å^{-1}. And $\boldsymbol{\kappa}$ = 1.2 × 10^{-20} J [127] and C_p = 0.2 nm^{-1} kbar^{-1} [93]. $(\frac{dlnk}{dP})^{Lamellar}$ and $(\frac{dlnk}{dP})^{QIIG}$ for the forward and reverse transitions are given in Table 7.2.

Therefore, N_{coop}^{L} = 112 ±19 lipids and N_{coop}^{G} = 76 ± 5 lipids.

The number of lipids in a unit cell for a Q_{II}^G phase can be calculated using Equation 7.8.

$$N_{unit\ cell} = \frac{2\,\sigma_0\,a^2\,(1+<K>\xi^2}{A_n}$$ Equation 7-8

Where σ_0 = 3.091; a =114.1 Å; $< K >$= -0.0188 Å^{-1}; ξ = 12.23 Å; A_n= 36.79 Å^2 giving $N_{unit\ cell} = 1766$ lipids.

The cooperative unit describes the number of molecules which undergo a cooperative change to drive the phase transition. For the lamellar to Q_{II}^G phase transition the precise nature of the cooperative unit is still unclear and may refer to the number of lipids acting cooperatively to form ILAs or the number of lipids which transform from ILAs to the Q_{II}^G phase. The calculations show that approximately 80 lipids (4.5% of Q_{II}^G unit cell) make up the cooperative unit. Although this value may seem small compared to N_{coop} in the Q_{II}^G to Q_{II}^D phase transition where 1-2 unit cells transform

cooperatively [93] it is physically reasonable for only a small number of lipids to be involved in ILA formation or Q_{II}^{G} phase formation since results described in Chapter 5 show that the lamellar phase maintains its integrity despite the formation of ILAs and Q_{II}^{G} phase. For this to occur a small number of lipids will transform into ILAs and/or the Q_{II}^{G} phase.

N_{coop} obtained from Q_{II}^{G} phase analysis has a smaller error (7 %) compared to the lamellar phase (18 %) suggesting that rate constant values obtained from model fitting are more accurate for the Q_{II}^{G} phase than the lamellar phase.

7.5 Activation energy

It has already been shown in Figure 7.1 that $\left(\frac{dlnk}{dP}\right)$ for lamellar phase decay and Q_{II}^{G} phase growth has a linear dependence with temperature for a 22.1 wt% water sample. Using the Arrhenius equation (Equation 7.8) $\Delta H^{\neq}$, the enthalpy of activation can be obtained from ln *k'* at varying temperatures. Ln *k'* is the natural log of the rate constant at the phase boundary (P_{amp} = 0 bar) and is obtained from the intercept of a linear fit to ln *k* vs P_{amp} (Chapter 6, Figures 6.9-6.10). Ln *k'* is summarised for a 22.1 wt% water sample in Table 6.11.

$$ln\, k'_{L-G} = ln\,(A) + \frac{\Delta S^{\neq\prime}}{R} - \frac{\Delta H^{\neq}}{RT} \qquad \text{Equation 7-9}$$

A is the pre-exponential factor, $\Delta S^{\neq}$ is the activation entropy and *R* is the gas constant, 8.3145 J K^{-1} mol^{-1}. Plotting *ln k'* vs $\frac{1}{T}$ (Figure 7.3) and fitting linearly gives $-\frac{\Delta H^{\neq}}{R}$ as the gradient of the line and $ln\,(A) + \frac{\Delta S^{\neq\prime}}{R}$ as its intercept.

Chapter 6 discusses the use of different kinetic models to fit the experimental data. The exponential decay model is used to fit the latter part of the lamellar phase decay whilst the Avrami model was used to fit all of the Q_{II}^{G} phase growth. The activation energy for ILA formation was determined by plotting ln *k'* against $\frac{1}{T}$ for the Q_{II}^{G} phase.

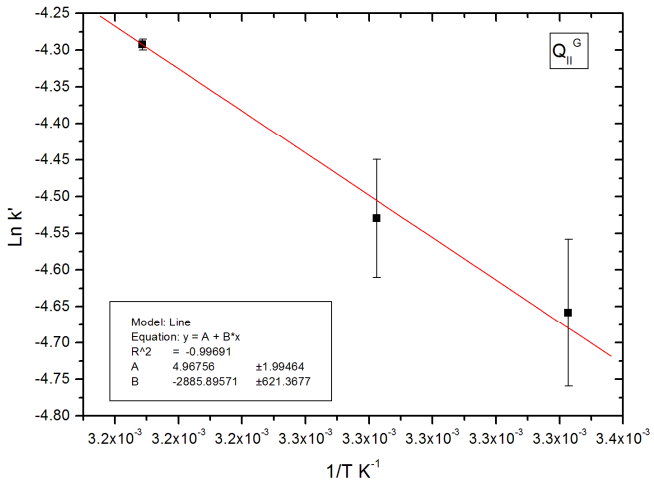


Figure 7.3. Plot of ln k' as a function of 1/T for the Q_{II}^{G} phase growth. Ln k' data was obtained from linear regression to pressure dependence on the rate constant from Q_{II}^{G} experimental data at 26 ^{o}C, 31.6 ^{o}C and 38.4 ^{o}C for forward transition pressure jumps on a 22.1 wt% water sample.

From linear fits to ln *k'* vs $\frac{1}{T}$, $\Delta H^{\#}$ is obtained from the gradient of the slope and is equal to 24.0 ± 5.2 kJ mol^{-1}. Having obtained N_{coop} in Section 7.4 the activation energy per cooperative unit is 693.8 ± 149.2 kT.

Positive activation energy indicates that energy input is required for ILA formation and the transition to occur. This energy is provided by a change in the thermodynamic parameter and drives the transition to a preferred curvature.

Activations energies have been experimentally obtained for the L_{β} to L_{α} transition, where there is no change in cuvature, [14, 144] in monoelaidin and various glycolipids and for the Q_{II}^{G} to Q_{II}^{D}

transition in 2:1 LA DLPC system [28]. For the L_β to L_α transition in glycolipids the activation energy is estimated to lie between 140-160 kJ mol^{-1}, for the same transition in ME the activation energy is an order of magnitude smaller (18 kJ mol^{-1}). The large difference in activation energies can be attributed to differences in lipid structure where lipid interactions dictate the amount of energy required for a phase transition. For a Q_{II}^G to Q_{II}^D phase transition in 2:1 LA:DLPC system the activation energy has been found to be 50 kJ mol^{-1}.

Activation energies calculated for limited hydrated ML (29 ± 7.0 kJ mol^{-1}) are in the same order of magnitude as the Q_{II}^G to Q_{II}^D phase transition in 2:1 LA:DLPC and the L_β to L_α phase transition in ME. More experiments will be required to establish trends between phase transitions in different systems.

7.7. Volume of activation

The volume of activation, $\Delta V^{\#}$, is obtained by plotting $\left(\frac{dlnk}{dP}\right)$ against $\left(\frac{1}{T}\right)$, where the gradient of a linear fit gives $-\frac{\Delta V^{\#}}{R}$ (Equation 7.9). $\Delta V^{\#}$ was determined from rate constants obtained from fitting experimental absolute intensity data to kinetic models for the Q_{II}^G phase growth in a 22.1 wt% water sample. $\left(\frac{dlnk}{dP}\right)$ was plotted against $\left(\frac{1}{T}\right)$ and $\Delta V^{\#}$ was obtained (Figure 7.4):

$$\Delta V^{\#} = -RT\left(\frac{dlnK_{AB}}{dP}\right) \qquad \text{Equation 7-10}$$

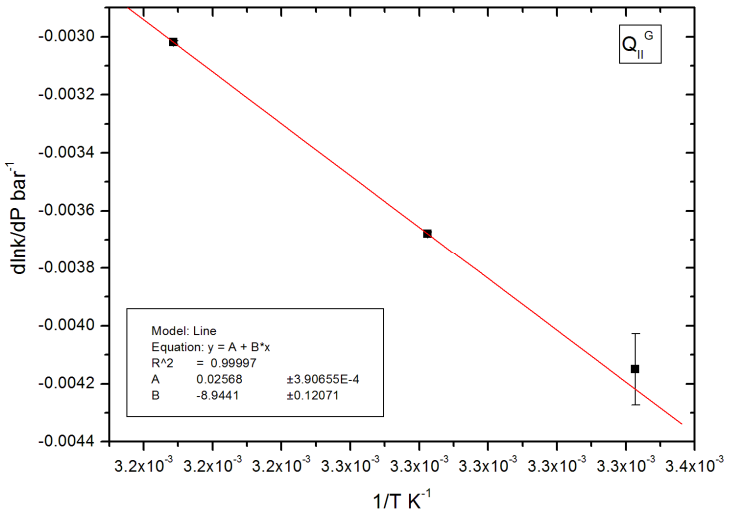


Figure 7.4. dlnk/dp was plotted as a function of 1/T to obtain the volume of activation for the lamellar to Q_{II}^{G} phase transition. dlnk/dp was obtained at three different temperatures, 26 ^{o}C, 31.6 ^{o}C and 38.4 ^{o}C from analysis of the Q_{II}^{G} phase for the lamellar to Q_{II}^{G} phase transition for a 22.1 wt% water sample.

From Figure 7.4 $\Delta V_G^{\#} = 74.4(\mathrm{cm}^3\mathrm{mol}^{-1}) \pm 1.0.$

$\Delta V^{\#}$ is defined as the difference between partial molar volume of the transition state and the reactants. This analysis has generally been used for protein folding and unfolding where a positive change in activation volume describes an increase in size of the protein and negative change in the activation volume describes a decrease in the size of the protein.

Analysis of volumes of activation for the lamellar to inverse bicontinuous phase transition in limited hydrated ML indicates an increase in volume from the initial state to the transition state. $\Delta V^{\#}$ = 8648 Å^3 N_{coop}^{-1} (~ 123.5 Å ^{3} lipid^{-1}) from analysis of Q_{II}^{G} phase growth. If the molecular volume of ML is approximately 700 Å ^{3}, volumes of activation obtained from experimental data suggest that the volume per lipid molecule lipid will increase approximately 20% from its initial state to the transition state. An increase in the lipid volume at the transition state is a precursory step to Q_{II}^{G} phase formation where the volume of the lipid is likely to be greater than the lamellar phase where the bilayer adopts a negative curvature.

7.7. Summary

In this chapter, it has been shown for the first time that a quantitative description of the transition state for the lamellar to inverse bicontinuous phase transition can be attained by using the Squires model. Even though precise definitions of the transition state parameter, N_{coop} is still unclear, estimates of $H^{\#}$ and N_{coop} obtained from analysis of pressure dependent behaviour on the rate constant for a 18.1 wt% water ML sample have given physically reasonable values. N_{coop} is approximately 4.5 % of a Q_{II}^{G} unit cell and the relative curvature of the transition state is closer to the Q_{II}^{G} phase than the lamellar phase (~ 0.8) which agrees with what is already known about the ILA. To increase the accuracy of $H^{\#}$ and N_{coop} experimental data for the forward and reverse processes at constant temperature and experimental values for C_p and κ for monolinolein would be required.

Furthermore, experimental kinetic data for the forward process was used to calculate the activation energies and volumes of activation for the reaction for a 22.1 wt% water sample. It has been found that energy input is required for the phase transition to occur and further experiments for different phase transitions and different lipid systems are required to begin to understand some of the factors contributing to the activation energy.

It should be noted that the Squires model only accounts for contributions to the total free energy from the curvature elastic energy. In a cubic to cubic transition, where hydrocarbon chain packing is likely to be quite similar between the initial and final phase, contributions to the energy from packing frustration will cancel out. However, for the lamellar to Q_{II}^{G} phase transition where the topology and geometry of the initial and final state are different, packing frustration will make a larger contribution to the free energy of the transition state.

Chapter 8 : Summary and further work

The work presented in this thesis has focused on the equilibrium and kinetic behaviour of monolinolein and water. The phase behaviour of ML and water was characterised using SAXs as a function of pressure and temperature. The aim of this study was to build upon a body of knowledge relating structure of the lipid to mesophase behaviour. The ultimate objective of this work is to make theoretical predictions of lipid phase behaviour. In order to be able to make accurate, theoretical energy calculations on mesophases the location of the pivotal surface is required. The existence of a pivotal surface was confirmed in a limited hydrated Q_{II}^{G} phase (ML) and the temperature and pressure dependence of the location of the pivotal surface was discussed.

Further relations between lipid structure and mesophase behaviour would be required to gain a deeper understanding of the specific parameters which affect mesophase stability. To this end, the phytantriol / water system is being characterised by SAXS. This work is still in progress and was undertaken with S. Squire [145]. Phytantriol (3, 7, 11, 15-tetramethyl-1,2,3-hexadecanetriol) has a trialcohol head group and branched, fully saturated hydrocarbon chain (Figure 8.1). Despite the differences in molecular structure between phytantriol and monolinolein it is been found that both systems have similar phase behaviour when temperature and water content are varied [52, 113].

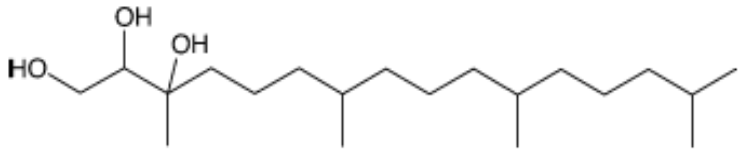


Figure 8.1 Structure of phytantriol (3, 7, 11, 15-tetramethyl-1,2,3-hexadecanetriol).

Characterisation of the phytantriol phase behaviour was undertaken using the same methodologies outlined in Chapter 2 and 3 and the partial phase diagram is shown in (Figure 8.2) for phytantriol with 99% purity.

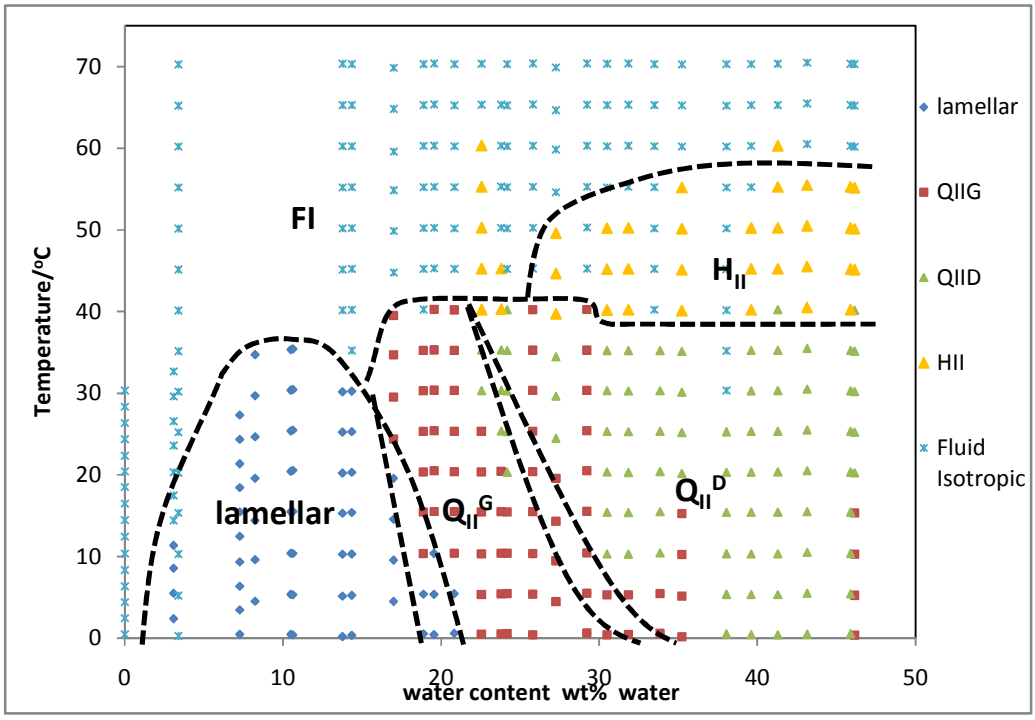


Figure 8.2 Data obtained with S.Squire [145] for characterisation of phase behaviour of 99% pure phytantriol at varying water contents and from 0 °C to 70 °C using SAXS. Dotted lines indicate the general boundary for different phases. More experiments are required to fully verify the location of the phase boundaries.

Once the phytantriol phase behaviour has been fully characterised, swelling data can be applied to the pivotal surface models with the methodology outlined in Chapter 4. By doing this, it will confirm or deny the concept of a universal pivotal surface in the inverse bicontinuous phases which can be used to calculate the energetics of mesophases. Furthermore, if the pivotal surface is

confirmed in the phytantriol system quantitative and qualitative deductions can be made about the factors which affect mesophase stability in Type II systems.

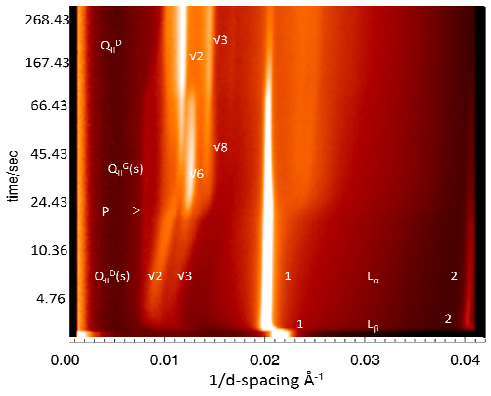
The second part of this thesis discusses the mechanisms and kinetics of the lamellar to Q_{II}^{G} phase transition for a limited hydrated ML sample using the Pressure jump time-resolved technique. Time resolved studies on lyotropic phase transitions is still in its infancy, however it has been shown that initial Q_{II}^{G} phase formation is limited by the rate of ILA nucleation and diffusion. When the Q_{II}^{G} phase forms it will form with a stretched bilayer and insufficient curvature. Bilayer relaxation in the Q_{II}^{G} phase drives the phase to equilibrium. In addition, absolute intensity data from pressure jumps experiments were used to quantify the kinetics of the lamellar to Q_{II}^{G} phase transition in the forward and reverse directions. It is argued that the Avrami model is a physically relevant model appropriate for tracking the kinetics of the lamellar to Q_{II}^{G} phase transitions. The rate constants obtained from model fitting to kinetic data have been used to show the potential of the Squires model for describing lamellar to Q_{II}^{G} phase transitions. Analysis of the kinetic data shows that N_{coop} and $H^{\#}$ are physically plausible; however, more kinetic data would be required to further test this model.

It has been shown that it is possible to extract meaningful quantitative information regarding the lamellar to Q_{II}^{G} phase transition. In order to obtain accurate descriptions of the transition state values for curvature elastic modulus, κ, the spontaneous mean curvature, H_0, and the rate constant, k, are required to a greater precision and consistency .

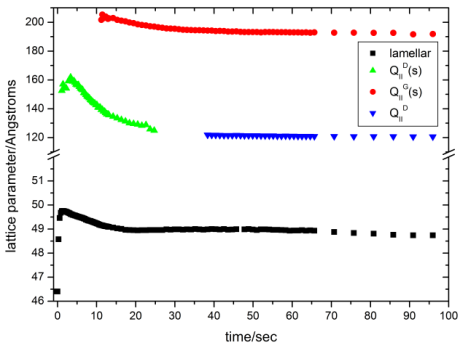
All time resolved experiments described in this thesis have been undertaken on limited hydrated ML samples and the final discussion will focus on a lamellar to Q_{II}^{D} phase transition at 5.7 ^{o}C for a 60 wt% water ML sample (i.e. under excess water conditions). A summary of the data from the jump is shown in Figure 8.3 and the methodology has previously been outline in Chapter 5.

Under excess water conditions, an effectively unlimited amount of water is available to the system and the formation of a precursor seed structure is apparent. Less than 5 s after the pressure jump is triggered, a Q_{II}^{D} (diamond cubic) phase is seen with a lattice parameter of 160 Å (Figure 8.4 i) and a calculated water content of 59 wt% water. The lattice parameter of this Q_{II}^{D} phase decreases with time but the intensity stays fairly constant. After 10 sec, a Q_{II}^{G} phase (calculated to be 49 wt% water) is seen in coexistence with the seed Q_{II}^{D} and lamellar phase (Figure 8.4 ii). Once the Q_{II}^{G} phase has formed and is in coexistence with the lamellar phase the intensity and lattice parameter of both phases decrease, indicating that there is a structural relationship between the lamellar

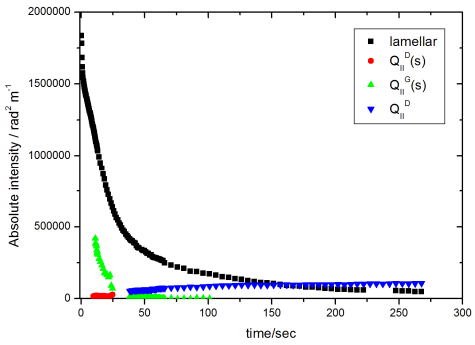
phase and the swollen Q_{II}^{G} phase. Once the intensity of the Q_{II}^{G} phase is close to zero a new Q_{II}^{D} phase forms (the equilibrium structure) whose lattice parameter stays fairly constant as its intensity increases. A distinct difference in the excess water jump, compared to the jump at limited hydration, is the appearance of another transient cubic which has been identified as a swollen Q_{II}^{G} phase (48.4 wt% water) (Figure 8.4 ii). It is not apparent why a Q_{II}^{G} phase would form alongside the Q_{II}^{D} phase; from equilibrium studies (Chapter 3) it was seen that the Q_{II}^{G} phase forms at lower water hydration and therefore higher curvature than the Q_{II}^{D} phase and an analogous situation arises here.



i)



ii)



iii)

Figure 8.3 Analysis of pressure jump2 at 5.7 ^{o}C for 60 wt% water sample. i). Stack plot of pressure jump with labelled reflections for lamellar phase (gel and fluid) (1 and 2); Q_{II}^{D}(s) (√2 and √3); Q_{II}^{G} (s) (√6 and √8); Q_{II}^{D}(√2 and √3) and peak P which is attributed to the scatter from the diamond windows. ii) shows the change in lattice parameter as a function of time. Iii) plot of absolute intensity of each phase as a function of time. Lamellar –black squares; Q_{II}^{G}(s) red circles; Q_{II}^{D}(s) green triangle; Q_{II}^{D} inverted blue triangles.

Throughout the pressure jump, there is a sharp reflection with low intensity at high d-spacing, indicated by P in the stack plot, which arises from scatter from the diamond windows.

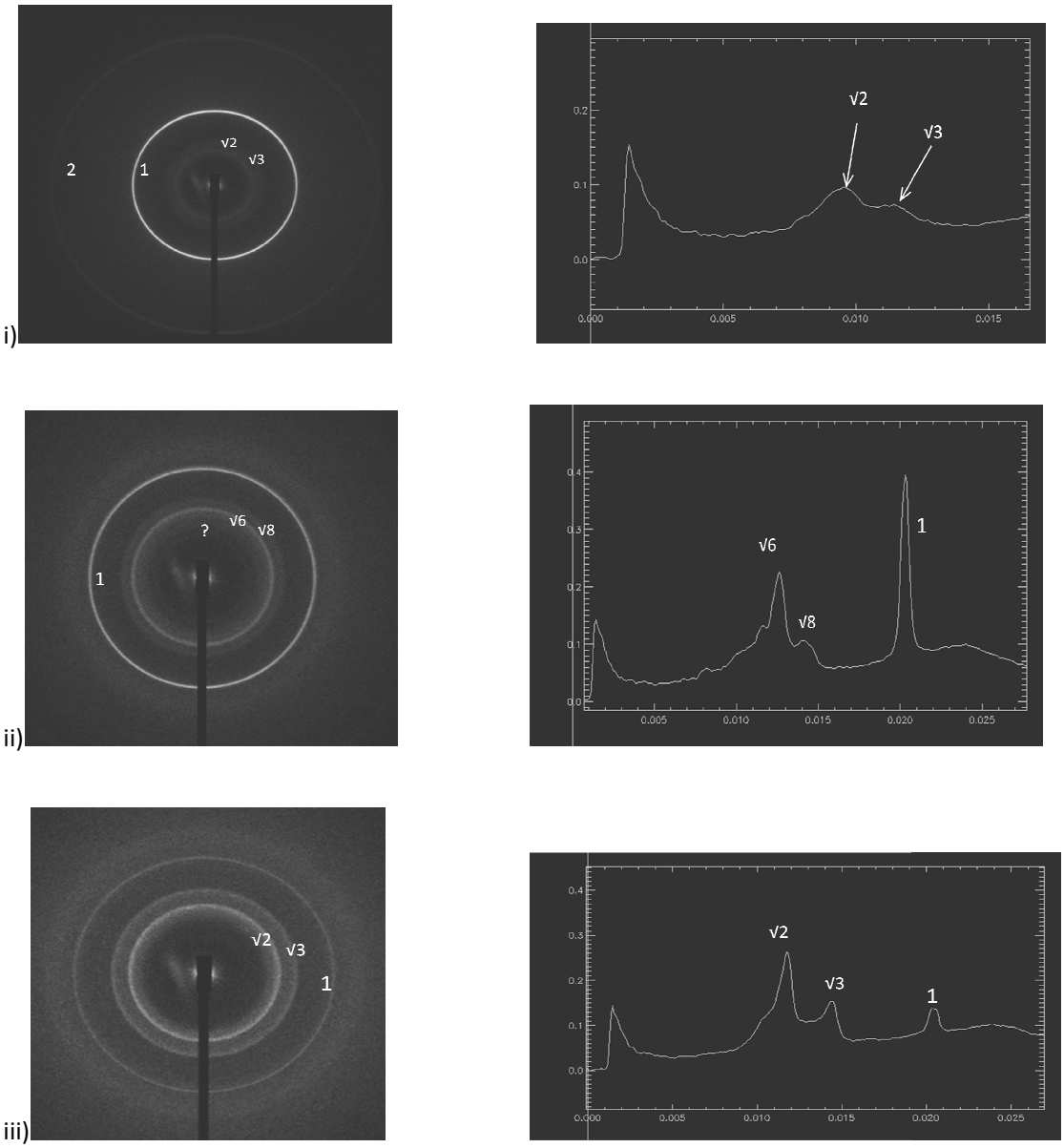


Figure 8.4 Examples of diffraction patterns and 1-D plots of swollen intermediates from pressure jump 2 at 5.7 ^{o}C for the lamellar to Q_{II}^{D} phase transition under excess water conditions. i) Lamellar phase coexisting with swollen Q_{II}^{D} phase (√2 and √3 reflections) ii) Lamellar phase coexisting with swollen Q_{II}^{G} phase (√6 and √8 reflections) iii) Lamellar phase coexisting with final Q_{II}^{D} phase (√2 and √3 reflections).

Intermediate swollen cubic phases are not seen under limited hydrated conditions for monolinolein but have been observed [69] under excess water conditions for ME where it has been postulated that swollen cubic phases act as a water storage vessels which release water to assist formation of a new equilibrium structure. It is likely that the swollen cubics form due to the increased amount of water in the system.

The observation of cubic phases which can swell to 50 wt% water is fascinating. Theoretical calculations have predicted that swollen cubic structures are stable at low temperatures and excess water conditions [122]. The indications that highly swollen cubics can form, albeit as transient structures and in phase coexistence, begs the question as to whether these structures can be isolated as equilibrium structures as suggested by theory.

Further experiments would be required to form more rigorous descriptions of the transformation mechanism for excess water samples as well as to probe the swelling capacity of the transient intermediates. Improved time resolution of the detector as well as a pressure cell capabilities exceeding 5 kbar will make further experiments in this area more facile.

Bibliography

1. Siegel, D.P., *Role of Gaussian curvature elastic energy in membrane fusion.* Abstracts of Papers of the American Chemical Society, 2005. **230**: p. U1075-U1076.
2. Mariani, P., V. Luzzati, and H. Delacroix, *Cubic phases of lipid-containing systems : Structure analysis and biological implications.* Journal of molecular biology, 1988. **204**(1): p. 165-189.
3. Luzzati, V., et al., *Cubic Phases of Lipid-Containing Systems - Elements of a Theory and Biological Connotations.* Journal of Molecular Biology, 1993. **229**(2): p. 540-551.
4. Larsson, K., *Cubic lipid-water phases: structures and biomembrane aspects.* J. Phys. Chem., 1989. **93**(21): p. 7304-7314.
5. Haque, M.E. and B.R. Lentz, *Roles of curvature and hydrophobic interstice energy in fusion: Studies of lipid perturbant effects.* Biochemistry, 2004. **43**(12): p. 3507-3517.
6. Gulik-Krzywicki T, *electron microscopy of cryofixed biological specimens.* Biology of the cell, 1994. **80**: p. 161-163.
7. Delacroix, H., et al., *Freeze-fracture Electron Microscope Study of Lipid Systems : The Cubic Phase of Space Group Pm3n.* Journal of Molecular Biology, 1993. **229**(2): p. 526-539.
8. Albertsson, P.A. and H. Leyon, *The structure of chloroplasts : V. Chlorella pyrenoidosa Pringsheim studied by means of electron microscopy.* Experimental Cell Research, 1954. **7**(1): p. 288-290.
9. Nissen, H.-U., *Crystal Orientation and Plate Structure in Echinoid Skeletal Units.* Science, 1969. **166**(3909): p. 1150-1152.
10. Andersson, S., et al., *Minimal surfaces and structures:from inorganic and metal crystals to cell membranes and biopolymers.* Chem. Rev, 1988. **88**: p. 221-242.
11. McGrath, K.M., et al., *Formation of a Silicate L$_3$ Phase with Continuously Adjustable Pore Sizes.* Science, 1997. **277**(5325): p. 552-556.
12. Balasubramanian, K. and A.J. Schroit, *AMINOPHOSPHOLIPID ASYMMETRY: A Matter of Life and Death.* Annual Review of Physiology, 2003. **65**(1): p. 701-734.
13. Caffrey, M., J. Briggs, and H. Chung, *The temperature-Composition Phase Diagram and Mesophase Structure characterization of the Monoolein/Water system.* J.Phys.II France, 1996. **6**: p. 723-751.
14. Czeslik, C., et al., *Temperature-Dependent and Pressure-Dependent Phase-Behavior of Monoacylglycerides Monoolein and Monoelaidin.* Biophysical Journal, 1995. **68**(4): p. 1423-1429.
15. Qiu, H. and M. Caffrey, *The phase diagram of the monoolein/water system: metastability and equilibrium aspects.* Biomaterials, 2000. **21**(3): p. 223-234.
16. Chung, H. and M. Caffrey, *Polymorphism, mesomorphism, and metastability of monoelaidin in excess water.* Biophysical Journal, 1995. **69**(5): p. 1951-1963.
17. Bender, J., et al., *Lipid cubic phases for improved topical drug delivery in photodynamic therapy.* Journal of Controlled Release, 2005. **106**(3): p. 350-360.

18. Ericsson, B., et al., *Cubic Phases as Delivery Systems for Peptide Drugs*, in *Polymeric Drugs and Drug Delivery Systems*. 1991, American Chemical Society: Washington, DC. p. 251-265.

19. Carlsson, N., et al., *Diamond Cubic Phase of Monoolein and Water as an Amphiphilic Matrix for Electrophoresis of Oligonucleotides.* The Journal of Physical Chemistry B, 2005. **109**(39): p. 18628-18636.

20. Chang, C., *Swelling of and drug release from monoglyceride-based drug delivery systems.* Journal of pharmaceutical sciences, 1997. **86**(6): p. 747-752.

21. Alfons Katarina, E.S., *Drug compatibility with the sponge phases formed in monoolein, water, and propylene glycol or poly(ethylene glycol).* Journal of Pharmaceutical Sciences, 1998. **87**(12): p. 1527-1530.

22. Fennell Evans, D. and H. Wennerstrom, *The Colloidal Domain: Where Physics, Chemistry, Biology and Technology Meer*. Second ed. 1999: Wiley-VCH.

23. Evans, D.F. and H. Wennerstrom, *The colloidal domain, where Physics, chemistry, biology and technology meet*. 1999.

24. Ramos, L., et al., *Equilibrium onions?* Europhysics Letters, 2004. **66**(6): p. 888-894.

25. Shearman, G.C., et al., *Inverse lyotropic phases of lipids and membrane curvature.* Journal of Physics-Condensed Matter, 2006. **18**(28): p. S1105-S1124.

26. Schoen, A.H. 1970, NASA: Washington DC.

27. Schwarz, H., *Gesammelte Mathematische Abhandlungen*. 1890, Berlin: Springer.

28. Squires, A.M., et al., *Kinetics and mechanism of the interconversion of inverse bicontinuous cubic mesophases.* Physical Review E, 2005. **72**(1).

29. Seddon, J.M., *An Inverse Face-Centered Cubic Phase Formed by Diacylglycerol Phosphatidylcholine Mixtures.* Biochemistry, 1990. **29**(34): p. 7997-8002.

30. Seddon, J.M., et al., *Inverse micellar phases of phospholipids and glycolipids.* Phys. Chem. Chem. Phys., 2000. **2**: p. 4485-4493.

31. Seddon, J.M., et al., *An Fd3m Lyotropic Cubic Phase in a Binary Glycolipid/Water System.* Langmuir, 1996. **12**(22): p. 5250-5253.

32. Delacroix, H., T. Gulik Krzywicki, and T. Seddon JM, *Freeze fracture electron microscopy of lyotropic lipid systems:quantitative analysis of the inverse Micellar cubic phase of space group Fd3m (Q(227)).* Journal of Molecular Biology, 1996. **258**: p. 88-103.

33. Shearman, G.C., et al., *A 3-D Hexagonal Inverse Micellar Lyotropic Phase.* Journal of the American Chemical Society, 2009. **131**(5): p. 1678-1679.

34. Helfrich, W., *Elastic Properties of Lipid Bilayers - Theory and Possible Experiments.* Zeitschrift Fur Naturforschung C-a Journal of Biosciences, 1973. **C 28**(11-1): p. 693-703.

35. Szleifer, I., et al., *Molecular theory of curvature elasticity in surfactant films.* The Journal of Chemical Physics, 1990. **92**(11): p. 6800-6817.

36. Anderson, D.M., S.M. Gruner, and S. Leibler, *Geometrical aspects of the frustration in the cubic phases of lyotropic liquid crystals.* Proceedings of the National Academy of Sciences of the United States of America, 1988. **85**(15): p. 5364-5368.

37. Briggs, J., H. Chung, and M. Caffrey, J. Phys. II, 1996. **6**: p. 723.

38. Lee, W.B., R. Mezzenga, and G.H. Fredrickson, *Anomalous Phase Sequences in Lyotropic Liquid Crystals.* Physical Review Letters, 2007. **99**(18): p. 187801.

39. Lee, W.B., R. Mezzenga, and G.H. Fredrickson, *Self-consistent field theory for lipid-based liquid crystals: Hydrogen bonding effect.* The Journal of Chemical Physics, 2008. **128**(7): p. 074504.

40. Kozlov, M.M. and M. Winterhalter, *Elastic-Moduli for Strongly Curved Monolayers - Position of the Neutral Surface.* Journal De Physique Ii, 1991. **1**(9): p. 1077-1084.

41. Kozlov, M. and R. Winterhalter, *Elastic-moduli for strongly curved monolayers-position of the neutral surface.* Journal De Physique, 1991. **1**(9): p. 1077-1084.

42. Rand RP, F.N., Gruner SM, Parsegian VA, *Membrane curvature, Lipid segregation, and structural transitions for phospholipids under Dual-Solvent Stress.* Biochemistry, 1990. **29**: p. 76-87.

43. Leikin, S., et al., *Measured effects of diacylglycerol on structural and elastic properties of phospholipid membranes.* 1996. **71**(5): p. 2623-2632.

44. Templer, R.H., et al., *Modeling the phase behavior of the inverse hexagonal and inverse bicontinuous cubic phases in 2 : 1 fatty acid phosphatidylcholine mixtures.* Journal of Physical Chemistry B, 1998. **102**(37): p. 7262-7271.

45. Hyde, S.T., et al., *A Cubic Structure Consisting of a Lipid Bilayer Forming an Infinite Periodic Minimum Surface of the Gyroid Type in the Glycerolmonooleate-Water System.* Zeitschrift Fur Kristallographie, 1984. **168**(1-4): p. 213-219.

46. *Proceedings of the International workshop on geometry and interfaces*. in *International workshop on geometry and interfaces*. 1990: Journal de Physique Colloques.

47. Tenchov, B., R. Koynova, and G. Rapp, *Accelerated Formation of Cubic Phases in Phosphatidylethanolamine Dispersions.* Biophysical Journal, 1998. **75**(2): p. 853-866.

48. Conn, C.E., et al., *A Pressure-Jump Time-Resolved X-ray Diffraction Study of Cubic-Cubic Transition Kinetics in Monoolein.* Langmuir, 2008. **24**(6): p. 2331-2340.

49. Templer, R.H., J.M. Seddon, and N.A. Warrender, *Measuring the elastic parameters for inverse bicontinuous cubic phases.* Biophysical chemistry, 1994. **49**: p. 1-12.

50. Templer, R.H., et al., *Inverse Bicontinuous Cubic Phases in 2:1 Fatty Acid/Phosphatidylcholine Mixtures. The Effects of Chain Length, Hydration, and Temperature.* J. Phys. Chem. B, 1998. **102**(37): p. 7251-7261.

51. Kulkarni, C.V., *In-Cubo crystallization of membrane proteins*, in *Chemistry*. 2008, Imperial College: London. p. 343.

52. Barauskas, J. and T. Landh, *Phase Behavior of the Phytantriol/Water System.* Langmuir, 2003. **19**(23): p. 9562-9565.

53. Schwarz, U.S. and G. Gompper, *Stability of Inverse Bicontinuous Cubic Phases in Lipid-Water Mixtures.* Physical Review Letters, 2000. **85**(7): p. 1472 LP - 1475.

54. Turner, D.C., et al., *Structural study of the inverted cubic phases of di-dodecyl alkyl-beta-D-glucopyranosyl-rac-glycerol.* J. Phys. II France, 1992. **2**(11): p. 2039-2063.

55. Templer, R.H., *On the Area Neutral Surface of Inverse Bicontinuous Cubic Phases of Lyotropic Liquid Crystals.* Langmuir, 1995. **11**(1): p. 334-340.

56. Brakke, K.A., *The Surface Evolver.* Exp. Math., 1992. **1**: p. 141.

57. Grosse-Brauckmann, K., *On Gyroid Interfaces.* Journal of Colloid and Interface Science, 1997. **187**(2): p. 418-428.

58. Cherezov, V., et al., *The kinetics of non-lamellar phase formation in DOPE-Me: Relevance to biomembrane fusion.* Journal of Membrane Biology, 2003. **195**(3): p. 165-182.

59. Gawrisch, K., et al., *Energetics of a hexagonal-lamellar-hexagonal-phase transition sequence in dioleoylphosphatidylethanolamine membranes.* Biochemistry, 1992. **31**(11): p. 2856-2864.

60. Kozlovsky, Y., et al., *Stalk Phase Formation: Effects of Dehydration and Saddle Splay Modulus.* Biophys. J., 2004. **87**(4): p. 2508-2521.

61. Kozlovsky, Y. and M.M. Kozlov, *Membrane Fission: Model for Intermediate Structures.* Biophys. J., 2003. **85**(1): p. 85-96.

62. Kozlovsky, Y. and M.M. Kozlov, *Stalk Model of Membrane Fusion: Solution of Energy Crisis.* Biophys. J., 2002. **82**(2): p. 882-895.

63. Kuzmin, P.I., et al., *A quantitative model for membrane fusion based on low-energy intermediates.* Proceedings of the National Academy of Sciences of the United States of America, 2001. **98**(13): p. 7235-7240.

64. Siegel, D.P., *Energetics of intermediates in membrane fusion: comparison of stalk and inverted micellar intermediate mechanisms.* Biophys. J., 1993. **65**(5): p. 2124-2140.

65. Siegel, D.P., *The Modified Stalk Mechanism of Lamellar/Inverted Phase Transitions and Its Implications for Membrane Fusion.* Biophys. J., 1999. **76**(1): p. 291-313.

66. Cheng, A.C. and M. Caffrey, *Interlamellar transition mechanism in model membranes.* Journal of Physical Chemistry, 1996. **100**(14): p. 5608-5610.

67. Kriechbaum, M. and P. Laggner, *States of phase transitions in biological structures.* Progress in Surface Science, 1996. **51**(3): p. 233-261.

68. Squires, A.M., Templer RH, Seddon JM, Woenckhaus J, Winter R, Finet S, Theyencheri N, *Kinetics and Mechanism of the Lamellar to Gyroid Inverse Bicontinuos Cubic Phase transition.* Langmuir, 2002. **18**: p. 7384-7392.

69. Conn, C.E., et al., *Dynamics of Structural Transformations between Lamellar and Inverse Bicontinuous Cubic Lyotropic Phases.* Physical Review Letters, 2006. **96**(10): p. 108102.

70. Epand, R.M., *Membrane fusion - Overview.* Bioscience Reports, 2000. **20**(6): p. 435-441.

71. Ellens, H., et al., *Membrane-Fusion and Inverted Phases.* Biochemistry, 1989. **28**(9): p. 3692-3703.

72. Siegel, D.P., *Mechanism of the Transitions between Lamellar and Inverted Hexagonal Phases.* Biophysical Journal, 1985. **47**(2): p. A250-A250.

73. Siegel, D.P., *Stalk Structures as Intermediates in Membrane-Fusion and Bilayer Nonbilayer Phase-Transitions.* Biophysical Journal, 1993. **64**(2): p. A186-A186.

74. Siegel, D.P., *A Stalk-Mediated Mechanism for Lamellar Inverted Cubic and Lamellar Inverted Hexagonal Phase-Transitions.* Biophysical Journal, 1994. **66**(2): p. A174-A174.

75. Hui, S.W., et al., *Membrane Fusion through Point Defects in Bilayers.* Science, 1981. **212**(4497): p. 921-923.

76. Efrat, A., L.V. Chernomordik, and M.M. Kozlov, *Point-Like Protrusion as a Prestalk Intermediate in Membrane Fusion Pathway.* 2007. **92**(8): p. L61-L63.

77. Pelham, H.R.B., *SNAREs and the specificity of membrane fusion.* 2001. **11**(3): p. 99-101.

78. Chen, Y.A. and R.H. Scheller, *Snare-mediated membrane fusion.* Nature Reviews molecular cell biology, 2001. **2**(2): p. 98-106.

79. Kozlov, M.M. and V.S. Markin, *Possible Mechanism of Membrane-Fusion.* Biofizika, 1983. **28**(2): p. 242-247.

80. Markin, V.S. and J.P. Albanesi, *Membrane fusion: Stalk model revisited.* Biophysical Journal, 2002. **82**(2): p. 693-712.

81. Kozlov, M., *Stalk mechanism of membrane fusion: Solution of energy crisis.* Biophysical journal, 2002. **82**(1): p. 543A.

82. Kozlovsky, Y., L.V. Chernomordik, and M.M. Kozlov, *Lipid Intermediates in Membrane Fusion: Formation, Structure, and Decay of Hemifusion Diaphragm.* Biophys. J., 2002. **83**(5): p. 2634-2651.

83. Siegel, D.P. and M.M. Kozlov, *The Gaussian curvature elastic modulus of N-monomethylated dioleoylphosphatidylethanolamine: Relevance to membrane fusion and lipid phase behavior.* Biophysical Journal, 2004. **87**(1): p. 366-374.

84. Yang, L. and H. Huang, W, *Observation of a membrane Fusion Intermediate Structure.* Science, 2002. **297**: p. 1877-1879.

85. Yang, L. and H.W. Huang, *A rhombohedral phase of lipid containing a membrane fusion intermediate structure.* Biophysical Journal, 2003. **84**(3): p. 1808-1817.

86. Siegel, D.P. and R.M. Epand, *The mechanism of lamellar-to-inverted hexagonal phase transitions in phosphatidylethanolamine: Implications for membrane fusion mechanisms.* Biophysical Journal, 1997. **73**(6): p. 3089-3111.

87. Sadoc, J.F. and J. Charvolin, *Infinite Periodic Minimal-Surfaces and Their Crystallography in the Hyperbolic Plane.* Acta Crystallographica Section A, 1989. **45**: p. 10-20.

88. Benedicto, A.D. and D.F. O'Brien, *Bicontinuous Cubic Morphologies in Block Copolymers and Amphiphile/Water Systems: Mathematical Description through the Minimal Surfaces.* Macromolecules, 1997. **30**(11): p. 3395-3402.

89. Fogden, A. and S.T. Hyde, *Continuous transformations of cubic minimal surfaces.* European Physical Journal B, 1999. **7**(1): p. 91-104.

90. Schroder, G.E., et al., *Medial surfaces of hyperbolic structures.* European Physical Journal B, 2003. **35**(4): p. 551-564.

91. Schroder, G.E., et al., *A rhombohedral family of minimal surfaces as a pathway between the P and D cubic mesophases.* Physica A: Statistical Mechanics and its Applications, 2004. **339**(1-2): p. 137-144.

92. Schroeder-Turk, G.E., A. Fogden, and S.T. Hyde, *Bicontinuous geometries and molecular self-assembly: comparison of local curvature and global packing variations in genus-three cubic, tetragonal and rhombohedral surfaces.* European Physical Journal B, 2006. **54**(4): p. 509-524.

93. Squires, A., et al., *Quantitative model for the kinetics of lyotropic phase transitions involving changes in monolayer curvature.* Soft Matter, 2009. **5**: p. 4773-4779.

94. Koberl, M., et al., *Cooperativity of glycolipid phase transitions: a critical comparison of results from equilibrium X-ray, density and microcalorimetric measurements.* Chemistry and Physics of Lipids, 1998. **95**(1): p. 59-82.

95. Strey, R., *Microemulsion microstructure and interfacial curvature.* Colloid & polymer science, 1994. **272**(8): p. 1005-1019.

96. Lutton, E.S., *Phase behaviour of Aqueous Systems in monoglycerides.* The Journal of the American Oil Chemist's Society, 1965. **42**: p. 1068-1070.

97. Briggs, J. and M. Caffrey, *The temperature-composition phase diagram of monomyristolein in water: equilibrium and metastability aspects.* Biophys. J., 1994. **66**(3_Pt_1): p. 573-587.

98. Cheng, A.C., A. Mencke, and M. Caffrey, *Manipulating mesophase behavior of hydrated DHPE: An x-ray diffraction study of temperature and pressure effects.* Journal of Physical Chemistry, 1996. **100**(1): p. 299-306.

99. Qiu, H. and M. Caffrey, *Lyotropic and thermotropic phase behavior of hydrated monoacylglycerols: Structure characterization of monovaccenin.* Journal of Physical Chemistry B, 1998. **102**(24): p. 4819-4829.

100. Conn, C.E., *Dynamics of Structural Transformations between lyotropic Liquid Crystalline Phases*, in *Chemistry*. 2007, Imperial College: London. p. 241.

101. Dean. J, R., et al., *Practical Skills in Chemistry*. 2002, Harlow: Prentice Hall.

102. Woolfson, M.M., *An introduction to X-ray crystallography*. 2 ed. 1997: Cambridge University Press.

103. Hammond, C., *The basics of crystallography and diffraction*. 2009: Oxford University Press. 432.

104. Pecahrsky, V., K, *Fundamentals of powder diffraction and structural characterization of materials*. 2009: Springer. 741.

105. Gauthe, B.L.L.E., et al., *A high pressure cell for simultaneous osmotic pressure and x-ray diffraction measurements.* Review of Scientific Instruments, 2009. **80**(3): p. 035107.

106. Heron, A., *Stored Curvature Elastic Stress in Lipid Membranes and its Effect upon the activity of CTO:Phosphocholine Cytidylyltransferase*, in *Department of Chemistry*. 2005, Imperial College, London: London. p. 401.

107. Woenckhaus, J., *High pressure-jump apparatus for kinetic studies of protein folding reactions using the small-angle synchrotron x-ray scattering technique.* Review of scientific instruments, 2000. **71**(10): p. 3895-3899.

108. *International tables for crystallography*, ed. T. Hahn and D. Reidel. 1983, Dordrechet.

109. Seddon, J.M., et al., *Pressure-jump X-ray studies of liquid crystal transitions in lipids.* Philosophical Transactions of the Royal Society a-Mathematical Physical and Engineering Sciences, 2006. **364**(1847): p. 2635-2655.

110. Ohvo-Rekilä, H., et al., *Cholesterol interactions with phospholipids in membranes.* Progress in Lipid Research, 2002. **41**(1): p. 66-97.

111. Caffrey, M., *Structural, Mesomorphic and Time-Resolved Studies of Biological Liquid-Crystals and Lipid-Membranes Using Synchrotron X-Radiation.* Topics in Current Chemistry, 1989. **151**: p. 75-109.

112. Campo de, L., et al., *reversible Phase transitions in Emulsified Nanostructured Lipid systems.* Langmuir, 2004. **20**: p. 5254-5261.

113. Dong, Y.-D., et al., *Impurities in Commercial Phytantriol Significantly Alter Its Lyotropic Liquid-Crystalline Phase Behavior.* Langmuir, 2008. **24**(13): p. 6998-7003.

114. Duesing, P.M., et al., *Pressure effects on the lamellar and Inverse Curved Phases of fully hydrated dialkyl Phosphatidylethanolamines and beta-D-Xylopyranosyl-sn-glycerols.* Langmuir, 1997. **13**: p. 2655-2664.

115. Winter, R., *Effects of hydrostatic pressure on lipid and surfactant phases.* Current Opinion in Colloid & Interface Science, 2001. **6**(3): p. 303-312.

116. Winter, R., *Effect of pressure on the stability, phase behaviour and transformation kinetics between structures of lyotropic lipid mesophases and model membrane systems*, in *Journal of physics. Condensed matter*. 1998. p. 11499.

117. Jeworrek, C., M. Puhse, and R. Winter, *X-ray Kinematography of Phase Transformations of Three-Component Lipid Mixtures: A Time-Resolved Synchrotron X-ray Scattering Study Using the Pressure-Jump Relaxation Technique.* Langmuir, 2008. **24**(20): p. 11851-11859.

118. Pisani, M., et al., *Compressing inverse lyotropic systems: Structural behavior and energetics of dioleoyl phosphatidyl ethanolamine.* Physical Review E, 2003. **68**(2): p. 021924.

119. Winter, R., et al., *Inverse bicontinuous cubic phases in fatty acid/phosphatidylcholine mixtures II. The effects of pressure and lipid composition.* physical Chemistry Chemical Physics, 1998. **1**: p. 887-893.

120. Mezzenga, R., et al., *Shear rheology of lyotropic liquid crystals: A case study.* Langmuir, 2005. **21**(8): p. 3322-3333.

121. Sierro, P. and D. Roux, *Structure of a Lyotropic Lamellar Phase under Shear.* Physical Review Letters, 1997. **78**(8): p. 1496 LP - 1499.

122. Shearman GC, C.O., Templer RH, Soft Matter, 2010.

123. Andersson, S., et al., *Minimal surfaces and structures: from inorganic and metal crystals to cell membranes and biopolymers.* Chem. Rev., 1988. **88**(1): p. 221-242.

124. Hamm, M., *Elastic energy of tilt and bending of fluid membranes.* The European physical journal. E, Soft matter, 2000. **3**(4): p. 323-335.

125. Schwarz, U.S. and G. Gompper, *Bending Frustration of Lipidâˆ'Water Mesophases Based on Cubic Minimal Surfaces1.* Langmuir, 2001. **17**(7): p. 2084-2096.

126. Chung, H. and M. Caffrey, *The neutral area surface of the cubic mesophase: location and properties.* Biophys. J., 1994. **66**(2_Pt_1): p. 377-381.

127. Vacklin, H., *The bending elasticity of 1-monoolein upon relief of packing stress.* Langmuir, 2000. **16**(10): p. 4741-4748.

128. *Handbook of Chemistry and Physics*, ed. D.R. Lide. 1996, Boca Raton, Florida: CRC Press.

129. Reiss-Husson, F. and V. Luzzati, *The Structure of the Micellar Solutions of Some Amphiphilic Compounds in Pure Water as Determined by Absolute Small-Angle X-Ray Scattering Techniques.* The Journal of physical chemistry, 1964. **68**(12): p. 3504-3511.

130. Siegel, D.P., et al., *Intermediates in membrane fusion and bilayer/nonbilayer phase transitions imaged by time-resolved cryo-transmission electron microscopy.* Biophys. J., 1989. **56**(1): p. 161-169.

131. Gabke, A., et al., *Using pressure in combination with x-ray and neutron scattering techniques for studying the structure, stability and phase behaviour of soft condensed matter and biomolecular systems* Journal of Physics: Condensed Matter2005. **17**(40): p. S20077-S3092.

132. Caffrey, M., *Kinetics and Mechanism of the Lamellar Gel Lamellar Liquid-Crystal and Lamellar Inverted Hexagonal Phase-Transition in Phosphatidylethanolamine - a Real-Time X-Ray-Diffraction Study Using Synchrotron Radiation.* Biochemistry, 1985. **24**(18): p. 4826-4844.

133. Caffrey, M., *Kinetics and Mechanism of Transitions Involving the Lamellar, Cubic, Inverted Hexagonal, and Fluid Isotropic Phases of Hydrated Monoacylglycerides Monitored by Time-Resolved X-Ray-Diffraction.* Biochemistry, 1987. **26**(20): p. 6349-6363.

134. Czeslik, C., et al., *High pressure synchrotron X-ray diffraction studies of biological molecules using the diamond anvil technique.* Nuclear Instruments and Methods in Physics Research Section A: Accelerators, Spectrometers, Detectors and Associated Equipment, 1996. **368**(3): p. 847-851.

135. Erbes, J., et al., *Kinetics of phase transformations between lyotropic lipid mesophases of different topology: a time-resolved synchrotron X-ray diffraction study using the pressure-jump relaxation technique.* Physical Chemistry Chemical Physics, 2000. **2**(1): p. 151-162.

136. Kraineva J, N.R., Kondrashkina E, Thiyagarajan P, Winter R, *Kinetics of lamellar to cubic and intercubic Phase transitions of pure and cytochrome c containing Monolein Dispersions Monitored by Time Resolved Small Angle X-Ray Diffraction.* Langmuir, 2005. **21**: p. 3559-3271.

137. Siegel, D.P., *Inverted micellar intermediates and the transitions between lamellar, cubic, and inverted hexagonal lipid phases. II. Implications for membrane-membrane interactions and membrane fusion.* Biophysical Journal, 1986. **49**(6): p. 1171-1183.

138. Tate, M.W., et al., *Kinetics of the lamellar-inverse hexagonal phase transition determined by time-resolved x-ray diffraction.* Biochemistry, 1992. **31**(4): p. 1081-1092.

139. Tristram-Nagle, S., et al., *Kinetics of subgel formation in DPPC: X-ray diffraction proves nucleation-growth hypothesis.* Biochimica et Biophysica Acta (BBA) - Biomembranes, 1994. **1191**(1): p. 14-20.

140. Yang, C.P. and J.F. Nagle, *Phase transformations in lipids follow classical kinetics with small fractional dimensionalities.* Physical Review A, 1988. **37**(10): p. 3993 LP - 4000.

141. Ye, Q., W.W. van Osdol, and R.L. Biltonen, *Gel-liquid crystalline transition of some multilamellar lipid bilayers follows classical kinetics with a fractional dimensionality of approximately two.* 1991. **60**(5): p. 1002-1007.

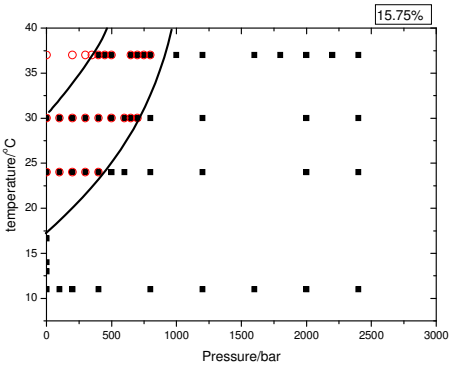
142. Jabarin, S.A. and R.S. Stein, *Light scattering and microscopic investigations of mesophase transitions of cholesteryl myristate. II. Kinetics of spherulite formation.* The Journal of physical chemistry, 1973. **77**(3): p. 409-413.

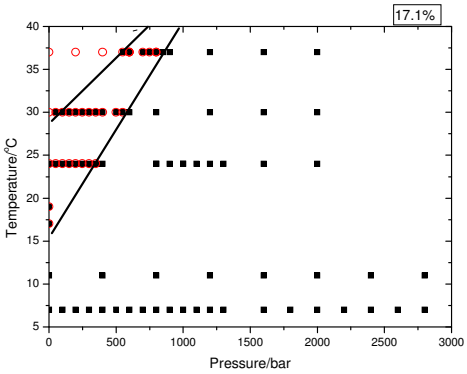
143. Pisani, M., et al., *Pressure Induced Cubic-to-Cubic Phase Transition in Monoolein Hydrated System*, in *The journal of physical chemistry. B, Condensed matter, materials, surfaces, interfaces & biophysical*. 2001. p. 3109-3119.

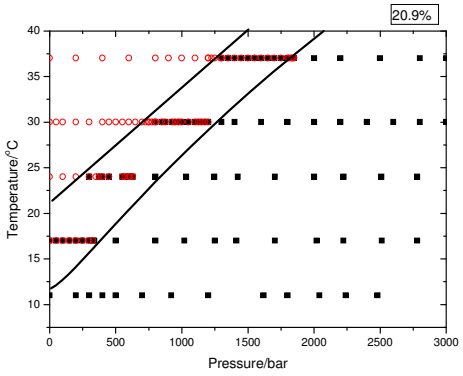
144. Schoppe, A., et al., *Activation energies and kinetics of glycolipid phase transitions.* Chemistry and Physics of Lipids, 1999. **103**(1-2): p. 95-115.

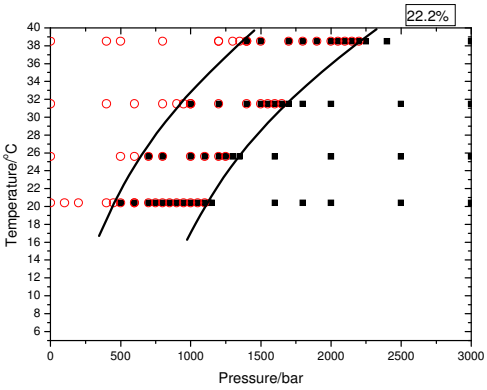
145. Squire, S., *Jumping phases-lyotropic phase transitions*, in *Chemistry*. 2009, Imperial College: London.

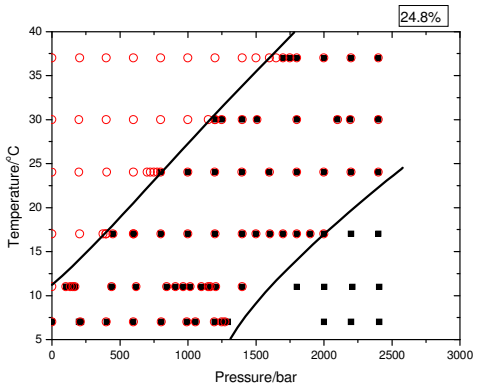
Appendix A

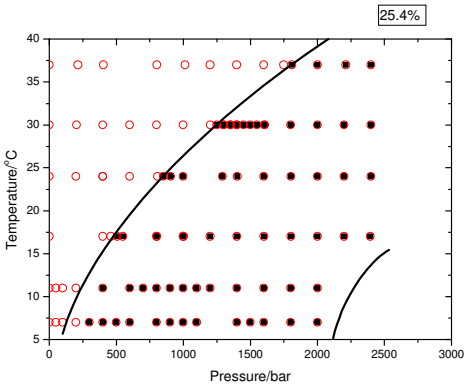

15.75%
temperature/°C
Pressure/bar


17.1%
Temperature/°C
Pressure/bar


20.9%
Temperature/°C
Pressure/bar


22.2%
Temperature/°C
Pressure/bar


24.8%
Temperature/°C
Pressure/bar


25.4%
Temperature/°C
Pressure/bar

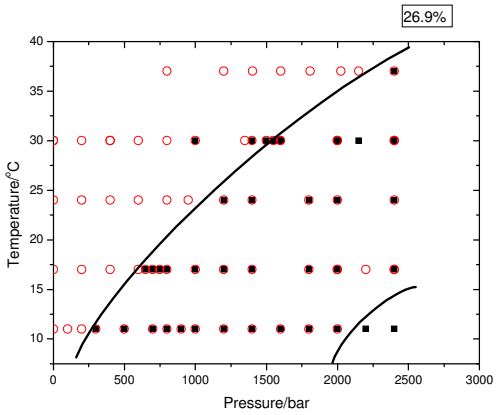


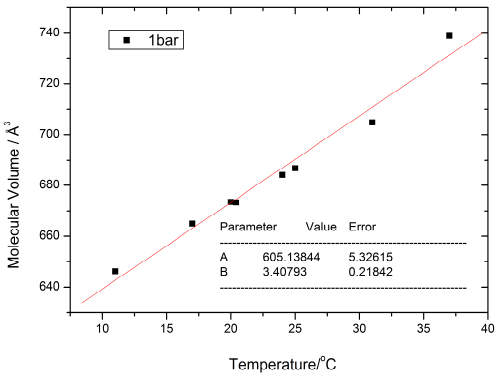
Figure A-1 Pressure-temperature composition phase diagrams for varying ML water samples obtained at ID02 at ESRF and I22 at DLS. Black squares denote the fluid lamellar phase; red circles the Q_{II}^{G} phase. Regions which show black squares and red circles indicate a region of phase coexistence between the lamellar and Q_{II}^{G} phases. Thin black lines denote phase boundaries.

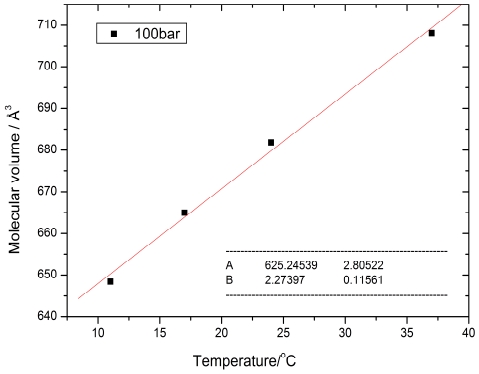
Appendix B

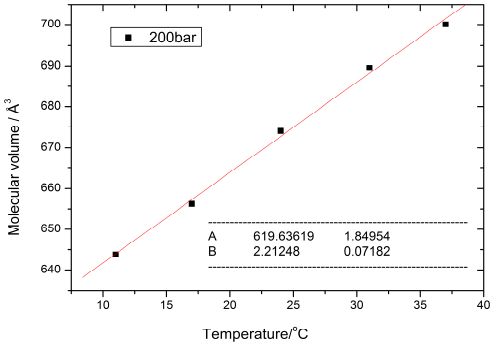
i) Molecular volume at any pressure or temperature:

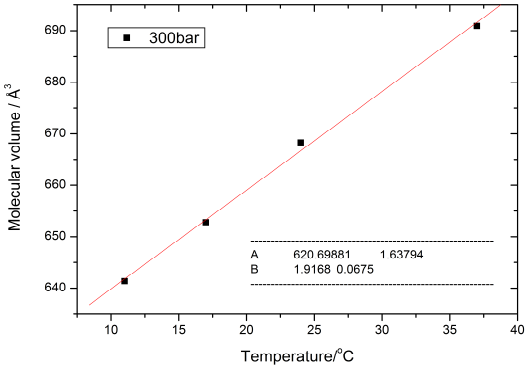
To obtain the molecular volumes at any required pressures or temperature the experimental data was plot and a linear fit made to the data. From the linear fit molecular volumes can be calculated for any temperature and pressure using Equation B-1.

$$V = A + BT \qquad \text{Equation 8-1}$$









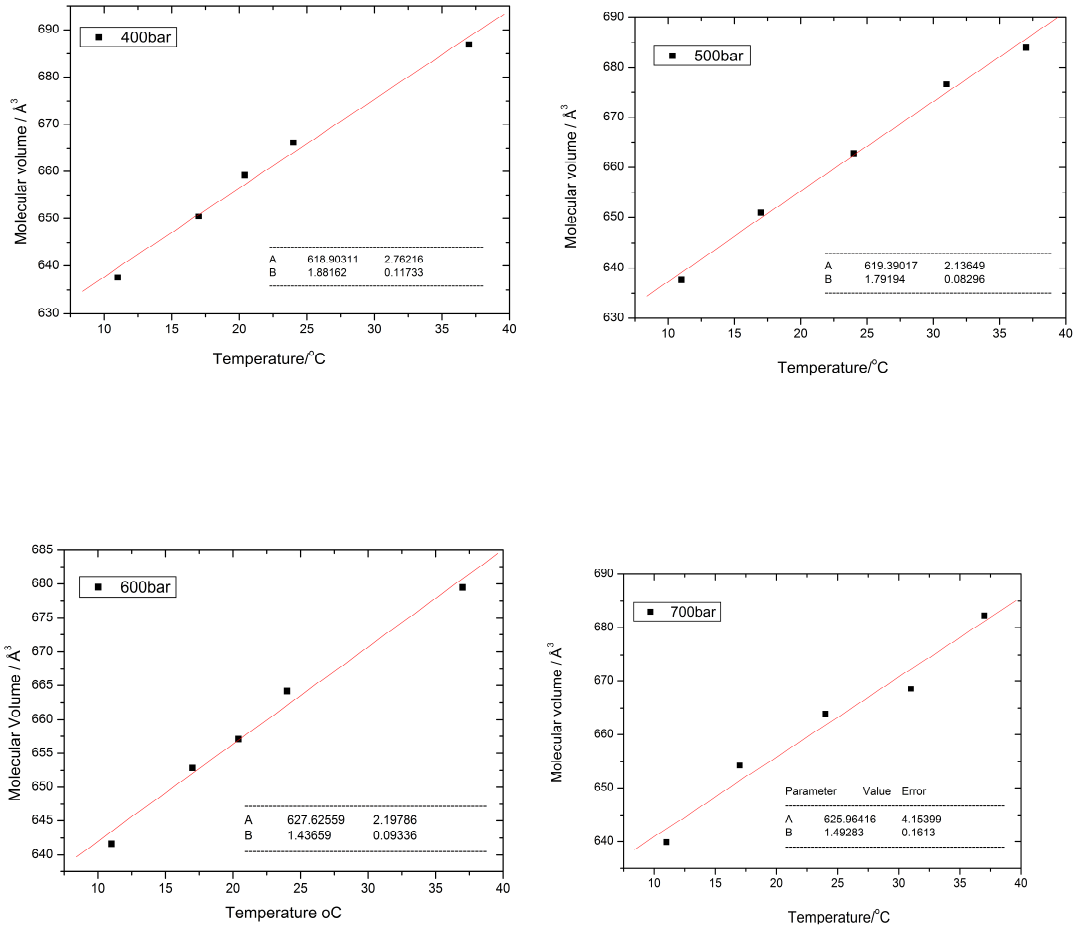


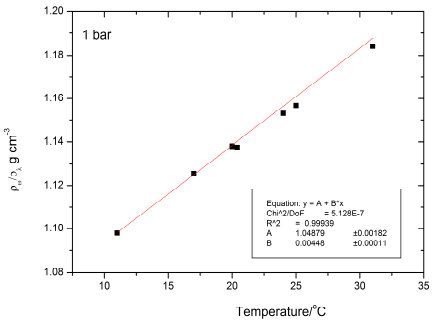
Figure B-1 linear fits to experimental molecular volume data for limited hydration (24 wt% water) at constant pressure and varying temperatures. A is the intercept and B is the gradient of the slope. From the linear fits the molecular volume at any pressure and temperature can be calculated from extrapolation.

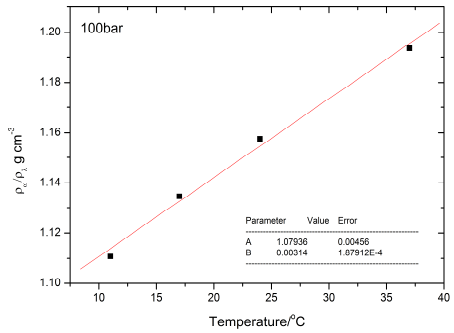
ii) Obtaining $\frac{\rho_w}{\rho_l}$ at any pressure or temperature:

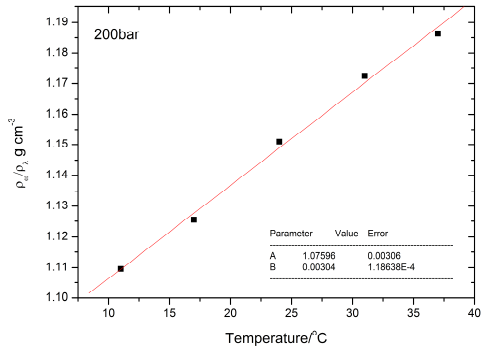
$\frac{\rho_w}{\rho_l}$ was calculated from experimental data and plot as a function of temperature at constant pressure from 1 bar to 700 bar. A linear fit was fit to the data and the data was extrapolated to obtain $\frac{\rho_w}{\rho_l}$ at an required temperature or pressure using Equation B-2.

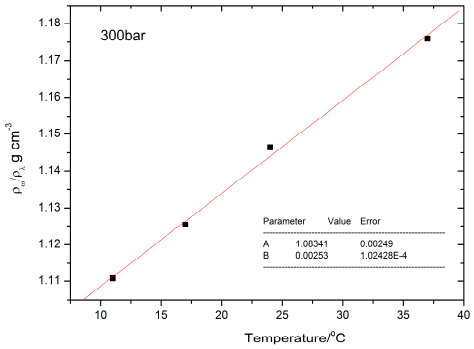
$$\frac{\rho_w}{\rho_l} = A + BT$$ Equation 8-2

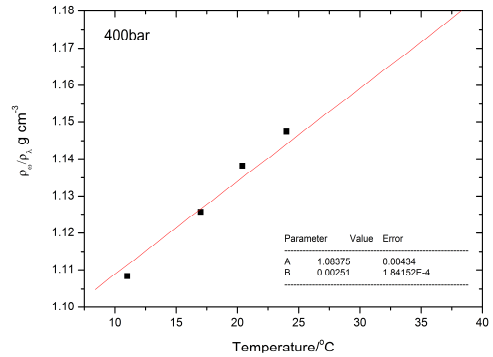
Where *A* is the intercept and *B* is the gradient and *T* is the temperature.

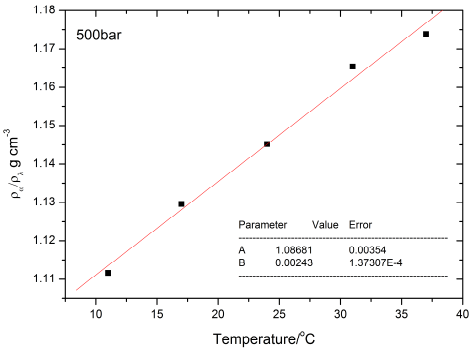


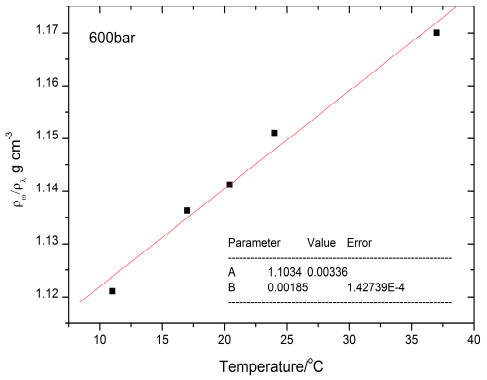












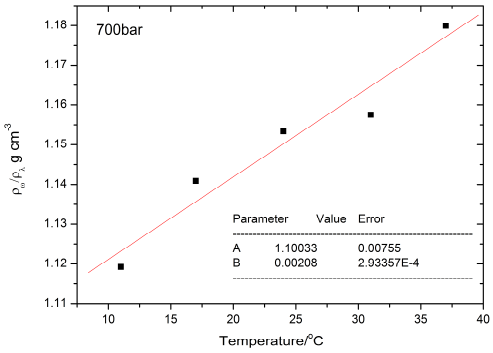


Figure B-2 linear fits to experimental $\frac{\rho_w}{\rho_l}$ data for limited hydration (24 wt% water) at constant pressure and varying temperatures. *A* is the intercept and *B* is the gradient of the slope. From the linear fits the molecular volume at any pressure and temperature can be calculated from extrapolation.

Parallel Interface model code

Recaculation of water contents:

$$\phi_w := 1 - \left(4 V^3 \sigma^3 \left(a^3 A^3 V^6 \sigma^6 + \sqrt{V^{12} \sigma^9 \left(a^6 A^6 \sigma^3 - \left(a^2 A^2 \sigma - 6 \pi vn^2 \chi\right)^3\right)}\right)^{\frac{1}{3}}\right) \Big/ \left(a^2 A^2 V^4 \sigma^4 - 6 \pi V^4 vn^2 \sigma^3 \chi + \left(a^3 A^3 V^6 \sigma^6 + \sqrt{V^{12} \sigma^9 \left(a^6 A^6 \sigma^3 - \left(a^2 A^2 \sigma - 6 \pi vn^2 \chi\right)^3\right)}\right)^{\frac{2}{3}}\right)$$

```
water =
 Evaluate[
  Re[ϕw /. {vn -> 607.85, V -> 707.3764, A -> 37.13, χ -> -8,
     σ -> 3.0915, a → 110.909}]]
```

iii)

Model fitting code

```
data =
  {{0.185174, 108.03}, {0.217742, 117.5730791}, {0.222999, 118.0325052},
   {0.236958, 121.5675216}, {0.194088, 110.88425}};
```

$$a[\phi\_] := \frac{v}{A\times(1-\phi)} \times \left(-2\times\sigma + 2^{\frac{5}{3}}\times\sigma^2 \Big/ \left(4\times\sigma^3 + 9\times\pi\times\chi\times(1-\phi)^2\times\left(\frac{vn}{v}\right)^2 + 3\times(1-\phi)\times\left(\frac{vn}{v}\right)\times\sqrt{\pi\times\chi\times\left(8\times\sigma^3 + 9\times\pi\times\chi\times(1-\phi)^2\times\left(\frac{vn}{v}\right)^2\right)}\right)^{\frac{1}{3}} + 2^{\frac{1}{3}}\times\left(4\times\sigma^3 + 9\times\pi\times\chi\times(1-\phi)^2\times\left(\frac{vn}{v}\right)^2 + 3\times(1-\phi)\times\left(\frac{vn}{v}\right)\times\sqrt{\pi\times\chi\times\left(8\times\sigma^3 + 9\times\pi\times\chi\times(1-\phi)^2\times\left(\frac{vn}{v}\right)^2\right)}\right)^{\frac{1}{3}}\right)$$

```
RHTmod = Evaluate[Re[a[x] /. {v → 707.3763, χ -> -8, σ → 3.0915}]]
nlm = NonlinearModelFit[data,
  {RHTmod , {20 ≤ A ≤ 39, 500 ≤ vn ≤ 1000}}, {A, vn}, x]
Normal[nlm];
nlm[0.1];
nlm["ParameterTable"]
nlm["FitResiduals"]
ListPlot[%, Filling → Axis, Frame → True,
 PlotLabel → 10 oC, FrameLabel → {"data point", "Residual"},
 LabelStyle → Directive[Black, Bold]]
Show[ListPlot[data, PlotStyle → {PointSize[0.02], Black}],
 Plot[nlm[x], {x, 0.18, 0.25}, PlotStyle → Directive[Thick, Blue]],
 FrameLabel → {"Φw", "a / Å"}, LabelStyle → Directive[Black, Bold],
 Frame → True, PlotLabel → PIM 1 bar]
nlm["FitCurvatureTable"]
Grid[
 Transpose[{#, nlm[#]} &[{"AdjustedRSquared", "AIC", "BIC", "RSquared"}]],
 Alignment → Left]
```

Constant mean curvature code:

Recalculation of water contents code:

```
vn = 592.3;
v = 707.3764;
A = 37.48;
χ = -8;
σ0 = 3.0915;
σ1 = -1.3317;
σ2 = -0.19974;
σ3 = -0.80113;
a = 108.51;
Solve[(2 × ((v/(A×(1-ϕ))) ×
        ((σ0 × ((vn/v) × (1 - ϕ))^0) + (σ1 × ((vn/v) × (1 - ϕ))^2) +
          (σ2 × ((vn/v) × (1 - ϕ))^4) + (σ3 × ((vn/v) × (1 - ϕ))^6)))) == a, ϕ]
```

Model fitting code

```
data =
  {{0.184183, 108.03}, {0.217712, 117.5730791}, {0.222974, 118.0325052},
   {0.236959, 121.5675216}, {0.194073, 110.88425}};
a[ϕ_] := 2 × ((v/(A×(1-ϕ))) × ((σ0 × ((vn/v) × (1 - ϕ))^0) + (σ1 × ((vn/v) × (1 - ϕ))^2) +
        (σ2 × ((vn/v) × (1 - ϕ))^4) + (σ3 × ((vn/v) × (1 - ϕ))^6)))
mcmod = Evaluate[Re[a[x] /. {v → 707.3763, χ -> -8, σ0 -> 3.0915,
      σ1 -> -1.3317, σ2 → -0.19974, σ3 → -0.80113}]];
nlm = NonlinearModelFit[data, {mcmod, {20 ≤ A ≤ 80, 400 ≤ vn ≤ 800}},
   {A, vn}, x];
Normal[nlm];
nlm[0.1];
nlm["BestFitParameters"];
nlm["FitResiduals"]
ListPlot[%, Filling → Axis, Frame → True,
 PlotLabel → 30 oC, FrameLabel → {"data point", "Residual"},
 LabelStyle → Directive[Black, Bold]]
grph2 = Show[ListPlot[data, PlotStyle → {PointSize[0.02], Black}],
  Plot[nlm[x], {x, 0.15, .3}, PlotStyle → Directive[Thick, Blue]],
  FrameLabel → {"Φw", "a / Å"}, LabelStyle → Directive[Black, Bold],
  Frame → True, PlotLabel → CMC - 1 bar]
Grid[Transpose[{#, nlm[#]} &[
   {"AdjustedRSquared", "AIC", "BIC", "RSquared"}]], Alignment → Left]
nlm["ParameterTable"]
```

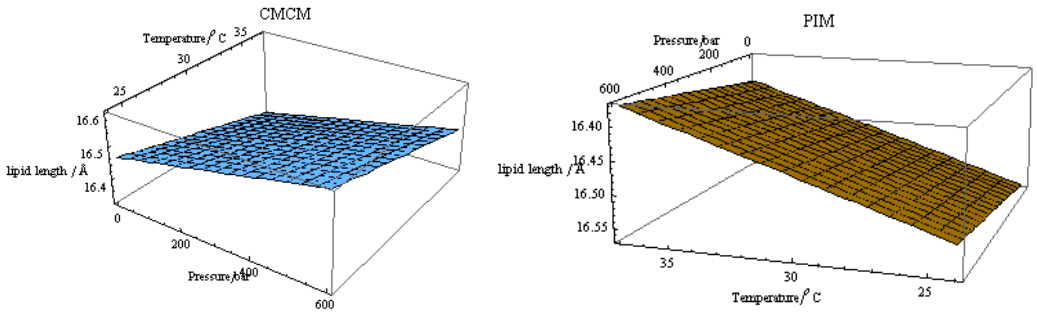
Lipid length and distance to pivotal surface

code

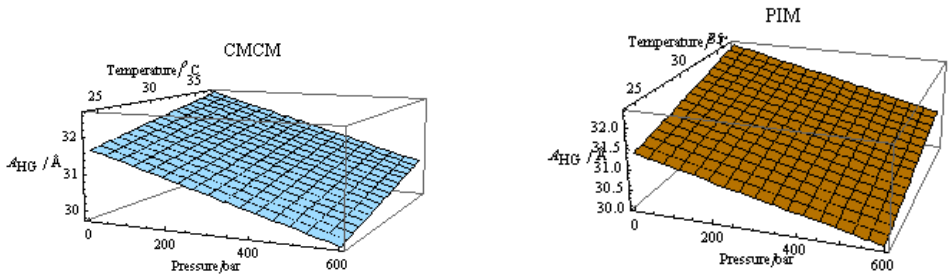
```
ϕ1 = 0.758497;
a = 121.2381;
σ = 3.0915;
χ = -8;
V = 0.83184;
Solve[2 σ (1/a) + 4/3 Pi χ (1/a)^3 == (ϕ1 * V), l]
Solve[2 σ (P/a) + 4/3 Pi χ (P/a)^3 == ϕ1, P]
```

iv) Temperature and pressure dependence of molecular parameters for the parallel interface model and the constant mean curvature model.

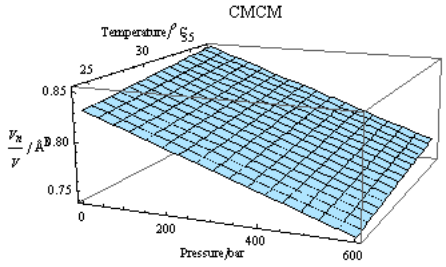
a)

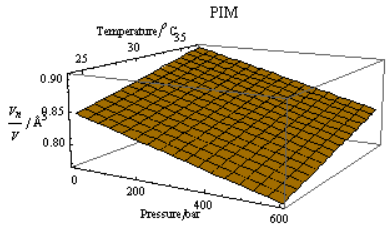


b)

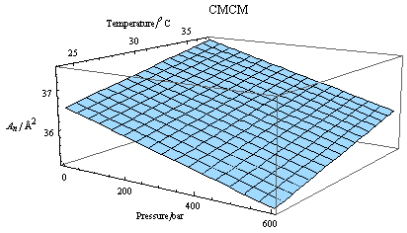


c)





d)



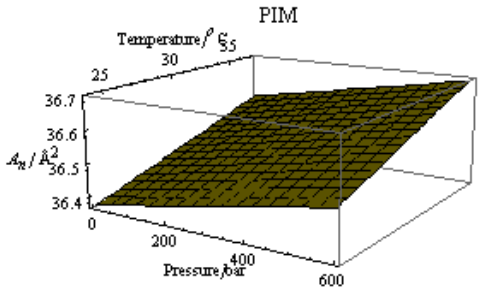


Figure B-3 a) Plots of lipid length as a function of pressure (1 bar to 600 bar) and temperature (24 °C to 37 °C) b) A_{HG} as a function of pressure (1 bar to 600 bar) and temperature (24 °C to 37 °C) c) $\frac{V_n}{V}$ as a function of pressure (1 bar to 600 bar) and temperature (24 °C to 37 °C) d) A_n as a function of pressure (1 bar to 600 bar) and temperature (24 °C to 37 °C) obtained from the CMCM and PIM models and experimental lattice parameter data obtained at ID02 and I22 beamlines at ESRF and DLS respectively.

v) Code and data used in Mathematica 7 for 3dplots of structural parameters Figure B-3

CMCM A_n:

```
data = {{1, 24, 35.75}, {200, 24, 35.1057}, {400, 24, 35.3734}, {1, 30, 36.96}, {200, 30, 36.10}, {400, 30, 36.40}, {600, 30, 36.84}, {200, 37, 35.8854},
   {400, 37, 35.9704}, {1, 25, 37.77}, {1, 30, 37.48}, {1, 35, 38.62}};

plane = Fit[data, {1, x, y}, {x, y}]

34.7527 - 0.00236988 x + 0.0756225 y

graph1 = Plot3D[plane, {x, 0, 600}, {y, 24, 37}, AxesLabel → {"Pressure/bar", "Temperature/°C", "A_n/ Å^2"}, PlotLabel → CMCM]
```

CMCM $\frac{V_n}{V}$:

```
data = {{1, 24, 0.8569}, {200, 24, 0.864}, {400, 24, 0.8337}, {600, 24, 0.571}, {1, 30, 0.85}, {200, 30, 0.85}, {400, 30, 0.83}, {600, 30, 0.8}, {1, 37, 0.771},
   {200, 37, 0.862}, {400, 37, 0.8374}, {600, 37, 0.733}, {1, 25, 0.776}, {1, 30, 0.837}, {1, 35, 0.814}};

plane = Fit[data, {1, x, y}, {x, y}]

0.789673 - 0.0001512 x + 0.00173157 y

graph2 = Plot3D[plane, {x, 0, 600}, {y, 24, 37}, AxesLabel → {"Pressure/bar", "Temperature/°C", "V_n/ V/ Å^3"}, PlotLabel → CMCM]
```

PIM A_n:

```
data = {{1, 24, 35.18}, {200, 24, 34.3534}, {400, 24, 35.0443}, {600, 24, 40.27}, {1, 30, 36.37}, {200, 30, 36.22}, {400, 30, 35.86}, {600, 30, 36.24}, {1, 37, 39.4037},
   {200, 37, 31.9544}, {400, 37, 37.1539}, {1, 25, 37.52}, {1, 30, 37.13}, {1, 35, 38.39}};

plane = Fit[data, {1, x, y}, {x, y}]

36.0278 + 0.000229063 x + 0.0144155 y

graph3 = Plot3D[plane, {x, 0, 600}, {y, 24, 37}, AxesLabel → {"Pressure/bar", "Temperature/°C", "A_n/ Å^2"}, PlotStyle → Orange, PlotLabel → PIM, PlotRange → Full]
```

PIM $\frac{V_n}{V}$:

```
data = {{1, 24, 0.8875771}, {200, 24, 0.8982138}, {400, 24, 0.8627257}, {600, 24, 0.6017239}, {1, 30, 0.88}, {200, 30, 0.86}, {400, 30, 0.86}, {600, 30, 0.83},
   {1, 37, 0.83540023}, {200, 37, 0.99079493}, {400, 37, 0.834287961}, {1, 25, 0.79}, {1, 30, 0.86}, {1, 35, 0.83}};

plane = Fit[data, {1, x, y}, {x, y}]

0.73859 - 0.000134471 x + 0.00451964 y

graph4 = Plot3D[plane, {x, 0, 600}, {y, 24, 37}, AxesLabel → {"Pressure/bar", "Temperature/°C", "V_n/ V/ Å^3"}, PlotStyle → Orange, PlotLabel → PIM, PlotRange → Full]
```

CMCM lipid length:

```
data = {{1, 24, 16.52006}, {200, 24, 16.5132}, {400, 24, 16.50334}, {600, 24, 16.654}, {1, 30, 16.38336}, {200, 30, 16.50095}, {400, 30, 16.4272}, {600, 30, 16.47618},
   {1, 37, 16.18458}, {200, 37, 16.47425}, {400, 37, 16.56856}, {600, 37, 16.397}};

plane = Fit[data, {1, x, y}, {x, y}]

16.7264 + 0.000221516 x - 0.0107493 y

graph5 = Plot3D[plane, {x, 0, 600}, {y, 24, 37}, AxesLabel → {"Pressure/bar", "Temperature/°C", "lipid length / Å"}, PlotLabel → CMCM]
```

CMCM A_{HG}:

```
data = {{1, 24, 31.13262}, {200, 24, 30.87465}, {400, 24, 30.38046}, {600, 24, 30.1797}, {1, 30, 32.2848}, {200, 30, 31.34265}, {400, 30, 30.89139}, {600, 30, 30.75025},
   {1, 37, 34.34322}, {200, 37, 30.77208}, {400, 37, 30.3584}, {600, 37, 31.05138}};

plane = Fit[data, {1, x, y}, {x, y}]

29.8506 - 0.00311857 x + 0.0752474 y

graph6 = Plot3D[plane, {x, 0, 600}, {y, 24, 37}, AxesLabel → {"Pressure/bar", "Temperature/°C", "A_HG / Å"}, PlotLabel → CMCM]
```

PIM lipid length:

```
data = {{1, 24, 16.51412}, {200, 24, 16.5045}, {400, 24, 16.49736}, {600, 24, 16.64643}, {1, 30, 16.54966}, {200, 30, 16.50098}, {400, 30, 16.42128}, {600, 30, 16.46885},
   {1, 37, 16.58525}, {200, 37, 16.25178}, {400, 37, 16.31472}, {600, 37, 16.39623}};

plane = Fit[data, {1, x, y}, {x, y}]

16.853 - 0.000072567 x - 0.0118769 y

graph7 = Plot3D[plane, {x, 0, 600}, {y, 24, 37}, AxesLabel → {"Pressure/bar", "Temperature/°C", "lipid length / Å"}, PlotStyle → Orange, PlotLabel → PIM, PlotRange → Full]
```

PIM A_{HG}:

```
data = {{1, 24, 31.1534}, {200, 24, 30.90221}, {400, 24, 30.40073}, {600, 24, 30.20383}, {1, 30, 31.91809}, {200, 30, 31.34257}, {400, 30, 30.91193}, {600, 30, 30.77527},
   {1, 37, 32.92051}, {200, 37, 31.58991}, {400, 37, 31.14656}, {600, 37, 31.05468}};

plane = Fit[data, {1, x, y}, {x, y}]

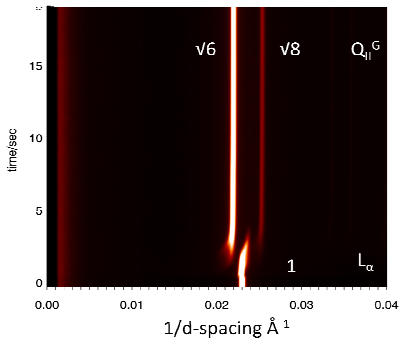
29.5063 - 0.00221096 x + 0.0775021 y

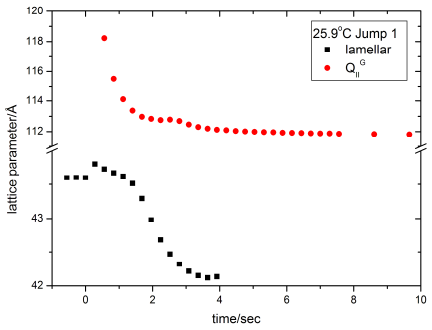
graph8 = Plot3D[plane, {x, 0, 600}, {y, 24, 37}, AxesLabel → {"Pressure/bar", "Temperature/°C", "A_HG / Å"}, PlotStyle → Orange, PlotLabel → PIM, PlotRange → Full]
```

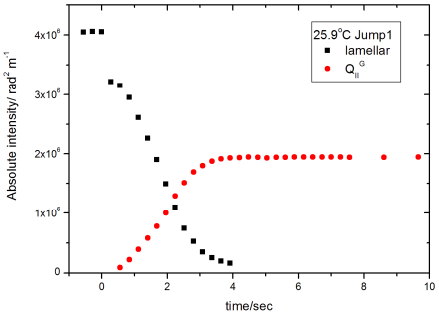
Appendix C

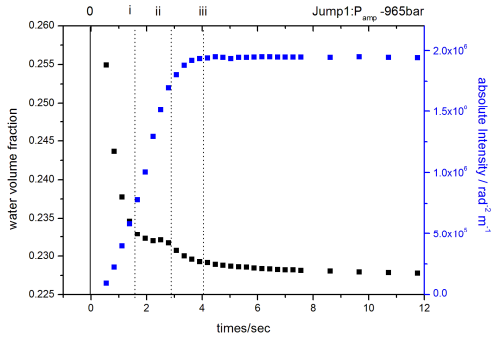
Experimental data for varying pressure jumps at 26 ^{o}C for a 22.1 wt% water ML sample for the lamellar to Q_{II}^{G} phase transition. The results show the stack plot (obtained from AXcess) for each jump, lattice parameter and absolute intensity data for the incoming (Q_{II}^{G}) and outgoing (lamellar) phases as well as the water content and absolute intensity change for the QIIG phase during the phase transition.

JUMP 1 : P_{amp} = -965 bar

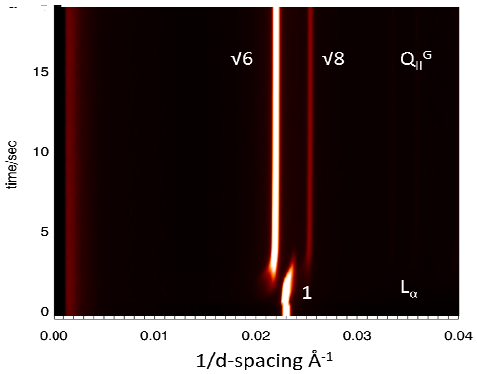


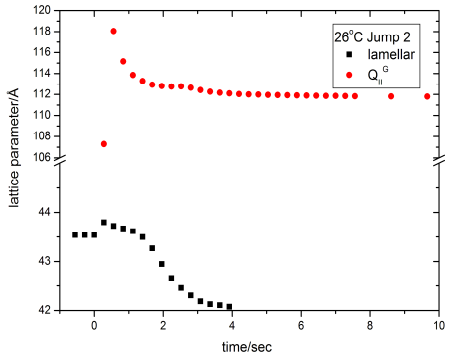


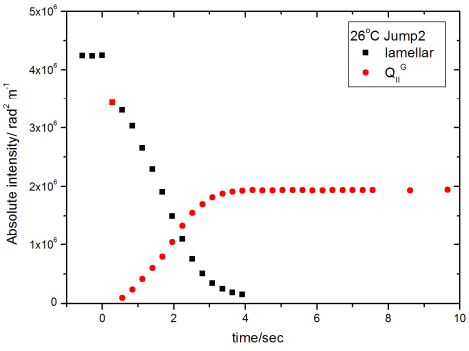


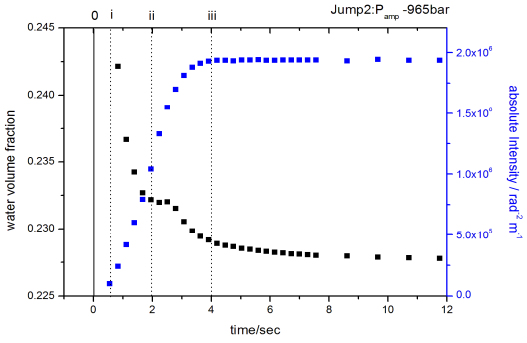


JUMP 2 : P_{amp} = -965 bar

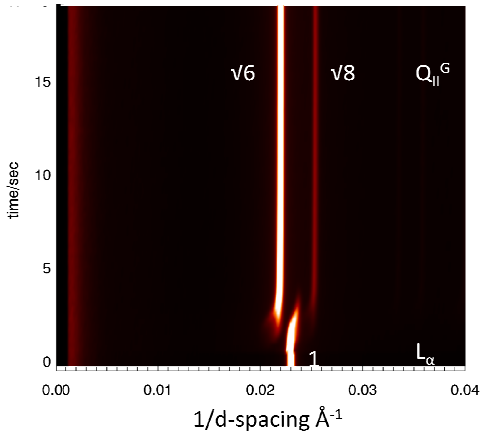


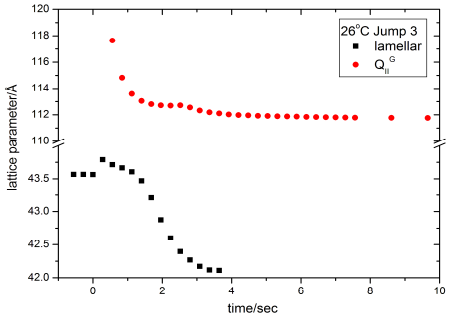


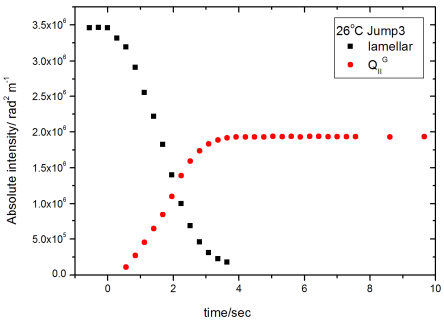


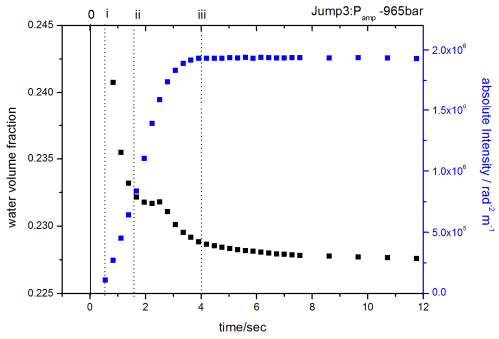


JUMP 3 : P_{amp} = -965 bar

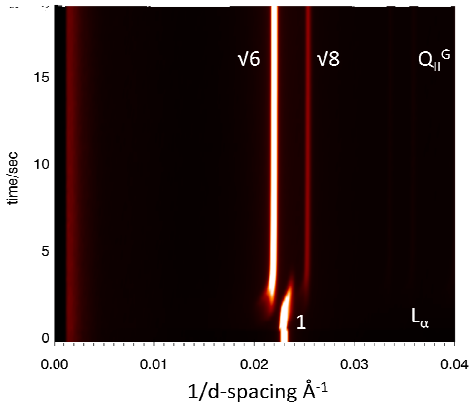


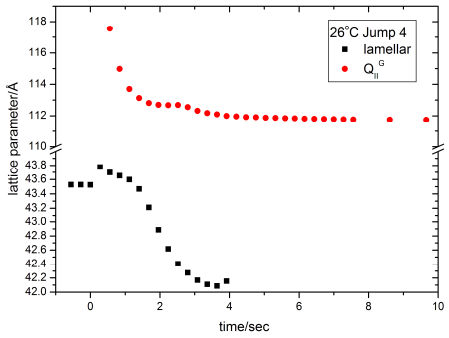


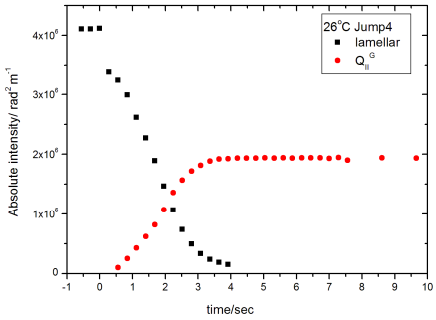


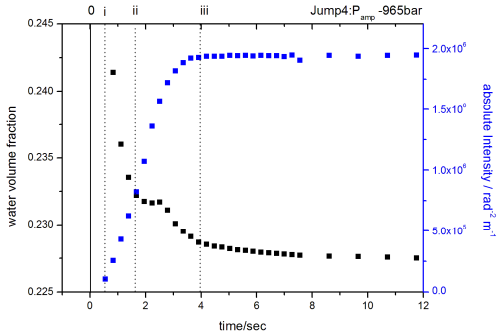


JUMP 4 : P_{amp} = -965 bar

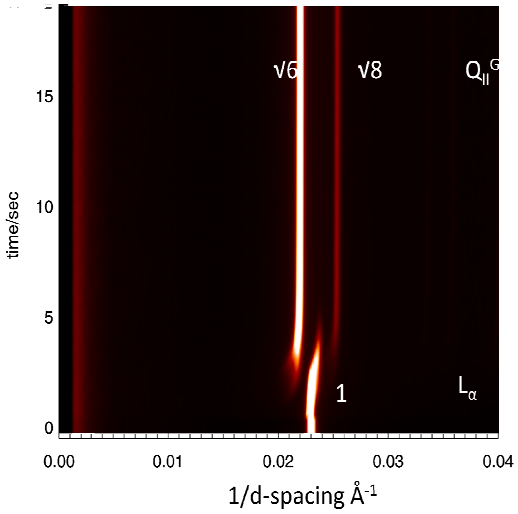


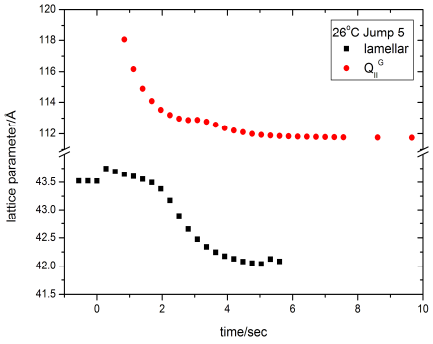


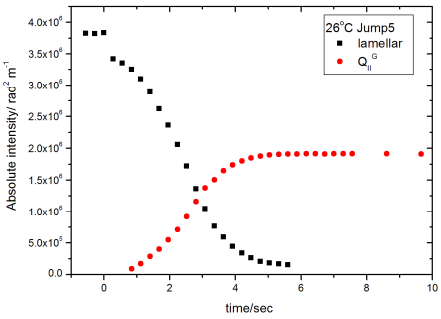


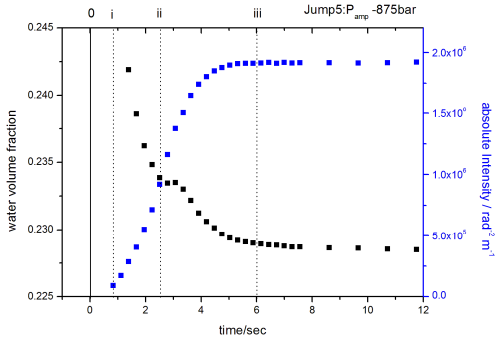


JUMP 5 : P_{amp} = -875 bar

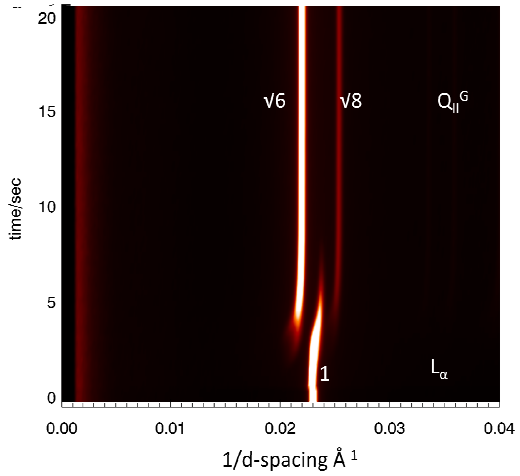


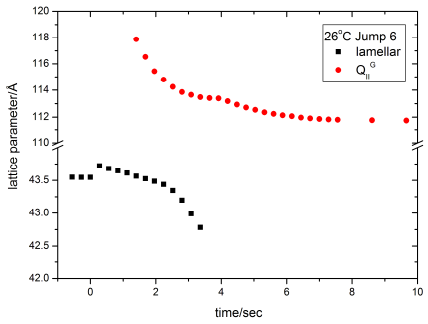


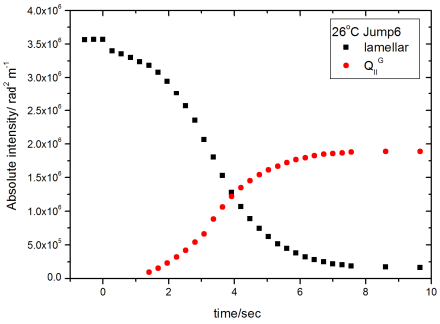


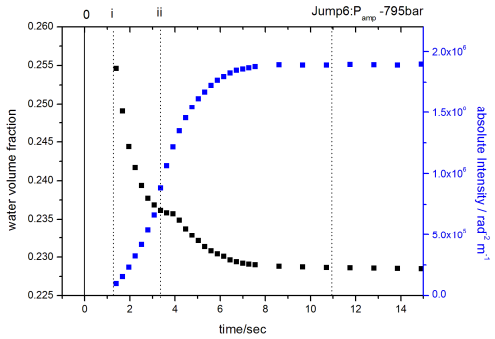


JUMP 6 : P_{amp} = -795 bar

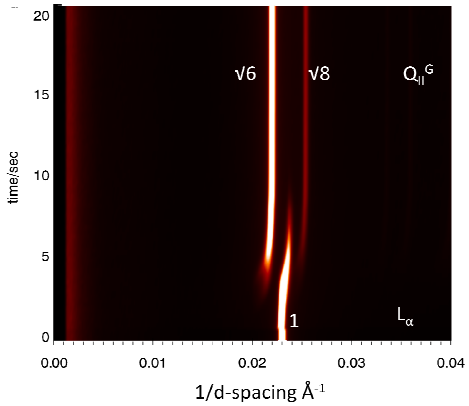


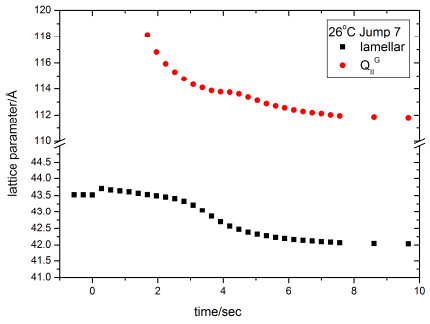


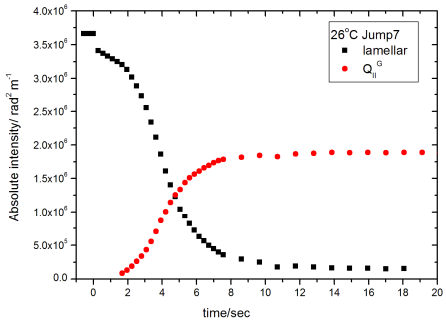


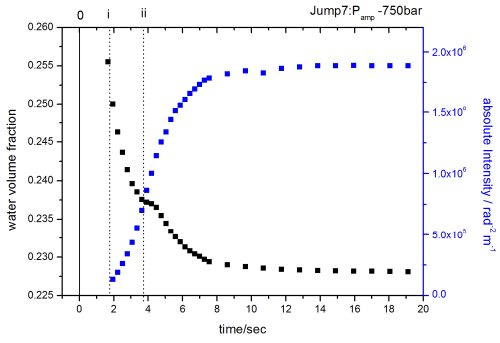


JUMP 7 : P_{amp} = -750 bar

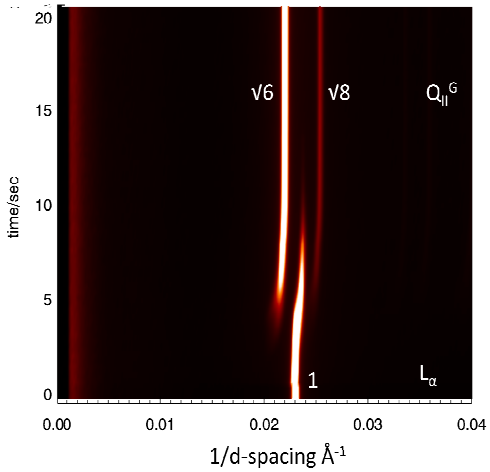


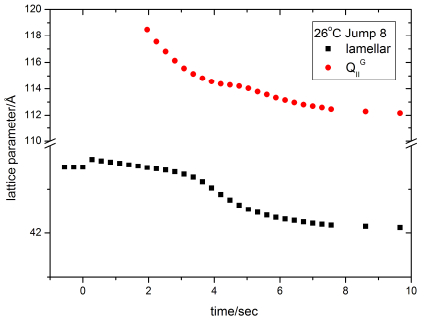


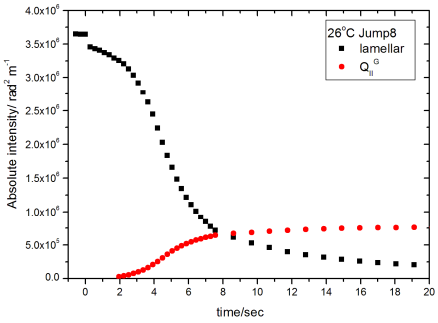


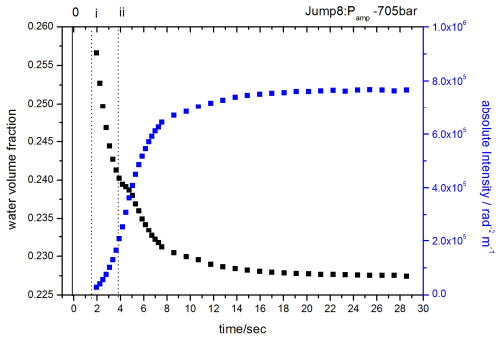


JUMP 8 : P_{amp} = -705 bar

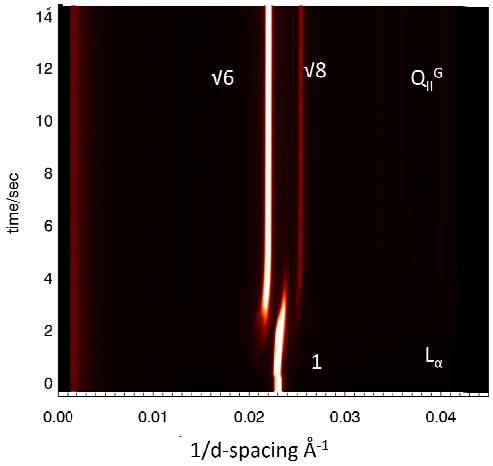


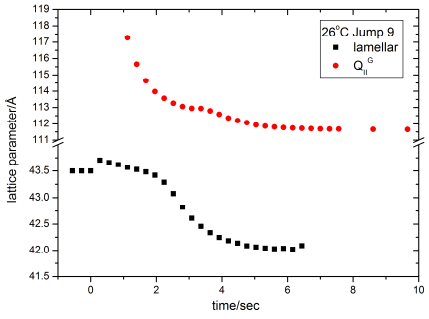


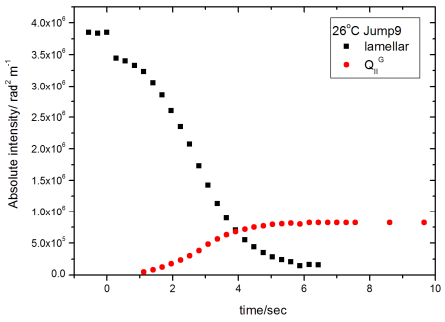


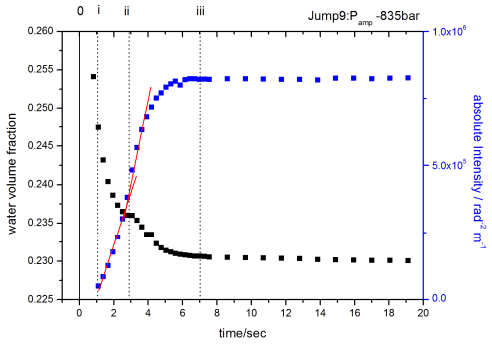


JUMP 9 : P_{amp} = -835 bar

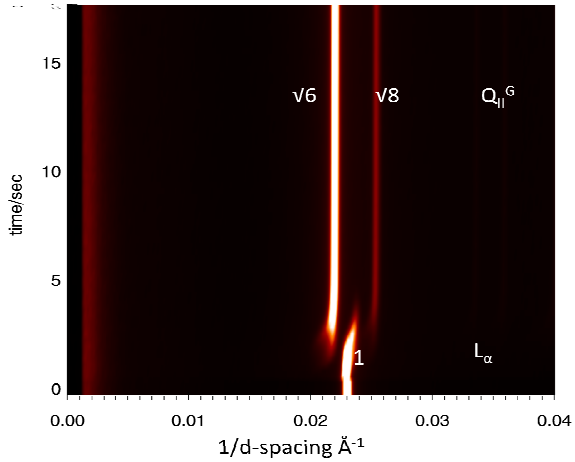


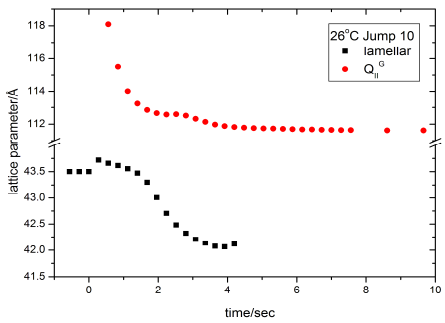


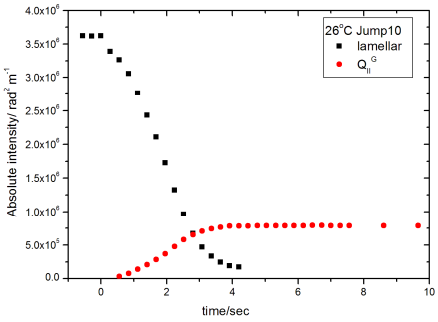


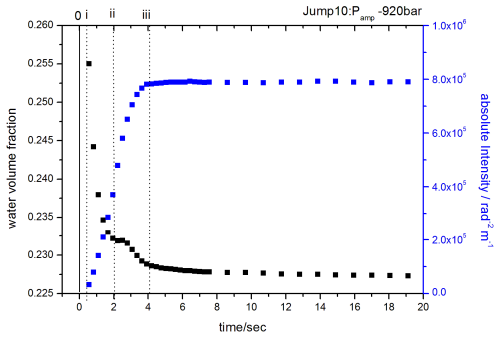


JUMP 10 : P_{amp} = -920 bar

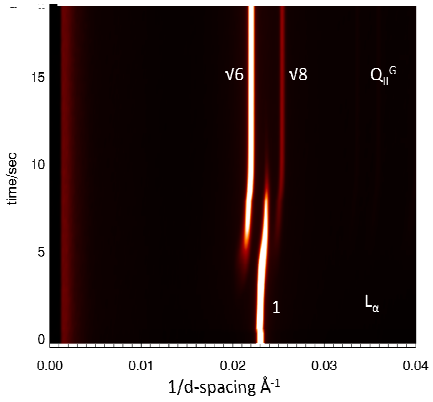


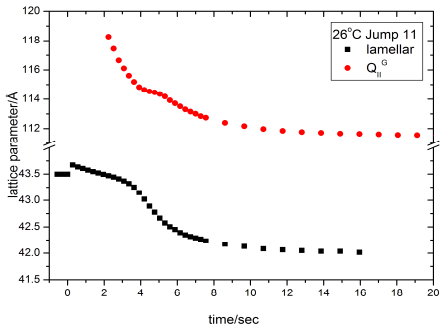


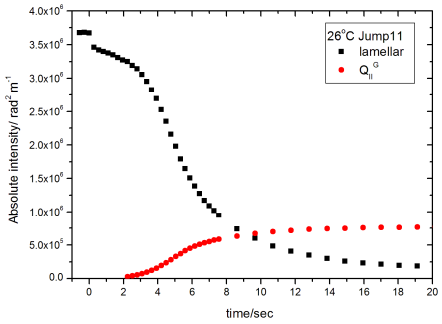


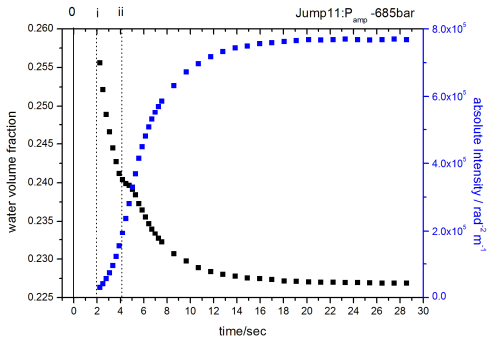


JUMP 11 : P_{amp} = -685 bar



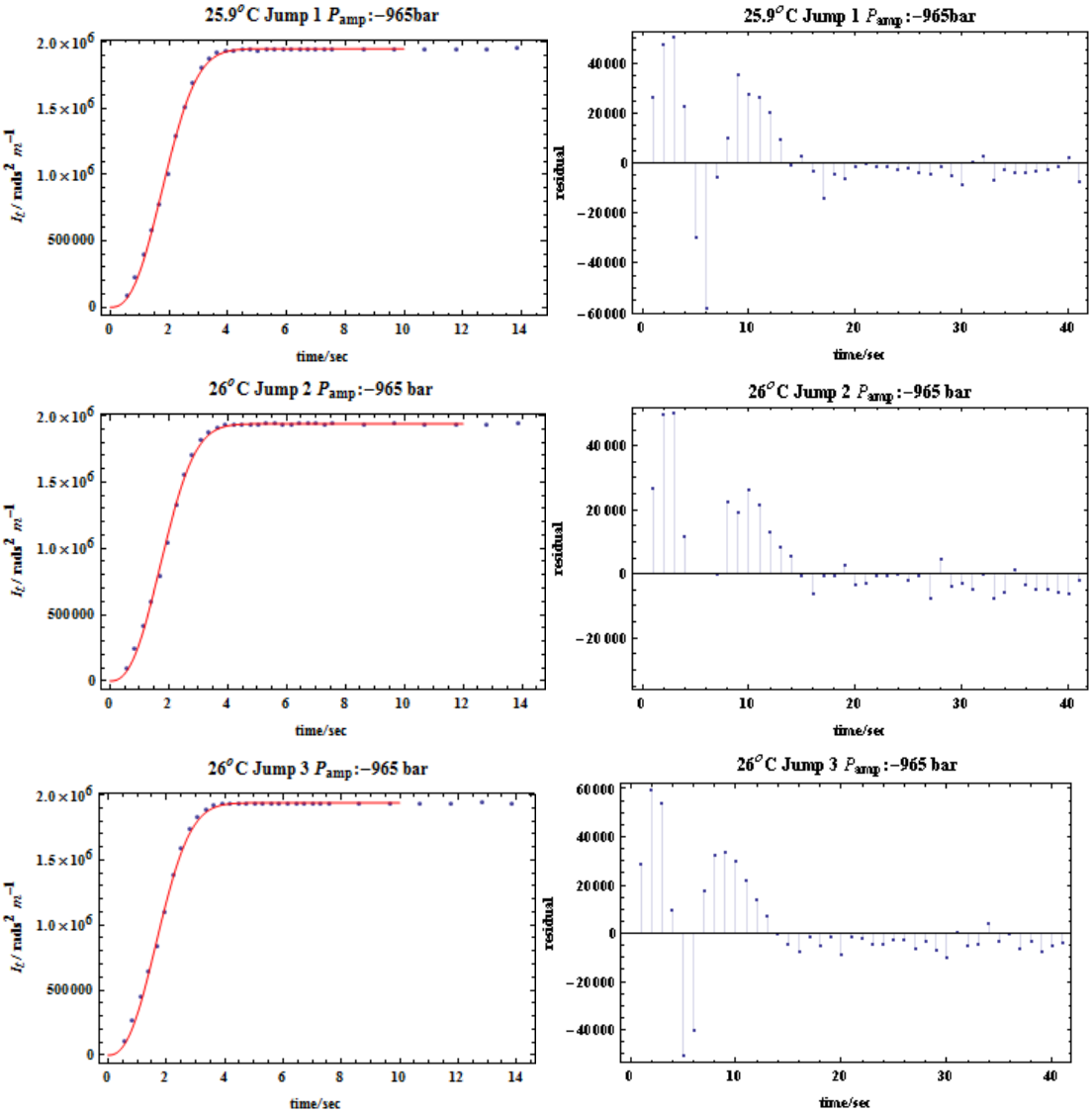


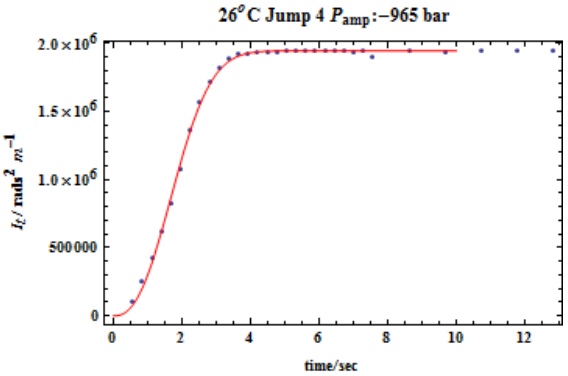


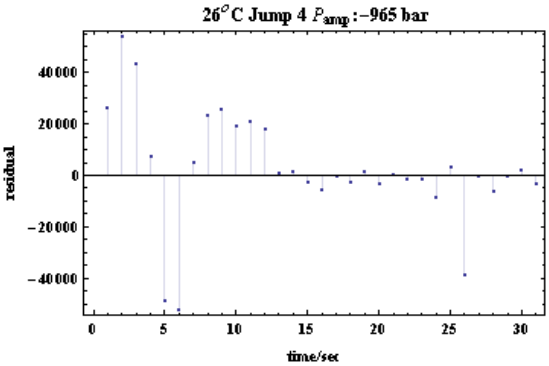


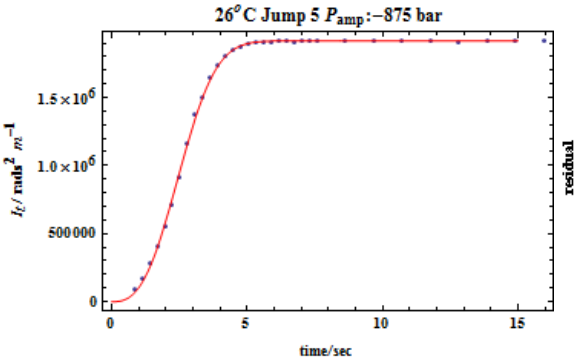
Appendix D

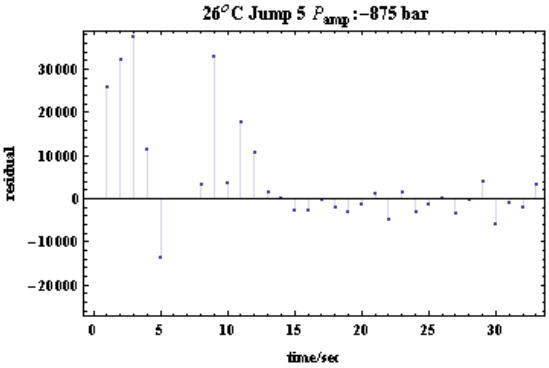
i) Avrami model fitting to kinetic data for Q_{II}^{G} phase growth at varying temperatures (please see specific graphs for experimental conditions.) for 22.1 wt% water.

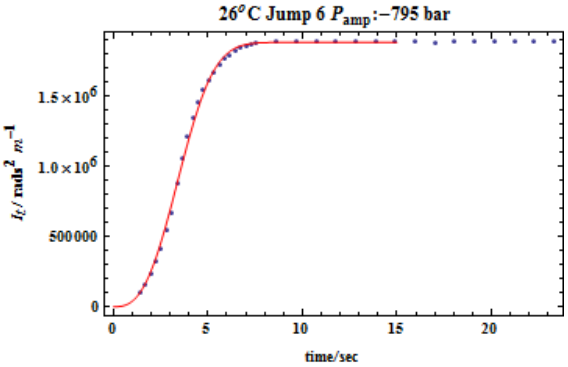


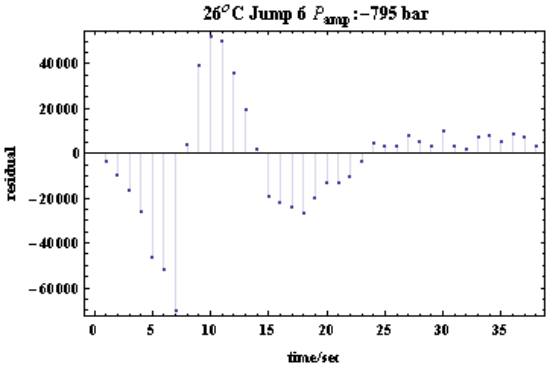

26°C Jump 4 P_{amp}:−965 bar
I_t/ rads^2 m^{-1}
time/sec

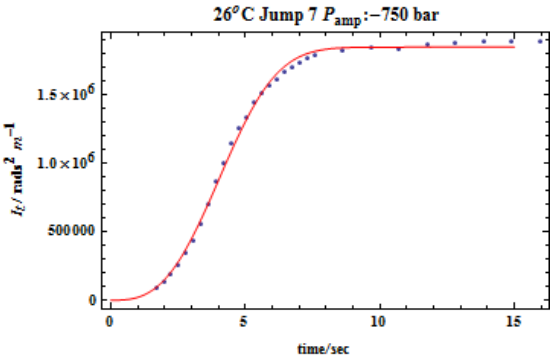

26°C Jump 4 P_{amp}:−965 bar
residual
time/sec

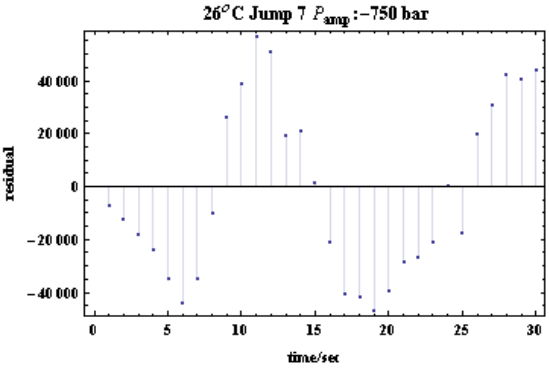

26°C Jump 5 P_{amp}:−875 bar
I_t/ rads^2 m^{-1}
time/sec


26°C Jump 5 P_{amp}:−875 bar
residual
time/sec


26°C Jump 6 P_{amp}:−795 bar
I_t/ rads^2 m^{-1}
time/sec


26°C Jump 6 P_{amp}:−795 bar
residual
time/sec


26°C Jump 7 P_{amp}:−750 bar
I_t/ rads^2 m^{-1}
time/sec


26°C Jump 7 P_{amp}:−750 bar
residual
time/sec

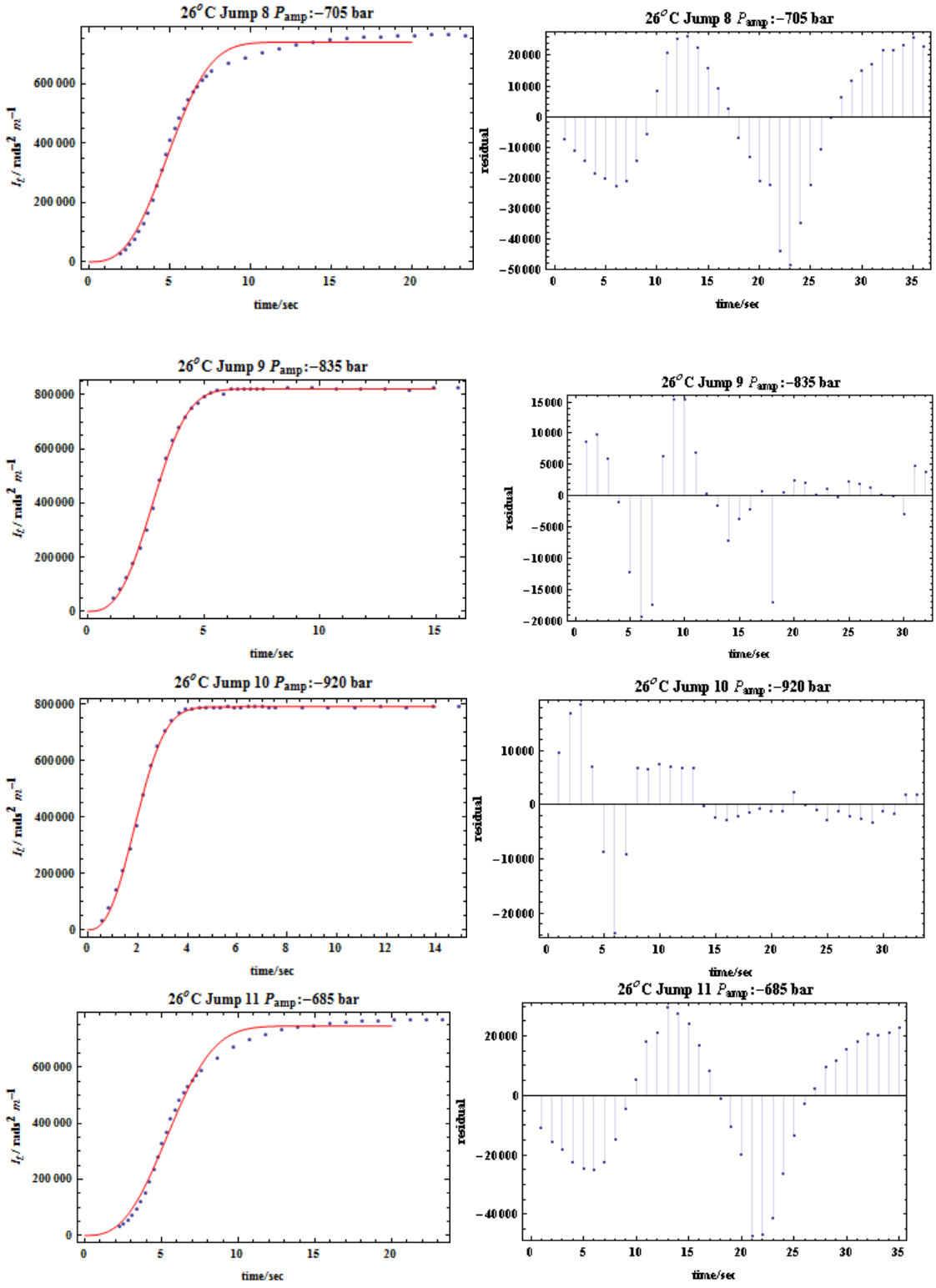
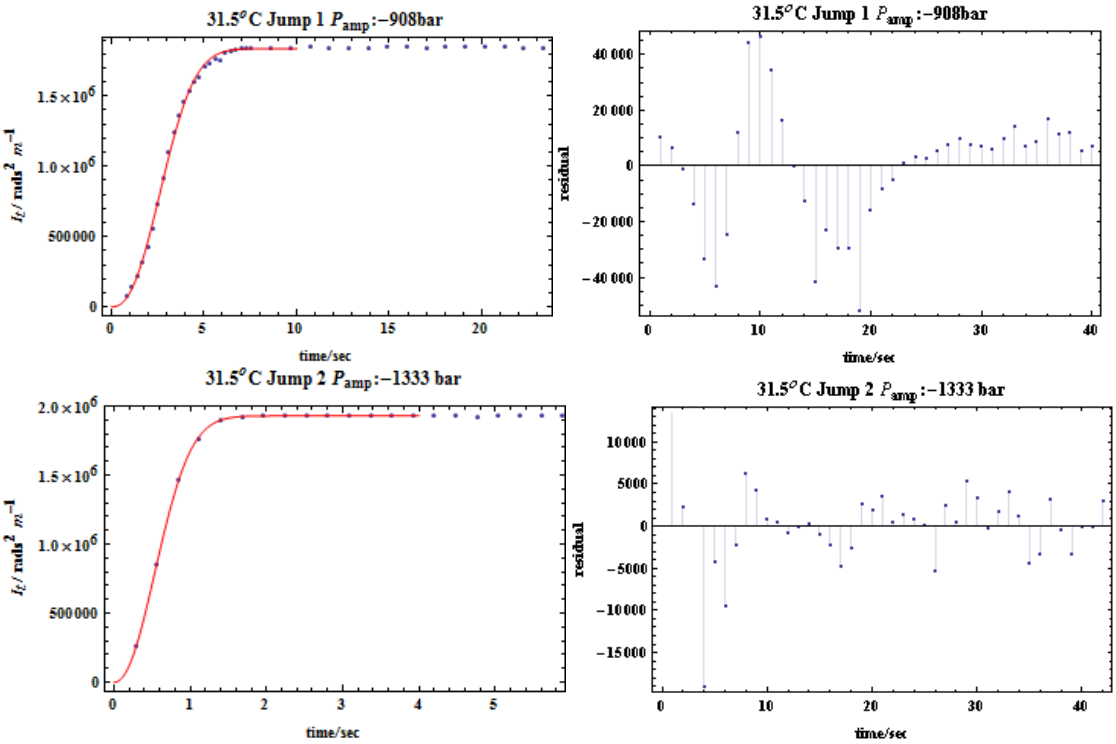
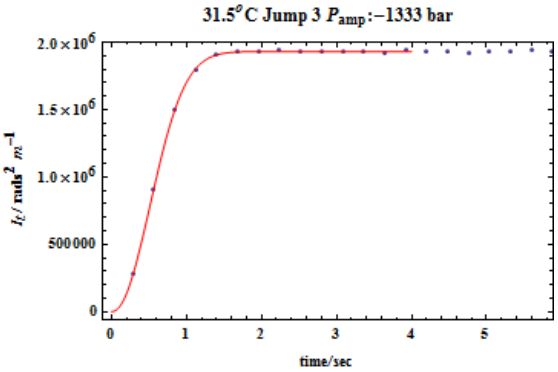


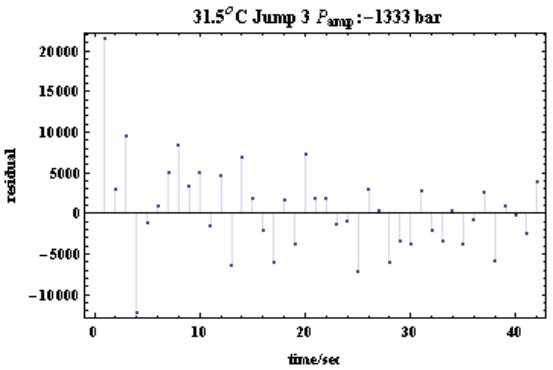
Figure D-1 Avrami model fits to experimental absolute intensities for varying pressure jump amplitudes at 26 °C for a 22.1 wt% water sample. The residuals from model fitting are shown on the right.

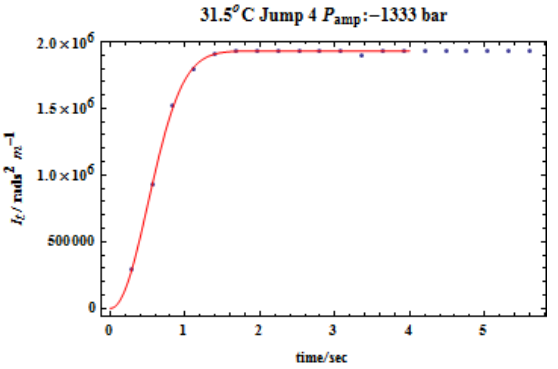
jump	P_{amp} / bar	k/ s^{-1}	error	n	error	R^2	ln k	error
1	-965	0.463	0.002	2.491	0.041	0.99989	-0.770	0.005
2	-965	0.474	0.003	2.464	0.048	0.999843	-0.747	0.006
3	-965	0.487	0.003	2.419	0.051	0.999826	-0.721	0.007
4	-965	0.480	0.003	2.436	0.049	0.99984	-0.733	0.006
5	-875	0.347	0.001	2.741	0.038	0.999901	-1.057	0.004
6	-795	0.252	0.001	2.836	0.055	0.999722	-1.376	0.006
7	-750	0.214	0.002	2.904	0.069	0.999481	-1.540	0.007
8	-835	0.177	0.002	2.850	0.103	0.998646	-1.728	0.010
9	-835	0.309	0.001	2.805	0.042	0.999869	-1.176	0.004
10	-920	0.440	0.002	2.516	0.041	0.999885	-0.821	0.005
11	-685	0.160	0.002	2.814	0.109	0.998345	-1.832	0.012

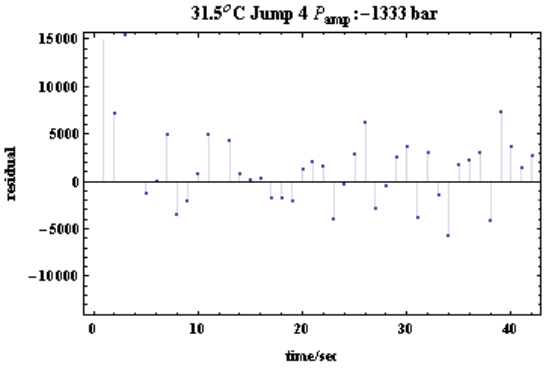
Table D-1 Summary of model fitting parameters obtained from experimental data fitting at 26 °C for Q_{II}^{G} phase growth at 22.1 wt% water sample. *k* is the rate constant, *n* is the dimensionality.

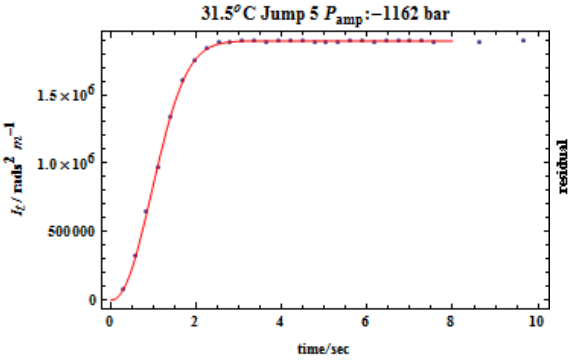


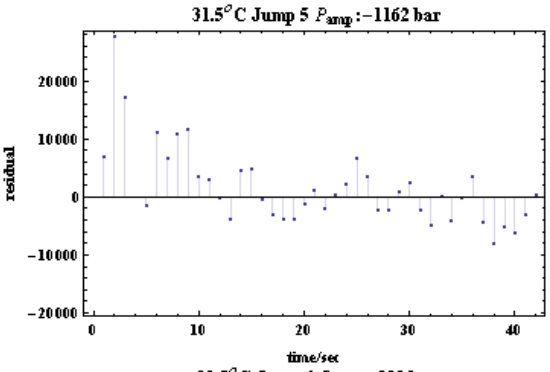

31.5°C Jump 3 P_{amp}:−1333 bar
I_E / rads^2 m^{-1}
time/sec

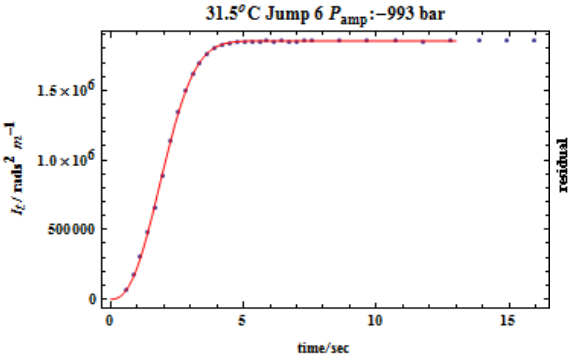

31.5°C Jump 3 P_{amp}:−1333 bar
residual
time/sec

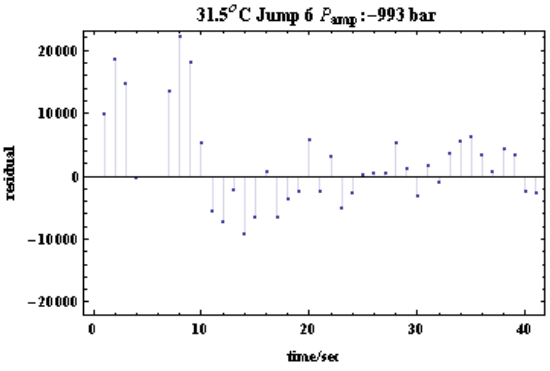

31.5°C Jump 4 P_{amp}:−1333 bar
I_E / rads^2 m^{-1}
time/sec

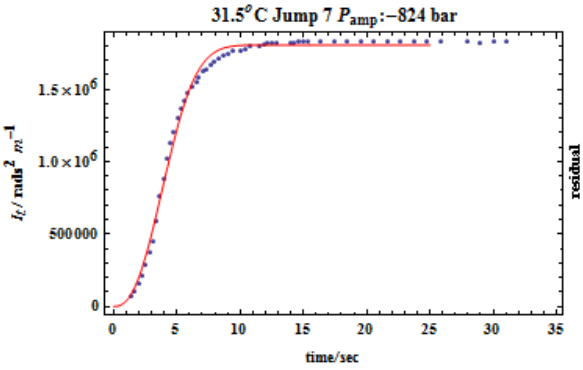

31.5°C Jump 4 P_{amp}:−1333 bar
residual
time/sec

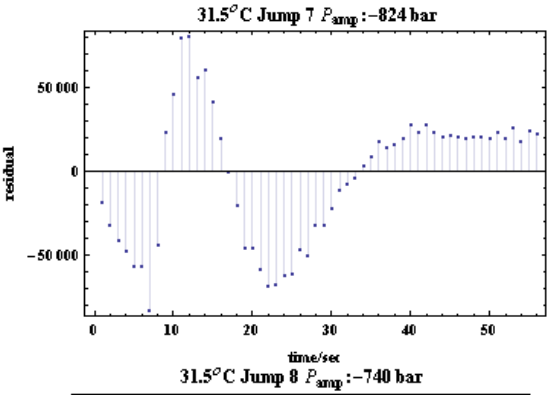

31.5°C Jump 5 P_{amp}:−1162 bar
I_E / rads^2 m^{-1}
time/sec

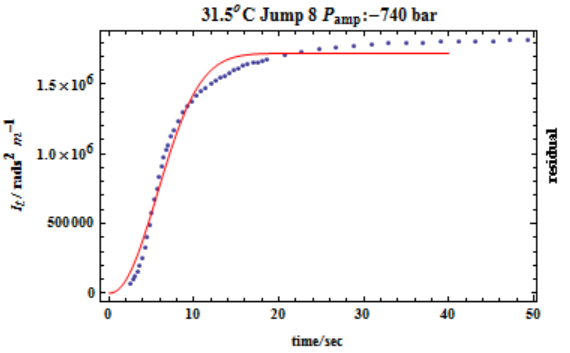

31.5°C Jump 5 P_{amp}:−1162 bar
residual
time/sec

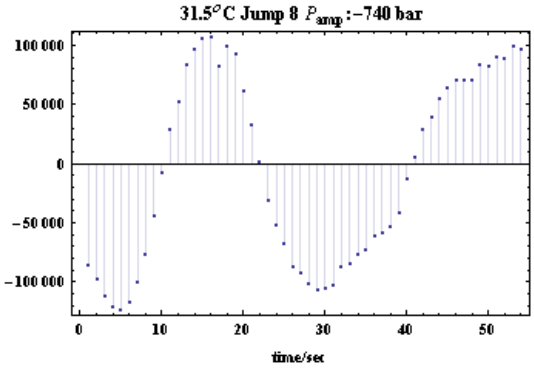

31.5°C Jump 6 P_{amp}:−993 bar
I_E / rads^2 m^{-1}
time/sec

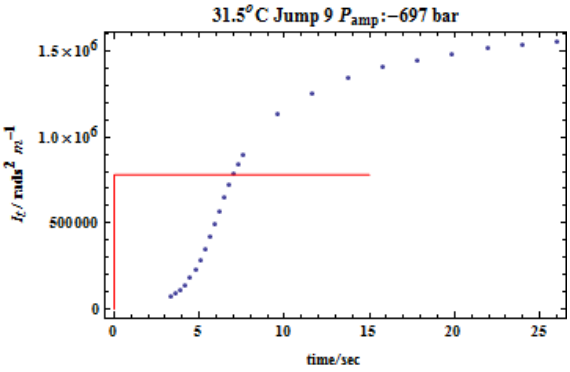

31.5°C Jump 6 P_{amp}:−993 bar
residual
time/sec

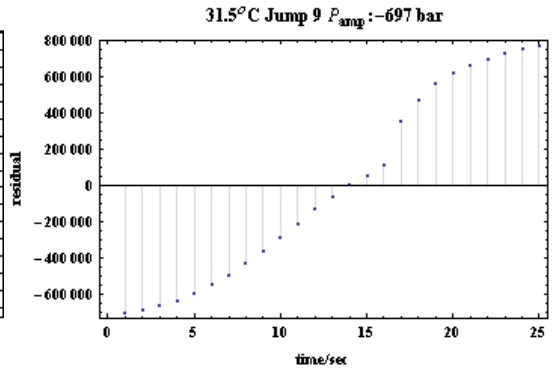

31.5°C Jump 7 P_{amp}:−824 bar
I_t / rads^2 m^{-1}
time/sec

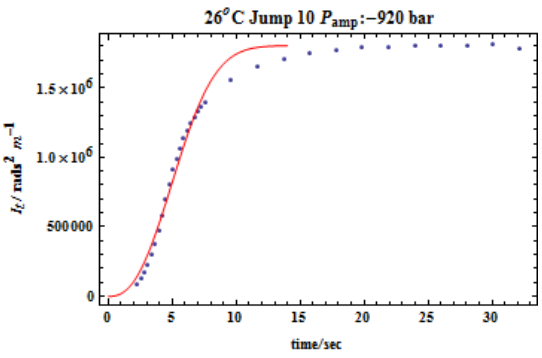

31.5°C Jump 7 P_{amp}:−824 bar
residual
time/sec

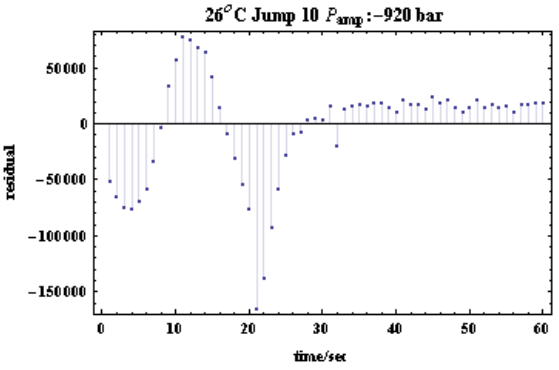

31.5°C Jump 8 P_{amp}:−740 bar
I_t / rads^2 m^{-1}
time/sec


31.5°C Jump 8 P_{amp}:−740 bar
residual
time/sec


31.5°C Jump 9 P_{amp}:−697 bar
I_t / rads^2 m^{-1}
time/sec


31.5°C Jump 9 P_{amp}:−697 bar
residual
time/sec


26°C Jump 10 P_{amp}:−920 bar
I_t / rads^2 m^{-1}
time/sec


26°C Jump 10 P_{amp}:−920 bar
residual
time/sec

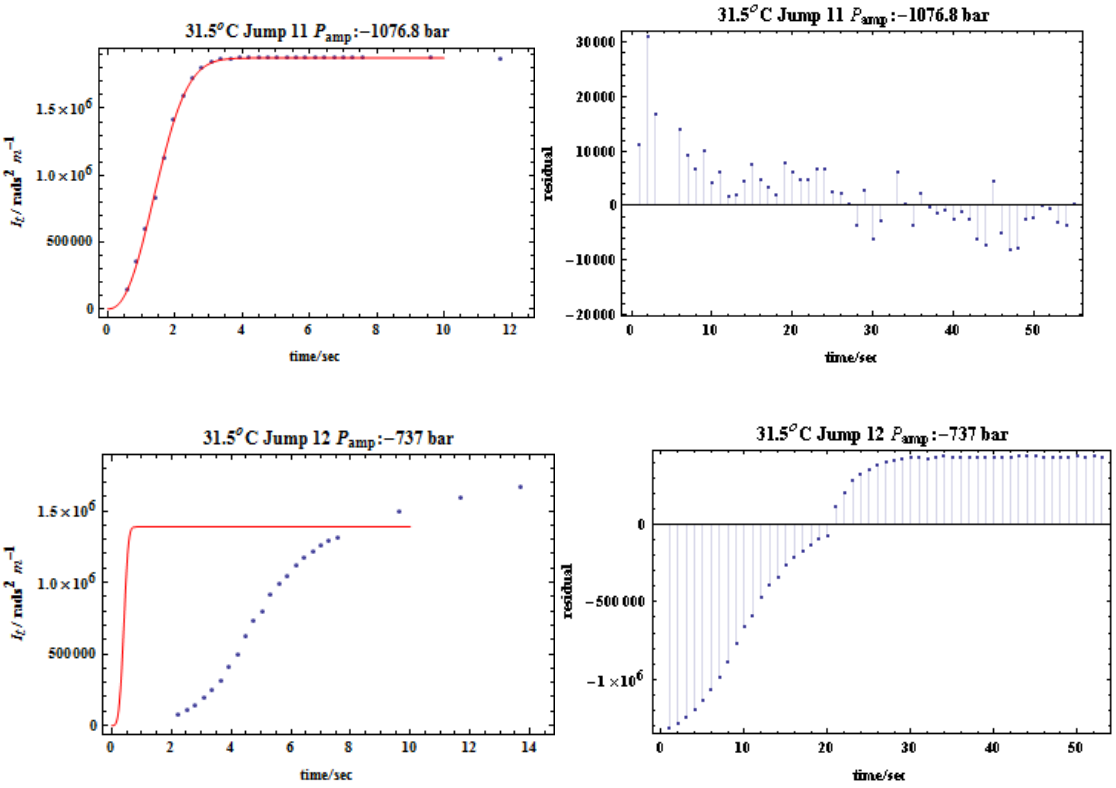
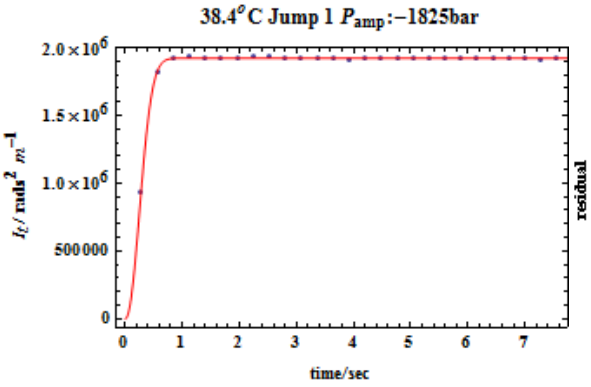
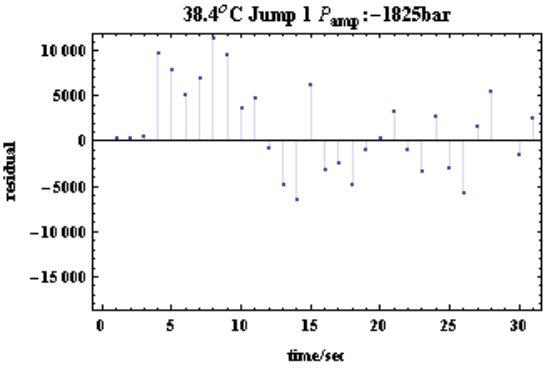


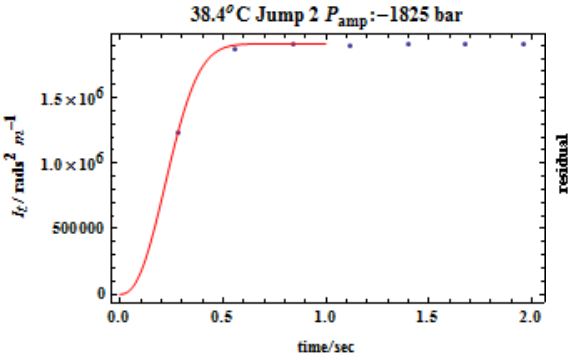
Figure D-2 Avrami model fits to experimental absolute intensities for varying pressure jump amplitudes at 31.5 °C for a 22.1 wt% water sample. The residuals from model fitting are shown on the right.

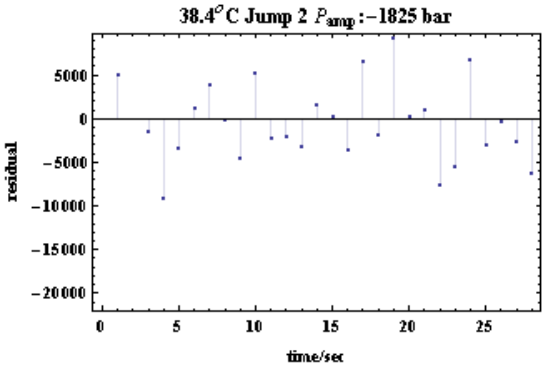
jump	P_{amp} / bar	k s^{-1}	error	n	error	R^2	ln k	error
1	-908	0.305	0.002	2.415	0.040	0.999817	-1.188	0.005
2	-1333	1.390	0.004	2.140	0.018	0.999991	0.329	0.003
3	-1333	1.435	0.004	2.104	0.017	0.999991	0.361	0.003
4	-1333	1.455	0.005	2.094	0.023	0.999984	0.375	0.004
5	-1162	0.788	0.003	2.179	0.023	0.999973	-0.238	0.004
6	-993	0.435	0.001	2.423	0.022	0.999963	-0.833	0.003
7	-824	0.210	0.002	2.454	0.064	0.999361	-1.558	0.008
8	-740	0.132	0.003	2.134	0.106	0.996707	-2.029	0.019
9	-697	-	-	-	-	-	-	-
10	-780	0.164	0.002	2.479	0.084	0.999098	-1.810	0.010
11	-1076.8	0.583	0.002	2.352	0.024	0.999966	-0.539	0.003
12	-737	-	-	-	-	-	-	-

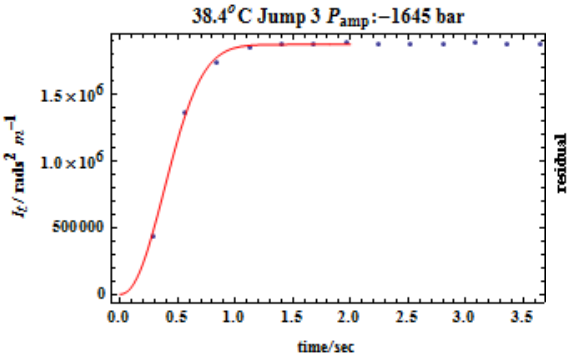
Table D-2 Summary of Avrami model fitting parameters obtained from experimental data fitting at 31.5 °C for Q_{II}^{G} phase growth at 22.1 wt% water sample. k is the rate constant, n is the dimensionality.

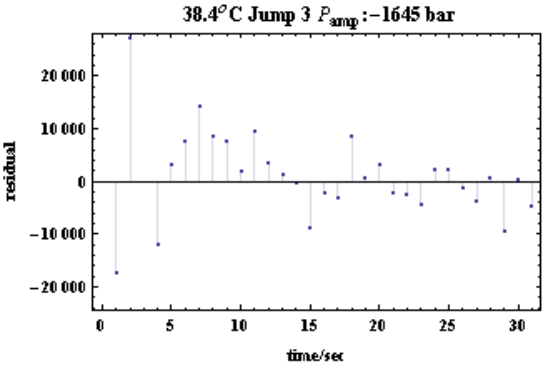

38.4°C Jump 1 P_{amp}:−1825bar
I_E/ rads^2 m^{-1}
time/sec

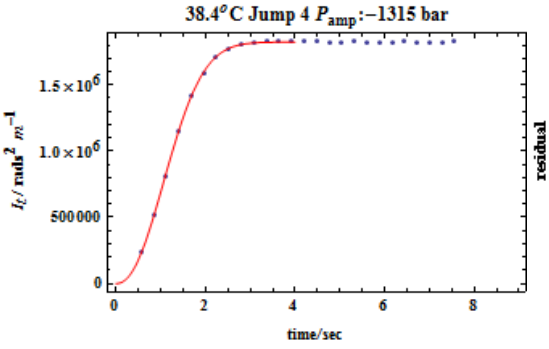

38.4°C Jump 1 P_{amp}:−1825bar
residual
time/sec

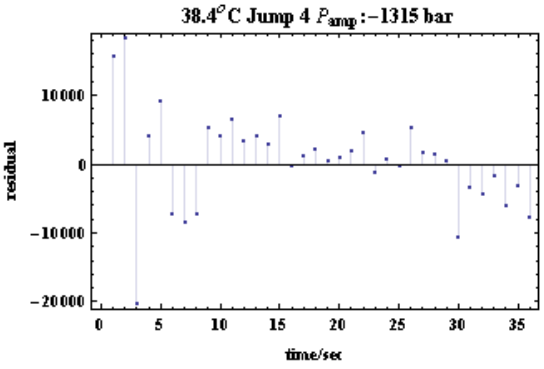

38.4°C Jump 2 P_{amp}:−1825 bar
I_E/ rads^2 m^{-1}
time/sec

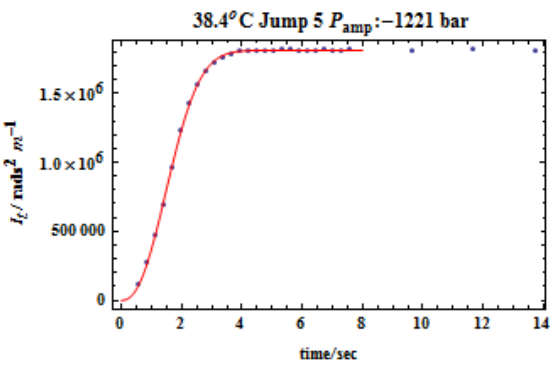

38.4°C Jump 2 P_{amp}:−1825 bar
residual
time/sec

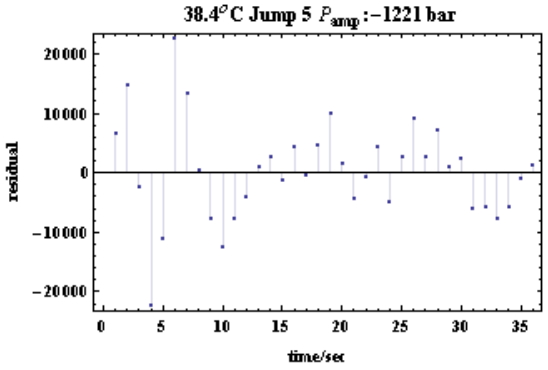

38.4°C Jump 3 P_{amp}:−1645 bar
I_E/ rads^2 m^{-1}
time/sec

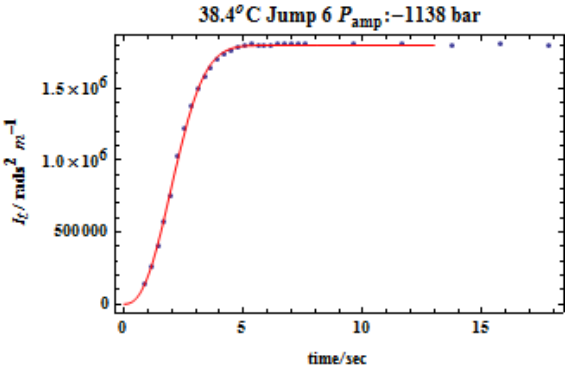

38.4°C Jump 3 P_{amp}:−1645 bar
residual
time/sec

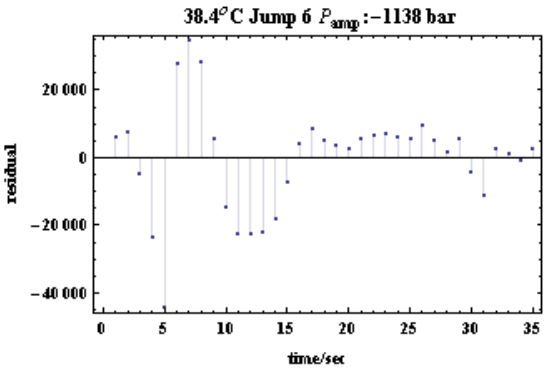

38.4°C Jump 4 P_{amp}:−1315 bar
I_E/ rads^2 m^{-1}
time/sec

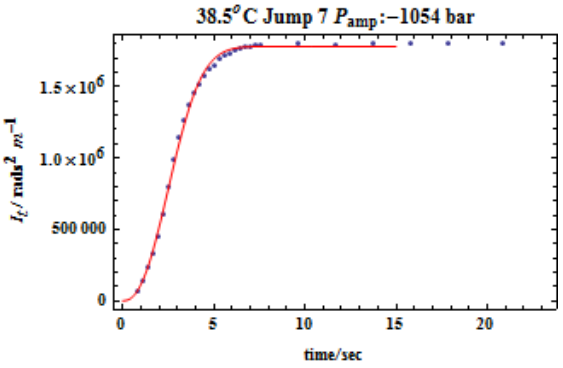

38.4°C Jump 4 P_{amp}:−1315 bar
residual
time/sec

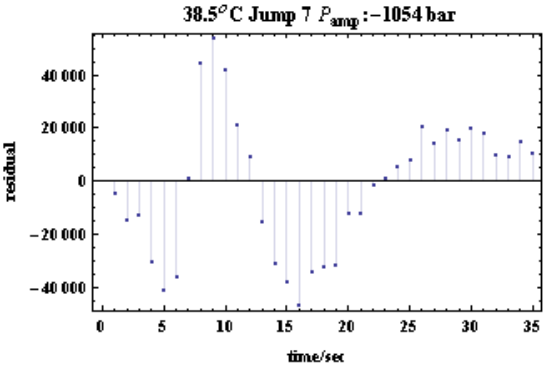

38.4°C Jump 5 P_{amp}:−1221 bar
I_t/ rads^2 m^{-1}
time/sec

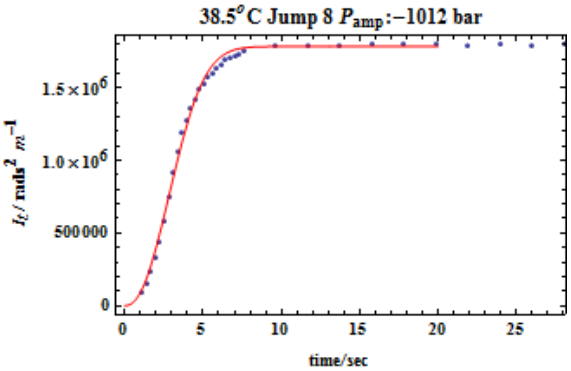

38.4°C Jump 5 P_{amp}:−1221 bar
residual
time/sec

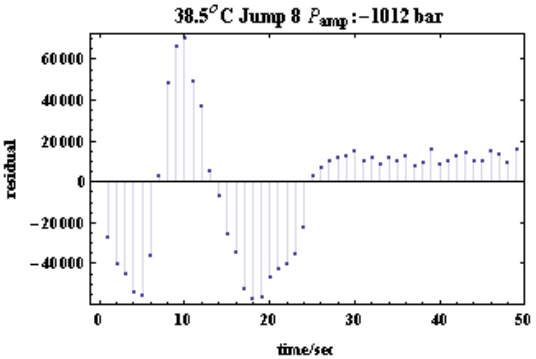

38.4°C Jump 6 P_{amp}:−1138 bar
I_t/ rads^2 m^{-1}
time/sec


38.4°C Jump 6 P_{amp}:−1138 bar
residual
time/sec


38.5°C Jump 7 P_{amp}:−1054 bar
I_t/ rads^2 m^{-1}
time/sec


38.5°C Jump 7 P_{amp}:−1054 bar
residual
time/sec


38.5°C Jump 8 P_{amp}:−1012 bar
I_t/ rads^2 m^{-1}
time/sec


38.5°C Jump 8 P_{amp}:−1012 bar
residual
time/sec

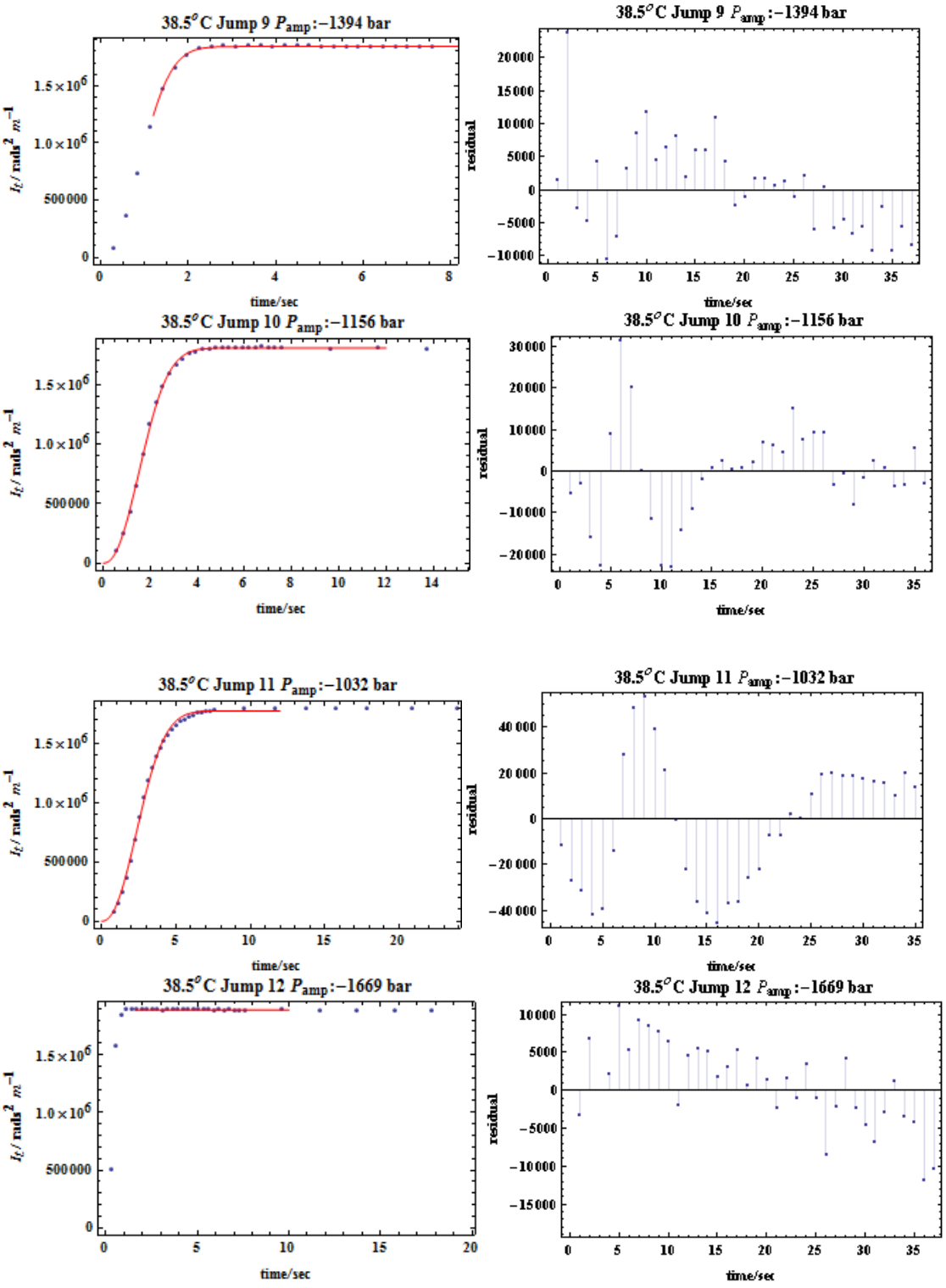
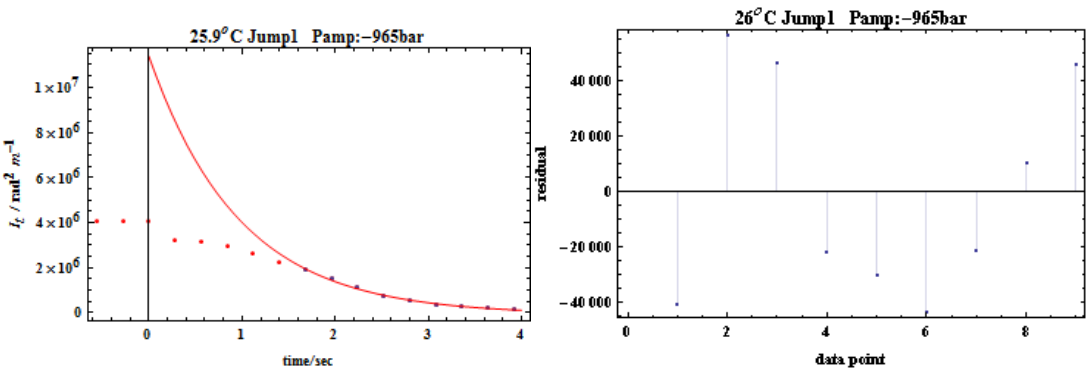


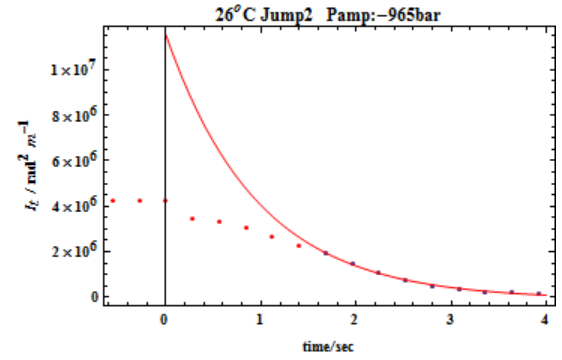
Figure D-3 Avrami model fits to experimental absolute intensities for varying pressure jump amplitudes at 38.5 °C for a 22.1 wt% water sample. The residuals from model fitting are shown on the right.

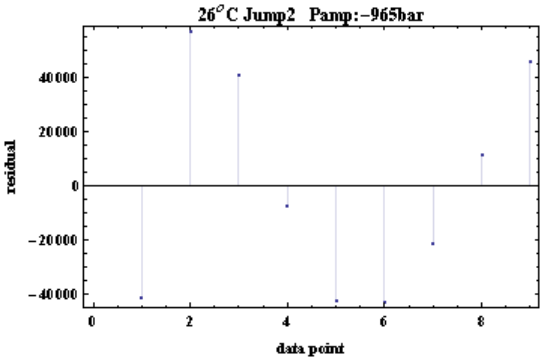
Jump	P_{amp}/bar	k/ s^{-1}	error	n	error	R^2	ln k	error
1	-1825	2.954	0.020	2.141	0.053	0.999975	1.083	0.007
2	-1825	3.615	0.018	2.355	0.228	0.999991	1.285	0.005
3	-1645	1.969	0.013	2.166	0.040	0.999966	0.678	0.006
4	-1315	0.714	0.002	2.202	0.018	0.999983	-0.337	0.003
5	-1221	0.533	0.001	2.324	0.019	0.999976	-0.630	0.003
6	-1138	0.409	0.002	2.421	0.034	0.999909	-0.893	0.004
7	-1054	0.318	0.002	2.370	0.049	0.999722	-1.147	0.007
8	-1012	0.272	0.002	2.276	0.053	0.999596	-1.300	0.008
9	-1394	0.880	0.002	2.215	0.0191	0.999984	-0.128	0.003
10	-1156	0.507	0.002	2.231	0.0244	0.999954	-0.678	0.004
11	-1032	0.327	0.003	2.247	0.051	0.999675	-1.117	0.008
12	-1669	2.254	0.011	2.490	0.034	0.999982	0.813	0.005

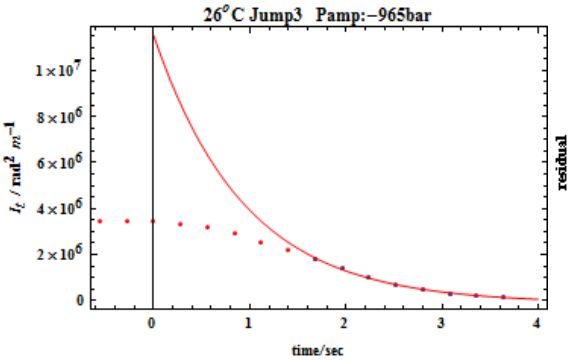
Table D-3 Summary of Avrami model fitting parameters obtained from experimental data fitting at 38.5 °C for Q_{II}^{G} phase growth at 22.1 wt% water sample. k is the rate constant, n is the dimensionality.

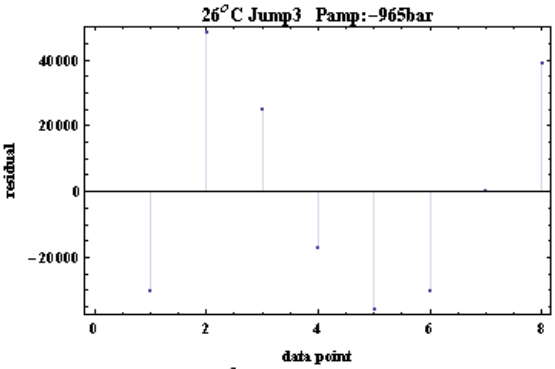
ii) Exponential model fitting to kinetic data for lamellar phase decay at varying temperatures(please see specific graphs for experimental conditions.) for 22.1 wt% water.

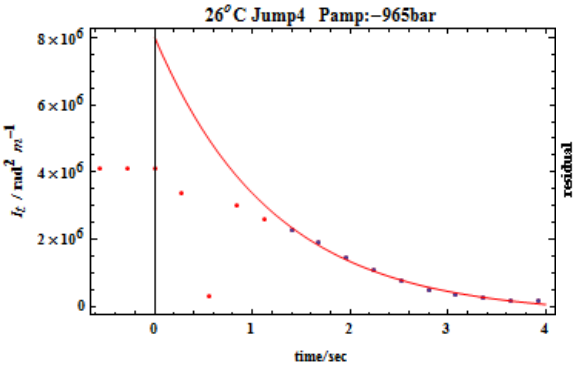


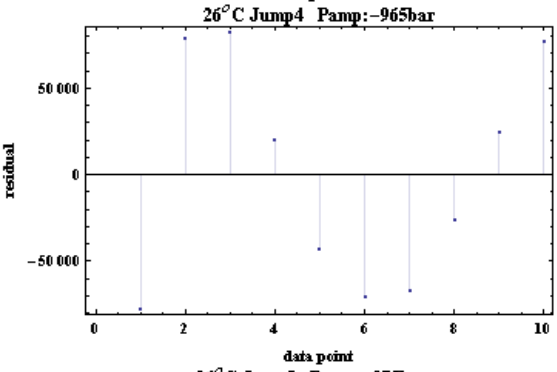

26°C Jump2 Pamp:−965bar
I_t / rad^2 m^{-1}
time/sec

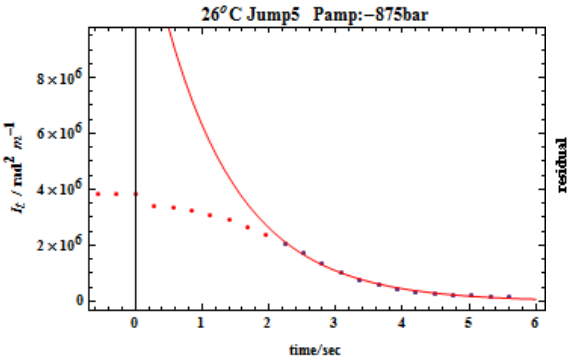

26°C Jump2 Pamp:−965bar
residual
data point

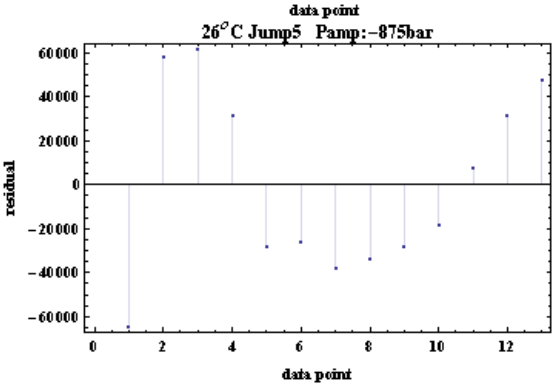

26°C Jump3 Pamp:−965bar
I_t / rad^2 m^{-1}
time/sec

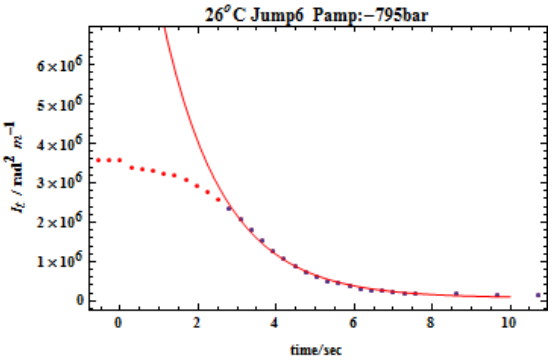

26°C Jump3 Pamp:−965bar
residual
data point

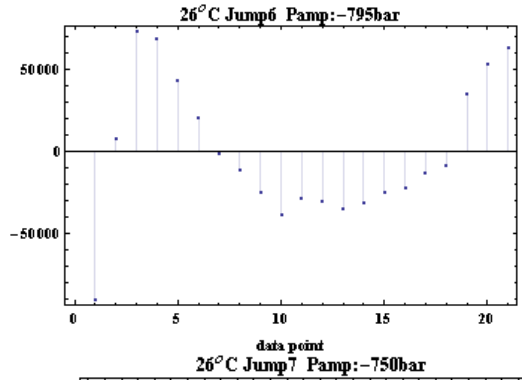

26°C Jump4 Pamp:−965bar
I_t / rad^2 m^{-1}
time/sec

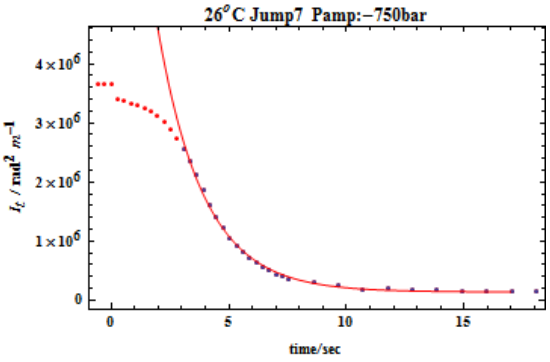

26°C Jump4 Pamp:−965bar
residual
data point

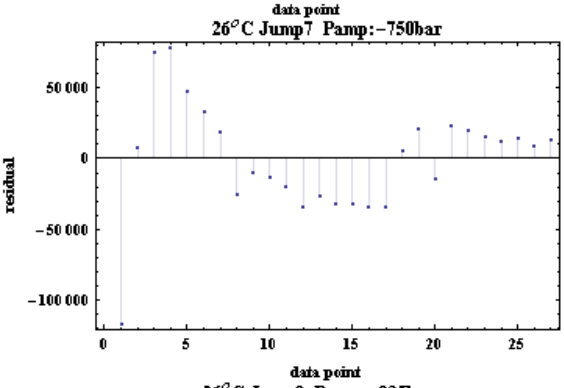

26°C Jump5 Pamp:−875bar
I_t / rad^2 m^{-1}
time/sec

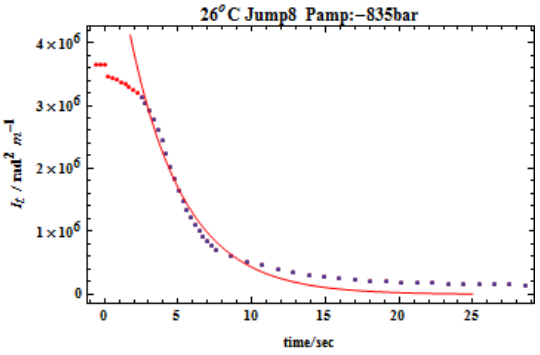

26°C Jump5 Pamp:−875bar
residual
data point

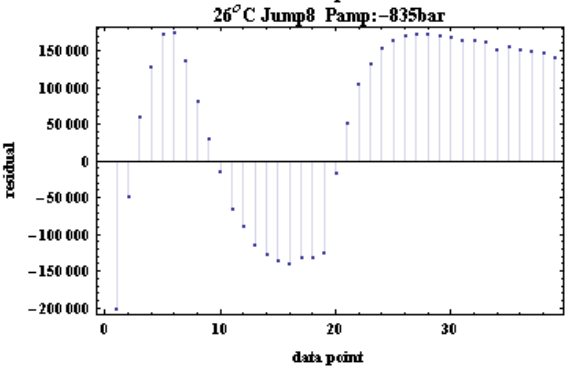

26°C Jump6 Pamp:−795bar
I_t / rad^2 m^{-1}
time/sec


26°C Jump6 Pamp:−795bar
residual
data point


26°C Jump7 Pamp:−750bar
I_t / rad^2 m^{-1}
time/sec


26°C Jump7 Pamp:−750bar
residual
data point


26°C Jump8 Pamp:−835bar
I_t / rad^2 m^{-1}
time/sec


26°C Jump8 Pamp:−835bar
residual
data point

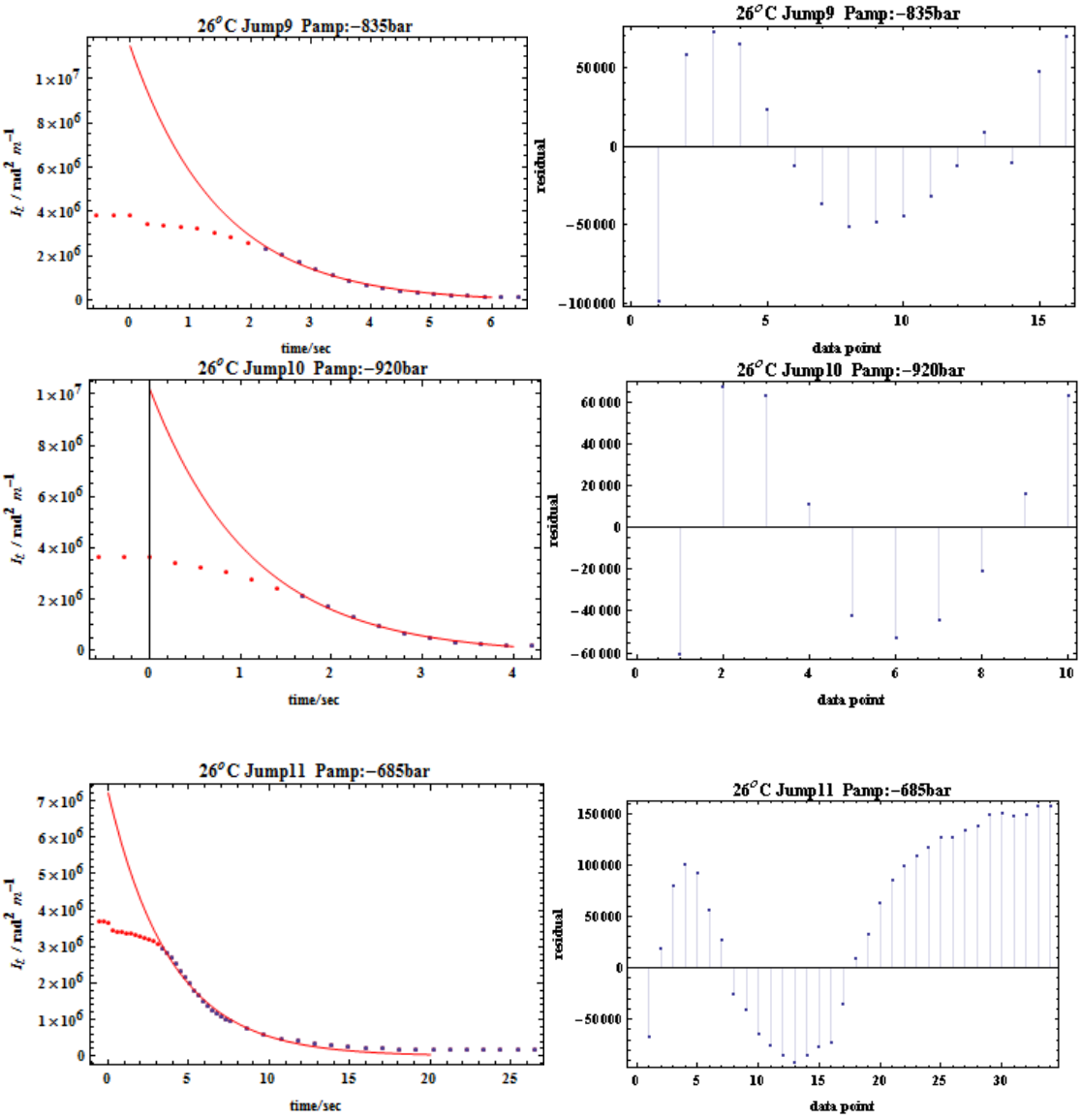
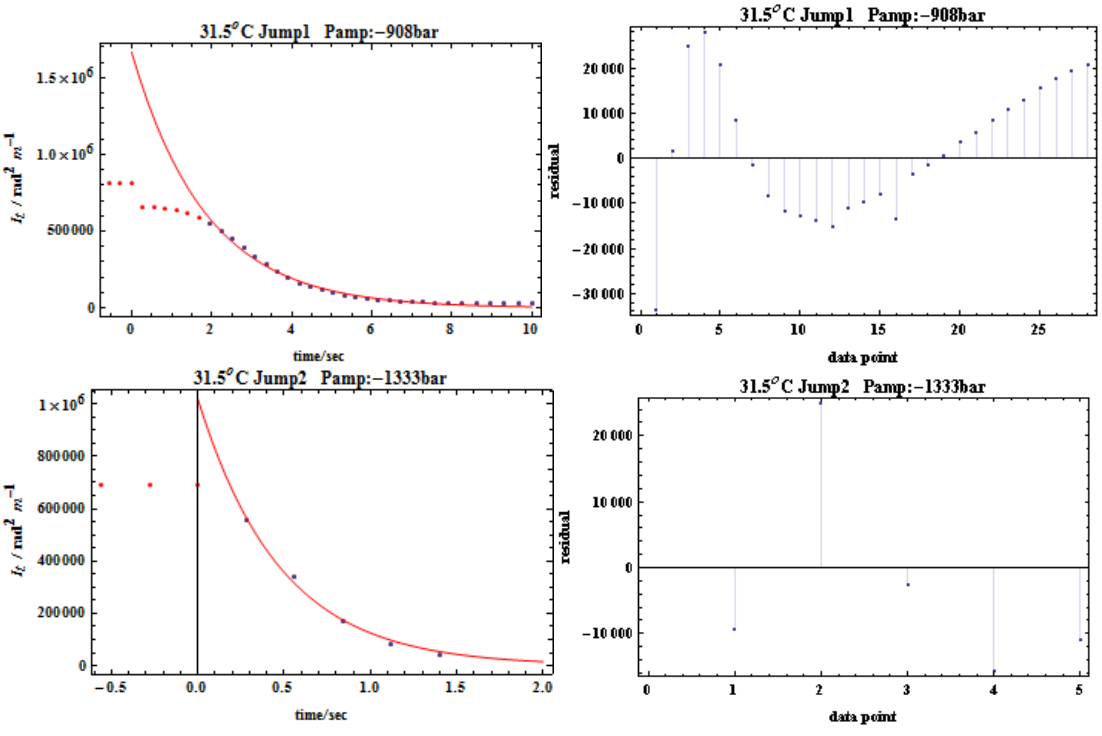
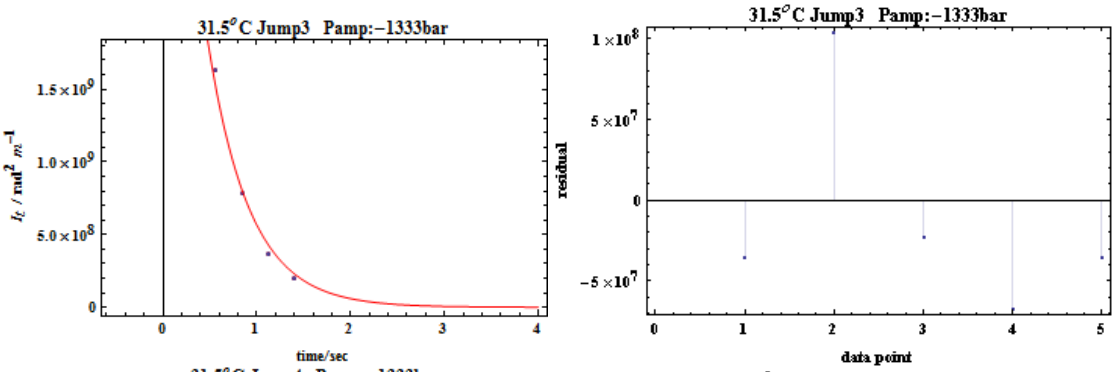


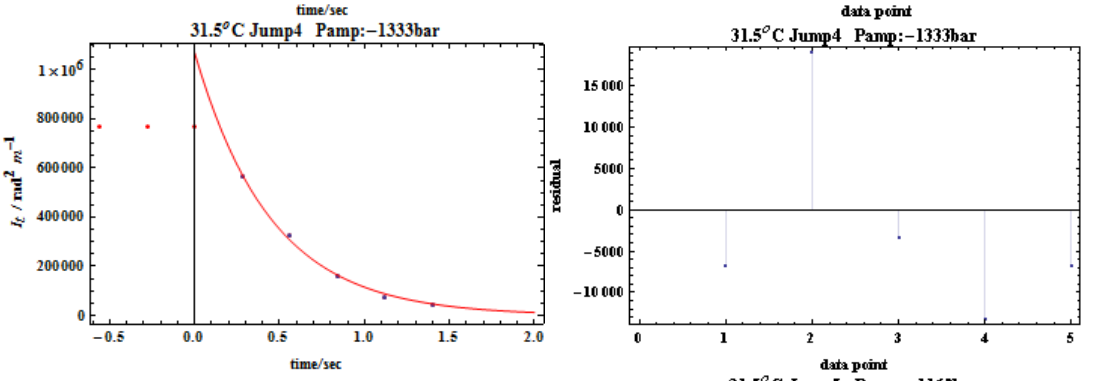
Figure D-4 Exponential model fits to experimental absolute intensities for varying pressure jump amplitudes at 26 °C for a 22.1 wt% water sample. The residuals from model fitting are shown on the right.

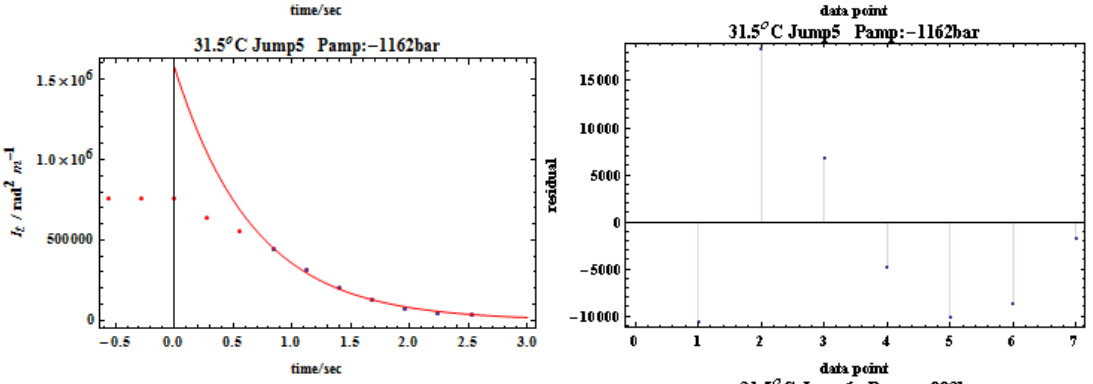
jump	P_{amp}/ bar	k / s^{-1}	error	R^2	ln k	error
1	-965	1.010	0.056	0.994698	0.001	0.054
2	-965	1.029	0.056	0.994911	0.028	0.053
3	-965	1.067	0.060	0.995385	0.065	0.054
4	-965	1.036	0.056	0.994958	0.035	0.053
5	-875	0.813	0.031	0.995975	-0.206	0.038
6	-795	0.553	0.015	0.996536	-0.593	0.027
7	-750	0.426	0.014	0.994226	-0.854	0.033
8	-835	0.273	0.011	0.990466	-1.298	0.040
9	-835	0.619	0.029	0.992214	-0.479	0.045
10	-920	0.915	0.054	0.993261	-0.088	0.057
11	-685	0.259	0.009	0.994626	-1.349	0.035

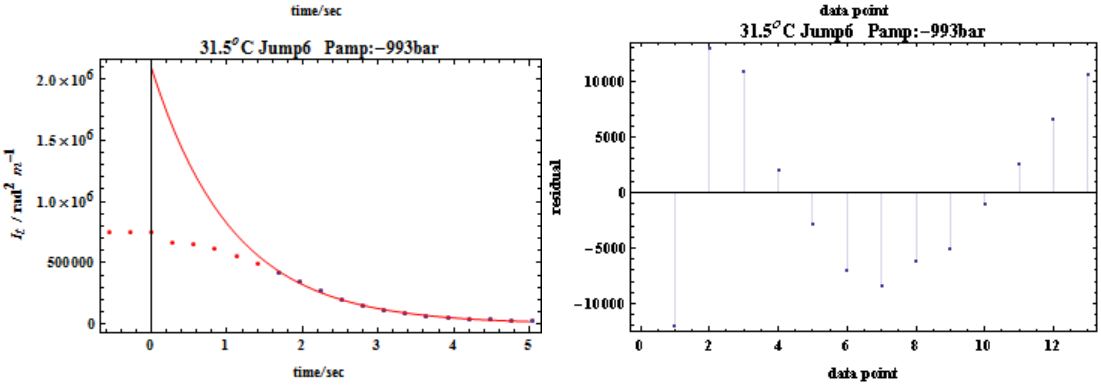
Table D-4 Summary of exponential model fitting parameters obtained from experimental data fitting at 26 °C for lamellar phase decay at 22.1 wt% water sample where k is the rate constant.

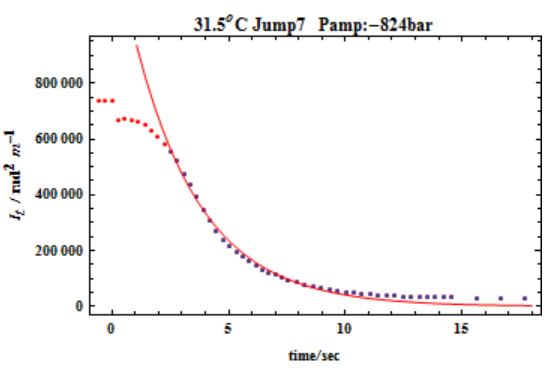


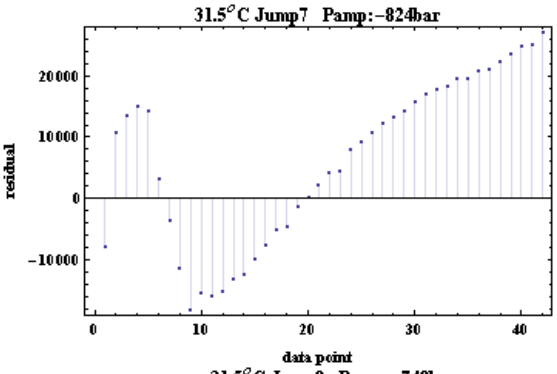

31.5°C Jump3 Pamp:−1333bar
I_t / rad^2 m^{-1}
time/sec
31.5°C Jump3 Pamp:−1333bar
residual
data point

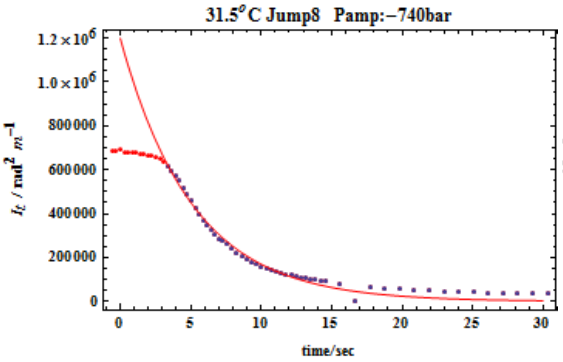

31.5°C Jump4 Pamp:−1333bar
I_t / rad^2 m^{-1}
time/sec
31.5°C Jump4 Pamp:−1333bar
residual
data point

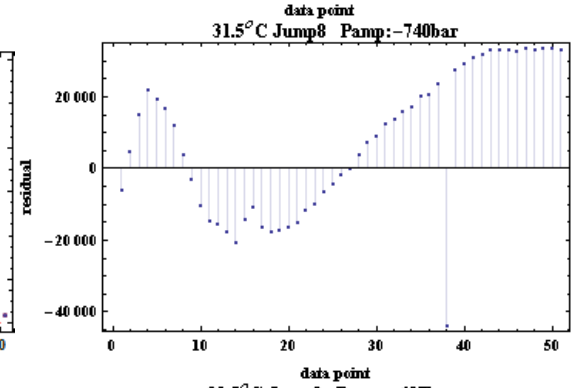

31.5°C Jump5 Pamp:−1162bar
I_t / rad^2 m^{-1}
time/sec
31.5°C Jump5 Pamp:−1162bar
residual
data point

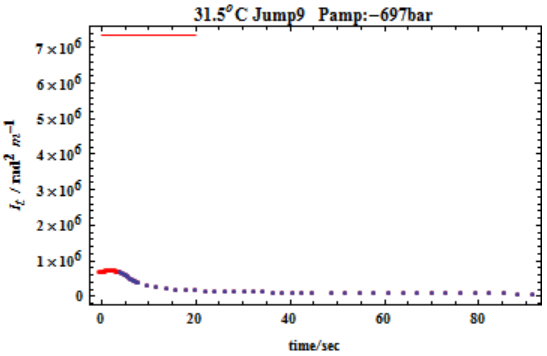

31.5°C Jump6 Pamp:−993bar
I_t / rad^2 m^{-1}
time/sec
31.5°C Jump6 Pamp:−993bar
residual
data point

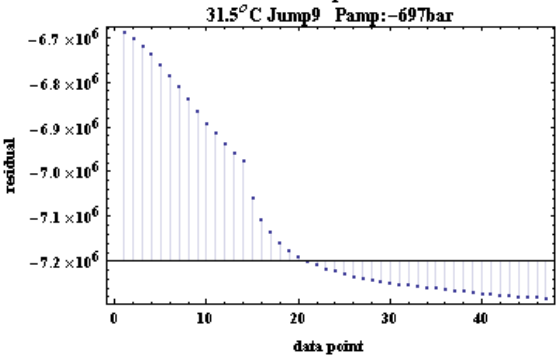

31.5°C Jump7 Pamp:−824bar
800 000
600 000
400 000
200 000
0
0
5
10
15
time/sec


31.5°C Jump7 Pamp:−824bar
20000
10000
0
−10000
residual
0
10
20
30
40
data point


31.5°C Jump8 Pamp:−740bar
1.2×10^6
1.0×10^6
800000
600000
400000
200000
0
0
5
10
15
20
25
30
time/sec


31.5°C Jump8 Pamp:−740bar
20 000
0
−20 000
−40 000
residual
0
10
20
30
40
50
data point


31.5°C Jump9 Pamp:−697bar
7×10^6
6×10^6
5×10^6
4×10^6
3×10^6
2×10^6
1×10^6
0
0
20
40
60
80
time/sec


31.5°C Jump9 Pamp:−697bar
−6.7×10^6
−6.8×10^6
−6.9×10^6
−7.0×10^6
−7.1×10^6
−7.2×10^6
residual
0
10
20
30
40
data point

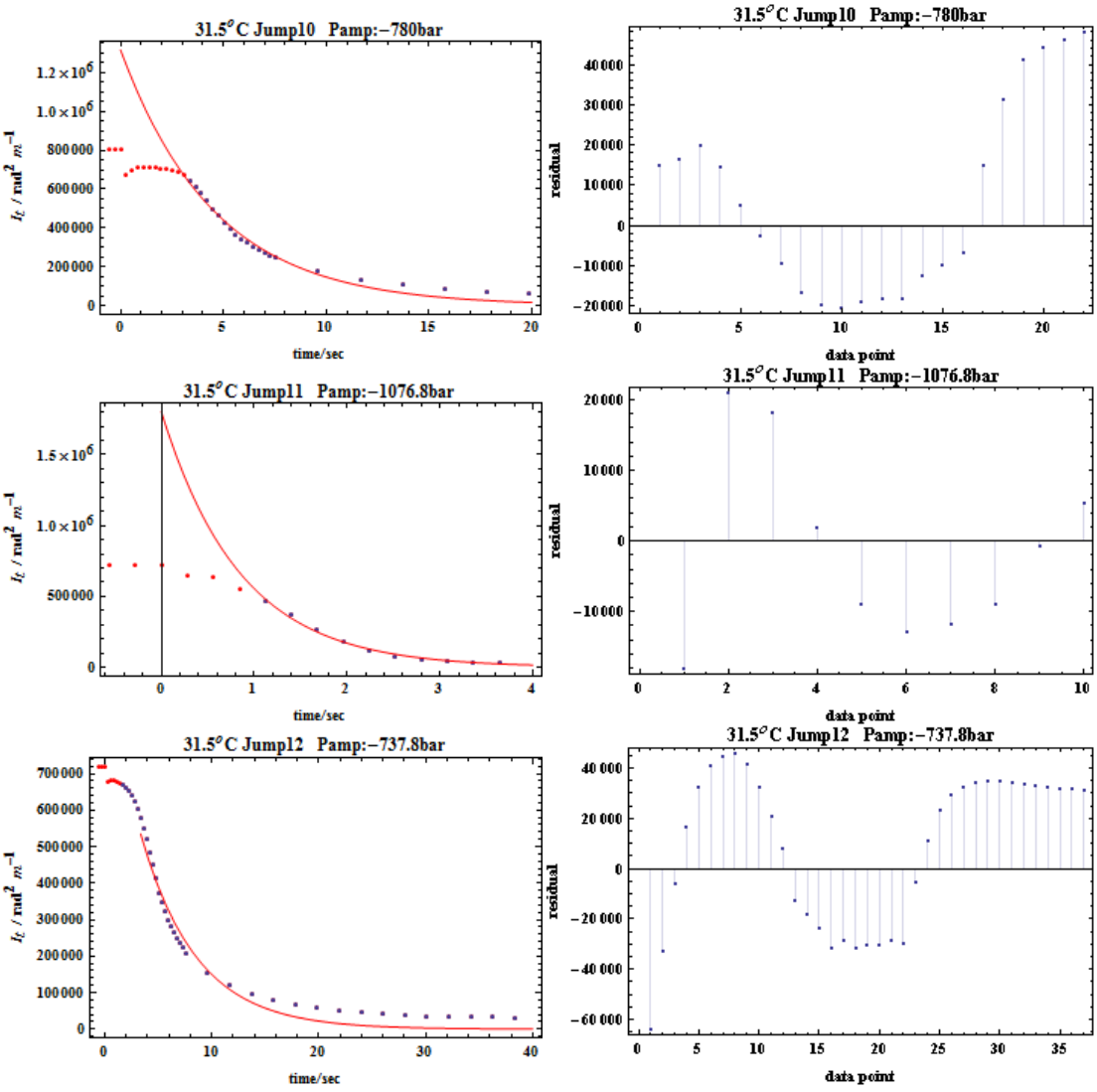
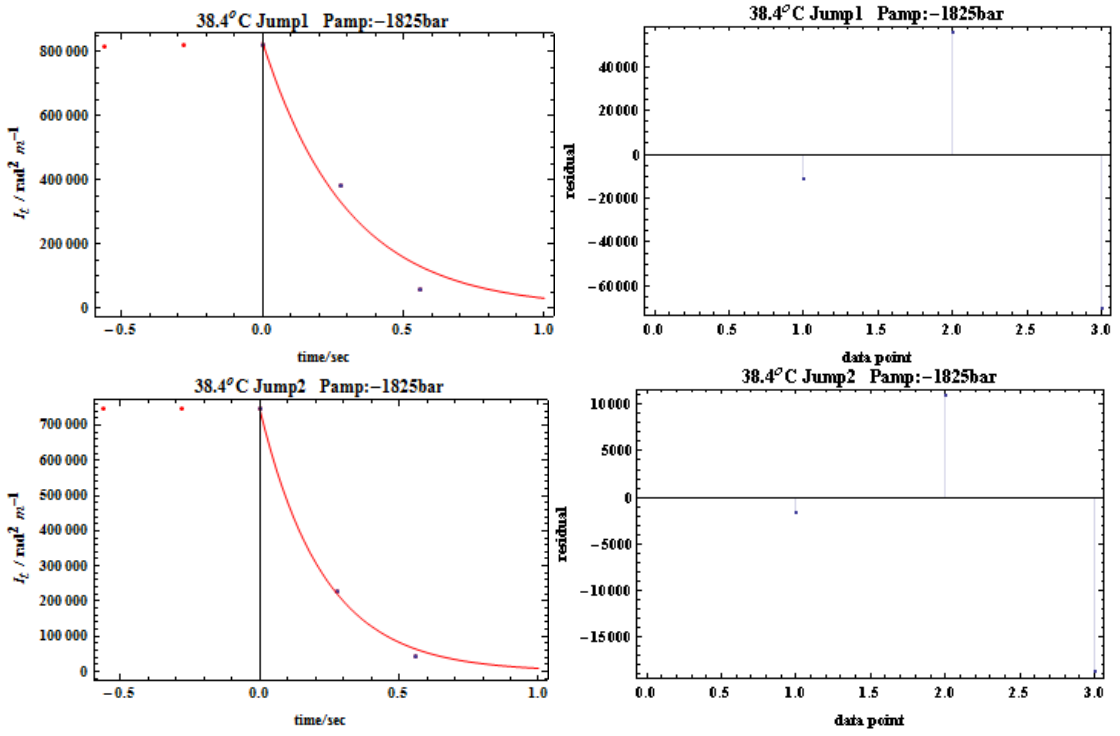
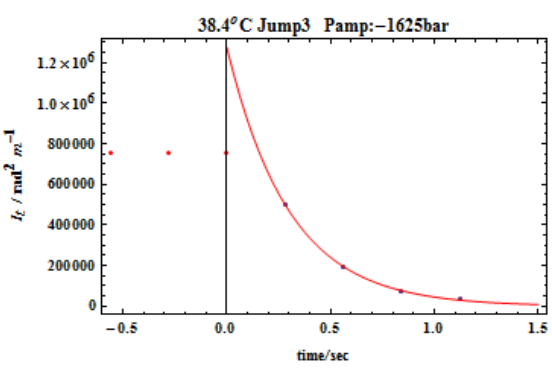


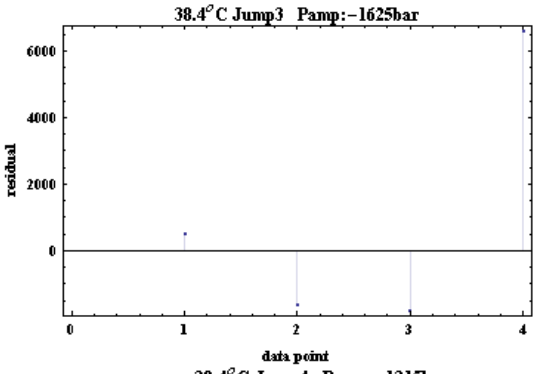
Figure D-5 Exponential model fits to experimental absolute intensities for varying pressure jump amplitudes at 31.5 °C for a 22.1 wt% water sample. The residuals from model fitting are shown on the right.

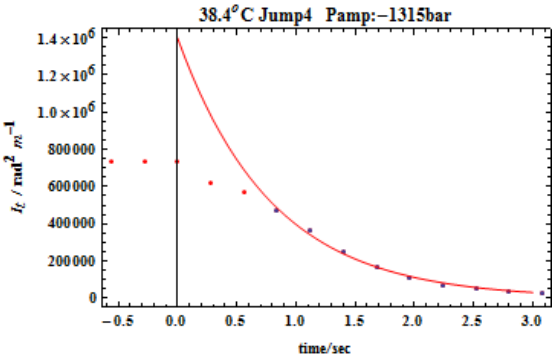
jump	P_{amp} / bar	k/ s^{-1}	error	R^2	ln k	error
1	-908	0.567	0.015	0.996021	-0.568	0.025
2	-1333	2.010	0.131	0.997669	0.742	0.060
3	-1333	-	-	-	-	-
4	-1333	2.227	0.107	0.999697	0.801	0.047
5	-1162	1.666	0.032	0.998039	0.510	0.019
6	-993	0.989	0.023	0.998715	-0.011	0.023
7	-824	0.349	0.010	0.993161	-1.053	0.028
8	-740	0.160	0.007	0.984982	-1.835	0.044
9	-697	-	-	-	-	-
10	-780	0.186	0.012	0.992704	-1.683	0.064
11	-1076.8	1.179	0.050	0.9967	0.164	0.041
12	-737	0.208	0.009	0.991986	-1.570	0.043

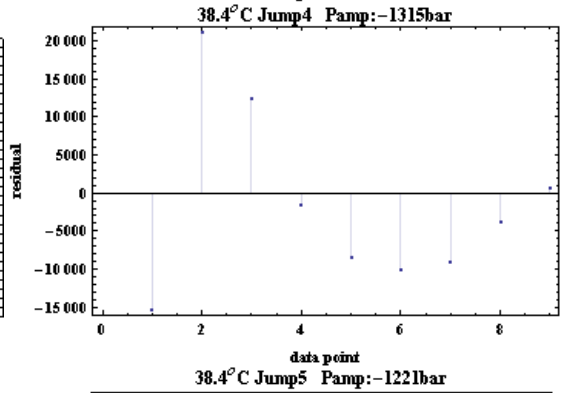
Table D-5 Summary of exponential model fitting parameters obtained from experimental data fitting at 31.5 °C for lamellar phase decay at 22.1 wt% water sample where k is the rate constant.

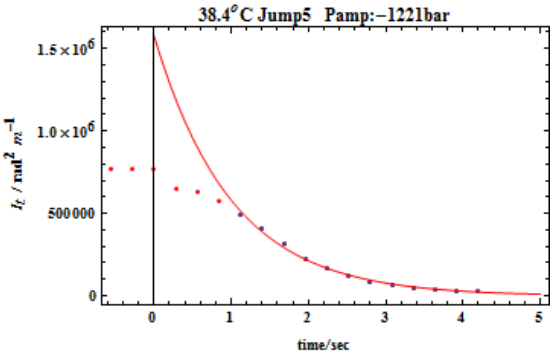


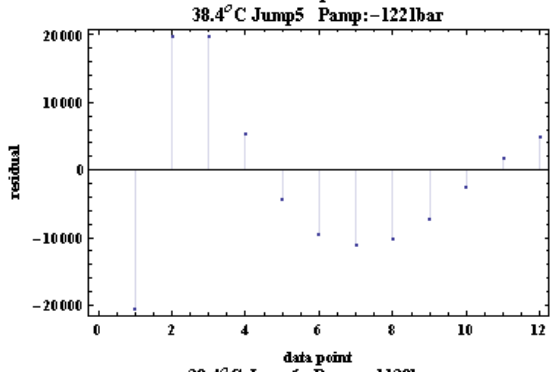

38.4°C Jump3 Pamp:−1625bar
I_t / rad^2 m^{-1}
time/sec

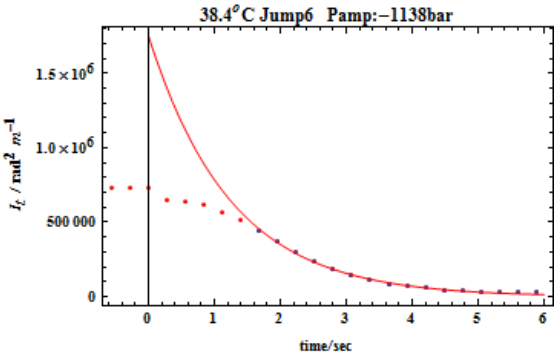

38.4°C Jump3 Pamp:−1625bar
residual
data point

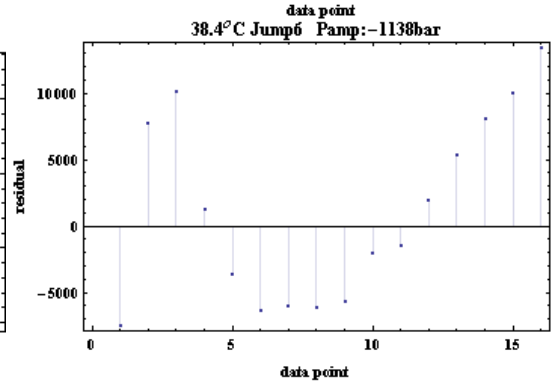

38.4°C Jump4 Pamp:−1315bar
I_t / rad^2 m^{-1}
time/sec

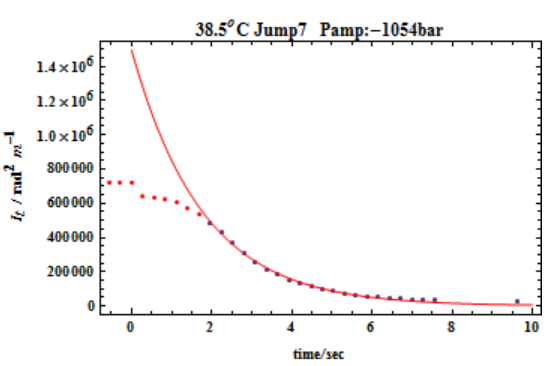

38.4°C Jump4 Pamp:−1315bar
residual
data point

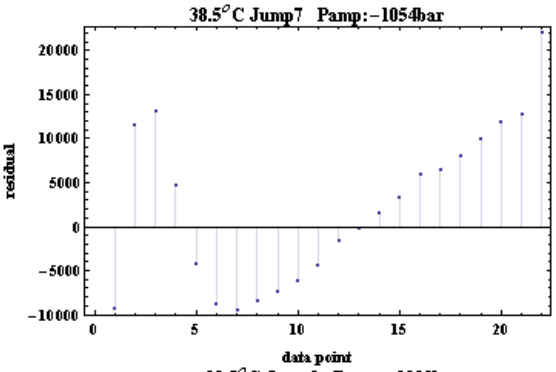

38.4°C Jump5 Pamp:−1221bar
I_t / rad^2 m^{-1}
time/sec

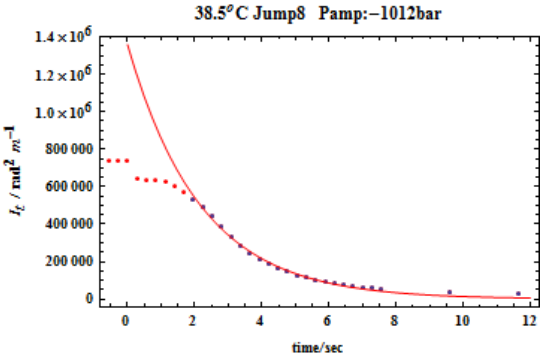

38.4°C Jump5 Pamp:−1221bar
residual
data point

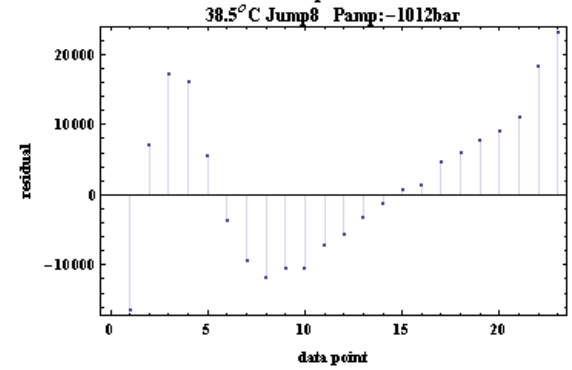

38.4°C Jump6 Pamp:−1138bar
I_t / rad^2 m^{-1}
time/sec

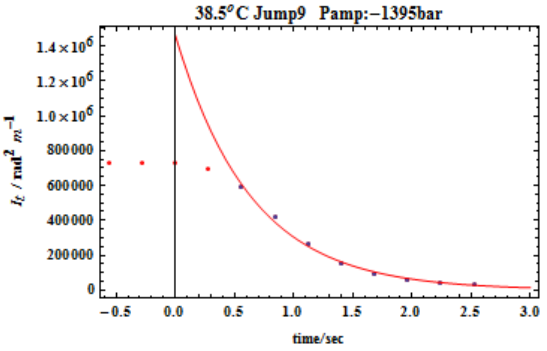

38.4°C Jump6 Pamp:−1138bar
residual
data point

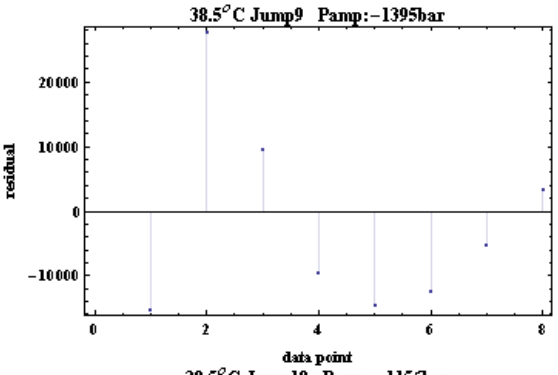

38.5°C Jump7 Pamp:−1054bar
time/sec

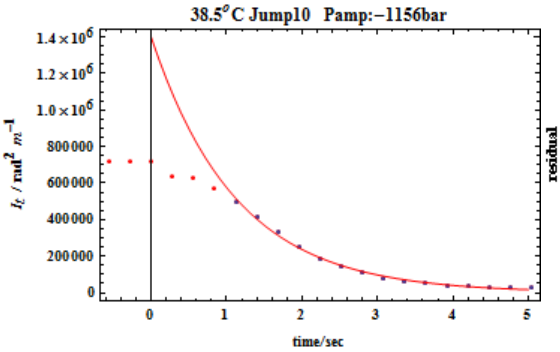

38.5°C Jump7 Pamp:−1054bar
residual
data point

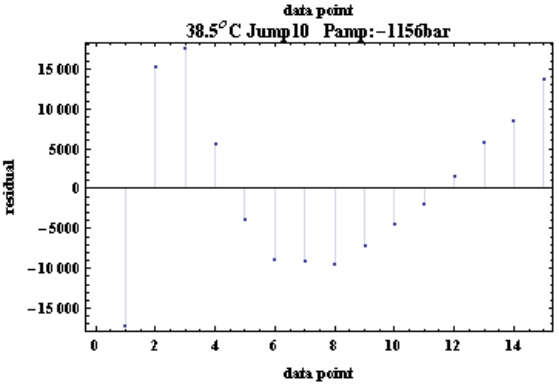

38.5°C Jump8 Pamp:−1012bar
time/sec


38.5°C Jump8 Pamp:−1012bar
residual
data point


38.5°C Jump9 Pamp:−1395bar
time/sec


38.5°C Jump9 Pamp:−1395bar
residual
data point


38.5°C Jump10 Pamp:−1156bar
time/sec


38.5°C Jump10 Pamp:−1156bar
residual
data point

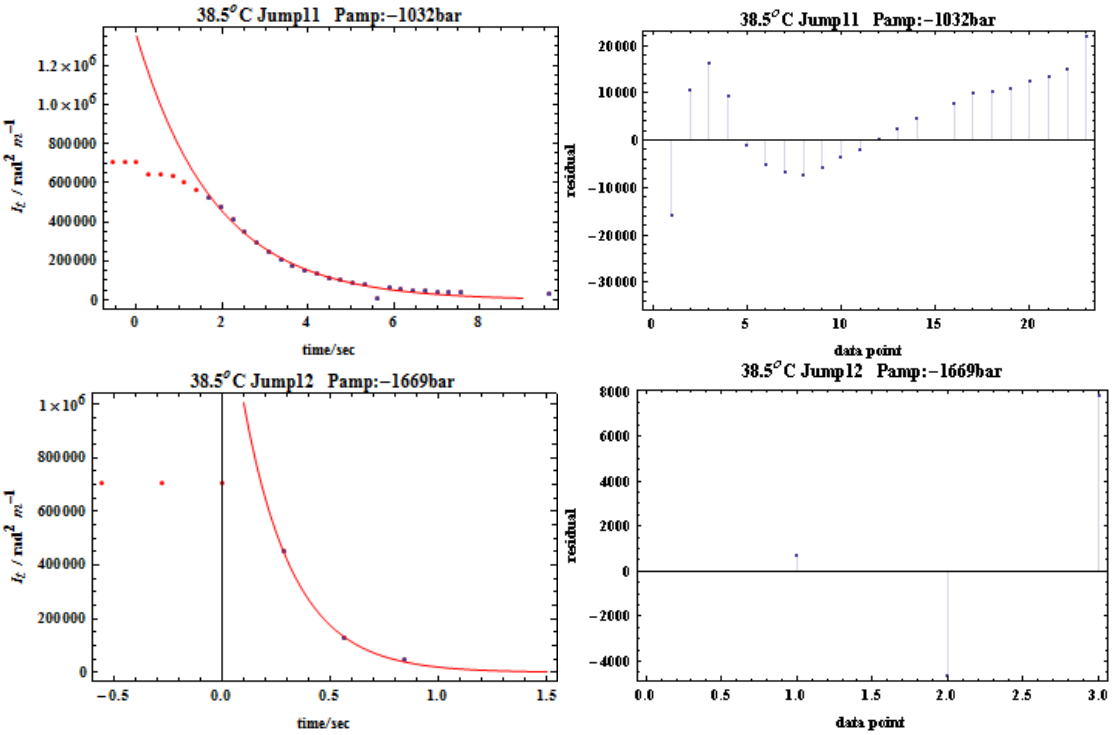
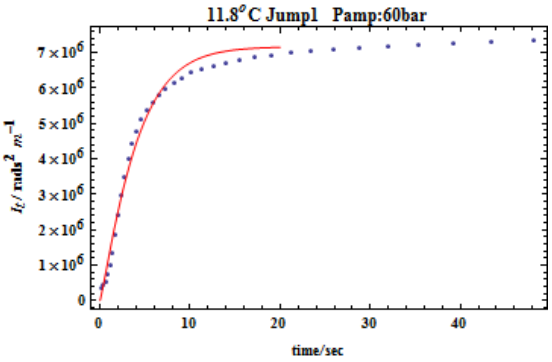


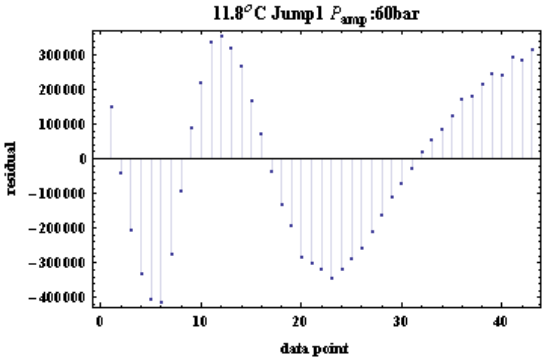
Figure D-6 Exponential model fits to experimental absolute intensities for varying pressure jump amplitudes at 38.5 °C for a 22.1 wt% water sample. The residuals from model fitting are shown on the right.

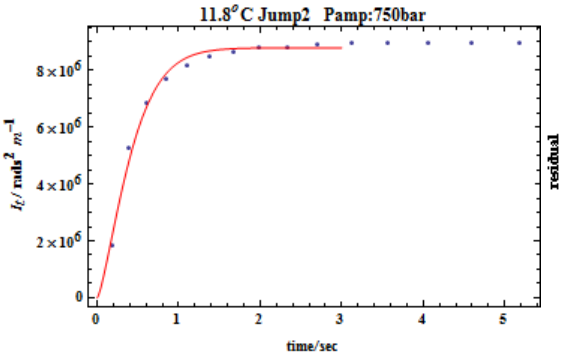
jump	P_{amp}/bar	k /s^{-1}	error	R^2	ln k	error
1	-1825	3.317	0.835	0.990007	1.199	0.225
2	-1825	4.350	0.334	0.999136	1.470	0.074
3	-1645	3.342	0.072	0.999832	1.207	0.021
4	-1315	1.259	0.049	0.997615	0.230	0.038
5	-1221	1.00	0.034	0.997305	0.001	0.034
6	-1138	0.804	0.016	0.998659	-0.219	0.019
7	-1054	0.566	0.011	0.997954	-0.569	0.021
8	-1012	-0.355	0.235	0.205338	-	-
9	-1394	1.572	0.068	0.997467	0.453	0.043
10	-1156	-	-	-	-	-
11	-1032	-	-	-	-	-
12	-1669	4.323	0.199	0.999688	1.464	0.045

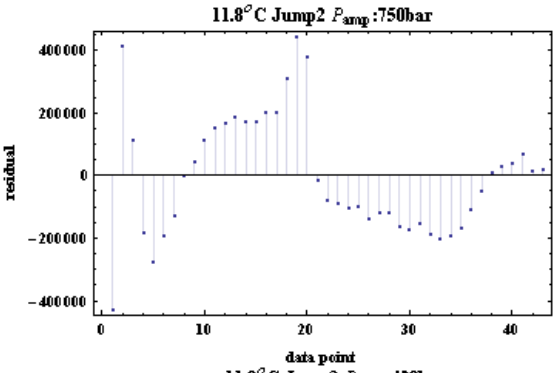
Table D-6 Summary of exponential model fitting parameters obtained from experimental data fitting at 38.5 ^{o}C for lamellar phase decay at 22.1 wt% water sample where *k* is the rate constant.

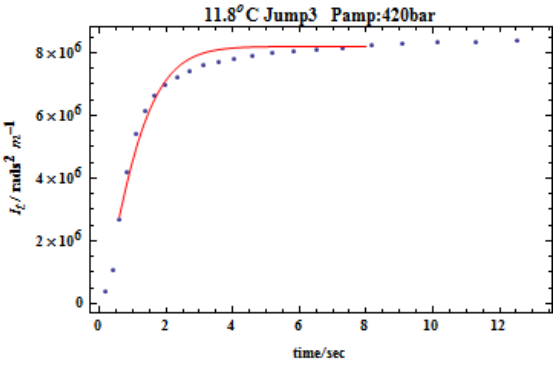
iii) Model fitting to experimental data for an 18.1 wt% water sample.

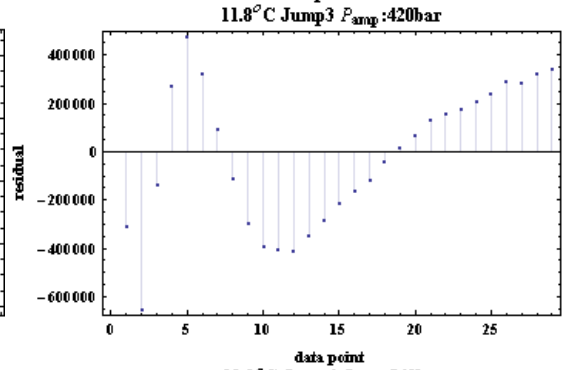


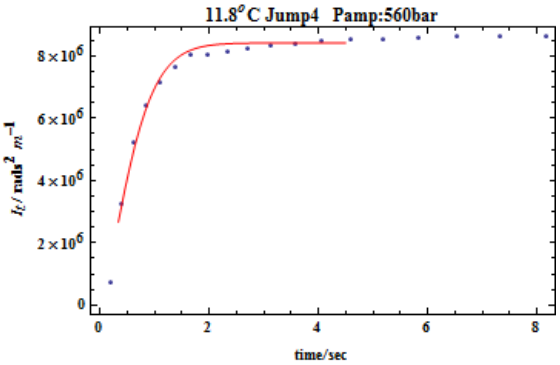


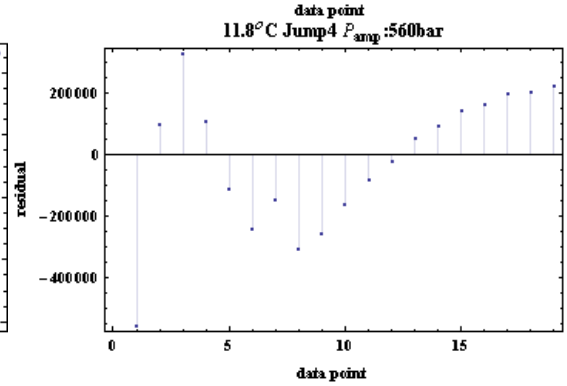












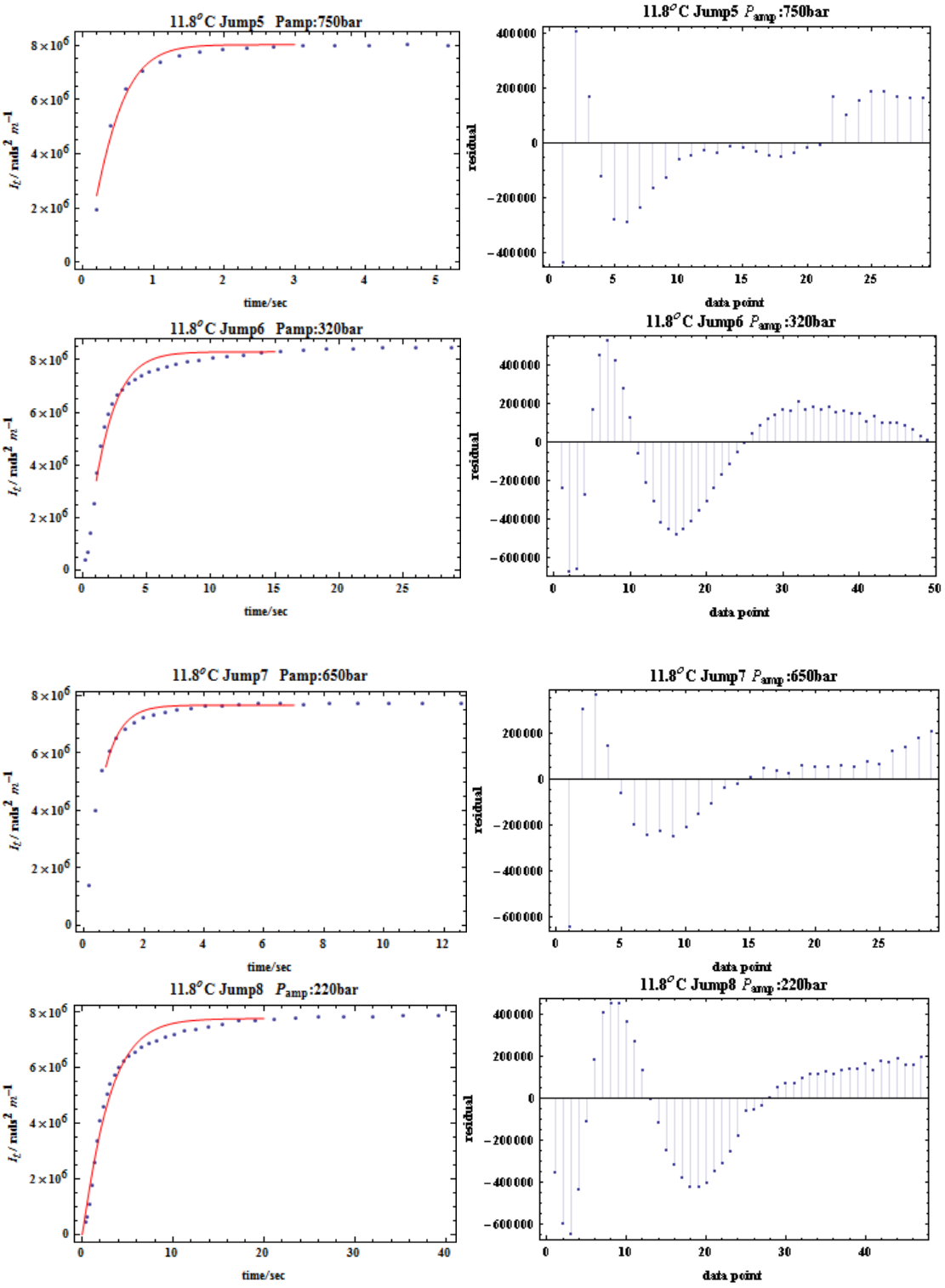
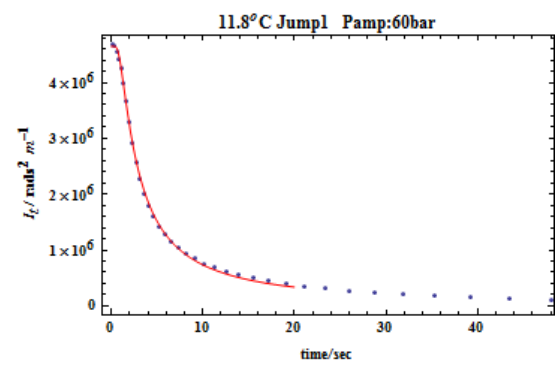
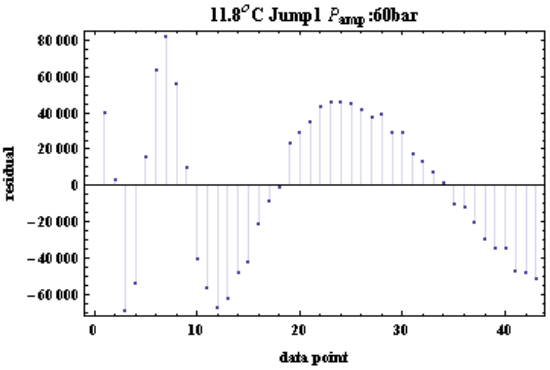


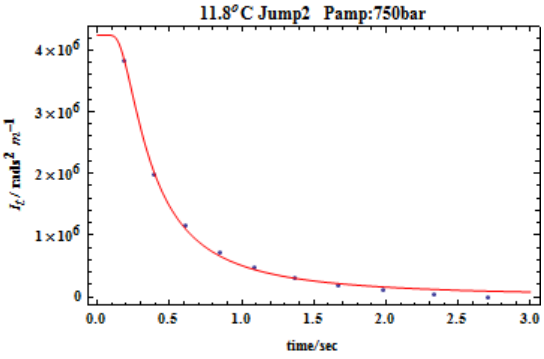
Figure D-7 Avrami model fits to experimental absolute intensities for varying pressure jump amplitudes at 11.8 °C for a 18.1 wt% water sample for lamellar phase growth for the Q_{II}^{G} to lamellar phase transition. The residuals from model fitting are shown on the right.

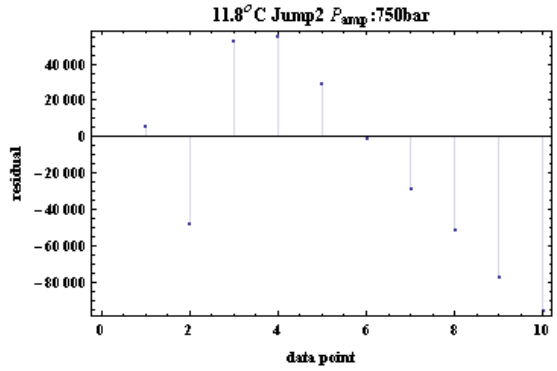
Jump	P_{amp} / bar	k/ s^{-1}	error	n	error	R^2	ln k	error
1	60	0.241	0.007	1.151	0.048	0.998385	-1.422	0.028
2	750	2.166	0.060	1.356	0.076	0.999515	0.773	0.027
3	420	0.855	0.031	1.325	0.087	0.998472	-0.157	0.035
4	560	1.490	0.048	1.411	0.089	0.999177	0.398	0.032
5	750	2.244	0.071	1.241	0.073	0.99948	0.808	0.031
6	320	0.5413	0.017	1.127	0.056	0.998689	-0.614	0.030
7	650	1.721	0.063	1.056	0.062	0.999277	0.543	0.036
8	220	0.337	0.010	1.100	0.052	0.998424	-1.087	0.031

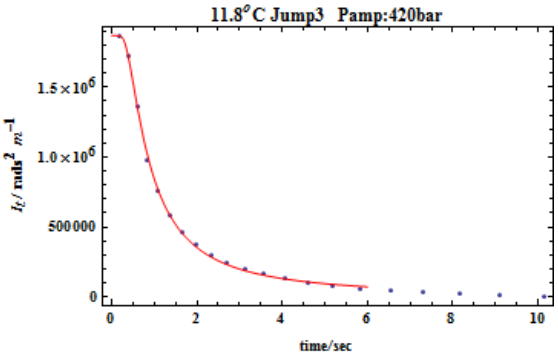
Table D-7 Summary of Avrami model fitting parameters obtained from experimental data fitting at 11.8 °C for lamellar phase decay at 18.1 wt% water sample where *k* is the rate constant.

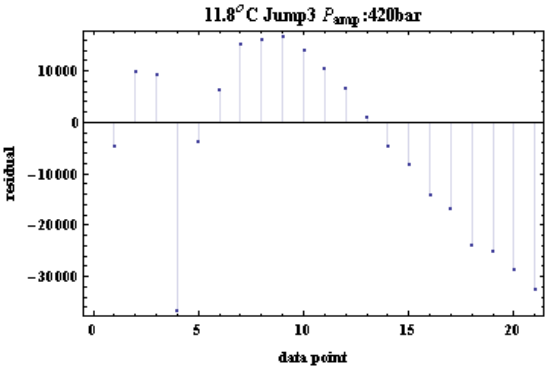

11.8°C Jump1 Pamp:60bar
I_t / rads^2 m^{-1}
time/sec

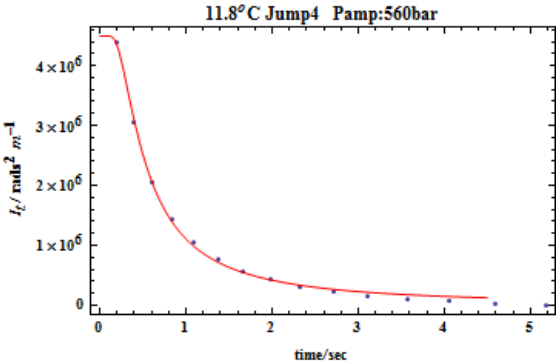

11.8°C Jump1 P_{amp} :60bar
residual
data point

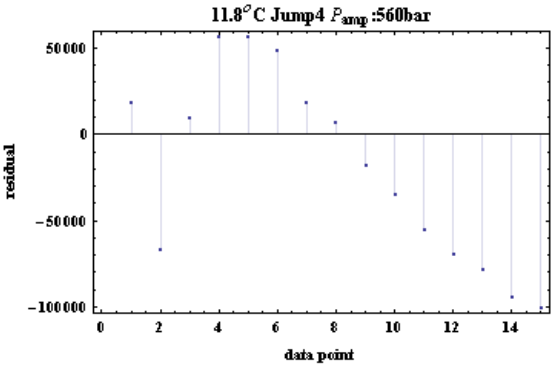

11.8°C Jump2 Pamp:750bar
I_t / rads^2 m^{-1}
time/sec


11.8°C Jump2 P_{amp} :750bar
residual
data point


11.8°C Jump3 Pamp:420bar
I_t / rads^2 m^{-1}
time/sec


11.8°C Jump3 P_{amp} :420bar
residual
data point


11.8°C Jump4 Pamp:560bar
I_t / rads^2 m^{-1}
time/sec


11.8°C Jump4 P_{amp} :560bar
residual
data point

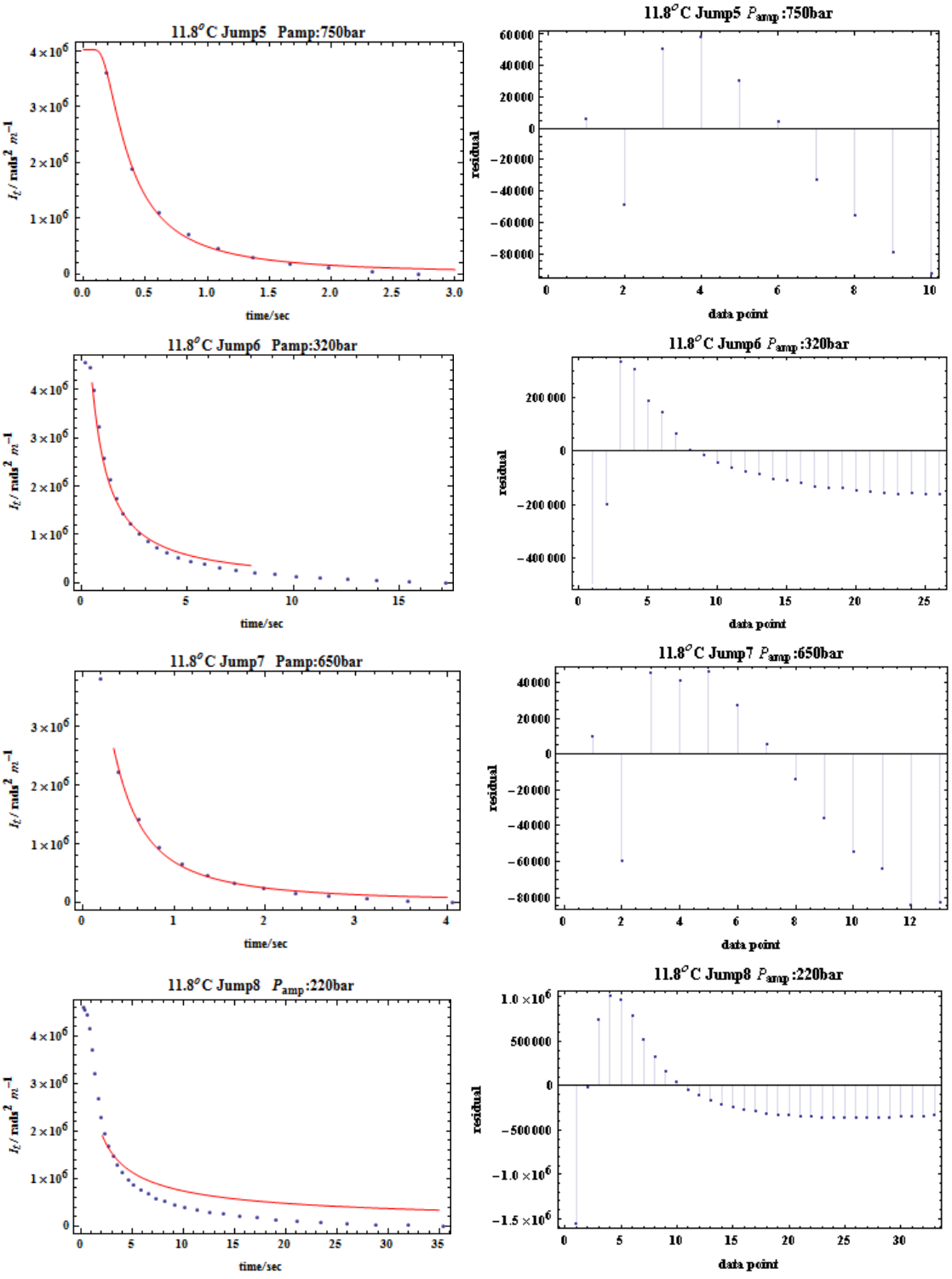
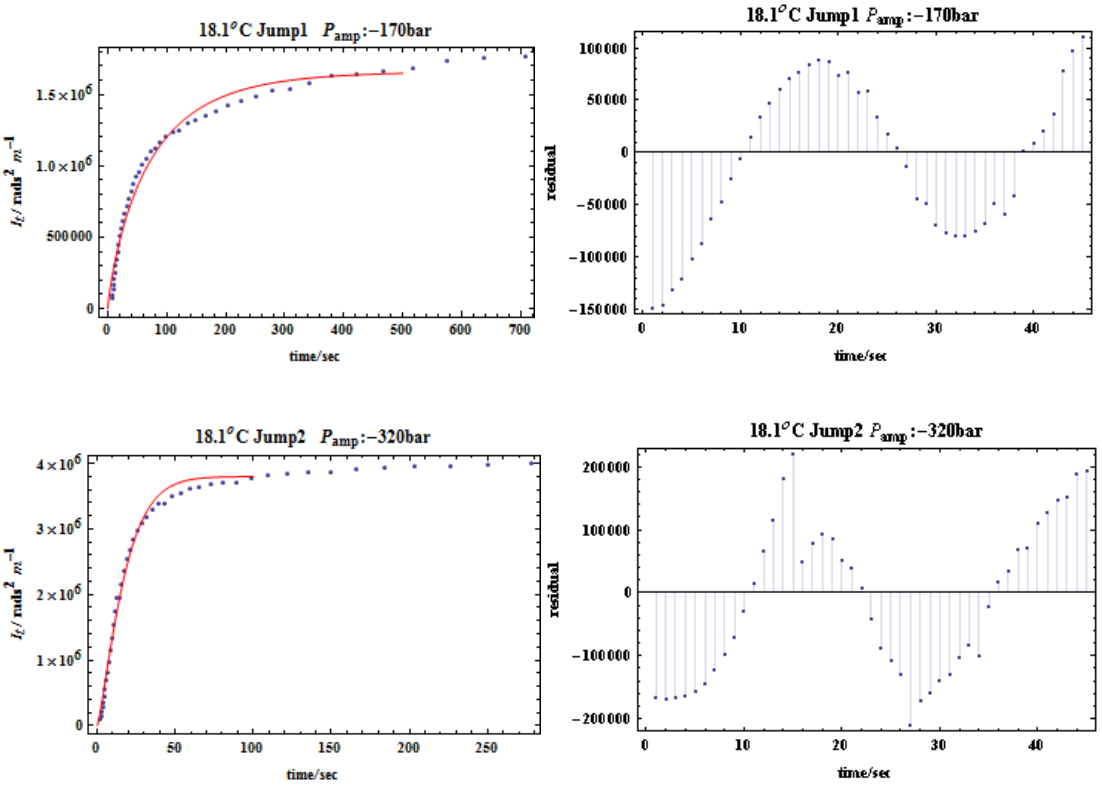
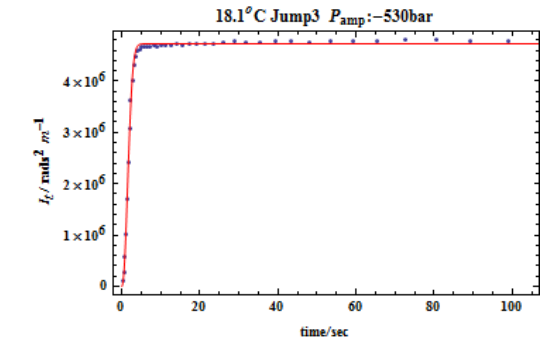


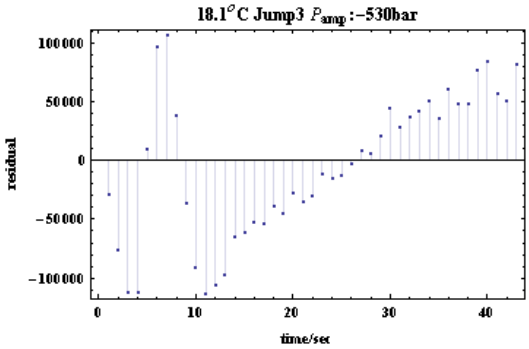
Figure D-8 Avrami model fits to experimental absolute intensities for varying pressure jump amplitudes at 11.8 °C for a 18.1 wt% water sample for Q_{II}^{G} phase decay for the Q_{II}^{G} to lamellar phase transition. The residuals from model fitting are shown on the right.

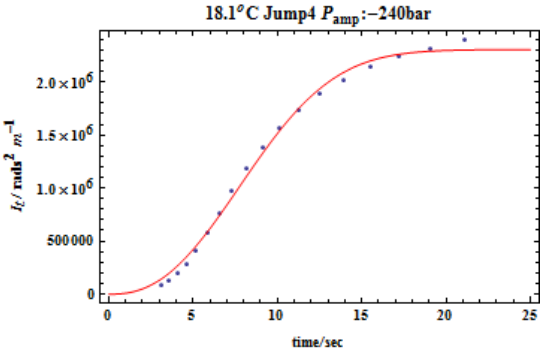
jump	P_{amp} / bar	k / s^{-1}	error	n	error	R^2	ln k	error
1	60	0.241	0.007	1.151	0.048	0.998385	-1.422	0.028
2	750	2.166	0.060	1.356	0.076	0.999515	0.773	0.027
3	420	0.855	0.030	1.324	0.087	0.998472	-0.157	0.035
4	560	1.489	0.048	1.411	0.089	0.999177	0.398	0.032
5	750	2.244	0.071	1.241	0.073	0.99948	0.808	0.031
6	320	0.541	0.017	1.127	0.056	0.998689	-0.614	0.030
7	650	1.721	0.063	1.056	0.062	0.999277	0.5428	0.036
8	220	0.337	0.010	1.100	0.052	0.998424	-1.087	0.031

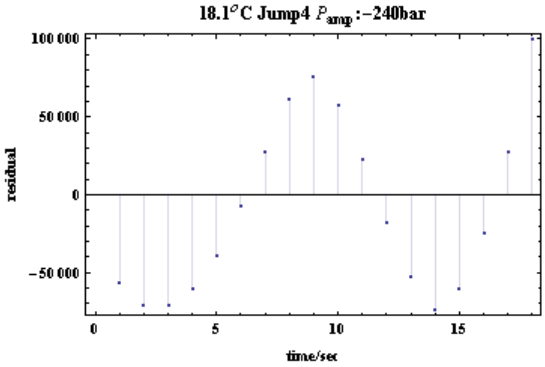
Table D-8 Summary of Avrami model fitting parameters obtained from experimental data fitting at 11.8 °C for lamellar phase decay at 18.1 wt% water sample where *k* is the rate constant.

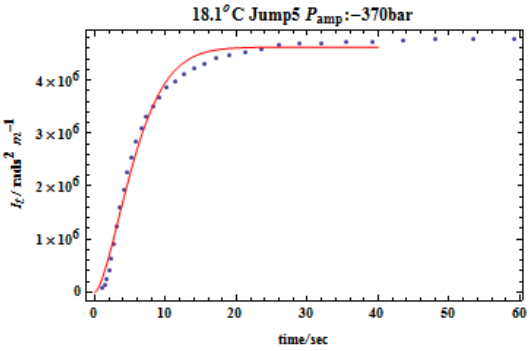


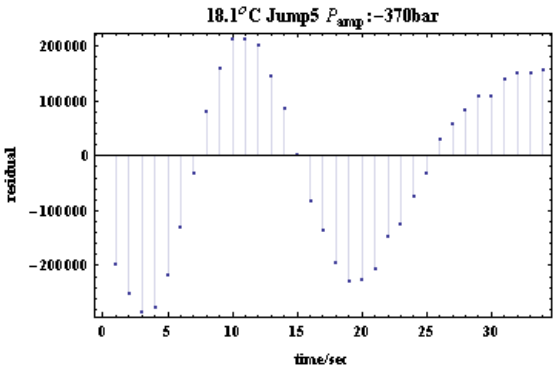

18.1°C Jump3 P_{amp}:−530bar
I_t/ rads^2 m^{-1}
time/sec

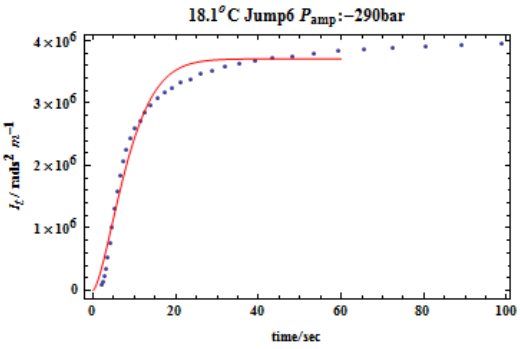

18.1°C Jump3 P_{amp}:−530bar
residual
time/sec

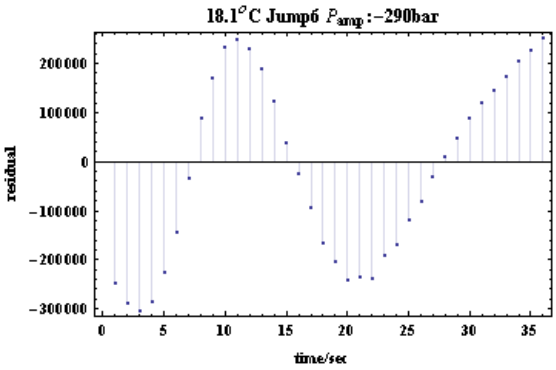

18.1°C Jump4 P_{amp}:−240bar
I_t/ rads^2 m^{-1}
time/sec


18.1°C Jump4 P_{amp}:−240bar
residual
time/sec


18.1°C Jump5 P_{amp}:−370bar
I_t/ rads^2 m^{-1}
time/sec


18.1°C Jump5 P_{amp}:−370bar
residual
time/sec


18.1°C Jump6 P_{amp}:−290bar
I_t/ rads^2 m^{-1}
time/sec


18.1°C Jump6 P_{amp}:−290bar
residual
time/sec

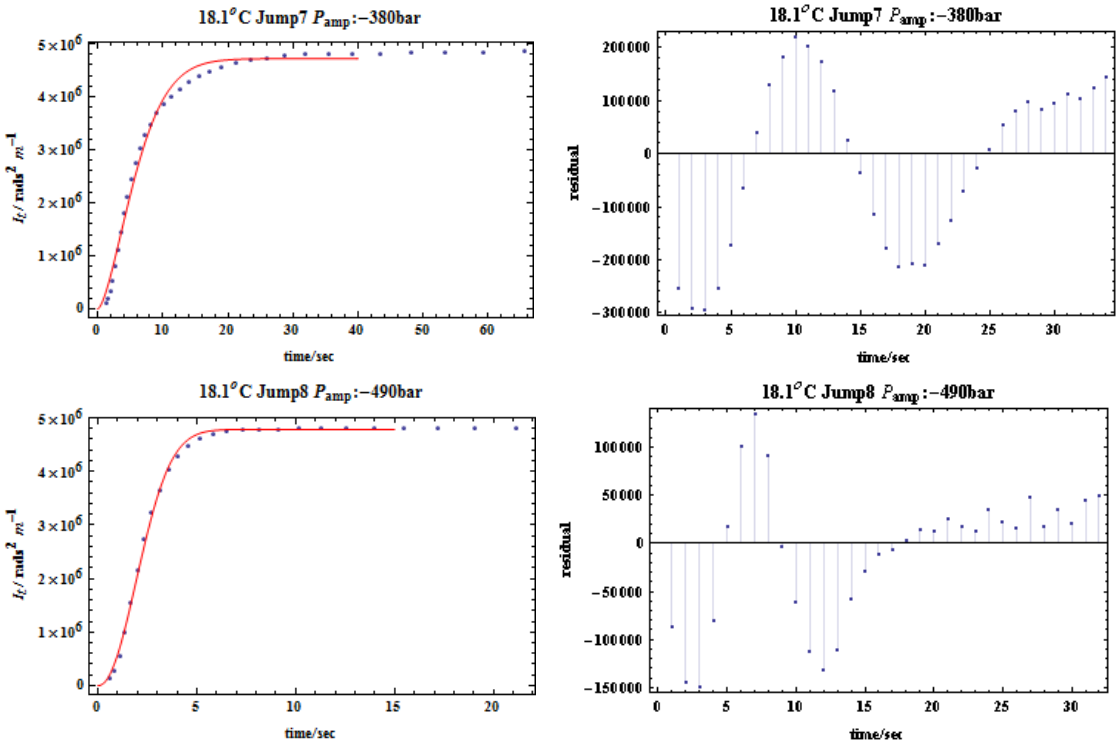
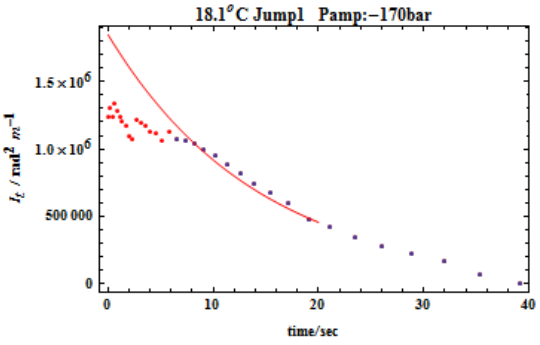
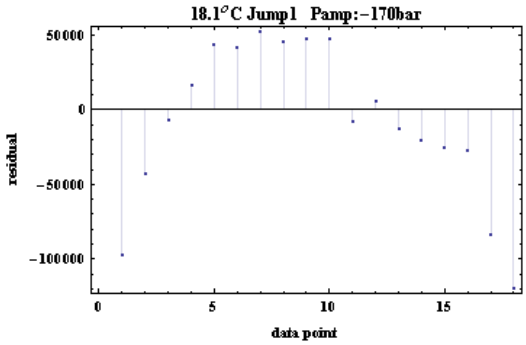


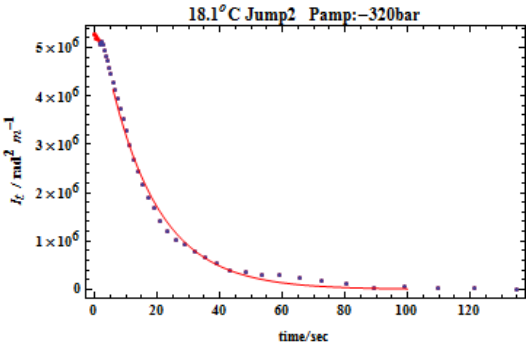
Figure D-9 Avrami model fits to experimental absolute intensities for varying pressure jump amplitudes at 18.1 °C for a 18.1 wt% water sample for Q_{II}^{G} phase growth for the lamellar to Q_{II}^{G} phase transition. The residuals from model fitting are shown on the right.

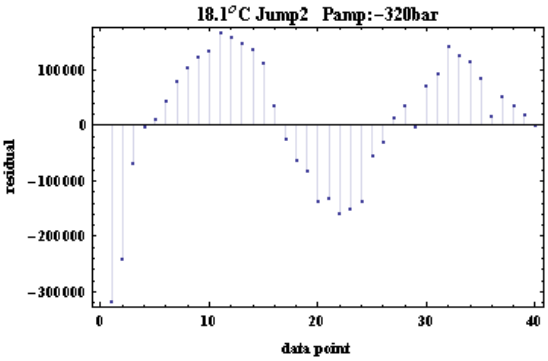
jump	P_{amp}/bar	k / s^{-1}	error	*n*	error	R^2	ln *k*	error
1	60	0.435	0.004	-1.197	0.012	0.999615	-0.833	0.011
2	750	3.262	0.222	-1.738	0.093	0.998676	1.182	0.066
3	420	1.393	0.023	-1.527	0.025	0.99941	0.332	0.016
4	560	2.275	0.076	-1.537	0.047	0.998698	0.822	0.033
5	750	3.273	0.244	-1.723	0.099	0.998477	1.186	0.072
6	320	1.712	0.267	-1.061	0.087	0.977824	0.537	0.145
7	650	2.925	0.167	-1.576	0.063	0.998586	1.073	0.052
8	220	4.834	6.657	-0.646	0.112	0.937311	1.576	0.866

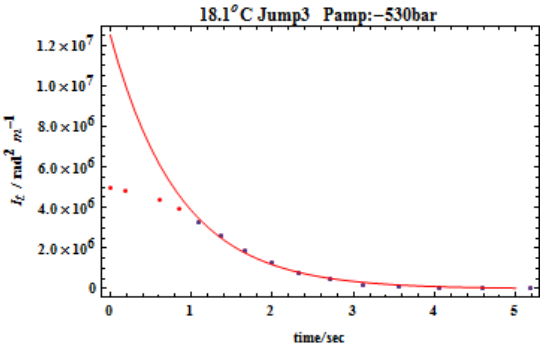
Table D-9 Summary of Avrami model fitting parameters obtained from experimental data fitting at 11.8 °C for Q_{II}^{G} phase growth for the lamellar to Q_{II}^{G} phase transition at 18.1 wt% water sample where *k* is the rate constant.

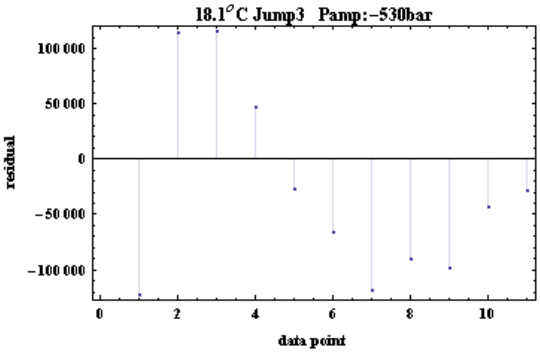

18.1°C Jump1 Pamp:−170bar
I_E / rad^2 m^{-1}
time/sec

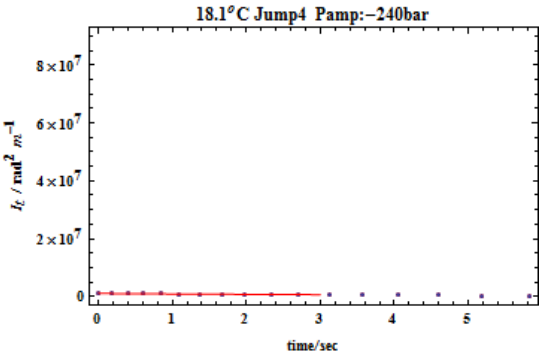

18.1°C Jump1 Pamp:−170bar
residual
data point

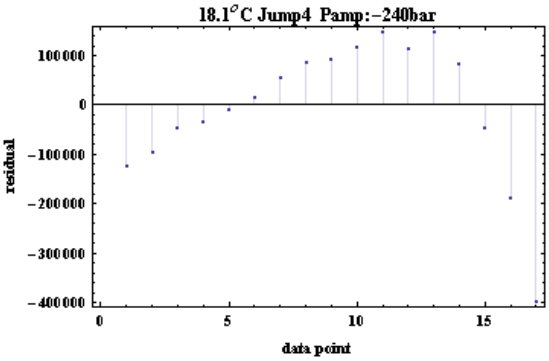

18.1°C Jump2 Pamp:−320bar
I_E / rad^2 m^{-1}
time/sec


18.1°C Jump2 Pamp:−320bar
residual
data point


18.1°C Jump3 Pamp:−530bar
I_E / rad^2 m^{-1}
time/sec


18.1°C Jump3 Pamp:−530bar
residual
data point


18.1°C Jump4 Pamp:−240bar
I_E / rad^2 m^{-1}
time/sec


18.1°C Jump4 Pamp:−240bar
residual
data point

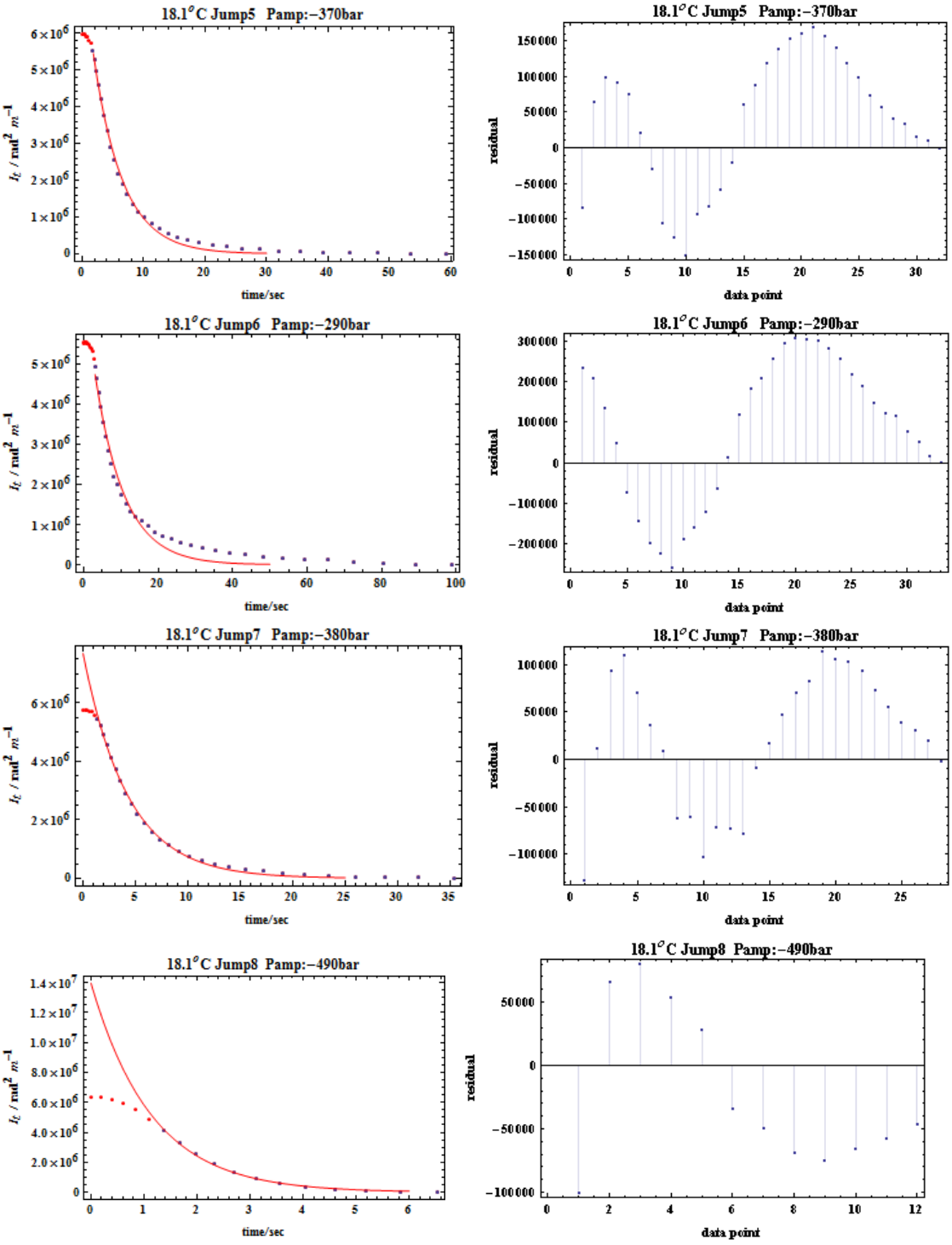


Figure D-10 Avrami model fits to experimental absolute intensities for varying pressure jump amplitudes at 18.1 °C for a 18.1 wt% water sample for lamellar phase decay for the lamellar to Q_{II}^{G} phase transition. The residuals from model fitting are shown on the right.

jump	P_{amp}/bar	k / s^{-1}	error	R^2	ln k	error
1	-170	0.070	0.004	0.994544	-2.660	0.052
2	-320	0.063	0.001	0.998491	-2.764	0.019
3	-530	1.177	0.052	0.996505	0.163	0.043
4	-240	0.172	0.032	0.970475	-1.759	0.172
5	-370	0.211	0.004	0.998274	-1.556	0.020
6	-290	0.128	0.006	0.991393	-2.056	0.044
7	-380	0.235	0.003	0.999163	-1.449	0.015
8	-490	0.876	0.022	0.998819	-0.133	0.024

Table D-10 Summary of Avrami model fitting parameters obtained from experimental data fitting at 18.1 ^{o}C for lamellar phase decay for the lamellar to Q_{II}^{G} phase transition at 18.1 wt% water sample where *k* is the rate constant.